Numerical Simulation For Viscoplastic Fluids Via Finite Element Methods

Dissertation

zur Erlangung des Grades eines
Doktors der Naturwissenschaften

Der Fakultät für Mathematik der Technischen Universität Dortmund
vorgelegt am 2012 von

Mohamed El-Borhamy

Numerical Simulation For Viscoplastic Fluids Via Finite Element Methods

Mohamed El-Borhamy

Dissertation eingereicht am: 09. 11. 2011
Tag der mündlichen Prüfung: 21. 03. 2012

Mitglieder der Prüfungskommission

Prof. Dr. Stefan Turek (1. Gutachter, Betreuer)
Prof. Dr. Heribert Blum (2. Gutachter)
Prof. Dr. Rudolf Scharlau
Prof. Dr. Joachim Stöckler
Dr. Matthias Möller

ABSTRACT

The design of efficient, robust and flexible numerical schemes to cope with nonlinear CFD problems has become the main nerve in the field of numerical simulation. This work has developed and analyzed the Newton-Multigrid process in the frame of monolithic approaches to solve stationary and nonstationary viscoplastic fluid problems. From the mathematical point of view, the viscoplastic problem exhibits several severe problems which might be arisen to draw the mathematical challenges. The major difficulty is the unbounded value of the viscosity which needs regularization. Several regularization techniques have been proposed to cope with this problem yet, while the accuracy is still not even close to be compared to the real model. Herein, two methods are used for the treatment of the non-differentiability, namely Bercovier-Engelman and modified bi-viscous models regularizations. To compute the solution at very small values of the regularization parameter which can be considered numerically as zero, we use the continuation technique. Other difficulties would be addressed in the circle of the nonlinearity, the solenoidal velocity field, as well as the convection dominated problem which are typically involved in the standard Navier-Stokes equation.

The use of mixed higher order finite element methods for flow problems is advantageous, since one can partially avoid the addition of stabilization terms to handle for instance the lack of coercivity, the domination of the convective part as well as the incompressibility. In the case of mixed lower order finite element methods, edge oriented stabilization has been introduced to provide results in the case of the lack of coercivity and convection dominated problems. The main drawback of this stabilizer is to optimize or choose appropriately the free parameters to maintain high accuracy results from the scheme.

Viscoplastic fluids are involved in many industrial applications which require numerical simulation to get a big mathematical insight and to predict the fluids behavior. The dependence of pressure on the viscoplastic constitutive law is confirmed as much as the dependence of velocity. Moreover, the behavior of the pressure is strongly related to the yield property for the unyielded regimes. In the case of a constant yield stress value together with the absence of the external densities, the field of pressure is prescribed by the null value wherever the null value of the deformation tensor is considered. Real life examples to prescribe the behavior of the viscoplastic fluids might be described in case of standard benchmarks: viscoplastic flow in channel, viscoplastic flow in a lid driven cavity and viscoplastic flow around a cylinder. In each case we confirm the experimental and theoretical results which are used to analyze viscoplastic problems for the physical behavior with respect to the unyielded regimes and the cessation of time.

Key words: Viscoplastic Fluids, Finite Element Method, Time Stepping Schemes, Newton Method, Multigrid Method.

To my mother
and my father

Acknowledgment

First of all, I would like to express my thanks to Prof. Stefan Turek who has been always helpful and acquainted me with the beauty of numerical analysis as well as for his valuable guidance and his comments with constructive criticism on my work throughout the time of supervision. I am particulary thankful to Prof. Heribert Blum for his valuable lectures in finite element method and theory of elasticity and my special thanks go to Prof. B. Schweizer and Prof. M. Röger to participate their lectures in partial differential equations. I am very grateful to Jun. Prof. D. Göddeke for his providing to the English revision and generally, I would like to acknowledge the FEATFLOW developers, since without the implementation of the code this work would not go to the light, specially the developer of the new version of FEATFLOW. My special thanks go to Dr. A. Ouazzi, since he always has been helpful and patient with my discussion during the time of guidance and M. Köster for his guidance to learn "FEATFLOW2". I would like to acknowledge the departmental server administrators Dr. C. Becker and S. Buijssen for their support to use the LSIII servers and finally, I would like to thank every one from LSIII who has directly and indirectly co-operated with me and contributed to my thesis and to my colleagues for their support on my research.

Dortmund, March 21, 2012

Mohamed El-Borhamy

Contents

1

Introduction

1.1 Motivation

So far, the growing interest in complex fluids has been motivated by experimental investigations and findings of the mechanical properties in order to predict the complete behavior of the material. Typically, the experimental results require huge cost and time and therefore, an alternative source becomes a pressing variable need. With the development of computational mathematics and computers, the mathematical modeling and simulation are raised to be significant alternatives to the experiments. Hence, the creation of new efficient algorithms to simulate the real behavior of complex fluids becomes an appealing tool in the computational field due to the reduction in time and cost. Furthermore, the variety of the constitutive laws used to describe such behavior of the complex fluids, is conceived of the complement part to encourage new mathematical techniques in the study of existence, behavior and numerical approximation of the solutions for a large class of mixed fluid problems. Therefore, from this harmony between mathematics and physics of fluids, the use of computational mathematics has rapidly developed in various directions. This work presents new flexible, efficient and robust algorithms in the field of nonlinear CFD problems. The involved mathematical methods are an extension of the original research work in the field of finite element methods and fast iterative solvers.

1.2 Viscoplastic Fluids

The description of viscoplastic fluids (Bingham viscoplastic fluids) is typically related to a yield limit which is an intriguing phenomenon that can occur in complex fluids. When a certain function of the stress passes this limit, the medium starts to flow. Viscoplastic fluids always have different regimes inside the flow domain, then one might describe the flow media by one homogeneous medium containing two or three homogeneous phases of flow. This difference comes from its own constitutive law which involves the main properties of the viscoplastic fluids

$$\boldsymbol{\tau} = \begin{cases} (2\mu + \frac{\tau_s}{\|\mathbf{D}\|})\mathbf{D}(u) \text{ if} & \|\mathbf{D}\| \neq 0, \\ \leq \boldsymbol{\tau}_s \text{ if} & \|\mathbf{D}\| = 0. \end{cases} \tag{1.1}$$

The first definition of the constitutive law describes the shear region in which the medium acts as a viscous fluid. The second definition describes the two different regimes associated to the value of the velocity. If the value of the velocity is equal to zero then it is interpreted as a rigid medium while, if the value is constant the medium can be interpreted as plug medium which is moving with the flow with constant velocity. The aim here is to prove that the pressure is not far away from the constitutive equation, and it is constitutive dependent. The distribution of the pressure is related strongly to the yield stress parameter

$\boldsymbol{\tau}_s$. In the shear region $\|\mathbf{D}\| \neq 0$ the distribution of the pressure is similar to the distribution of a viscous fluid while, in the case $\|\mathbf{D}\| = 0$, the pressure follows the behavior of Pressure-Yield-Force equation. For example, the predicted pressure distribution in the case of zero external forces and constant yield stress for the viscoplastic flow in channel is a zero distribution over the plug regime and a linear distribution over the shear regime. This is quite similar to the velocity distribution but one degree less, which is a constant distribution over the plug regime and a quadratic distribution over the shear regime.

1.3 Contribution of the Thesis

This thesis presents a monolithic numerical schemes for stationary viscoplastic fluids and non-stationary viscoplastic fluids with Bingham type to investigate the behavior of viscoplastic fluids. The challenge is to construct numerical algorithms to cope theoretically and numerically with the naturally inherent mathematical difficulties of viscoplastic fluids. It is based on discretization techniques with different finite elements and special solvers, to provide high accuracy and to simulate the real properties for the viscoplastic fluid in the real life. The mathematical contribution of the thesis is to demonstrate the monolithic approach for viscoplastic fluids represented by the following system:

$$\frac{\partial \boldsymbol{u}}{\partial t} + \boldsymbol{u} \cdot \boldsymbol{\nabla} \boldsymbol{u} + \boldsymbol{\nabla} p = \boldsymbol{\nabla} \cdot \boldsymbol{\tau} + \boldsymbol{f} \quad in \quad \boldsymbol{\Omega} \times (0, T), \tag{1.2a}$$

$$\boldsymbol{\nabla} \cdot \boldsymbol{u} = 0 \quad in \quad \boldsymbol{\Omega} \times (0, T), \tag{1.2b}$$

$$\boldsymbol{u}(\boldsymbol{x}, t) = \boldsymbol{u}^o \quad on \quad \partial\boldsymbol{\Omega} \times (0, T), \tag{1.2c}$$

$$\boldsymbol{u}(\boldsymbol{x}, 0) = \boldsymbol{u}_o \quad in \quad \boldsymbol{\Omega}, \tag{1.2d}$$

$$\boldsymbol{\tau} = \begin{cases} (2\mu + \frac{\tau_s}{\|\mathbf{D}\|})\mathbf{D}(u) \text{ if} & \|\mathbf{D}\| \neq 0, \\ \leq \boldsymbol{\tau}_s \text{ if} & \|\mathbf{D}\| = 0. \end{cases} \tag{1.2e}$$

The methodology of discretization for the nonstationary problem is based on a separation between time and space. The typical former step is to discretize in time by a one step scheme which is represented by forward Euler, backward Euler, Crank-Nicklson methods or the fractional theta-step scheme method. The consequent step is to discretize in space by the mixed finite element method utilizing the element $Q_2 P_1^{np}$ (unmapped pressure approach). We confirm by the presented results that can be obtained compared to the optimal convergence for the primitive variables $\tilde{Q}_1 Q_0$(unmapped constant pressure approach) and $Q_2 P_1$ (mapped pressure approach), for highly perturbed meshes. After the discretization, the primitive variables are coupled monolithicaly via a global linearized saddle point problem for each time step and utilizing the Newton process as outer nonlinear loop and the multigrid as inner linear loop with cell oriented Vanka smoothers.
Due to the strong coupling between the partial differential equations, a strong flexible nonlinear solver must be developed to cope with the inherent nonlinearity of the problem, and robust linear solvers are required to cover the whole accuracy. These approaches are tackled in the frame of continuous Newton-Multigrid methods. The idea behind the continuous Newton method is to avoid the cumbersome task to choose appropriately the length step for the difference method to calculate the Jacobian matrix. Moreover, the control parameters to switch adaptively between the fixed point defect correction method and the full Newton method are easy to handle.
The base of the monolithic approach is to use the complete set of nonlinear algebraic equations that have arisen from the coupled discretization of the balance equations, involving the constitutive equation to solve as a whole for each time step. The difference between segregated and monolithic methods might be involved in the cost, accuracy and stability. It is widely believed that monolithic solvers are too computationally expensive, and it is hard to design an efficient global preconditioner to maintain the state of the art of the scheme. On the other hand, the monolithic approach is generally acknowledged to be more accurate and robust. The results produced in both the stationary and nonstationary cases are

generally quite reliable describing totally the behavior of viscoplastic fluids.
The presented monolithic approach is validated by using well-known exact solutions from benchmark problems namely, channel flow for Newtonian and viscoplastic fluids, cavity flow for Newtonian, shear thickening and shear thinning fluids in the sense of the error calculations, as well as the computed reference parameters for flow around cylinder. However, to fulfill the objective engineering need of the study, configurations of viscoplastic flow behavior to predict and to highlight the main properties of the fluid with Bingham type are examined. The description of the pressure field and its association with the constitutive law and the cessation of time represented by the decaying of velocity are presented and confirmed with mathematical derivations (see Fig.1.1 and Fig.1.3 respectively). The empiric verification for the behavior of the flow in a lid driven cavity as well as around a cylinder to prove the existence of different flow regimes inside the flow domain are confirmed with coincidence of theoretical and experimental results (see Fig.1.2).

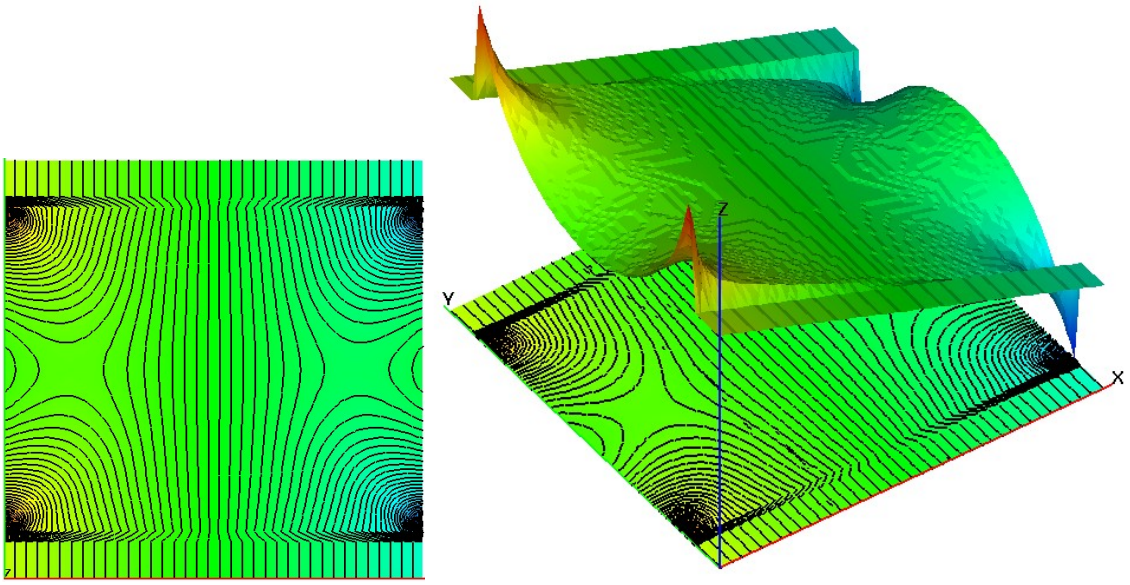

Fig. 1.1. *Bingham flow in Channel:* Pressure 2D/3D diagrams for Bingham viscoplastic flow in channel.

1.4 Organization

The work in this thesis is organized as follows:

Chapter 2 provides the mathematical description of the fluid media in the form of strong formulations and weak formulations associated with the constitutive theory to provide the constitutive laws for different type of fluids. The mathematical description of the viscoplastic fluid from the mathematical and engineering point of view highlights the phenomenological viscoplastic properties; the existence of the yielded and unyielded (plug and dead) regions, the cessation property and the prediction of the pressure distribution are presented. The derivation of the drag and lift forces is provided in terms of line integrals and volume integrals for the generalized Newtonian fluids.

Chapter 3 exposes the standard Galerkin principle in the discretization techniques for the viscoplastic problem. The discretizations are based on the nonconforming finite element method and the conforming

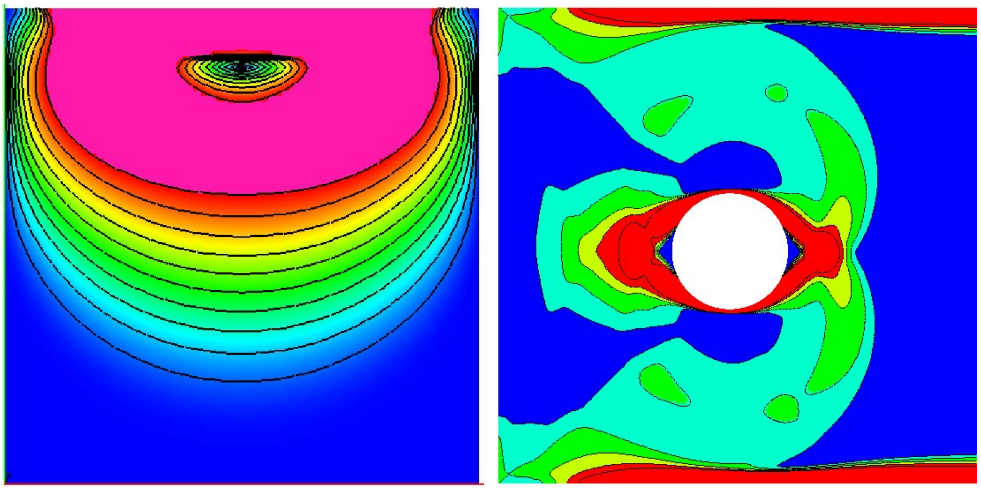

Fig. 1.2. The yielded and unyielded regimes for Bingham viscoplastic flow in lid cavity and around cylinder.

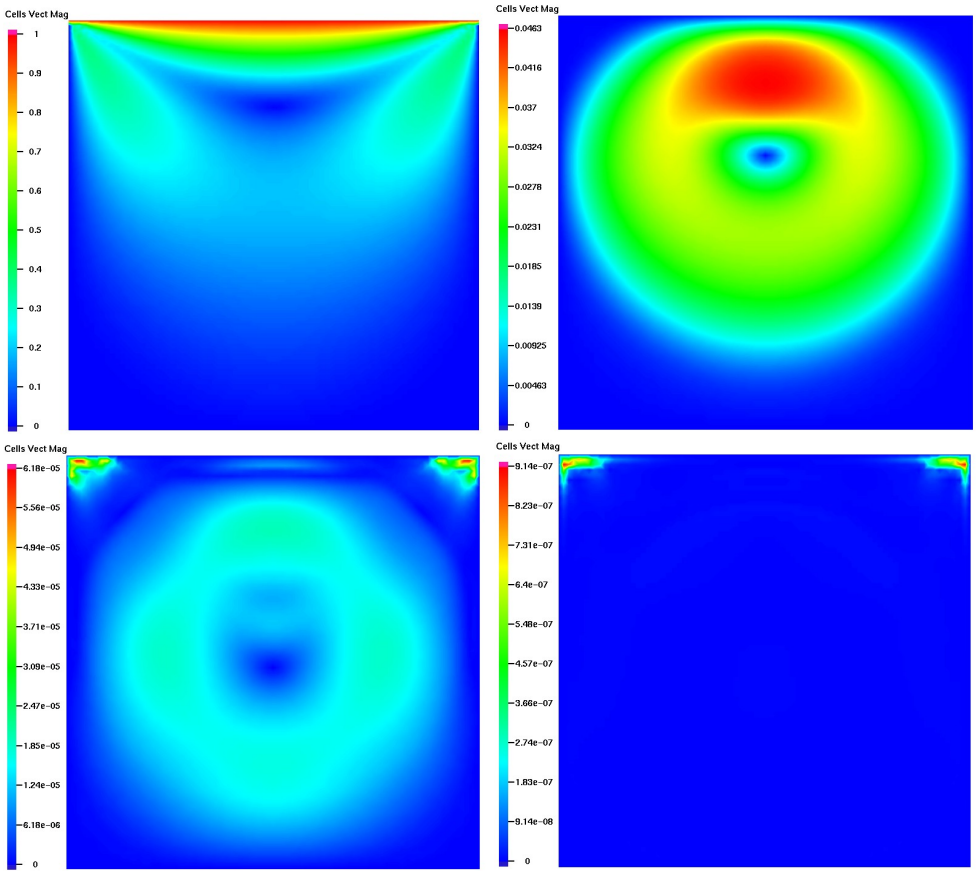

Fig. 1.3. Decaying of velocity for Bingham viscoplastic flow in a lid driven cavity after the upper lid stopped at time=0.5 (Velocity at the instants t=0.499,0.511 (top), t=0.516, 0.520 (bottom) for $\boldsymbol{\tau}_s = 100$ and $\Delta t = 10^{-3}$).

finite element method which are represented by $\tilde{Q}_1 Q_0$ and $Q_2 P_1$ respectively. For the lower order finite element method, one can not avoid stabilization in the symmetric deformation form due to the lack of

coercivity, and this is done by edge oriented stabilization. The aim is to expose the difference between the global and local approaches to handle the pressure problem for a highly perturbed mesh in order to compare the accuracy with respect to the exact solution in the sense of error norms.

Chapter 4 presents solvers for the saddle point problem which arises from the discretization of viscoplastic problems. The treatment of the nonlinearity is handled by the continuous Newton method and the corresponding linear solver is handled by a multigrid technique in combination with multilevel pressure Schur complement methods.

Chapter 5 presents the monolithic approach to solve the stationary viscoplastic problem. The nonlinearity and the solution of the linear problem are handled by the continuous Newton method and the geometric multigrid solver respectively. This approach is used to analyze the behavior of viscoplastic fluids in terms of the phenomenological properties in the standard benchmarks. The presented simulation is used to confirm the well-known physical behavior of viscoplastic fluids.

Chapter 6 presents the monolithic approach for the nonstationary viscoplastic problem. A comprehensive description of time discretization techniques coupled with the finite element method is explained. Careful attention is given to predict the temporary viscoplastic properties in case of cessation and vortex shedding. Consideration is taken with respect to the influence of the yield value on the theoretical upper bound of stopping time and on the frequency of vortex shedding.

Chapter 7 presents the conclusion and future outlook and finally the references.

2

Mathematical Modeling of Viscoplastic Fluids

This chapter presents a general mathematical description of the motion of the continuum viscoplastic fluid media. It begins with the principals of the basic knowledge from the mathematical basis of the continuum media until the complete mathematical cast for the viscoplastic fluid medium.
Depending on the laws of incompressible flow media and variational formulation together with the corresponding constitutive equation, three formulations for the viscoplastic fluid problem: the strong form (equations of balance of momentum and mass), the variational formulation and the dual variational formulation are derived. From the mathematical point of view, the alternative constitutive equations are provided to cope with a severe problem in viscoplastic constitutive laws. On the other side, an extra equation is added by using the tensor valued function or its inverse to deal with the problematic terms separately in the dual problem.
The main scope is divided into three issues for the viscoplastic problem; the mathematical treatment of the well-posedness of the three alternative formulations, the exact solution for the velocity and the predicted pressure distribution, and the phenomenological properties of the viscoplastic medium. Finally, the derivation of drag and lift coefficients for the generalized Newtonian fluids is taken into consideration.

2.1 Introduction

The theory of the continuum media represents now a mature branch of solid and fluid mechanics. Due to its firm mathematical basis, significant developments in the mathematical and computational fields have been evolved, and the understanding of their governing equations can be said to be almost complete. Likewise; theoretical, computational and algorithmic work on approximations in the spatial and time domains are at a stage at which approximations of desired accuracy can be achieved with confidence.
However, our deep concerning will be in viscoplasticity which is a field in continuum mechanics that describes the rate-dependent inelastic behavior of fluids. Rate-dependence means the deformation of the fluid medium that depends on the rate at which loads are applied. The inelastic behavior, the subject of viscoplasticity is plastic deformation, which means the material undergoes unrecoverable deformations when a load level is reached. Rate-dependent plasticity is important for transient plasticity calculations. The main difference between rate-independent plastic and viscoplastic fluid models is, the latter not only exhibit permanent deformations after the application of loads but continue to undergo a creep flow as a function of time under the influence of the applied load as well (see [100]).
In this study; the behavior of the continuous fluid media conveniently begins with a development of a suitable framework within which the motion of the body can be described. This framework is quite dependent on the agencies acting on the body, and also the constitution of the body. In other words; we are concerned in the first instance solely with the geometry of motion which is known as kinematics

and the influence of the inertia forces which is known as kinetics. Then, we will proceed to set out a framework that will be adequate for our problem need.

2.2 Continuous Formulation for the Fluid Media

This section is based on the basic concepts and general principals of continuous medium. The elements of kinematics, the balance law and the stress tensors as well as the constitutive laws in the study of the continuous media will be presented.

2.2.1 Material and Spatial Description

Let us assume a continuous medium (i.e. a body which completely fills the space that it occupies, leaving no pores or empty spaces) which at time t=0 occupies a bounded subset $\boldsymbol{\Omega}$ of $\mathbb{R}^3$ with smooth boundary $\partial\boldsymbol{\Omega}$ which called the reference configuration or the non deformed configuration and at the time $t > 0$, occupies a bounded subset $\boldsymbol{\Omega}_t$ of $\mathbb{R}^3$ which called the actual configuration or the deformed configuration of the body.
Let $\boldsymbol{X} = (X_1, X_2, X_3)$ be the position of arbitrary particle P in the basis (e_1, e_2, e_3) at t=0 and let $\boldsymbol{x} = (x_1, x_2, x_3)$ be the same particle at $t > 0$. The motion of the body is determined by the position $\boldsymbol{x}$ of the material points in space as a function of the reference position $\boldsymbol{X}$ and the time t, which defined by

$$\boldsymbol{x} = \chi(\boldsymbol{X}, t), \tag{2.1}$$

where, $\chi(., t) : \boldsymbol{\Omega} \to \chi(\boldsymbol{\Omega}, t) = \boldsymbol{\Omega}_t$ for every $t > 0$.
Let us assume that for every $t > 0$, $\chi(., t)$ is a continuous injective function, and denote by $\chi^{-1}(., t) : \boldsymbol{\Omega}_t \to \boldsymbol{\Omega}$ the inverse of χ with respect to its first argument, that is

$$\boldsymbol{X} = \chi^{-1}(\boldsymbol{x}, t). \tag{2.2}$$

By using Eq.(2.1) and Eq.(2.2) every quantity defined on the body can be regarded either as a function of $\boldsymbol{X}$ and t (the case of material description), or as a function of $\boldsymbol{x}$ and t (the case of the spatial description). So, the first derivative of $\boldsymbol{X}$ with respect to time gives us the velocity and the second derivative of $\boldsymbol{X}$ with respect to time of the particle at the time $t > 0$ gives us the acceleration which can be written as follows:

$$\boldsymbol{u} = \frac{d\boldsymbol{x}}{dt} = \frac{d}{dt}\chi(\boldsymbol{X}, t). \tag{2.3}$$

$$\mathbf{a} = \frac{d\boldsymbol{u}}{dt} = \frac{d^2x}{dt^2} = \frac{d^2}{dt^2}\chi(\boldsymbol{X}, t). \tag{2.4}$$

Of course the velocity vector $\boldsymbol{u}$ defined in the Eulerian frame depends on $\boldsymbol{x} \in \boldsymbol{\Omega}_t$ and $t > 0$. So that the material derivative of the velocity with respect to time can be represented by the following:

$$\mathbf{a} = \frac{\partial \boldsymbol{u}}{\partial t} + (\boldsymbol{u} \cdot \boldsymbol{\nabla})\boldsymbol{u}, \tag{2.5}$$

where the first part called the spatial derivative term and the second part called the convective term.

2.2.2 Rate of Deformation and Spin Tensors

A deformation of the reference configuration $\boldsymbol{\Omega}$ is the function χ which defined by (2.1) for a fixed $t > 0$. The deformation gradient can be defined at each point of $\boldsymbol{\Omega}$ by the following matrix,

$$\mathbf{F} = (F_{ij}), \qquad F_{ij} = \frac{\partial \chi_i}{\partial X_j}. \tag{2.6}$$

So, the spatial gradient of the velocity $\boldsymbol{u} = (u_1, u_2, u_3)$ can be denoted by $\mathbf{L}$ which is

$$\mathbf{L} = \boldsymbol{\nabla}_x \boldsymbol{u}, \qquad L_{ij} = \frac{\partial u_i}{\partial x_j}, \tag{2.7}$$

and in the matrix form

$$\mathbf{L} = \begin{pmatrix} \frac{\partial u_1}{\partial x} & \frac{\partial u_1}{\partial y} & \frac{\partial u_1}{\partial z} \\ \frac{\partial u_2}{\partial x} & \frac{\partial u_2}{\partial y} & \frac{\partial u_2}{\partial z} \\ \frac{\partial u_3}{\partial x} & \frac{\partial u_3}{\partial y} & \frac{\partial u_3}{\partial z} \end{pmatrix}. \tag{2.8}$$

The second invariant of the gradient can be expressed by

$$\|\mathbf{L}\|^2 = \frac{1}{2} \sum_{i,j=1}^{3} [L_{ij}]^2. \tag{2.9}$$

The relation between the tensor $\mathbf{L}$ and the gradient of deformation $\mathbf{F}$ follows from the chain rule

$$\mathbf{L}_{ij} = \frac{\partial u_i}{\partial x_j} = \frac{\partial u_i}{\partial X_k} \frac{\partial \chi_i^{-1}}{\partial x_j}, \tag{2.10}$$

by using Eq.(2.3) and Eq.(2.6) one can get the following

$$\mathbf{L} = \dot{\mathbf{F}}\mathbf{F}^{-1}, \qquad L_{ij} = \dot{F}_{ik} F_{kj}^{-1}. \tag{2.11}$$

The symmetric part of $\mathbf{L}$ is called the rate of deformation tensor and is denoted by $\mathbf{D}$:

$$\mathbf{D} = \frac{1}{2}(\mathbf{L} + \mathbf{L}^T) = \frac{1}{2}(\frac{\partial u_i}{\partial x_j} + \frac{\partial u_j}{\partial x_i}). \tag{2.12}$$

and in its matrix form

$$\mathbf{D} = \frac{1}{2} \begin{pmatrix} 2\frac{\partial u_1}{\partial x} & \frac{\partial u_1}{\partial y} + \frac{\partial u_2}{\partial x} & \frac{\partial u_1}{\partial z} + \frac{\partial u_3}{\partial x} \\ \frac{\partial u_2}{\partial x} + \frac{\partial u_1}{\partial y} & 2\frac{\partial u_2}{\partial y} & \frac{\partial u_2}{\partial z} + \frac{\partial u_3}{\partial y} \\ \frac{\partial u_3}{\partial x} + \frac{\partial u_1}{\partial z} & \frac{\partial u_3}{\partial y} + \frac{\partial u_2}{\partial z} & 2\frac{\partial u_3}{\partial z} \end{pmatrix}. \tag{2.13}$$

In order to deduce the significance of this definition, let us do the following:
By differentiating Eq.(2.1) for t=const, one can get

$$d\boldsymbol{x} = \mathbf{F} d\boldsymbol{X} \qquad (dx_i = F_{ij} dX_j), \tag{2.14}$$

differentiate again Eq.(2.14) w.r.t time to get

$$\frac{d}{dt}(d\boldsymbol{x}) = \frac{d\mathbf{F}}{dt} d\boldsymbol{X}, \tag{2.15}$$

by using the definition of spatial gradient one can get

$$\frac{d}{dt}(d\boldsymbol{x}) = \mathbf{L} d\boldsymbol{X}, \qquad \frac{d}{dt}(dx_i) = L_{ij} dX_j, \tag{2.16}$$

it follows that

$$\frac{d}{dt}|d\boldsymbol{x}|^2 = 2\mathbf{D} d\boldsymbol{x} \cdot d\boldsymbol{x}. \tag{2.17}$$

Hence the rate of deformation tensor characterizes the rate of variation of the distances between adjoint material points in a Eulerian frame. The spin tensor is the skew-symmetric part of the gradient tensor $\mathbf{L}$, i.e.

$$\mathbf{W} = \frac{1}{2}(\mathbf{L} - \mathbf{L}^T), \qquad W_{ij} = \frac{1}{2}(\frac{\partial u_i}{\partial x_j} + \frac{\partial u_j}{\partial x_i}). \tag{2.18}$$

and in matrix form

$$\mathbf{W} = \frac{1}{2}\begin{pmatrix} 0 & \frac{\partial u_1}{\partial y} - \frac{\partial u_2}{\partial x} & \frac{\partial u_1}{\partial z} - \frac{\partial u_3}{\partial x} \\ \frac{\partial u_2}{\partial x} - \frac{\partial u_1}{\partial y} & 0 & \frac{\partial u_2}{\partial z} - \frac{\partial u_3}{\partial y} \\ \frac{\partial u_3}{\partial x} - \frac{\partial u_1}{\partial z} & \frac{\partial u_3}{\partial y} - \frac{\partial u_2}{\partial z} & 0 \end{pmatrix}. \tag{2.19}$$

This tensor characterizes the instantaneous rotation velocity at the spatial point $\boldsymbol{x}$ and the current moment t.

2.2.3 The Balance Laws and Stress Tensor

2.2.3.a Cauchy Stress Tensor

The stress tensor $\boldsymbol{\sigma}$ represents the state of the stress in the deformable body. Assume the resultant force($\boldsymbol{f}_n$) across an infinitesimal surface element $d\mathbf{S}$ with unit normal $\boldsymbol{n}$ is $d\boldsymbol{f}_n$, then the corresponding traction vector(Cauchy stress vector) is defined by

$$\boldsymbol{t}_n = \frac{d\boldsymbol{f}_n}{d\mathbf{S}}. \tag{2.20}$$

The Cauchy stress tensor ($\boldsymbol{\sigma}$) is the second order tensor related to the Cauchy stress vector vector $\boldsymbol{t}_n$ by

$$\boldsymbol{t}_n = \boldsymbol{\sigma}\boldsymbol{n}, \tag{2.21}$$

when $\boldsymbol{\sigma}$ can be decomposed on the orthonormal basis in the the deformed configuration as $\boldsymbol{\sigma} = \sigma_{ij}\boldsymbol{e}_i\boldsymbol{e}_j$, i,j=1,2,3 (see [70]).

2.2.3.b The Mass Balance

Consider $\rho = \rho(\boldsymbol{x}, t)$ is a continuous mass density function, the conservation of mass requires that $dm = \rho d\boldsymbol{x}$, where the dm is the mass of the element occupying the volume $d\boldsymbol{x}$, is constant during the deformation process. By differentiating one can obtain the mass balance law as the following:

$$\frac{d\rho}{dt} + \boldsymbol{\nabla} \cdot (\rho\boldsymbol{u}) = 0. \tag{2.22}$$

If the deformation process is volume preserving(isochoric), then the density is constant, the mass balance equation is reduced to

$$\boldsymbol{\nabla} \cdot \boldsymbol{u} = 0, \tag{2.23}$$

which means the velocity field is a divergence free vector field(solenoidal) (see [70]).

2.2.3.c The Momentum and Moment Laws of Balances

Consider an elementary external resultant force $\boldsymbol{f}(\boldsymbol{x},t)$ is exerted on the elementary volume dV at each point $\boldsymbol{x}$ of the deformed configuration such that the resultant of applied body forces acting on $\boldsymbol{\Omega}_t$ is $\int_{\boldsymbol{\Omega}_t} \boldsymbol{f}(\boldsymbol{x},t)d\boldsymbol{x}$. Suppose that there exists the vector $\boldsymbol{t}_n$ which depends on the point $\boldsymbol{x}$ and also on the direction of the normal $\boldsymbol{n}$ such that an elementary force $\boldsymbol{t}_n d\mathbf{S}$ is exerted on the elementary area $d\mathbf{S}$ at the point $\boldsymbol{x}$. So that, the applied forces corresponding to the resultant vector field $\boldsymbol{f}(\boldsymbol{x},t) : \boldsymbol{\Omega}_t \to \mathbb{R}^3$ and the surface forces corresponding to the vector field $\boldsymbol{t}_n(.,.,t) : \boldsymbol{\Omega}_t \times \mathbf{S} \to \mathbb{R}^3$ form a system of forces. The following two principles hold for every continuous medium subjected to a system of forces, which represented by the following equations for every $t > 0$,

$$\frac{d}{dt}\int_{\boldsymbol{\Omega}} \rho \boldsymbol{u} d\boldsymbol{x} = \int_{\boldsymbol{\Omega}} \rho \boldsymbol{f} d\boldsymbol{x} + \int_{\partial\boldsymbol{\Omega}} \boldsymbol{t}_n d\mathbf{S}, \tag{2.24}$$

$$\frac{d}{dt}\int_{\boldsymbol{\Omega}} \boldsymbol{x} \otimes \rho \boldsymbol{u} d\boldsymbol{x} = \int_{\boldsymbol{\Omega}} \boldsymbol{x} \otimes \rho \boldsymbol{f} d\boldsymbol{x} + \int_{\partial\boldsymbol{\Omega}} \boldsymbol{x} \otimes \boldsymbol{t}_n d\mathbf{S}. \tag{2.25}$$

The equation(2.24) represents the balance law of momentum and the equation (2.25) represents the balance law of angular momentum and $\otimes$ is the exterior product in $\mathbb{R}^3$.

2.2.3.d Cauchy Theorem

From the laws of balances, one can derive the most famous three consequences in the continuum mechanics, these consequences can be summarized in the following theorem (Cauchy theorem) (see [70]),

Theorem 2.2.1 *Assume that the applied body force density $\boldsymbol{f}$; $\boldsymbol{\Omega}_t \to \mathbb{R}^3$ is continuous and that the stress vector field $\boldsymbol{t}_n(.,.,t) : \boldsymbol{\Omega}_t \times \mathbf{S} \to \mathbb{R}^3$ is continuously differentiable w.r.t the variable $\boldsymbol{x} \in \boldsymbol{\Omega}_t$ for each $\boldsymbol{n} \in \mathbf{S}$ and continuous w.r.t. the variable $\boldsymbol{n} \in \mathbf{S}$ for each $\boldsymbol{x} \in \boldsymbol{\Omega}_t$. Then the momentum balance principle and the balance law of angular momentum imply that there exists a continuously differentiable tensor field $\boldsymbol{\sigma}(.,t) : \boldsymbol{\Omega}_t \times \mathbf{S} \to \mathbb{M}^3$ such that:*

(1)

$$\boldsymbol{t}_n(\boldsymbol{x},\boldsymbol{n},t) = \boldsymbol{\sigma}(\boldsymbol{x},t)\boldsymbol{n} \quad \forall \boldsymbol{x} \in \boldsymbol{\Omega}, \quad \boldsymbol{n} \in \mathbf{S}, \quad t > 0 \tag{2.26}$$

(2)

$$\rho\frac{d\boldsymbol{u}}{dt} = \boldsymbol{\nabla}_{\boldsymbol{x}} \cdot \boldsymbol{\sigma}(\boldsymbol{x},t) + \rho\boldsymbol{f} \quad \forall \boldsymbol{x} \in \boldsymbol{\Omega}_t, \quad t > 0 \tag{2.27}$$

(3)

$$\boldsymbol{\sigma}(\boldsymbol{x},t) = \boldsymbol{\sigma}^T(\boldsymbol{x},t) \quad \forall \boldsymbol{x} \in \boldsymbol{\Omega}_t, \quad t > 0 \tag{2.28}$$

where $\boldsymbol{\nabla}_{\boldsymbol{x}} \cdot \boldsymbol{\sigma}$ represents the divergence of the tensor $\boldsymbol{\sigma}$ w.r.t. the spatial coordinates $\boldsymbol{x}$.

In the static equilibrium of the incompressible media, the cauchy stress tensor is identical to the hydrostatic pressure tensor,

$$\boldsymbol{\sigma} = -p\mathbf{I}, \tag{2.29}$$

where p is the pressure. In this case the cauchy stress vector $\boldsymbol{t}_n(\boldsymbol{x},\boldsymbol{n},t) = -p(t)\boldsymbol{n}$, is always normal to the elementary surface elements, its length is constant in space and it is directed inward if $p(t) > 0$(because of the minus sign) or outward if $p(t) < 0$. The main property of the pressure tensor is isotropic, i.e., its components are unchanged by rotation of the frame reference.
In the flowing incompressible media, the stress tensor consists of an isotropic part or pressure part, which

is in general different from the hydrostatic pressure tensor and an anisotropic or viscous part which resists the relative motion,

$$\boldsymbol{\sigma} = -p\mathbf{I} + \boldsymbol{\tau}, \tag{2.30}$$

the viscous stress tensor $\boldsymbol{\tau}$ is of course zero in static equilibrium. Generally, The viscous stress tensor can be quantified or approximated by the Rivlin-Ericksen strain tensors as a functional of rate of deformation form and its substantial derivatives which can be casted in the following form (see [150]):

$$\mathbf{A}_n = \frac{d^n}{d\tau^n}\mathbf{G}_t(\tau)|_{\tau=t}, \tag{2.31}$$

$$\boldsymbol{\sigma} = -p\mathbf{I} + \boldsymbol{\tau}(\mathbf{A}_1, \mathbf{A}_2, ...) = -p\mathbf{I} + \boldsymbol{\tau}(\mathbf{D}, \dot{\mathbf{D}}, \ddot{\mathbf{D}}, ...), \quad \mathbf{A}_1 = \dot{\mathbf{D}}, \mathbf{A}_2 = \ddot{\mathbf{D}}, ..., \tag{2.32}$$

where $\mathbf{G}_t(\tau)$ is the Green relative strain tensor, and the dots indicate differentiation w.r.t. time. Due to the above equation Eq.(2.32), the fluid media can be categorized to the order of Rivilin-Ericksen tensor being zero order fluid, first order fluid and so on.

2.3 Constitutive Theory

In Fact, the principles of balances do not distinguish a material from another, i.e. these equations are not closed set of equations to describe the behavior of a certain deformable material. Therefore, in order to distinguish between different types of material, a constitutive model must be introduced (see [70]). This required another auxiliary equation in appropriate form to specify the material behavior. The constitutive equation can be defined as a rule at a given state, which determines one when the others are known. In this section we expose briefly the fundamental axioms that define a rather general class of constitutive models of continuum fluids. Particularly, the general properties of the constitutive equation for viscoplastic medium.

2.3.1 The Properties of Constitutive Models

Let us address the most general features for the constitutive models:

(a) Constitutive laws do not have the universal character of the balance laws, rather they characterize the behavior of each kind of continuous fluid medium.

(b) The origins of the constitutive laws are often experimental, though they have to obey certain rules of invariance.

(c) In the fluid medium, the dependent variable is often the stress tensor and always is associated with the rate of deformation tensor, pressure and the temperature are considered as independent variables.

2.3.2 Constitutive Axioms

These three axioms are general statements which must be satisfied for any constitutive model (see [150, 193]).

2.3.2.a First Axiom: Thermodynamic Determinism

This axiom postulates:
"the history of the thermokinetic process to which a neighborhood of a point has been subjected determines a calorodynamic process at that point".

2.3.2.b Second Axiom: Material Objectivity

The second basic axiom of the constitutive theory is the principal of material objectivity or frame invariance which postulates:
"the material response is independent of the observer".
This means that; the motion $\boldsymbol{m}^*$ is related to the motion $\boldsymbol{m}$ by a change in observer if

$$\boldsymbol{m}^*(\boldsymbol{x},t) = \boldsymbol{x} + \mathbf{Q}[\boldsymbol{m}(\boldsymbol{x},t) - \boldsymbol{x}_0], \tag{2.33}$$

where $\boldsymbol{x}(t)$ is a point in space, $\mathbf{Q}(t)$ is a rotation and $\boldsymbol{m}(\boldsymbol{x},t) - \boldsymbol{x}_0$ is the position vector of $\boldsymbol{m}(\boldsymbol{x},t)$ relative to an arbitrary origin $\boldsymbol{x}_0$. This relation corresponds to a rigid relative movement between the different observers and the deformation gradient corresponding to $\boldsymbol{m}^*$ is given by

$$\mathbf{F}^* = \mathbf{QF}. \tag{2.34}$$

The cauchy stress tensor transforms according to the rule

$$\boldsymbol{\sigma}^* = \mathbf{Q}\boldsymbol{\sigma}\mathbf{Q}. \tag{2.35}$$

2.3.2.c Third Axiom: Material Symmetry

This axiom defines the symmetry of material which is the set of density preserving changes of reference configuration under which material response functionals are not affected and postulates:
" the symmetry of the material is the set of rotations of the reference configuration under which the response functionals remain unchanged".

2.4 Constitutive Models for Fluids Media

2.4.1 Inviscid Flow(Zero Order Fluid)

Inviscid flow is conceived of as an ideal fluid which has no shear stress or as zero order fluids describing its motion as the rest case of the fluids. The resulting stress is determined fully by the zero order Rivlin-Ericksen tensor,

$$\mathbf{A}_0 \equiv \mathbf{I}. \tag{2.36}$$

Therefore, the inviscid flow is characterized by a constitutive equation of the form

$$\boldsymbol{\sigma} = -p\mathbf{I}, \quad \textit{and} \quad \boldsymbol{\tau} = 0, \tag{2.37}$$

where p is a scalar function which is the pressure, and the minus sign is introduced by convention, in order to conform the traditional form. So that, the Cauchy stress tensor is always directed along the normal to the surface which means it is parallel to the unit normal to the surface.

2.4.2 Unmemorized Viscous Fluids(Fluids with no Memory)

The viscous fluids are conceived of as shear fluids which have shear stress to resist the relative motion among the particles and unmemorized which exhibit no memory. The local stress is entirely due to the local rate of deformation excluding any rate of deformation incorporates history effect(the time derivative part). The general constitutive equation of these fluids can be casted as the following:

$$\boldsymbol{\sigma} = -p\mathbf{I} + \boldsymbol{\tau}(\mathbf{D}). \tag{2.38}$$

Due to the above equation, these fluids can be categorized due to the function $\boldsymbol{\tau}(\mathbf{D})$ to the following:

2.4.2.a The Newtonian Fluid(First Order Fluids)

The constitutive equation of these fluids between the shear stress tensor and the rate of deformation tensor is characterized by the linear relation with slop equal to the kinetics viscosity of the fluids. This relation might be casted as follows:

$$\boldsymbol{\tau} = \nu\mathbf{D}, \tag{2.39}$$

where $\nu = 2\mu$ being the viscosity of the fluids and here has a constant value.

2.4.2.b Generalized Newtonian Fluids(First Order Fluids)

The constitutive equation of these fluids is characterized by the non-linear relation between the shear stress and rate of deformation tensors:

$$\boldsymbol{\tau} = \nu(\|\mathbf{D}\|, p)\mathbf{D}, \tag{2.40}$$

where ν is the nonlinear viscosity as a function of pressure(p) and the norm of rate of deformation tensor($\|\mathbf{D}\|^2 = \frac{1}{2}\sum_{i,j=1}^{3}[D_{ij}]^2$ where D_{ij} are the components of $\mathbf{D}$). Depending on the nonlinear viscosity fluids can be categorized to the following three main parts:

(a)**Shear Thinning Fluids**

These fluids are characterized by the decreasing of the nonlinear viscosity with increasing the shear rate, and are described by the following viscosity functions(see Fig.2.1)
Power law

$$\nu = 2\mu\|\mathbf{D}\|^{n-1}, \quad n < 1, \tag{2.41}$$

Carreau law

$$\frac{\nu - \nu_\infty}{\nu_0 - \nu_\infty} = (1 + 2\mu\|\mathbf{D}\|^2)^{(n-1)/2}, \quad n < 1, \tag{2.42}$$

Ellis Model

$$\frac{\nu}{\nu_0} = (1 + \frac{\|\boldsymbol{\tau}\|}{\|\boldsymbol{\tau}\|_{\frac{1}{2}}})^{-1}. \tag{2.43}$$

(b)**Viscoplastic Fluids**

These fluids are characterized by the property of yield stress, and are described by the following viscosity functions(see Fig.2.1)

Casson Model

$$\nu = \frac{(\sqrt{2\mu \|\mathbf{D}\|} + \sqrt{\tau_s})^2}{\|\mathbf{D}\|}, \tag{2.44}$$

Bingham Model

$$\nu = 2\mu + \frac{\tau_s}{\|\mathbf{D}\|}, \tag{2.45}$$

Herschel-Bulkley Model

$$\nu = 2\mu + \tau_s \|\mathbf{D}\|^{n-1}. \tag{2.46}$$

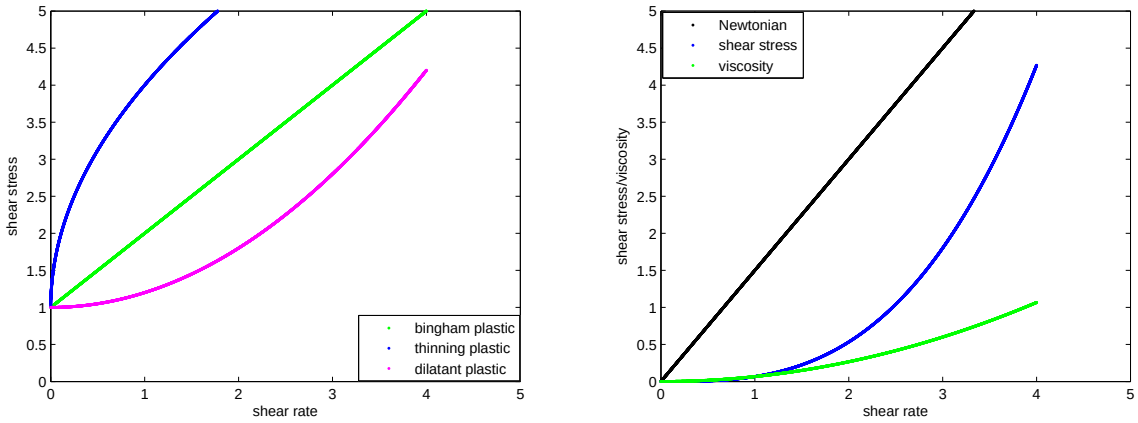

Fig. 2.1. Constitutive equations for viscoplastic fluids(left), and shear thickening fluids(right).

(c)**Shear Thickening Fluids**

These fluids are characterized by the increasing of viscosity with increasing of the shear rate and can be dealt easily by the following power law viscosity function when the power index is more than one

$$\nu = 2\mu \|\mathbf{D}\|^{n-1}, \quad n > 1. \tag{2.47}$$

2.4.3 Memorized Viscous Fluids(Fluids with Memory)

These fluids have the ability to remember and return to their undeformed state, once the gradient driving is removed. This memory arises from the elastic properties of the involved molecules, which when stretched, compressed or twisted develop internal forces that resist deformation and tend to spontaneously return to their undeformed or unstressed state. The simplest constitutive equation to describe such fluids is

$$\boldsymbol{\tau} = c_1\mathbf{D} + c_2\mathbf{D}^2 + c_3\dot{\mathbf{D}}, \tag{2.48}$$

where c_1, c_2, c_3 are material constants or functions.

2.5 Newtonian Fluids

In Newtonian fluids, the stress tensor $\boldsymbol{\sigma}$ is expressed by

$$\boldsymbol{\sigma} = -p\mathbf{I} + 2\mu\mathbf{D}, \tag{2.49}$$

where p is the pressure. In fact, this equation originates from the following equation which was proposed by Stokes in [200]

$$\boldsymbol{\sigma} = -(p - \eta_\nu \boldsymbol{\nabla}\cdot\boldsymbol{u})\mathbf{I} + \mu(\boldsymbol{\nabla}\boldsymbol{u} + (\boldsymbol{\nabla}\boldsymbol{u})^T - \frac{2}{3}\boldsymbol{\nabla}\cdot\boldsymbol{u}), \tag{2.50}$$

where η_ν is the bulk viscosity. The relation between the viscosity and the bulk viscosity reads:

$$\eta_\nu = \lambda + \frac{2}{3}\mu, \tag{2.51}$$

where λ is the second viscosity coefficient which is taken to make the bulk viscosity to be zero. By substituting this equation into the momentum equation one gets the viscous compressible laminar flow:

$$\rho(\frac{\partial \boldsymbol{u}}{\partial t} + \boldsymbol{u}\cdot\boldsymbol{\nabla}\boldsymbol{u}) = -\boldsymbol{\nabla}p + (\lambda+\mu)\boldsymbol{\nabla}(\boldsymbol{\nabla}\cdot\boldsymbol{u}) + \mu\Delta\boldsymbol{u} + \rho\boldsymbol{f}. \tag{2.52}$$

If we assumed that the fluid is incompressible and homogenous, so that in this case the continuity equation is reduced to the divergence free condition:

$$\boldsymbol{\nabla}\cdot\boldsymbol{u} = 0, \tag{2.53}$$

then taking in our account the definitions for the kinematic viscosity $\mu = \frac{\mu}{\rho}$, the kinetic pressure $p = \frac{p}{\rho}$ and mass density of body forces $\boldsymbol{f} = \frac{\boldsymbol{f}}{\rho}$, the momentum equation is reduced to Navier-Stokes for a viscous incompressible homogenous flow and reads in its strong form:

$$\frac{\partial \boldsymbol{u}}{\partial t} + \boldsymbol{u}\cdot\boldsymbol{\nabla}\boldsymbol{u} - \mu\Delta\boldsymbol{u} + \boldsymbol{\nabla}p = \boldsymbol{f}, \tag{2.54a}$$

$$\boldsymbol{\nabla}\cdot\boldsymbol{u} = 0. \tag{2.54b}$$

2.5.1 The Weak Form of Navier-Stokes Equations

The weak formulation is obtained by multiplying the equations by test functions $\boldsymbol{v} \in \mathbf{H}^1$ and $q \in \mathbf{L}^2$ and integrating the result over $\boldsymbol{\Omega}$. The test function $\boldsymbol{v}$ is assumed to be divergence free and to satisfy the same boundary condition as the solution $\boldsymbol{u}$. After the integration by parts one can obtain the following compact form:

$$(\frac{d\boldsymbol{u}}{dt}, \boldsymbol{v}) + \mu a(\boldsymbol{u},\boldsymbol{v}) + b(\boldsymbol{u},\boldsymbol{u},\boldsymbol{v}) - (p, \boldsymbol{\nabla}\cdot\boldsymbol{v}) = (\boldsymbol{f},\boldsymbol{v}) \quad in \quad \boldsymbol{\Omega}\times(0,T), \tag{2.55a}$$

$$(\boldsymbol{\nabla}\cdot\boldsymbol{u}, q) = 0 \quad in \quad \boldsymbol{\Omega}\times(0,T), \tag{2.55b}$$

$$\boldsymbol{u}(\boldsymbol{x},t) = \boldsymbol{u}^o \quad on \quad \partial\boldsymbol{\Omega}\times(0,T), \tag{2.55c}$$

$$\boldsymbol{u}(\boldsymbol{x},0) = \boldsymbol{u}_o \quad in \quad \boldsymbol{\Omega}. \tag{2.55d}$$

From this equation, one can obtain the energy equation from the weak formulation by substituting $\boldsymbol{u}$ instead $\boldsymbol{v}$ to have the following:

$$\frac{1}{2}\frac{d}{dt}\left\|\boldsymbol{u}\right\|_0^2 + \mu\sum_{i,j=1}^{d}\left\|\frac{\partial u_i}{\partial x_j}\right\|_0^2 = (\boldsymbol{f},\boldsymbol{u}). \tag{2.56}$$

where the first term represents the change of kinetic energy, the second is the energy dissipation rate by viscosity, and the rhs is the power supplied by the external volume forces.

2.5.2 Existence and Uniqueness of Solutions for Navier-Stokes Equations

We present the main results for the existence and uniqness for the Navier-Stokes equations which will involve the two types of solutions strong and weak. Now, It is worth to say that for the 2D case; the mathematical theory is roughly complete i.e. the solutions are unique for a given initial condition and exist for all time. While in 3D the mathematical theory is not yet fairly complete; the weak solutions exist for all time but it is not known whether they are unique or not(for further details and the proofs of the theorems see [73, 102, 135]).

Theorem 2.5.1 *(Existence and uniqueness of weak solutions in 2D (see [73]))*
Assume that $\boldsymbol{u}_0$, $\boldsymbol{f}$ *and* $T > 0$ *are given and satisfy*

$$\boldsymbol{u}_0 \in \mathbf{H}, \boldsymbol{f} \in \mathbf{L}^2(0, T; \mathbf{H}). \tag{2.57}$$

Then; there exists a unique solution $\boldsymbol{u} = (u_1, u_2)$ *of Eq.(2.55) such that*

$$u_i, \quad \frac{\partial u_i}{\partial x_j} \in \mathbf{L}^2(\boldsymbol{\Omega} \times (0, T)), \quad i, j = 1, 2, \tag{2.58}$$

and $\boldsymbol{u}$ *is continuous from [0,T] into* $\mathbf{H}$*. Moreover the following energy equation holds on [0,T]:*

$$\frac{1}{2}\frac{d}{dt}\|\boldsymbol{u}\|_0^2 + \mu\|\boldsymbol{u}\|_1^2 = (\boldsymbol{f}, \boldsymbol{u}). \tag{2.59}$$

Theorem 2.5.2 *(Existence and uniqueness of strong solutions in 2D (see [73]))*
Assume that $\boldsymbol{u}_0$, $\boldsymbol{f}$ *and* $T > 0$ *are given and satisfy*

$$\boldsymbol{u}_0 \in \mathbf{V}, \boldsymbol{f} \in \mathbf{L}^2(0, T; \mathbf{H}). \tag{2.60}$$

Then there exists a unique solution $\boldsymbol{u} = (u_1, u_2)$ *of Eq.(2.55) satisfying*

$$u_i, \frac{\partial u_i}{\partial t}, \frac{\partial u_i}{\partial x_j}, \frac{\partial^2 u_i}{\partial x_j \partial x_k} \in \mathbf{L}^2(\boldsymbol{\Omega} \times (0, T)), \quad i, j, k = 1, 2, \tag{2.61}$$

and $\boldsymbol{u}$ *is continuous from [0,T] into* $\mathbf{V}$*.*

Theorem 2.5.3 *(Existence and uniqueness of weak solutions in 3D (see [73]))*
Assume that $\boldsymbol{u}_0$, $\boldsymbol{f}$ *and* $T > 0$ *are given and satisfy*

$$\boldsymbol{u}_0 \in \mathbf{H}, \boldsymbol{f} \in \mathbf{L}^2(0, T; \mathbf{H}). \tag{2.62}$$

Then there exists at least one solution $\boldsymbol{u} = (u_1, u_2, u_3)$ *of Eq.(2.55) such that*

$$u_i, \frac{\partial u_i}{\partial x_j} \in \mathbf{L}^2(\boldsymbol{\Omega} \times (0, T)), \quad i, j = 1, 2, 3 \tag{2.63}$$

and $\boldsymbol{u}$ *is weakly continuous from [0,T] into* $\mathbf{H}$*-that is, for every* $\boldsymbol{v} \in \mathbf{H}$*, the function*

$$t \mapsto (\boldsymbol{u}(t), \boldsymbol{v}) = \int_{\boldsymbol{\Omega}} \boldsymbol{u}(\boldsymbol{x}, t).\boldsymbol{v}(\boldsymbol{x}) d\boldsymbol{x} \tag{2.64}$$

is continuous. Moreover, the following energy inequality holds:

$$\int_{\boldsymbol{\Omega}} (-\frac{1}{2}\frac{d}{dt}\|\boldsymbol{u}\|_0^2 \psi(t) + \mu\|\boldsymbol{u}(t)\|_1^2 \psi(t)) dt \leq \frac{1}{2}\|\boldsymbol{u}(0)\|_0^2 \psi(0) + \int_{\boldsymbol{\Omega}} (\boldsymbol{f}, \boldsymbol{u})\psi(t) dt. \tag{2.65}$$

for all nonnegative real-valued C^1 *functions* ψ *on [0,T] such that* $\psi(T) = 0$*.*

Theorem 2.5.4 *(Existence and uniqness of strong solutions in 3D (see [73]))*
Assume that $\boldsymbol{u}_0$, $\boldsymbol{f}$ *and* $T > 0$ *are given and satisfy*

$$\boldsymbol{u}_0 \in \mathbf{V}, \boldsymbol{f} \in \mathbf{L}^2(0,T;\mathbf{H}). \tag{2.66}$$

Then there exists $T^*(0 < T^* \leq T)$*, depending on the data (namely,* $\boldsymbol{\Omega}, \nu, \boldsymbol{f}, \boldsymbol{u}_0$ *and* T*) such that on [0,*T^**) there exists a unique solution* $\boldsymbol{u} = (u_1, u_2, u_3)$ *of Eq.(2.55) satisfying*

$$u_i, \frac{\partial u_i}{\partial t}, \frac{\partial u_i}{\partial x_j}, \frac{\partial^2 u_i}{\partial x_j \partial x_k} \in \mathbf{L}^2(\boldsymbol{\Omega} \times (0,T)), \quad i,j,k = 1,2,3, \tag{2.67}$$

and $\boldsymbol{u}$ *is continuous from* $[0,T^*)$ *into* $\mathbf{V}$*. Moreover, the strong solutions are unique in the sense that there is no other strong solution in the sense of Eq.(2.66) and Eq.(2.67) and no other weak solution on [0,*T^**) in the sense of Theorem(2.5.3).*

Where $\mathbf{V} = \{\boldsymbol{v} \in ((\mathbf{H}_0^1(\boldsymbol{\Omega}))^d | \boldsymbol{\nabla} \cdot \boldsymbol{v} = 0\}$, $\mathbf{H} = \{\boldsymbol{v} \in (\mathbf{L}^2(\boldsymbol{\Omega}))^d | \boldsymbol{\nabla} \cdot \boldsymbol{v} = 0, \boldsymbol{v} \cdot \boldsymbol{n} = 0 \,\text{on}\, \partial\boldsymbol{\Omega}\}$, $\mathbf{H}^1(\boldsymbol{\Omega}) = \{\boldsymbol{v} : \boldsymbol{\Omega} \to \mathbb{R} | \boldsymbol{v}, \frac{\partial \boldsymbol{v}}{\partial x_i} \in \mathbf{L}^2(\boldsymbol{\Omega}), i = 1, ..., d = (2 \,\text{or}\, 3)\}$ and $\mathbf{H}_0^1(\boldsymbol{\Omega}) = \{\boldsymbol{v} \in \mathbf{H}^1(\boldsymbol{\Omega}) | \boldsymbol{v} = 0 \,\text{on}\, \partial\boldsymbol{\Omega}\}$.
$(\|.\|_0 = \|.\|_{\mathbf{L}^2(\boldsymbol{\Omega})}$, $\|.\|_1 = \|.\|_{\mathbf{H}^1(\boldsymbol{\Omega})}$ and $\|.\|_2 = \|.\|_{\mathbf{H}^2(\boldsymbol{\Omega})})$.

2.6 Generalized Newtonian Fluids

The description of a Non-Newtonian fluid is defined by the nonlinear relation between the shear stress and the deformation tensor, the equation must have a nonlinear term involving the viscosity $\nu(\|\mathbf{D}\|)$

$$\boldsymbol{\sigma} = -p\mathbf{I} + \boldsymbol{\tau}(\mathbf{D}), \tag{2.68a}$$
$$\boldsymbol{\tau}(\mathbf{D}) = \nu(\|\mathbf{D}\|)\mathbf{D}. \tag{2.68b}$$

The governing equations of the generalized Newtonian fluids can be obtained in the strong form the coupling of the momentum balance, mass balance and the constitutive model. In this coupled system; we are looking for the primitive variables $(\boldsymbol{u}, p)$ such that

$$\frac{\partial \boldsymbol{u}}{\partial t} + \boldsymbol{u} \cdot \boldsymbol{\nabla}\boldsymbol{u} + \boldsymbol{\nabla} p = \boldsymbol{\nabla} \cdot \boldsymbol{\tau} + \boldsymbol{f} \quad in \quad \boldsymbol{\Omega} \times (0,T), \tag{2.69a}$$
$$\boldsymbol{\nabla} \cdot \boldsymbol{u} = 0 \quad in \quad \boldsymbol{\Omega} \times (0,T), \tag{2.69b}$$
$$\boldsymbol{\tau}(\mathbf{D}) = \nu(\|\mathbf{D}\|)\mathbf{D}, \tag{2.69c}$$
$$\boldsymbol{u}(\boldsymbol{x},t) = \boldsymbol{u}^o \quad on \quad \partial\boldsymbol{\Omega} \times (0,T), \tag{2.69d}$$
$$\boldsymbol{u}(\boldsymbol{x},0) = \boldsymbol{u}_o \quad in \quad \boldsymbol{\Omega}. \tag{2.69e}$$

By dropping down the unsteady and convective terms to obtain the following simplified for the Stokes form

$$-\boldsymbol{\nabla} \cdot (\nu(\|\mathbf{D}\|)\mathbf{D}) + \boldsymbol{\nabla} p = \boldsymbol{f} \quad in \quad \boldsymbol{\Omega}, \tag{2.70a}$$
$$\boldsymbol{\nabla} \cdot \boldsymbol{u} = 0 \quad in \quad \boldsymbol{\Omega}, \tag{2.70b}$$
$$\boldsymbol{u}(\boldsymbol{x}) = \boldsymbol{u}^o \quad on \quad \partial\boldsymbol{\Omega}. \tag{2.70c}$$

This nonlinear equations Eq.(2.70) appear in the modeling of large class of Non-Newtonian fluids with the corresponding nonlinear viscosity such as power law model, Carreau model (see [13, 90, 136, 142, 184, 185]).

2.6.1 The Weak Form of Generalized Newtonian Fluids Problem

By multiplying the equation by the test functions $\boldsymbol{v} \in \mathbf{H}^1$ and $q \in \mathbf{L}^2(\boldsymbol{\Omega})$ and integrating it, we get the following compact form

$$(\frac{d\boldsymbol{u}}{dt}, \boldsymbol{v}) + \int_{\boldsymbol{\Omega}} \nu(\|\mathbf{D}\|)\mathbf{D}(\boldsymbol{u}) : \mathbf{D}(\boldsymbol{v}) + b(\boldsymbol{u}, \boldsymbol{u}, \boldsymbol{v}) - (p, \boldsymbol{\nabla} \cdot \boldsymbol{v}) = (\boldsymbol{f}, \boldsymbol{v}) \quad in \quad \boldsymbol{\Omega} \times (0, T), \tag{2.71a}$$

$$(q, \boldsymbol{\nabla} \cdot \boldsymbol{u}) = 0 \quad in \quad \boldsymbol{\Omega} \times (0, T), \tag{2.71b}$$

$$\boldsymbol{u}(\boldsymbol{x}, t) = \boldsymbol{u}^o \quad on \quad \partial\boldsymbol{\Omega} \times (0, T), \tag{2.71c}$$

$$\boldsymbol{u}(\boldsymbol{x}, 0) = \boldsymbol{u}_o \quad in \quad \boldsymbol{\Omega}. \tag{2.71d}$$

To obtain the Stokes equation, we drop the unsteady and convective terms

$$\int_{\boldsymbol{\Omega}} \nu(\|\mathbf{D}\|)\mathbf{D}(\boldsymbol{u}) : \mathbf{D}(\boldsymbol{v}) - (p, \boldsymbol{\nabla}.\boldsymbol{v}) = (\boldsymbol{f}, \boldsymbol{v}) \quad in \quad \boldsymbol{\Omega}, \tag{2.72a}$$

$$(q, \boldsymbol{\nabla} \cdot \boldsymbol{u}) = 0 \quad in \quad \boldsymbol{\Omega}, \tag{2.72b}$$

$$\boldsymbol{u}(\boldsymbol{x}) = \boldsymbol{u}^o \quad on \quad \partial\boldsymbol{\Omega}. \tag{2.72c}$$

In most of the articles, the workers prefer to work with the following gradient form of velocity instead of the symmetric deformation form

$$\int_{\boldsymbol{\Omega}} \nu(\|\boldsymbol{\nabla u}\|)\boldsymbol{\nabla u} : \boldsymbol{\nabla v} - (p, \boldsymbol{\nabla} \cdot \boldsymbol{v}) = (\boldsymbol{f}, \boldsymbol{v}) \quad in \quad \boldsymbol{\Omega}, \tag{2.73a}$$

$$(q, \boldsymbol{\nabla} \cdot \boldsymbol{u}) = 0 \quad in \quad \boldsymbol{\Omega}, \tag{2.73b}$$

$$\boldsymbol{u}(\boldsymbol{x}) = \boldsymbol{u}^o \quad on \quad \partial\boldsymbol{\Omega}. \tag{2.73c}$$

The disadvantage of this form is that, it does not describe the real situation but it has only advantageous mathematical simplification. There are several alternative ways to obtain certain weak formulations. In [90], the researchers have introduced the stokes problem in a continuous weak form to obtain the twofold saddle point equation (see [88, 89]) by using two additional unknowns. From the other side, In [151] Manouzi and Fahloul have studied a nonlinear power law model by using a dual-mixed variational formulation based on inverting the relation $\boldsymbol{\tau} = \nu(\|\boldsymbol{\nabla u}\|)\boldsymbol{\nabla u}$ to be obtained as an explicit function of $\boldsymbol{\nabla u}$ in $\boldsymbol{\tau}$. While, unfortunately this method is not general since it can not be applied to the complex forms to get an explicit version for $\boldsymbol{\nabla u}$ such as Carreau model.

2.6.2 Existence and Uniqueness of Solutions for Generalized Newtonian Fluids Problem

The existence of strong solutions for the generalized Newtonian fluid has been studied in several articles particulary, in the sense of power law model. The preferred standard models in most monographs to seek are

$$\nu(\|\mathbf{D}\|) = (1 + \|\mathbf{D}\|^2)^{\frac{p-2}{2}} \quad and \quad \nu(\|\mathbf{D}\|) = (1 + \|\mathbf{D}\|)^{p-2} \tag{2.74}$$

with $1 < p < \infty$.
In [16, 145, 146], the existence of global strong solutions is established for $p \geq \frac{3d+2}{d+2}$ where d is the dimension of the domain. In [148] the existence of a local in time strong solution for arbitrary data and the existence of a global strong solution for small data is proved in case of $p > \frac{3d-4}{d}$.

2.7 Bingham Viscoplastic Fluids

The Bingham model is conceived of as the simplest model used to describe the viscoplastic fluid behavior. This constitutive law is characterized by a flow curve which is a straight line having an intercept τ_s on

the shear stress axis. The shear stress must be exceeded over the yield condition to commence the flow, and the excess of the stress over the yield condition is linearly proportional to the shear rate. Typically, the fluid response after yield is taken to be linear in the deformation rate so that, the material may be viewed as a complicated generalized Newtonian fluid:

$$\boldsymbol{\tau} = \begin{cases} (2\mu + \frac{\tau_s}{\|\mathbf{D}\|})\mathbf{D} \text{ if} & \|\mathbf{D}\| \neq 0, \\ \leq \boldsymbol{\tau}_s \text{ if} & \|\mathbf{D}\| = 0, \end{cases} \tag{2.75}$$

or equivalently:

$$\mathbf{D} = \begin{cases} \frac{1}{2\mu}(1 - \frac{\tau_s}{\|\boldsymbol{\tau}\|})\boldsymbol{\tau} \text{ if} & \|\boldsymbol{\tau}\| > \tau_s, \\ 0 \text{ if} & \|\boldsymbol{\tau}\| \leq \tau_s. \end{cases} \tag{2.76}$$

We formally construct the strong form by deriving the governing equation for the Bingham viscoplastic fluids from the balances law together with the constitutive equation. Let $\boldsymbol{\Omega}$ be a bounded domain of $\mathbb{R}^3$, and $\partial\boldsymbol{\Omega}$ the boundary of the domain $\boldsymbol{\Omega}$. The isothermal incompressible viscoplastic fluid during the time interval [0,T] is modeled by the laws of balances with the constitutive equation leading to the following system of partial differential equations:
The law of Momentum balance

$$\frac{\partial \boldsymbol{u}}{\partial t} + \boldsymbol{u} \cdot \boldsymbol{\nabla}\boldsymbol{u} + \boldsymbol{\nabla} p = \boldsymbol{\nabla} \cdot \boldsymbol{\tau} + \boldsymbol{f} \quad in \quad \boldsymbol{\Omega} \times (0, T). \tag{2.77}$$

The law of Mass balance

$$\boldsymbol{\nabla} \cdot \boldsymbol{u} = 0 \quad in \quad \boldsymbol{\Omega} \times (0, T). \tag{2.78}$$

Bingham constitutive equation

$$\boldsymbol{\tau} = \begin{cases} (2\mu + \frac{\tau_s}{\|\mathbf{D}\|})\mathbf{D} \text{ if} & \|\mathbf{D}\| \neq 0, \\ \leq \boldsymbol{\tau}_s \text{ if} & \|\mathbf{D}\| = 0. \end{cases} \tag{2.79}$$

The boundary and initial conditions

$$\begin{cases} B.C. \quad \boldsymbol{u}(\boldsymbol{x}, t) = \boldsymbol{u}^o \quad on \quad \partial\boldsymbol{\Omega} \times (0, T), \\ I.C. \quad \boldsymbol{u}(\boldsymbol{x}, 0) = \boldsymbol{u}_o \quad with \quad (\boldsymbol{\nabla} \cdot \boldsymbol{u}_o = 0) \quad in \quad \boldsymbol{\Omega}. \end{cases} \tag{2.80}$$

This system of equations represents the nonstationary modeling case to look for the unknowns $\boldsymbol{u}$, p, and $\boldsymbol{\tau}$ to be velocity, pressure, and stress tensor respectively. From the Bingham constitutive equation, one can deduce that the fluid starts to flow only if the applied stress exceeds a certain limit, called the yield limit τ_s. Whenever the value of yield limit approaches zero, the system of equations is reduced to the Navier-stokes equations modeling isothermal incompressible Newtonian viscous fluids. As a Bingham model is a model of fluid body, it was also called the Bingham solid (see [165]). This model used to describe the deformation and flow of many solid bodies and often used in metal forming processes, it was first introduced for wire drawing (see [55, 56, 57, 58]).
To obtain the unsteady Stokes-Bingham problem by dropping down the convective part in the momentum equation, the system is now

$$\frac{\partial \boldsymbol{u}}{\partial t} + \boldsymbol{\nabla} p = \boldsymbol{\nabla} \cdot \boldsymbol{\tau} + \boldsymbol{f} \quad in \quad \boldsymbol{\Omega} \times (0, T), \tag{2.81a}$$

$$\boldsymbol{\nabla} \cdot \boldsymbol{u} = 0 \quad in \quad \boldsymbol{\Omega} \times (0, T), \tag{2.81b}$$

$$\boldsymbol{u}(\boldsymbol{x}, t) = \boldsymbol{u}^o \quad on \quad \partial\boldsymbol{\Omega} \times (0, T), \tag{2.81c}$$

$$\boldsymbol{u}(\boldsymbol{x}, 0) = \boldsymbol{u}_o \quad in \quad \boldsymbol{\Omega}, \tag{2.81d}$$

$$\boldsymbol{\tau} = \begin{cases} (2\mu + \frac{\tau_s}{\|\mathbf{D}\|})\mathbf{D} \text{ if} & \|\mathbf{D}\| \neq 0, \\ \leq \boldsymbol{\tau}_s, \text{ if} & \|\mathbf{D}\| = 0. \end{cases} \tag{2.81e}$$

2.7.1 Weak Form for Bingham Viscoplastic Fluids Problem

As usual by multiplying the equations by the test functions $\boldsymbol{v} \in \mathbf{H}^1$ and $q \in \mathbf{L}^2$ we get the following compact form:

Find $\boldsymbol{u} \in \mathbf{H}^1$, $p \in \mathbf{L}^2$ such that for any $\boldsymbol{v} \in \mathbf{H}^1$, $q \in \mathbf{L}^2$

$$(\frac{\partial \boldsymbol{u}}{\partial t}, \boldsymbol{v}) + 2\mu a(\boldsymbol{u}, \boldsymbol{v}) + \tilde{a}(\boldsymbol{u}, \boldsymbol{v}) + b(\boldsymbol{u}, \boldsymbol{u}, \boldsymbol{v}) - c(p, \boldsymbol{v}) = (\boldsymbol{f}, \boldsymbol{v}) \quad in \quad \boldsymbol{\Omega} \times (0, T), \tag{2.82a}$$

$$(q, \boldsymbol{\nabla} \cdot \boldsymbol{u}) = 0 \quad in \quad \boldsymbol{\Omega} \times (0, T), \tag{2.82b}$$

$$\boldsymbol{u}(\boldsymbol{x}, t) = \boldsymbol{u}^o \quad on \quad \partial\boldsymbol{\Omega} \times (0, T), \tag{2.82c}$$

$$\boldsymbol{u}(\boldsymbol{x}, 0) = \boldsymbol{u}_o \quad in \quad \boldsymbol{\Omega}. \tag{2.82d}$$

where $a(\boldsymbol{u}, \boldsymbol{v})$, $\tilde{a}(\boldsymbol{u}, \boldsymbol{v})$, $b(\boldsymbol{u}, \boldsymbol{u}, \boldsymbol{v})$ and $c(p, \boldsymbol{v})$ are the following forms

$$a(\boldsymbol{u}, \boldsymbol{v}) = \int_{\boldsymbol{\Omega}} \mathbf{D}(\boldsymbol{u}) : \mathbf{D}(\boldsymbol{v}) d\boldsymbol{x}, \tag{2.83a}$$

$$\tilde{a}(\boldsymbol{u}, \boldsymbol{v}) = \int_{\boldsymbol{\Omega}} \frac{\tau_s}{\|\mathbf{D}\|} \mathbf{D}(\boldsymbol{u}) : \mathbf{D}(\boldsymbol{v}) d\boldsymbol{x}, \tag{2.83b}$$

$$b(\boldsymbol{u}, \boldsymbol{v}, \boldsymbol{w}) = \int_{\boldsymbol{\Omega}} u_i v_{j,i} w_j d\boldsymbol{x}, \tag{2.83c}$$

$$c(p, \boldsymbol{v}) = \int_{\boldsymbol{\Omega}} p \boldsymbol{\nabla} \cdot \boldsymbol{v} d\boldsymbol{x}. \tag{2.83d}$$

2.7.2 The Variational Inequality

We formally exhibit the variational inequality or the variational form for the Bingham viscoplastic fluids. The idea is to merge the momentum equation and the constitutive equation together in a variational cast. So, Let us define the following for arbitrary vector fields $\boldsymbol{u}$, $\boldsymbol{v}$, and $\boldsymbol{w}$ (see [69]).

$$(\boldsymbol{v}, \boldsymbol{w}) = \int_{\boldsymbol{\Omega}} \boldsymbol{v} \cdot \boldsymbol{w} d\boldsymbol{x}, \tag{2.84a}$$

$$j(\boldsymbol{v}) = \int_{\boldsymbol{\Omega}} \|\mathbf{D}(\boldsymbol{v})\| \, d\boldsymbol{x}, \tag{2.84b}$$

$$a(\boldsymbol{v}, \boldsymbol{w}) = \int_{\boldsymbol{\Omega}} \mathbf{D}(\boldsymbol{v}) : \mathbf{D}(\boldsymbol{w}) d\boldsymbol{x}, \tag{2.84c}$$

$$b(\boldsymbol{u}, \boldsymbol{v}, \boldsymbol{w}) = \int_{\boldsymbol{\Omega}} u_i v_{j,i} w_j d\boldsymbol{x}, \tag{2.84d}$$

$$b(\boldsymbol{u}, \boldsymbol{u}, \boldsymbol{u}) = 0, \tag{2.84e}$$

$$b(\boldsymbol{u}, \boldsymbol{v}, \boldsymbol{w}) = -b(\boldsymbol{u}, \boldsymbol{w}, \boldsymbol{v}). \tag{2.84f}$$

So that, the system of equations is involved in the context of the following theorem :

Theorem 2.7.1 *(the variational form (see [69]))*
Assume that $\boldsymbol{f}$ *and* $\boldsymbol{u}_o$ *are given with* $\boldsymbol{f} \in \mathbf{L}^2(0, T; \acute{\mathbf{V}})$ *and* $\boldsymbol{u}_o \in \mathbf{H}$.
Then there exists a unique function $\boldsymbol{u}$ *that satisfies on a.e. [0,T] the following variational inequality*

$$(\frac{\partial \boldsymbol{u}}{\partial t}, \boldsymbol{v} - \boldsymbol{u}) + 2\mu a(\boldsymbol{u}, \boldsymbol{v} - \boldsymbol{u}) + b(\boldsymbol{u}, \boldsymbol{u}, \boldsymbol{v} - \boldsymbol{u}) + \tau_s(j(\boldsymbol{v}) - j(\boldsymbol{u})) - (p, \boldsymbol{\nabla} \cdot (\boldsymbol{v} - \boldsymbol{u})) \geq (\boldsymbol{f}, \boldsymbol{v} - \boldsymbol{u}), \tag{2.85a}$$

$$\boldsymbol{\nabla} \cdot \boldsymbol{u} = 0. \tag{2.85b}$$

and such that $\boldsymbol{u} \in \mathbf{L}^2(0,T;\acute{\mathbf{V}}), \quad \frac{\partial \boldsymbol{u}}{\partial t} \in \mathbf{L}^2(0,T;\acute{\mathbf{V}}), \quad$ *and* $\quad \boldsymbol{u}(0) = \boldsymbol{u}_o.$
(where $\acute{\mathbf{V}}$ *denotes the dual space of* $\mathbf{V}$ *when* $\mathbf{H}$ *is identified with its dual.)*

2.7.3 The Mixed Dual Weak Form(Tensor Valued Function)

We exhibit another form for the Bingham viscoplastic fluids merging the momentum equation and the constitutive equation together in a cast involved a tensor valued function $\boldsymbol{\lambda}$ which has the following definitions:

$$\boldsymbol{\lambda} \in (\mathbf{L}^\infty(\boldsymbol{\Omega} \times (0,T)))^{d\times d}, \quad \boldsymbol{\lambda} = \boldsymbol{\lambda}^l, \quad 1 \le d \le 3, \tag{2.86a}$$

$$\|\boldsymbol{\lambda}\| \le 1 \, a.e. \quad in \quad \boldsymbol{\Omega} \times (0,T) \tag{2.86b}$$

$$\boldsymbol{\nabla} : \boldsymbol{\lambda} = (\boldsymbol{\nabla} \cdot \boldsymbol{\lambda}_1, \boldsymbol{\nabla} \cdot \boldsymbol{\lambda}_2, \boldsymbol{\nabla} \cdot \boldsymbol{\lambda}_3), \tag{2.86c}$$

$$\|\boldsymbol{\lambda}\|^2 = \sum_{i,j=1}^{2} \lambda_{ij}\lambda_{ij}, \tag{2.86d}$$

$$trace(\boldsymbol{\lambda}) = 0, \tag{2.86e}$$

$$\boldsymbol{\lambda} : \boldsymbol{\nabla}\boldsymbol{v} = \boldsymbol{\lambda} : \mathbf{D}(\boldsymbol{v}), \tag{2.86f}$$

$$\int_{\boldsymbol{\Omega}} \boldsymbol{\lambda} : \mathbf{D}(\boldsymbol{u}) d\boldsymbol{x} = \int_{\boldsymbol{\Omega}} \|\mathbf{D}(\boldsymbol{u})\| \, d\boldsymbol{x}. \tag{2.86g}$$

So that, the system of equations is involved in the context of the following theorem (see [64, 183] and the references therein).

Theorem 2.7.2 *(the tensor valued function form)*
Assume that $\boldsymbol{f}$ *and* $\boldsymbol{u}_o$ *are given with* $\boldsymbol{f} \in \mathbf{L}^2(0,T;\acute{\mathbf{V}})$ *and* $\boldsymbol{u}_o \in \mathbf{H}$.
Let $\boldsymbol{u} \in (\mathbf{H}_0^1(\boldsymbol{\Omega}))^2$ *be the solution of the strong form. Then, there exists a tensor valued function* $\boldsymbol{\lambda}(\boldsymbol{x},t)$ *and scalar field (pressure)* $p = p(\boldsymbol{x},t)$ *defined on* $\boldsymbol{\Omega} \times (0,T)$ *such that*

$$\begin{aligned} \frac{\partial \boldsymbol{u}}{\partial t} + \boldsymbol{u} \cdot \boldsymbol{\nabla}\boldsymbol{u} - \mu \boldsymbol{\Delta}\boldsymbol{u} + \boldsymbol{\tau}_s \boldsymbol{\nabla} : \boldsymbol{\lambda} + \boldsymbol{\nabla} p = \boldsymbol{f} \quad in \quad \boldsymbol{\Omega} \times (0,T), \\ \boldsymbol{\nabla} \cdot \boldsymbol{u} = 0 \quad in \quad \boldsymbol{\Omega} \times (0,T), \\ \boldsymbol{\lambda} : \mathbf{D} = \|\mathbf{D}\| \quad in \quad \boldsymbol{\Omega} \times (0,T). \end{aligned} \tag{2.87}$$

2.7.4 The Mixed Dual Weak Form(Inverse Tensor Valued Function)

Another form is introduced in [7] by using an auxiliary symmetric tensor $\mathbf{W}$ such that:

$$\frac{\partial \boldsymbol{u}}{\partial t} + \boldsymbol{u} \cdot \boldsymbol{\nabla}\boldsymbol{u} - \mu \Delta \boldsymbol{u} + \tau_s \boldsymbol{\nabla} : \mathbf{W} + \boldsymbol{\nabla} p = \boldsymbol{f} \quad in \quad \boldsymbol{\Omega} \times (0,T), \tag{2.88a}$$

$$\|\mathbf{D}\| \, \mathbf{W} - \mathbf{D} = 0 \quad in \quad \boldsymbol{\Omega} \times (0,T), \tag{2.88b}$$

$$\boldsymbol{\nabla} \cdot \boldsymbol{u} = 0 \quad in \quad \boldsymbol{\Omega} \times (0,T). \tag{2.88c}$$

$$\tag{2.88d}$$

However, the weak formulation for the stokes problem reads: Find $\boldsymbol{u} \in \mathbf{H}_0^1$, $p \in \mathbf{L}_0^2$ and $\mathbf{W} \in \text{Ł}^2$ such that for any $\boldsymbol{v} \in \mathbf{H}_0^1$, $q \in \mathbf{L}_0^2$ and $\mathbf{Z} \in \text{Ł}^\infty$

$$\int_{\boldsymbol{\Omega}} 2\mu \mathbf{D}(\boldsymbol{u}) : \mathbf{D}(\boldsymbol{v}) - \int_{\boldsymbol{\Omega}} p \boldsymbol{\nabla} \cdot \boldsymbol{v} + \int_{\boldsymbol{\Omega}} \boldsymbol{\tau}_s \mathbf{D} : \mathbf{Z} - \int_{\boldsymbol{\Omega}} \boldsymbol{\tau}_s \|\mathbf{D}\| \, \mathbf{W} : \mathbf{Z} = \int_{\boldsymbol{\Omega}} \boldsymbol{f} \cdot \boldsymbol{v} \quad in \quad \boldsymbol{\Omega}, \tag{2.89a}$$

$$\int_{\boldsymbol{\Omega}} q \boldsymbol{\nabla} \cdot \boldsymbol{u} = 0 \quad in \quad \boldsymbol{\Omega}. \tag{2.89b}$$

The following theorem states the condition of the well-posedness for the viscoplastic problem

Theorem 2.7.3 *(for proof see [7])*

The mixed formulation has a unique solution $\{\boldsymbol{u}, \mathbf{W}, p\}$ *from* $\mathbf{H}_0^1 \times L^2 \times \mathbf{L}_0^2$ *such that:*

$$\|\boldsymbol{u}\|_1^2 + \epsilon\tau_s \|\mathbf{W}\|^2 \leq \|\boldsymbol{f}\|_{-1}, \quad \|p\|_0 \leq c(\|\boldsymbol{f}\|_{-1} + \tau_s min\{1, \epsilon^{-1} \|\boldsymbol{f}\|_{-1}\}). \tag{2.90}$$

where ϵ *is a regularized parameter and c is constant. Moreover* $\mathbf{W} \in L^\infty$ *and* $\|\mathbf{W}\|_{\mathbf{L}^\infty} \leq 1$.

Where $\mathbf{L}_0^2$ is the subspace of $\mathbf{L}^2$ of functions with zero mean over $\boldsymbol{\Omega}$, $\mathbf{H}_0^1$ is the space of functions in $\mathbf{H}^1$ with vanishing trace on $\partial\boldsymbol{\Omega}$ and L^2 and L^∞ are the corresponding spaces of $\mathbf{L}^2$ and $\mathbf{L}^\infty$ for symmetric tensors.

2.8 Bingham Viscoplastic Fluids in Pipes and Channels

The modeling of motion of viscoplastic fluid in pipes is presented in a several literatures due to its importance in the industrial application, for instance petroleum, food, and ceramics industries. Since, the pipe problem is easier to treat mathematically, the researchers have considered it as an effective test not only to check the robustness of numerical schemes but also to manifest the features of viscoplastic fluid on a compact way(cessation of flow and prediction the dead/plug/shear regions in the flow regimes). Bird [41] presented several closed form solutions for steady state flow in pipes in layers of constant thickness, and in parallel plates. In [160, 161, 162], the researchers have introduced an extensive mathematical study and impressive results on the existence and the shape of the rigid zones in the flow domain. Glowinski [65] recovered some properties and found new interesting results for the cessation of viscoplastic fluid which supported by Huilgol works in [44, 45]. Concerning the error estimation, a crucial work in the frame of the variational inequalities has been introduced by Zhang in [233].
To recast the pipe problem, let Ox be the axis of the pipe and Oyz the plane of the bounded cross section $\boldsymbol{\Omega} \subset \mathbb{R}^2$,and $f > 0$ be the constant applied force density. The velocity can be written as $\boldsymbol{u} = (u, 0, 0)$ where u is the first component along the Ox axis depends only upon y and z. The problem might be considered as a two dimensional, and the stress tensor is equivalent to a two shear stress components vector $\boldsymbol{\tau} = (\tau_{yx}, \tau_{zx})$. The strong form can be read from the following:

$$\frac{\partial u}{\partial t} + \frac{\partial p}{\partial x} = \boldsymbol{\nabla} \cdot \boldsymbol{\tau} + f \quad in \quad \boldsymbol{\Omega}, \tag{2.91a}$$

$$\frac{\partial u}{\partial y} + \frac{\partial u}{\partial z} = 0 \quad in \quad \boldsymbol{\Omega}, \tag{2.91b}$$

$$\boldsymbol{\tau} = \begin{cases} (2\mu + \frac{\boldsymbol{\tau}_s}{\|\mathbf{D}\|})\mathbf{D}(\boldsymbol{u}) \text{ if} & \|\mathbf{D}\| \neq 0, \\ \leq \boldsymbol{\tau}_s \text{ if} & \|\mathbf{D}\| = 0. \end{cases} \tag{2.91c}$$

The cast of the weak formulation is

$$(\frac{\partial u}{\partial t}, v - u) + 2\mu a(u, v - u) + \tau_s(j(v) - j(u)) - (p, \frac{\partial (v - u)}{\partial x}) \geq (f, v - u), \tag{2.92a}$$

$$\frac{\partial u}{\partial y} + \frac{\partial u}{\partial z} = 0. \tag{2.92b}$$

Regarding the rectilinear flow of a Bingham viscoplastic between to parallel walls located a distance apart 2h is considered as the one case of viscoplastic problems. Let x(horizontal axis), y(vertical axis) be a coordinate system attached to the wall such that the x and y are parallel and perpendicular the flow direction with one component of velocity u in x direction. Rectilinear flow in x-direction implies that:

$$u = u(y, t) \tag{2.93}$$

The governing equations, the continuity equation and the momentum equations in the cartesian coordinate system (x, y), in addition to the constitutive equation takes the following form:

$$\frac{\partial u}{\partial t} = -\frac{dp}{dx} + \frac{\partial \tau_{yx}}{\partial y} + f, \tag{2.94a}$$

$$\frac{\partial u}{\partial x} = 0, \tag{2.94b}$$

$$\mu \frac{\partial u}{\partial y} = \begin{cases} (1 - \frac{\tau_s}{\|\tau_{yx}\|})\tau_{yx} \text{ if} & \|\tau_{yx}\| > \tau_s, \\ 0 \text{ if} & \|\tau_{yx}\| \leq \tau_s. \end{cases} \tag{2.94c}$$

Since $\frac{\tau_{yx}}{\|\tau_{yx}\|}$, and $\frac{\partial u/\partial y}{\|\partial u/\partial y\|}$ are either $+1$ or -1. The variational form reads

$$(\frac{\partial u}{\partial t}, v-u) + 2\mu a(u, v-u) + \tau_s(j(v) - j(u)) - (p, \frac{\partial (v-u)}{\partial x}) \geq (f, v-u), \tag{2.95a}$$

$$\frac{\partial u}{\partial x} = 0. \tag{2.95b}$$

For unidirectional flow, Savage at el. in [3] have obtained the closed form for the one dimensional transient flow in a fracture with parallel walls that is subjected to applied pressure gradient over a finite time interval and constant over a time. Comparini in [53] was aimed to prove the global existence and uniqueness of a classical solution along, with some qualitative properties of the free boundary. Frigaard et al. [84]presented an excellent review on different regularization models and their implementations. In a similar fashion, some recent works, solved numerically the cessation of the plane Couette and plane and axisymmetric Poiseuille flows of Bingham plastics using the regularized constitutive equation proposed by Papanastasiou , in order to avoid the determination of the yielded and unyielded regions in the flow domain. Glowinski [95] and Huilgol et al. [114, 113] have provided explicit theoretical finite upper bounds on the time for a Bingham material to come to rest in various flows, such as the plane and circular Couette flows, the plane and axisymmetric Poiseuille flows.

To obtain a closed form for unidirectional flow, let us differentiate the both sides of Eq.(2.94) with respect to y, x, and t to get:

$$\frac{\partial \tau_{yx}}{\partial y} = \mu \frac{\partial^2 u}{\partial y^2}, \tag{2.96a}$$

$$\frac{\partial \tau_{yx}}{\partial x} = 0, \tag{2.96b}$$

$$\frac{\partial \tau_{yx}}{\partial t} = \mu \frac{\partial^2 u}{\partial y \partial t}. \tag{2.96c}$$

which implies that $\tau_{yx} = \tau_{yx}(y, t)$. In the absence of body force (f), the derivative of the pressure with respect to y is equal to zero, which implies that the pressure p is a function of x only, therefore by differentiating the Eq.(2.94) w.r.t y and t to have:

$$\frac{\partial^2 \tau_{yx}}{\partial y^2} = \frac{1}{\mu} \frac{\partial \tau_{yx}}{\partial t}. \tag{2.97}$$

Eq.(2.97) represents the second order differential equation that the shear stress τ_{yx} satisfies it when $|\tau_{yx}| > \tau_s$.

After dropping the local time derivative from Eq.(2.94a) to get the steady state. Let us examine the analytical solution under no external forces(f=0) and constant pressure gradient($\frac{dp}{dx} = -c$) and with the following homogenous boundary condition $u(y = 0) = 0, u(y = 2h) = 0, \tau_{yx}(y = h) = 0, \quad and \quad \tau_{yx}(y = y_s) = \tau_s$, where y_s the distance from the plug region.

By integrating Eq.(2.94a) to get:

$$\tau_{yx} = c(h - y), \tag{2.98}$$

plug in Eq.(2.94c) to have the following velocity distribution:

$$u = \begin{cases} \frac{c}{\mu} y(h - \frac{y}{2}) - \frac{\tau_s}{\mu} y \quad if \quad 0 \le y \le h - \frac{\tau_s}{c}, \\ \frac{c}{2\mu}(h - \frac{\tau_s}{c})^2 \quad if \quad h - \frac{\tau_s}{c} \le y \le h + \frac{\tau_s}{c}, \\ \frac{c}{\mu} y(h - \frac{y}{2}) - \frac{\tau_s}{\mu}(2h - y) \quad if \quad h + \frac{\tau_s}{c} \le y \le 2h. \end{cases} \tag{2.99}$$

Remark: It appears that when $\frac{\tau_s}{h} \ge c$ the velocity equals zero, this leads to the flow is completely blocked. Conversely, when $\frac{\tau_s}{h} \le c$ the velocity equals a constant in a certain region (plug region) and varies gradually in others (shear regions). Therefore, if we take $c = f^s = \frac{\tau_s}{h}$, then f^s called the critical value of the pressure gradient. Consequently, if $f < f^s$ the viscoplastic flow stops.

Let us examine for the unsteady state case the analytical solution with the following boundary conditions no external forces(f=0), constant pressure gradient($\frac{dp}{dx} = -c$), $u(y,0) = 0$, $u(2h,0) = 0$, $\tau_{yx}(h,t) = 0$, $\tau_{yx}(y,0) = \tau_s(1 - \frac{y}{h})$, and $\tau_{yx}(y_s,t) = \tau_s$; where y_s the distance till the plug region begins.
To get the profile of shear stress, by solving the Eq.(2.97) using separation of variable or Laplace transformation we get the following:

$$\tau_{yx}(y,t) = \frac{2\mu}{h} \sum_{n=0}^{\infty} (-1)^n sin(\frac{(2n+1)\pi}{2}(\frac{y}{h} - 1))(\int_0^t e^{-a\lambda}(-c + \frac{\tau_s}{h})d\lambda) + \tau_s(1 - \frac{y}{h}), \tag{2.100}$$

then, the velocity distribution reads as the following:

$$u(y,t) = \begin{cases} \frac{-4}{\pi} \sum_{n=0}^{\infty} \frac{(-1)^n}{2n+1} cos(\frac{(2n+1)\pi}{2}(\frac{y}{h} - 1))(\int_0^t e^{-a\lambda}(-c + \frac{\tau_s}{h})d\lambda) - \frac{\tau_s y^2}{2\mu h} \quad if \quad 0 \le y \le h - y_s, \\ \frac{-4}{\pi} \sum_{n=0}^{\infty} \frac{(-1)^n}{2n+1} cos(\frac{(2n+1)\pi}{2}(\frac{y_s}{h} - 1))(\int_0^t e^{-a\lambda}(-c + \frac{\tau_s}{h})d\lambda) - \frac{\tau_s y_s^2}{2\mu h} \quad if \quad h - y_s \le y \le h + y_s, \end{cases} \tag{2.101}$$

to get the thickness of the plug layer using the equation $\tau_{xy}(y_s,t) = \tau_s$ then:

$$y_s = \frac{2\mu}{h} \sum_{n=0}^{\infty} (-1)^n sin(\frac{(2n+1)\pi}{2}(\frac{y_s}{h} - 1))(\int_0^t e^{-a\lambda}(-c + \frac{\tau_s}{h})d\lambda), \tag{2.102}$$

where $a = \frac{(2n+1)^2\pi^2\mu}{4h^2}$.
It is obvious from Eq.(2.101) that the velocity field come to rest after a amount of time. That happens, if the pressure drop is less than the critical value($f \le f^s = \frac{\tau_s}{h}$) then the flow comes to rest in amount of time in contrast, the Newtonian fluid ceases in infinite amount of time(one can realize that by replacing the yield limit by zero), and it would be readily to compute the finite stopping time from Eq.(2.101).

2.9 Regularization Techniques

The nature of Bingham constitutive law for modeling the flow of viscoplastic fluids exhibits a mathematical difficulty which requires a special treatment and various modifications for the traditional handling concepts. This difficulty is raised by the non-differentiability which is involved in the constitutive model

$$\boldsymbol{\tau} = \begin{cases} (2\mu + \frac{\tau_s}{\|\mathbf{D}\|})\mathbf{D}(u) \text{ if} \quad \|\mathbf{D}\| \ne 0, \\ \qquad\quad \le \boldsymbol{\tau}_s \text{ if} \quad \|\mathbf{D}\| = 0, \end{cases} \tag{2.103}$$

with the nonlinear viscosity

$$\nu(\|\mathbf{D}\|) = 2\mu + \frac{\tau_s}{\|\mathbf{D}\|}. \tag{2.104}$$

The treatment of the non-differentiability has the most interesting part in Bingham viscoplastic problem due to the noticed effect on the solution. The source of this difficulty comes from the unbounded effective

viscosity where the zero value of deformation tensor. Therefore, we use the regularized models. Such regularization is used to approximate the viscosity to be a smooth and differential.
The simplest trial was by Allouche et al. [2] which introduced a simple regularized parameter added in the dominator having the dimension of the deformation tensor as follows:

$$\nu_\epsilon(\|\mathbf{D}\|) = 2\mu \ + \frac{\tau_s}{\epsilon + \|\mathbf{D}\|}. \tag{2.105}$$

In the same manner Bercovier and Engelman [18] proposed another regularized function as follows

$$\nu_\epsilon(\|\mathbf{D}\|) = 2\mu \ + \frac{\tau_s}{\sqrt{\epsilon^2 + \|\mathbf{D}\|^2}}, \tag{2.106}$$

they used the model to solve the flow in a closed square cavity subjected to a body force predicting the growth of a central unyielded zone and the dead zone at the corners. This model is also used by Taylor and Wilson [205] to simulate conduit flow of an incompressible Bingham fluid.
Tanner at el. [164] proposed a different model called bi-viscous model formed by

$$\nu_\epsilon(\|\mathbf{D}\|) = \begin{cases} 2\mu \ + \frac{\tau_s}{\|\mathbf{D}\|} \text{ if} & \|\mathbf{D}\| > \epsilon\tau_s, \\ \frac{2\mu}{\epsilon} \quad \text{if} & \|\mathbf{D}\| \leq \epsilon\tau_s. \end{cases} \tag{2.107}$$

This model is used to approximate only the solid regime by a highly viscous regime(unyielded viscosity) representing it by the term $\frac{1}{\epsilon}$. In [20] it is used to study the die swell in viscoelastic materials with yield stress, using an adopted value of $\frac{1}{\epsilon}$ equivalent to 2000μ for an optimum configuration of the flow field, in addition to, in [171] for the motion and deformation of drops in Bingham fluid without mentioning the chosen value of ϵ for the unyielded regime. In our work it is modified to have the following form

$$\nu_\epsilon(\|\mathbf{D}\|) = \begin{cases} 2\mu \ + \frac{\tau_s}{\|\mathbf{D}\|} \text{ if} & \|\mathbf{D}\| \geq TOL, \\ 2\mu + \frac{\tau_s}{\epsilon} \quad \text{if} & \|\mathbf{D}\| < TOL. \end{cases} \tag{2.108}$$

Papanastasiou [168] proposed a regularizing model with an exponential expression to hold for any shear rate by adding a small parameter leading to the smoothness and regularity of the non-differentiable function taking the following form.

$$\nu_\epsilon(\|\mathbf{D}\|) = 2\mu \ + \tau_s \frac{1 - exp(-\|\mathbf{D}\|/\epsilon)}{\|\mathbf{D}\|}. \tag{2.109}$$

Papanastasiou used this model to study several simple flows: one dimensional channel flow, two dimensional boundary layer flow and extrusion flow.
Indeed, from the computational point of view the regularized models are easier to implement, but they have some drawbacks due to the accuracy of the solutions. For instance, it is not easily to provide accurate solution results definitely in the interesting cases where the yield properties become important, furthermore the geometrical shape of the unyielded regions affected the connection between the plug and dead regions appeared as in [205, 222] . In [179] it is reported that, all the rigid zones could roughly disappeared as soon as the regularized model is used.
Therefore, for such viscoplastic problem the typical question arises about the value of regularization to ensure the close behavior for the regularized solution and the exact solution is argued. In [85], they examined the convergence of regularized models to those of the corresponding exact models for different types of flow exhibiting an asymptotic answer for types of flow and showing the maximum error happens when the shear stress equal the yield value for all regularized model.
Fortunately for the computational practitioners to overcome this discrepancy in practical computation, some researchers introduced an elegant method to make a solution for the viscoplastic problem almost as similar as Navier-stokes problem like augmented Lagrangian method due to Fortin and Glowinski [80] or modeling of Duvaut-Lions [69] which has been used recently by Dean and Glowinski [64] to cope with

the exact model.
To demonstrate the difference between the regularized models, a simple comparative studies can be deduced from the depicted figures . In Fig.2.2 and Fig.2.3, one can see that the simple model is the inferior at all values of regularization parameter, and for the bi-viscous model there is a jump where the shear stress is not defined and shrinks when the regularization parameter is going to be close to zero. In Fig.2.4 one notices that when the shear stress is closely to the yield stress value ($\tau \approx \tau_s$) the shear rate depends fully on the regularization parameter (because the shear rate at the yield limit is deviated from its exact zero value to else due to regularization). The maximum deviation happens for the bi-viscous model which is proportional linearly with the yield value, but the Bercovier and Papanastasiou models are going to be superior definitely at larger values of yield stress.

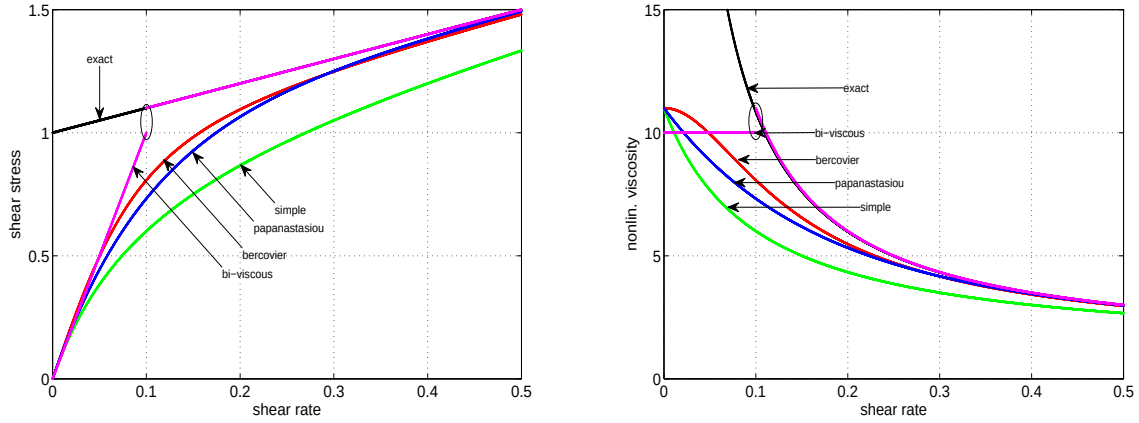

Fig. 2.2. The regularization models compared with the exact Bingham model: stress versus strain rate(left) effective viscosity versus strain rate(right) for $\epsilon = 0.1$, $\tau_s = 1$.

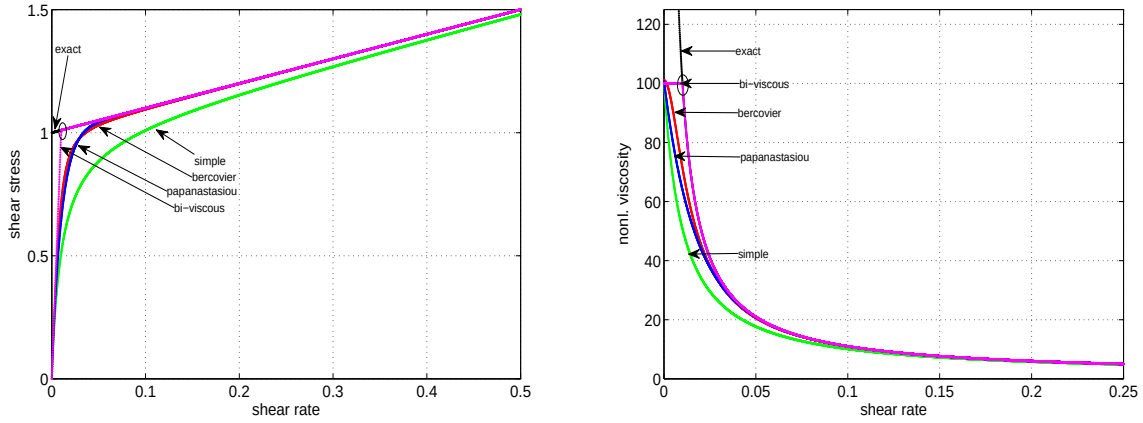

Fig. 2.3. The regularization models compared with the exact Bingham model: stress versus strain rate(left) effective viscosity versus strain rate(right) for $\epsilon = 0.01$, $\tau_s = 1$.

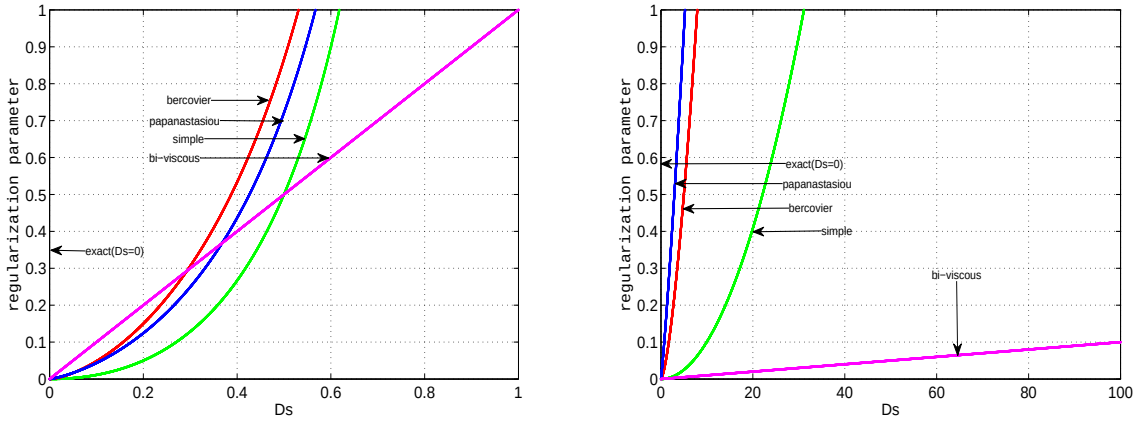

Fig. 2.4. the deviation of the shear rate when the stress equal the threshold value for regularization models for $\tau_s = 1(left), 1000(right)$.

2.10 Phenomenological Properties of Bingham Viscoplastic Fluids

2.10.1 Flow Zones

For viscoplastic fluids, it was noticed whenever considering any Bingham model three different zones in the flow domain (see Fig.2.5): the first zone is shear zone which is represented in case $\|\mathbf{D}\| \neq 0$. The second zone appears wherever the two conditions hold in the flow domain $\|\mathbf{D}\| = 0$ and $\boldsymbol{u} = \boldsymbol{c}$(constant vector). This zone can be described as rigid body which moves with constant velocity in the flow domain. The last zone appears wherever the two conditions hold in the flow domain $\|\mathbf{D}\| = 0$ and $\boldsymbol{u} = \mathbf{0}$. This zone can be described as stagnant zones which have no velocity in the flow domain and always near the boundary of the domain where the fluid does not move. This zone is responsible for forming the blocking in the flow domain. When the yield stress τ_s increases the dead zones are growing and if τ_s becomes sufficiently large

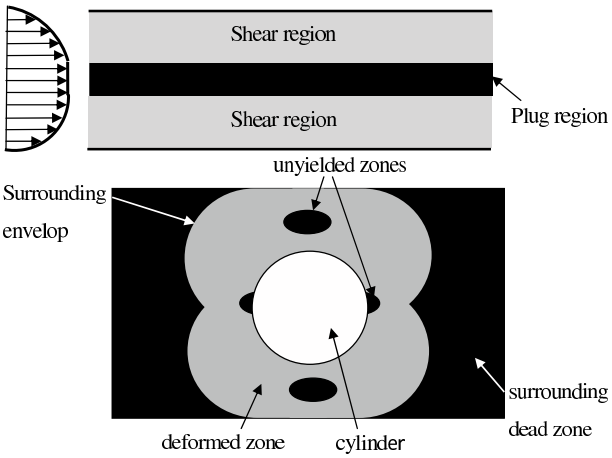

Fig. 2.5. viscoplastic fluid regimes in channel and around a cylinder.

, the fluid stops flowing. This phenomenon is called the blocking property. The blocking of the solid/fluid sometimes leads to unfortunate consequences such as in oil transport in pipelines in the process of oil drilling or in metal forming which considered as a catastrophic event for these industries. On the contrary,

in landslides modeling, the blocking phenomenon is natural configuration for the solid which ensures the stability of the slope and the beginning of a flow can be considered as a natural disaster. One can easily check that whether the fluid is blocked if and only if the following extra condition fulfills gathered with the dead zones conditions considering that the threshold value is domain dependent:
1) $\|\mathbf{D}\| = 0$,
2) $\boldsymbol{u} = \mathbf{0}$,
3) $\int_{\boldsymbol{\Omega}} \tau_s(\boldsymbol{x}) \|\mathbf{D}(\boldsymbol{v})\| \, d\boldsymbol{x} \geq \int_{\boldsymbol{\Omega}} \boldsymbol{f}(\boldsymbol{x}) \cdot \boldsymbol{v} d\boldsymbol{x}$.
Therefore, the study of the blocking properties implies finding the link between the external forces distribution and the yield limit distribution (see [27, 104, 116, 195]).

2.10.2 Cessation Property

For the Newtonian fluid, it is known that the volumetric flow rate decays exponentially with time. This property is proved experimentally, and theoretically for the Newtonian fluids, supporting that the stopping time of Newtonian fluid is infinite. In contrast, in viscoplastic fluids, it is proved experimentally and theoretically that the viscoplastic fluids cease at finite time or the flow rate decays in finite amount of time. The first to expose this property is Glowinski in [65] when he derived the theoretical upper bounds of the finite stopping time for Bingham viscoplastic fluids which can be exposed in the following theorem,

Theorem 2.10.1 *(theoretical bound for finite stopping time[64])*

Assume that $\boldsymbol{f} \in \mathbf{L}^2(\boldsymbol{\Omega})$ with $\|\boldsymbol{f}\|_{\mathbf{L}^2} < \beta\tau_s$; then if $\boldsymbol{u}$ is the solution of variational inequality Eq.(2.85), then we have

$$\|\boldsymbol{u}\|_{\mathbf{L}^2} = 0, \quad for \quad t \geq \frac{1}{\mu\lambda_o} Log(1 + \frac{\lambda_o \mu}{\beta\tau_s - \|\boldsymbol{f}\|_{\mathbf{L}^2}} \|\boldsymbol{u}_o\|_{\mathbf{L}^2}), \tag{2.110}$$

where λ_o is the smallest eigenvalue of $-\boldsymbol{\Delta} \in \mathbf{H}_0^1(\lambda_o > 0)$, and $\beta = inf_{\boldsymbol{v}\in\mathbf{V}} \frac{j(\boldsymbol{v})}{\|\boldsymbol{v}\|_{\mathbf{L}^2}}$.

2.10.3 The Pressure Jump Property

This is a recent property predicted in [71] for the distribution of pressure of the viscoplastic fluids. The evolved result is the pressure which has different distributions inside the flow domain corresponding to the flow regimes with local discontinuity at the interfacial boundaries between these regimes. These distributions depend mainly on the value of yield stress parameter which classifies the regime of fluid. The different distributions of pressure created a nonlinearity for the pressure isobars for the unidirectional flow which destroyed the linear relation between the pressure drop and the length (Darcy law) in contrast with Newtonian fluid. The result is summarized in the following theorem:

Theorem 2.10.2 *(The pressure jump property)*

For the fluid with yield, the distribution of the pressure is strongly related to the constitutive equation providing a nonuniform distribution over the flow domain with singularities at the interfacial boundary between the flow regimes. The predicted pressure distribution can be drawn over the whole domain whether there exist a solution for the following extra equation represented by the Pressure-Yield-Force equation over the unyielded regime

$$\boldsymbol{\Delta} p = \boldsymbol{\nabla} \cdot (\boldsymbol{\nabla} \cdot \boldsymbol{\tau}_s) + \boldsymbol{\nabla} \cdot \boldsymbol{f} \quad if \quad \|\mathbf{D}\| = 0. \tag{2.111}$$

Proof

Let us analyze the strong form of Bingham viscoplastic fluid for the steady case(Stokes equation) which is represented by following:

$$\boldsymbol{\nabla} p = \boldsymbol{\nabla} \cdot \boldsymbol{\tau} + \boldsymbol{f} \qquad in \quad \boldsymbol{\Omega}, \tag{2.112a}$$

$$\boldsymbol{\nabla} \cdot \boldsymbol{u} = 0 \qquad in \quad \boldsymbol{\Omega}, \tag{2.112b}$$

$$\boldsymbol{u} = \boldsymbol{u}^o \qquad on \quad \partial\boldsymbol{\Omega}, \tag{2.112c}$$

$$\boldsymbol{\tau} = \begin{cases} 2\mu \mathbf{D}(\boldsymbol{u}) + \frac{\tau_s}{\|\mathbf{D}\|}\mathbf{D}(\boldsymbol{u}) \text{ if} & \|\mathbf{D}\| \neq 0, \\ \leq \boldsymbol{\tau}_s \text{ if} & \|\mathbf{D}\| = 0. \end{cases} \tag{2.112d}$$

One can plug the the constitutive Eq.(2.112d) into Eq.(2.112a) to get the following cases

$$\boldsymbol{\nabla} p = \begin{cases} \boldsymbol{\nabla} \cdot (2\mu \mathbf{D}(\boldsymbol{u}) + \tau_s \frac{\mathbf{D}(\boldsymbol{u})}{\|\mathbf{D}\|}) + \boldsymbol{f} \text{ if} & \|\mathbf{D}\| \neq 0, \quad \boldsymbol{u} \neq \boldsymbol{c} \neq \mathbf{0} \quad in \quad \boldsymbol{\Omega}, \\ \boldsymbol{\nabla} \cdot \boldsymbol{\tau}_s + \boldsymbol{f} & \text{if} \quad \|\mathbf{D}\| = 0, \quad \boldsymbol{u} = \boldsymbol{c} \quad in \quad \boldsymbol{\Omega}, \\ \boldsymbol{\nabla} \cdot \boldsymbol{\tau}_s + \boldsymbol{f} & \text{if} \quad \|\mathbf{D}\| = 0, \quad \boldsymbol{u} = \mathbf{0} \quad in \quad \boldsymbol{\Omega}, \end{cases} \tag{2.113}$$

which can be reduced in the following form

$$\boldsymbol{\nabla} p = \begin{cases} \mu \boldsymbol{\Delta} \boldsymbol{u} + \boldsymbol{\nabla} \cdot (\tau_s \frac{\mathbf{D}(\boldsymbol{u})}{\|\mathbf{D})\|}) + \boldsymbol{f} \text{ if} & \|\mathbf{D}\| \neq 0, \quad \boldsymbol{u} \neq \boldsymbol{c} \neq \mathbf{0} \quad in \quad \boldsymbol{\Omega}, \\ \boldsymbol{\nabla} \cdot \boldsymbol{\tau}_s + \boldsymbol{f} & \text{if} \quad \|\mathbf{D}\| = 0, \quad \boldsymbol{u} = \boldsymbol{c} \quad in \quad \boldsymbol{\Omega}, \\ \boldsymbol{\nabla} \cdot \boldsymbol{\tau}_s + \boldsymbol{f} & \text{if} \quad \|\mathbf{D}\| = 0, \quad \boldsymbol{u} = \mathbf{0} \quad in \quad \boldsymbol{\Omega}. \end{cases} \tag{2.114}$$

Generally, Eq.(2.114) describes the pressure gradient distribution over the whole viscoplastic domain. Nevertheless, the RHS exhibits a different definitions of distributions which typically depends on the velocity field, the threshold value and the external forces. Let us allow to write it explicitly in the following form:

$$\boldsymbol{\nabla} p = \begin{cases} \mu \boldsymbol{\Delta} \boldsymbol{u} + \boldsymbol{\nabla} \cdot (\tau_s \frac{\mathbf{D}(\boldsymbol{u})}{\|\mathbf{D})\|}) + \boldsymbol{f} \text{ if} & \|\mathbf{D}\| \neq 0, \quad \boldsymbol{u} \neq \boldsymbol{c} \neq \mathbf{0} \quad in \quad \boldsymbol{\Omega}, \\ \boldsymbol{\nabla} \cdot \boldsymbol{\tau}_s + \boldsymbol{f} & \text{if} \quad \|\mathbf{D}\| = 0, \quad \boldsymbol{u} = \boldsymbol{c} \quad in \quad \boldsymbol{\Omega}, \\ \boldsymbol{\nabla} \cdot \boldsymbol{\tau}_s + \boldsymbol{f} & \text{if} \quad \|\mathbf{D}\| = 0, \quad \boldsymbol{u} = \mathbf{0} \quad in \quad \boldsymbol{\Omega}. \end{cases} \tag{2.115}$$

So, the existence of the null shear rate zones is associated with the value of velocity wherever its value is a maximum or vanishes corresponding to the existence of plug and dead regions respectively. Since the value the derivative of velocity vanishes in both cases, a bit from the above equation is remained to describe the pressure distribution for the plug region which is

$$\boldsymbol{\nabla} \cdot \boldsymbol{\nabla} p|_{plug/dead} = \begin{cases} \boldsymbol{\nabla} \cdot (\boldsymbol{\nabla} \cdot \boldsymbol{\tau}_s) + \boldsymbol{\nabla} \cdot \boldsymbol{f} & if \quad \|\mathbf{D}\| = 0, \quad \boldsymbol{u} = \boldsymbol{c} \quad in \quad \boldsymbol{\Omega}, \\ \boldsymbol{\nabla} \cdot (\boldsymbol{\nabla} \cdot \boldsymbol{\tau}_s) + \boldsymbol{\nabla} \cdot \boldsymbol{f} & if \quad \|\mathbf{D}\| = 0, \quad \boldsymbol{u} = \mathbf{0} \quad in \quad \boldsymbol{\Omega}. \end{cases} \tag{2.116}$$

Since, the pressure has two definitions over the flow domain which renders the pressure to have a discontinuity and singularity at the interfacial boundary between the plug/dead and shear zones. From Eq.(2.116) the pressure distribution has a strong connection with the threshold value and the external density forces. Since, with the known threshold value or the density of external force density, the distribution of pressure either only to solve the following Pressure-Yield-Force equation over the plug/dead zones with certain boundary conditions which depends mainly on the interfacial values of pressure between the plug and shear zones.

$$\boldsymbol{\Delta} p|_{plug/dead} = \boldsymbol{\nabla} \cdot (\boldsymbol{\nabla} \cdot \boldsymbol{\tau}_s) + \boldsymbol{\nabla} \cdot \boldsymbol{f}. \tag{2.117}$$

Therefore, needless to say the above equation shows a natural phenomenon for the fluids with yield which exhibits an extra property beside the plug regimes and cessation. Due to the difficulty to predict the plug

and dead regions in the flow domain then it is hardly to use Eq.(2.117) practically. So, the distribution of pressure can be defined approximately for the whole domain by solving one equation which can be extended to the following three partial differential equations

$$\boldsymbol{\nabla} p = \begin{cases} \mu \boldsymbol{\Delta u} + \boldsymbol{\nabla} \cdot (\tau_s \dfrac{\mathbf{D}(\boldsymbol{u})}{\|\mathbf{D}\|}) + \boldsymbol{f} \text{ if} & \|\mathbf{D}\| \neq 0, \boldsymbol{u} \neq \boldsymbol{c} \neq \mathbf{0} \\ \boldsymbol{\nabla} \cdot (\tau_s \dfrac{\mathbf{D}(\boldsymbol{u})}{\|\mathbf{D}\|}) + \boldsymbol{f} \text{ if} & \|\mathbf{D}\| = 0, \boldsymbol{u} = \boldsymbol{c}, \\ \boldsymbol{\nabla} \cdot (\tau_s \dfrac{\mathbf{D}(\boldsymbol{u})}{\|\mathbf{D}\|}) + \boldsymbol{f} \text{ if} & \|\mathbf{D}\| = 0, \boldsymbol{u} = \mathbf{0}. \end{cases} \tag{2.118}$$

2.10.4 The Influence of Regularization Techniques

Since it is quite hard to separate the domain to solve the corresponding pressure equation for each domain as well as our knowledge about the location of plug zones is not enough to define it precisely. Therefore, what we have between our hands only to cope each zone with the shear zone equation which is

$$\boldsymbol{\nabla} p = \boldsymbol{\nabla} \cdot (2\mu \mathbf{D}(\boldsymbol{u}) + \tau_s \frac{\mathbf{D}(\boldsymbol{u})}{\|\mathbf{D}\|}) + \boldsymbol{f}, \quad in \quad \boldsymbol{\Omega}. \tag{2.119}$$

Equation (2.119) can be approximated to the following for the different zones

$$\boldsymbol{\nabla} p = \begin{cases} \mu \boldsymbol{\Delta u} + \boldsymbol{\nabla} \cdot (\tau_s \dfrac{\mathbf{D}(\boldsymbol{u})}{\|\mathbf{D}\|}) + \boldsymbol{f} \text{ if} & \|\mathbf{D}\| \neq 0, \boldsymbol{u} \neq \boldsymbol{c} \neq \mathbf{0} \\ \boldsymbol{\nabla} \cdot (\tau_s \dfrac{\mathbf{D}(\boldsymbol{u})}{\|\mathbf{D}\|}) + \boldsymbol{f} \text{ if} & \|\mathbf{D}\| = 0, \boldsymbol{u} = \boldsymbol{c}, \\ \boldsymbol{\nabla} \cdot (\tau_s \dfrac{\mathbf{D}(\boldsymbol{u})}{\|\mathbf{D}\|}) + \boldsymbol{f} \text{ if} & \|\mathbf{D}\| = 0, \boldsymbol{u} = \mathbf{0}. \end{cases} \tag{2.120}$$

To approximate the function which defined the pressure distribution over the plug/dead zones $\boldsymbol{\nabla}.(\tau_s \frac{\mathbf{D}(\boldsymbol{u})}{\|\mathbf{D}\|})$ and avoid its discontinuity, it provided us to recognize and to choose which regularization is able to handle efficiently from the following four models:

$$\nu_\epsilon(\|\mathbf{D}\|) = 2\mu \ + \frac{\tau_s}{\epsilon + \|\mathbf{D}\|}, \tag{2.121a}$$

$$\nu_\epsilon(\|\mathbf{D}\|) = 2\mu \ + \frac{\tau_s}{\sqrt{\epsilon^2 + \|\mathbf{D}\|^2}}, \tag{2.121b}$$

$$\nu_\epsilon(\|\mathbf{D}\|) = 2\mu \ + \tau_s \frac{1 - exp(-\|\mathbf{D}\|/\epsilon)}{\|\mathbf{D}\|}, \tag{2.121c}$$

$$\nu_\epsilon(\|\mathbf{D}\|) = \begin{cases} 2\mu \ + \frac{\tau_s}{\|\mathbf{D}\|} \text{ if} & \|\mathbf{D}\| \geq TOL, \\ 2\mu + \frac{\tau_s}{\epsilon} \text{ if} & \|\mathbf{D}\| < TOL. \end{cases} \tag{2.121d}$$

From the definitions of (2.121a), (2.121b), and (2.121c), it can not be efficiently used since by the regularizing the equation already destroyed the discontinuous property (non-uniformity) of the pressure at the interfacial boundary between the regimes, which typically can be not noticed if it is expressed by the smooth function which supports some researchers to believe in the uniformity of pressure distribution over the fluid domain. In contrast for (2.121d) which has a nice property by splitting the function at the interfacial boundary to expose the difference among the pressure values. However, from the engineering point of view this pressure property allows us to say that the world of fluids has been always mystery for the primitive variables over the flow domain. This makes us to think again about the applications which depend mainly on the linear relation between the pressure drop and the length for unidirectional flow in pipe for the incompressible fluids. Not only this but also for every application of fluids which is focused on the linearity of pressure distribution.

2.10.5 Unidirectional Viscoplastic Flow

Let us make some simplicity by exposing one-dimensional problem to see obviously the case. From Eq.(2.115), the one dimensional the problem takes the following simplified form

$$\frac{dp}{dx} = \begin{cases} \mu\frac{d^2u}{dy^2} + \frac{d}{dy}(\tau_s\frac{\frac{du}{dy}}{|\frac{du}{dy}|}) + f \text{ if } \quad |\frac{du}{dy}| \neq 0, \quad u \neq const \neq 0 \quad in \quad \boldsymbol{\Omega}, \\ \frac{d\tau_s}{dy} + f \qquad\qquad\qquad\qquad \text{if } \quad |\frac{du}{dy}| = 0 \quad u = const, \quad in \quad \boldsymbol{\Omega}, \\ \frac{d\tau_s}{dy} + f \qquad\qquad\qquad\qquad\quad \text{if } \quad |\frac{du}{dy}| = 0 \quad u = 0 \quad in \quad \boldsymbol{\Omega}. \end{cases} \tag{2.122}$$

So, to get pressure drop by using the regularized models, one can regularize the following:

$$\frac{dp}{dx} = \begin{cases} \mu\frac{d^2u}{dy^2} + \frac{d}{dy}(\tau_s\frac{\frac{du}{dy}}{|\frac{du}{dy}|}) + f \text{ if } \quad |\frac{du}{dy}| \neq 0, \quad u \neq const \neq 0 \quad in \quad \boldsymbol{\Omega}, \\ \frac{d}{dy}(\tau_s\frac{\frac{du}{dy}}{|\frac{du}{dy}|}) + f \qquad\qquad \text{if } \quad |\frac{du}{dy}| = 0, \quad u = const \quad in \quad \boldsymbol{\Omega}, \\ \frac{d}{dy}(\tau_s\frac{\frac{du}{dy}}{|\frac{du}{dy}|}) + f \qquad\qquad\quad \text{if } \quad |\frac{du}{dy}| = 0, \quad u = 0 \quad in \quad \boldsymbol{\Omega}. \end{cases} \tag{2.123}$$

So, equation(2.123) can be written as the following to get the pressure drop(δp) over the flow regimes considering the parabolic profile for velocity in the shear regimes. Under the following condition, one can obtain the true exact solution of the pressure,
1) the yields stress is domain independent,
2) and the no external forces,
Therefore with the parts $\frac{d}{dy}(\tau_s\frac{\frac{du}{dy}}{|\frac{du}{dy}|}) = f = 0$, one can obtain the following pressure drop

$$\delta p = \begin{cases} c\delta x \quad \text{if } |\dfrac{du}{dy}| \neq 0, \quad u \neq 0, \\ 0 \quad\;\; \text{if } |\dfrac{du}{dy}| = 0, \quad u = const, \\ 0 \quad\;\; \text{if } |\dfrac{du}{dy}| = 0, \quad u = 0. \end{cases} \tag{2.124}$$

what it can be normally evolved from this equation is, the first definition shows the pressure drop in the shear regime which proportional linearly with the length of channel but the second and the third definitions have informed us to have a new term in the pressure definition which represents now the pressure drop for the plug/dead regime in the viscoplastic fluid and has zero value; as well as it can not be neglected at all. This term creates a discontinuity between the shear region and plug/dead regions which makes a pressure jump at interfacial boundary and nonuniform over the whole domain. The crucial of this term depends mainly on the yield stress parameter which is not appeared for the shear regime making conversion to the Newtonian fluid whenever its value equal zero. Thus, it is true to say that

For unidirectional fluids with yield stress the linearity of pressure existed only on the shear regions but never accepted for the whole flow domain.

Therefore, the complete solutions of the velocity/pressure for unidirectional flow problem for a channel with unit width a constant pressure gradient and the absence of external force can be written as the following:

$$\boldsymbol{u} = (u, 0), \tag{2.125}$$

where,

$$u=\begin{cases}\dfrac{c}{2\mu}y(1-y)-\dfrac{\tau_s}{\mu}y & \text{if} \quad 0\le y<\dfrac{1}{2}-\dfrac{\tau_s}{c},\\ \dfrac{c}{2\mu}(\dfrac{1}{2}-\dfrac{\tau_s}{c})^2 & \text{if} \quad \dfrac{1}{2}-\dfrac{\tau_s}{c}\le y\le\dfrac{1}{2}+\dfrac{\tau_s}{c},\\ \dfrac{c}{2\mu}y(1-y)-\dfrac{\tau_s}{\mu}(1-y) & \text{if} \quad \dfrac{1}{2}+\dfrac{\tau_s}{c}<y<1,\end{cases} \tag{2.126}$$

and the pressure,

$$p=\begin{cases}-cx+constant & \text{if} \quad 0\le y<\dfrac{1}{2}-\dfrac{\tau_s}{c},\\ 0 & \text{if} \quad \dfrac{1}{2}-\dfrac{\tau_s}{c}\le y\le\dfrac{1}{2}+\dfrac{\tau_s}{c},\\ -cx+constant & \text{if} \quad \dfrac{1}{2}+\dfrac{\tau_s}{c}<y<1.\end{cases} \tag{2.127}$$

2.10.6 Darcy's Law (Flow in Pipes)

This law represents a simple relation between the pressure drop and the discharge or length of the pipe governed by the linearity between the pressure drop and the pipe length, the question which should emit here is, does the pressure in viscoplastic fluid follow Darcy law in pipe which built on linearity of pressure. Of course not since the pressure has no such uniformity or linearity over the whole domain and connected strongly with the yield stress value which comes from the following

$$\frac{dp}{dx}=\begin{cases}\frac{\mu d^2u}{dy^2}+\frac{d}{dy}(\tau_s\frac{\frac{du}{dy}}{|\frac{du}{dy}|}) \quad if \quad |\frac{du}{dy}|\neq 0, \quad u\neq const\neq 0 \quad in \quad \boldsymbol{\Omega},\\ \frac{d}{dy}(\tau_s\frac{\frac{du}{dy}}{|\frac{du}{dy}|}) \quad if \quad |\frac{du}{dy}|=0, \quad u=const \quad in \quad \boldsymbol{\Omega},\\ \frac{d}{dy}(\tau_s\frac{\frac{du}{dy}}{|\frac{du}{dy}|}) \quad if \quad |\frac{du}{dy}|=0, \quad u=0 \quad in \quad \boldsymbol{\Omega}.\end{cases} \tag{2.128}$$

Therefore, it is not allowed to claim that the linearity between the pressure drop and the length of the pipe is global phenomenon for the incompressible fluids, therefore we are truly sure by Darcy's law destroyed in the generalized incompressible viscoplastic fluid. Thus, the importance of this claim lies in industry since the hydrodynamic machines for the incompressible fluids depends mainly on the linearity between pressure drop and the gravity and head losses as friction; in particularly hydrodynamic machines which are used to pumping viscoplastic fluids such as juices, concrete, oils and petrol wherever it can be taken into the account from the design point of view.

2.10.7 Well-Posedness of Pressure for Bingham Viscoplastic Problem

To address the properties of the Bingham model particularly the distribution of pressure, let us introduce the following weak form (see [7])

$$2\mu a(\boldsymbol{u},\boldsymbol{v})+\tilde{a}(\boldsymbol{u},\boldsymbol{v})-c(p,\boldsymbol{v})+c(q,\boldsymbol{u})=(\boldsymbol{f},\boldsymbol{v}). \tag{2.129}$$

where $\tilde{a}(\boldsymbol{u},\boldsymbol{v})=\int_\Omega \frac{\tau_s}{\|\mathbf{D}\|}\mathbf{D}(\boldsymbol{u}):\mathbf{D}(\boldsymbol{v})d\boldsymbol{x}$. It is easy to check the ellipticity condition for the bilinear form $a(\boldsymbol{u},\boldsymbol{v})$ by using Korn's inequality to have

$$a(\boldsymbol{u},\boldsymbol{u})\ge\alpha\|\boldsymbol{u}\|_1^2 \quad \forall\boldsymbol{u}\in\mathbf{H}_0^1. \tag{2.130}$$

Let us introduce the continuity and monotonicity for the regularized $\tilde{a}(\boldsymbol{u},\boldsymbol{v})$ to be $\tilde{a}_\epsilon(\boldsymbol{u},\boldsymbol{v})$ to have the following

$$\tilde{a}_\epsilon(\boldsymbol{u},\boldsymbol{v}) \leq \frac{\tau_s}{\epsilon}\left\|\boldsymbol{u}\right\|_1\left\|\boldsymbol{v}\right\|_1 \quad \forall \boldsymbol{u},\boldsymbol{v}\in \mathbf{H}_0^1, \tag{2.131a}$$

$$\tilde{a}_\epsilon(\boldsymbol{u},\boldsymbol{u}-\boldsymbol{v}) - \tilde{a}_\epsilon(\boldsymbol{v},\boldsymbol{u}-\boldsymbol{v}) \geq c\left\|\boldsymbol{u}-\boldsymbol{v}\right\|_1 \quad \forall \boldsymbol{u},\boldsymbol{v}\in \mathbf{H}_0^1. \tag{2.131b}$$

Theorem 2.10.3 *The weak form (Eq.(2.129))for Bingham viscoplastic fluid has a unique solution* $\{\boldsymbol{u},p\}\in \mathbf{H}_0^1\times \mathbf{L}_0^2$ *for a convex domain* $\boldsymbol{\Omega}$ *satisfying the following estimates*

$$\left\|p\right\|_0 \leq c(2\mu+\frac{\tau_s}{\epsilon})\left\|\boldsymbol{\nabla u}\right\|_0 + \left\|\boldsymbol{f}\right\|_{-1} \quad if \quad \left\|\boldsymbol{\nabla u}\right\|_0 \neq 0, \tag{2.132a}$$

$$\left\|p\right\|_0 \leq c\left\|\boldsymbol{f}\right\|_{-1} \quad if \quad \left\|\boldsymbol{\nabla u}\right\|_0 = 0. \tag{2.132b}$$

Proof

To prove the first estimate let us use substitute in the weak form Eq.(2.129)$\boldsymbol{v}=\boldsymbol{u}$, q=p and apply $(\boldsymbol{f},\boldsymbol{v}) \leq \left\|\boldsymbol{f}\right\|_{-1}\left\|\boldsymbol{\nabla v}\right\|_0$ so that, one can have

$$\frac{(\boldsymbol{\nabla}\cdot\boldsymbol{v},p)}{\left\|\boldsymbol{\nabla v}\right\|_0} \leq c(2\mu\left\|\boldsymbol{\nabla u}\right\|_0 + \tau_s|\boldsymbol{\Omega}|^{\frac{1}{2}} + \left\|\boldsymbol{f}\right\|_{-1}), \tag{2.133}$$

so that one can obtain the following estimate(see [7])

$$\left\|p\right\|_0 \leq c(2\mu+\frac{\tau_s}{\epsilon})\left\|\boldsymbol{\nabla u}\right\|_0 + \left\|\boldsymbol{f}\right\|_{-1}. \tag{2.134}$$

In the case of the existence of plug and dead zones $\left\|\boldsymbol{\nabla u}\right\|_0 = 0$ then the estimate takes the form

$$\left\|p\right\|_0 \leq c\left\|\boldsymbol{f}\right\|_{-1}. \tag{2.135}$$

2.11 Drag and Lift Forces

Two ways to compute the drag and lift forces for an immersed obstacle in a fluid are presented. The first utilizes the classical idea which based on surface integral of the normal component of the stress tensor over the surface. The second is built on the idea of the consistent force method via the consistent flux method. The latter has the benefit to circumvent the direct boundary integration in the finite element solution which is typically concomitant with poor results in drag and lift calculations. Because of this, an idea is presented for the former in which the availability to construct a function to identify the obstacle's domain with its gradient equals to the normal vector on the object's boundary to enhance the accuracy of the method in the finite element calculations. The computation of drag and lift coefficients of a body immersed in a fluid is the subject which attracts many researchers due to its practical importance in many applications. It has not only a big interest in industrial applications such as the automotive vehicles design (e.g. aircrafts), but also it is an effective benchmark problem to measure the accuracy of the proposed algorithms for the flow problems. John in [118] used the reference benchmark parameters as comparing factor of several finite element discretization with respect to the accuracy of the computed parameters. In [28] used it to investigate the accuracy of equal-order FEM based on piecewise quadratic shape functions with local projection stabilization for stationary laminar flows. Therefore, Our work now is to present the precise computations for the forces or the coefficients of drag and lift by using the classical methods(surface integral form) which based on the integral of the normal component of the traction stress tensor over the surface of the obstacle or the consistent force method (so-called volume integral form) which based on the idea of consistent flux method.
Let Γ_o be the boundary of the obstacle immersed in a fluid with velocity field $\boldsymbol{u}$ and pressure p in the

domain $\boldsymbol{\Omega}$ and its boundary $\partial\boldsymbol{\Omega}$. Assume U_m and ρ being the mean velocity of the fluid and the density respectively, and A is the projected area. So the drag and lift coefficients can be defined in the following way:

$$C_d = \frac{2F_d}{\rho U_m^2 A}, \tag{2.136a}$$

$$C_l = \frac{2F_l}{\rho U_m^2 A}. \tag{2.136b}$$

where F_d and F_l are the total drag and lift forces exerted on the obstacle by a fluid respectively.

2.11.1 Calculation of Drag and Lift Forces(Classical Method)

The classical way to calculate the drag and lift forces is to integrate the normal component of the stress tensor ($\boldsymbol{\sigma}$) over the surface($\mathbf{S}$) as follows:

$$\mathbf{F} = \int_{\Gamma_o} \boldsymbol{\sigma} \cdot \boldsymbol{n} d\mathbf{S}, \tag{2.137}$$

where, $\mathbf{n}$ is the outward unit normal on the boundary Γ_o of the surface($\mathbf{S}$). The resultant force $\mathbf{F}$ can be analyzed into the drag and lift components with respect to the horizontal and vertical directions(e_x, e_y) as well as the normal and tangential components with respect to the tangential and normal directions($\boldsymbol{n}, \boldsymbol{t}$)(see Fig.2.6) as follows:

$$\mathbf{F} = F_d e_x + F_l e_y = F_n \boldsymbol{n} + F_t \boldsymbol{t}. \tag{2.138}$$

where F_d and F_l are drag and the lift forces and F_n and F_t are the normal and tangential forces respectively on the object boundary. In order to calculate the force components where the object immersed in Newtonian fluid, the prescribed stress tensor for the Newtonian fluid can be written in the following form

$$\boldsymbol{\sigma} = -pI + 2\mu\mathbf{D}, \qquad \mathbf{D} = \frac{1}{2}(\boldsymbol{\nabla u} + \boldsymbol{\nabla u}^T) \tag{2.139}$$

where $\mathbf{D}$ represents the symmetric deformation form. Incorporating Eq.(2.139) into Eq.(2.137) and after simple calculations one can deduce the following expressions to obtain the complete form for the force components:

$$F_d = \int_{\Gamma_o} ((2\mu\frac{\partial u_1}{\partial x} - p)n_x + \mu(\frac{\partial u_1}{\partial y} + \frac{\partial u_2}{\partial x})n_y)ds, \tag{2.140a}$$

$$F_l = \int_{\Gamma_o} (\mu(\frac{\partial u_1}{\partial y} + \frac{\partial u_2}{\partial x})n_x + (2\mu\frac{\partial u_2}{\partial y} - p)n_y)ds, \tag{2.140b}$$

$$F_n = \int_{\Gamma_o} (2\mu(\frac{\partial u_1}{\partial x}n_x^2 + (\frac{\partial u_1}{\partial y} + \frac{\partial u_2}{\partial x})n_x n_y + \frac{\partial u_2}{\partial y}n_y^2) - p)ds, \tag{2.140c}$$

$$F_t = \int_{\Gamma_o} (\mu(2\frac{\partial u_1}{\partial x}t_x n_x + (\frac{\partial u_1}{\partial y} + \frac{\partial u_2}{\partial x})(t_x n_y + t_y n_x) + 2\frac{\partial u_2}{\partial y}t_y n_y))ds. \tag{2.140d}$$

In order to simplify the previous forms, one can choose the gradient form instead the symmetric deformation form in the stress tensor equation which will be read as follows:

$$\boldsymbol{\sigma} = -pI + 2\mu\boldsymbol{\nabla u}, \tag{2.141}$$

therefore the drag and lift forces can be written as follows

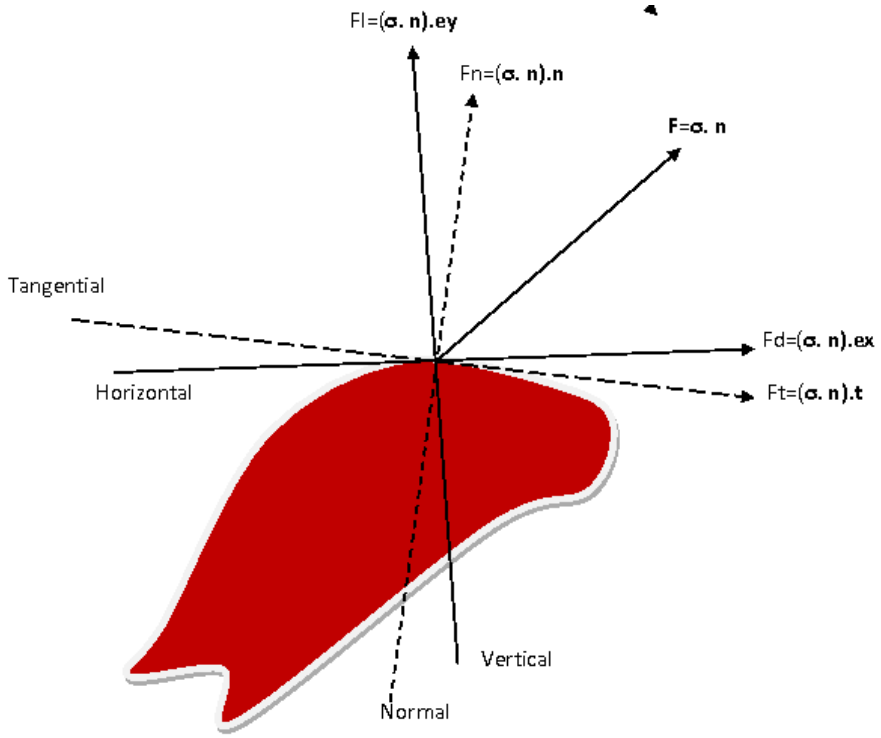

Fig. 2.6. Traction vector and the components of the forces on the boundary of an immersed surface in a fluid.

$$F_d = \int_{\Gamma_o} (2\mu(\frac{\partial u_1}{\partial x}n_x + \frac{\partial u_1}{\partial y}n_y) - pn_x)ds = \int_{\Gamma_o} (2\mu\frac{\partial u_1}{\partial \boldsymbol{n}} - pn_x)ds, \tag{2.142a}$$

$$F_l = \int_{\Gamma_o} (2\mu(\frac{\partial u_2}{\partial x}n_x + \frac{\partial u_2}{\partial y}n_y) - pn_y)ds = \int_{\Gamma_o} (2\mu\frac{\partial u_2}{\partial \boldsymbol{n}} - pn_y)ds \tag{2.142b}$$

Remark: In [118] it has been claimed the following formula to calculate the total drag

$$F_d = \int_{\Gamma_o} (2\mu\frac{\partial u_t}{\partial \boldsymbol{n}}n_y - pn_x)ds, \tag{2.143}$$

So, let us introduce the idea to check whether it is valid or not from the following derivation. Assume that the components of velocity $\boldsymbol{u}$ in cartesian coordinates as well as the normal and tangential coordinates will be as follows

$$\boldsymbol{u} = u_1 ex + u_2 ey = u_t \boldsymbol{t} + u_n \boldsymbol{n}, \tag{2.144}$$

where, u_1 and u_2 horizontal and vertical components of velocity and u_t and u_n tangential and normal components of velocity on the boundary. So from Fig.2.6 one can deduce the following

$$u_t = u_1 n_y - u_2 n_x \quad \rightsquigarrow \quad \frac{\partial u_t}{\partial \boldsymbol{n}} = \frac{\partial u_1}{\partial \boldsymbol{n}}n_y - \frac{\partial u_2}{\partial \boldsymbol{n}}n_x, \tag{2.145}$$

where $\boldsymbol{n} = (n_x \quad n_y)^T$, then one can deduce readily the following

$$\frac{\partial u_t}{\partial \boldsymbol{n}}ny = \frac{\partial u_1}{\partial \boldsymbol{n}}n_y^2 - \frac{\partial u_2}{\partial \boldsymbol{n}}n_x n_y, \tag{2.146}$$

since $\boldsymbol{n} = (n_x \quad n_y)^T$ which leads to $n_x^2 + n_y^2 = 1$, plug ny^2 into Eq.(2.146) to have the following

$$\frac{\partial u_t}{\partial \boldsymbol{n}} ny = \frac{\partial u_1}{\partial \boldsymbol{n}} - n_x(\frac{\partial u_1}{\partial \boldsymbol{n}} n_x - \frac{\partial u_2}{\partial \boldsymbol{n}} n_y), \tag{2.147}$$

in RHS the term $\frac{\partial u_1}{\partial \boldsymbol{n}} n_x - \frac{\partial u_2}{\partial \boldsymbol{n}} n_y$ should equal zero to have the same form in Eq.(2.143) and it is claimed that, this term equalize the incompressibility condition($\boldsymbol{\nabla}.\boldsymbol{u} = 0$), since the divergence of velocity in both coordinates is

$$\frac{\partial u_1}{\partial x} + \frac{\partial u_2}{\partial y} = \frac{\partial u_n}{\partial \boldsymbol{n}} + \frac{\partial u_t}{\partial \boldsymbol{t}} = 0, \tag{2.148}$$

which have an equivalence even if one simplified to the other one therefore, Eq.(2.143) can be used to calculate the drag force.

2.11.1.a Calculation of the Normal Vector

The concomitant difficulty with this method is to approximate the normal vector on the boundary. The first way to expose is to analyze at each node on the boundary the normal and tangent on the edges to facilitate to use Eq.(2.137) in the following way

$$\mathbf{F} = \Sigma_{\Gamma_o} \boldsymbol{\sigma}_i \cdot \boldsymbol{n}_i d\mathbf{S}_i. \tag{2.149}$$

Unfortunately this remedy has a defect always in accuracy whether the mesh is not refined so enough or not. However, the second choice is to provide a function to identify the interested boundary with a gradient equals to the normal vector. But it has some restrictions which can be outlined as follows:

(1) The function should have the following property to identify the solid and fluid regions:

$$\alpha(\boldsymbol{x}) = \begin{cases} 1, & \text{on} \quad \Gamma_o, \\ 0, & \text{on} \quad \Omega/\Gamma_o, \end{cases} \tag{2.150}$$

(2) The normal can be represented by gradient on the boundary Γ_o

$$\boldsymbol{n} = \boldsymbol{\nabla}\alpha(\boldsymbol{x}) \tag{2.151}$$

(3) The gradient of the function α is zero everywhere, except at solid-liquid interface

Therefore, which function typically does the above properties to convert Eq.(2.142) in the following way

$$F_d = \int_{\Gamma_o} (2\mu(\frac{\partial u_1}{\partial x}\frac{\partial \alpha}{\partial x} + \frac{\partial u_1}{\partial y}\frac{\partial \alpha}{\partial y}) - p\frac{\partial \alpha}{\partial x})ds, \tag{2.152a}$$

$$F_l = \int_{\Gamma_o} (2\mu(\frac{\partial u_2}{\partial x}\frac{\partial \alpha}{\partial x} + \frac{\partial u_2}{\partial y}\frac{\partial \alpha}{\partial y}) - p\frac{\partial \alpha}{\partial y})ds. \tag{2.152b}$$

2.11.2 The Force Consistent Method(Volume Integral Formula)

This method has a great importance to calculate the drag and lift forces for flow problems with finite element computations. In order to explain the main idea of the force consistent method which so-called volume integral formula to calculate the approximated drag and lift forces on an immersed object in a fluid, we will repeat the weak form for the momentum balance equation in stress-divergence form under the absence of external forces as follows:

$$-(\frac{\partial \boldsymbol{u}}{\partial t}+\boldsymbol{u}\cdot\boldsymbol{\nabla}\boldsymbol{u})+\boldsymbol{\nabla}\cdot\boldsymbol{\sigma}=0. \tag{2.153}$$

Now we multiply the above equation by a test function $\boldsymbol{v}$ and integrate to obtain the following:

$$-\int_{\boldsymbol{\Omega}}(\frac{\partial \boldsymbol{u}}{\partial t}\boldsymbol{v}+(\boldsymbol{u}\cdot\boldsymbol{\nabla}\boldsymbol{u})\boldsymbol{v})d\boldsymbol{x}+\int_{\boldsymbol{\Omega}}(\boldsymbol{\nabla}\cdot\boldsymbol{\sigma})\cdot\boldsymbol{v}d\boldsymbol{x}=0. \tag{2.154}$$

Apply the integration by parts for the RHS and by using the divergence theorem to get the following:

$$-\int_{\boldsymbol{\Omega}}(\frac{\partial \boldsymbol{u}}{\partial t}\boldsymbol{v}+(\boldsymbol{u}\cdot\boldsymbol{\nabla}\boldsymbol{u})\boldsymbol{v})d\boldsymbol{x}+\int_{\boldsymbol{\Omega}}\boldsymbol{\sigma}.\boldsymbol{\nabla}(\boldsymbol{v}))d\boldsymbol{x}=\int_{\partial\boldsymbol{\Omega}}(\boldsymbol{\sigma}\cdot\boldsymbol{n})\cdot\boldsymbol{v}ds, \tag{2.155}$$

where $\boldsymbol{n}$ is the outward unit normal on the boundary of the domain $\boldsymbol{\Omega}$. So, the term $(\boldsymbol{\sigma}\cdot\boldsymbol{n})$ in the RHS of the above equation shows the way to an appropriate natural boundary condition (NBC) which represents the physical applied force(traction) per unit area on the boundary, and typically can be prescribed as an input data for the interested problem. Nevertheless, the solution of the interested problem can be found once this force is specified. The easiest assumption is to take no action required which represents an another example of DO NOTHING boundary condition which always desired by the user. However, For this way which coming from the global force/momentum balance, it is already suggested to compute the forces exerted on the fluid by the boundary at all locations that used Dirichlet boundary condition for the velocity. It is called the consistent force method via flux consisted method to calculate the consistent flux on the boundary. Indeed, the equation will generate forces (e.g. li ft and drag) on the Dirichlet BC's whose accuracy is commensurate with that of the primary variables(pressure and velocity). So, our task now is to use this idea to calculate the force on the boundary for an immersed object in a Newtonian fluid which is readily to do the following.
The stress form used to describe the Newtonian fluid as mentioned before, reads as follows:

$$\boldsymbol{\sigma}=-pI+2\mu\mathbf{D},\qquad \mathbf{D}=\frac{1}{2}(\boldsymbol{\nabla}\boldsymbol{u}+\boldsymbol{\nabla}\boldsymbol{u}^T) \tag{2.156}$$

assume that, $\boldsymbol{u}=(u_1\quad u_2)^T$, and $\boldsymbol{v}=(v_d\quad v_l)^T$ are the components in cartesian coordinates for velocity and test function respectively and $\frac{D\boldsymbol{u}}{Dt}=\frac{\partial \boldsymbol{u}}{\partial t}+\boldsymbol{u}\cdot\boldsymbol{\nabla}\boldsymbol{u}$ the total time derivative of the velocity field, after simple calculation one can deduce the following in x and y directions:

$$\begin{aligned}&-\int_{\boldsymbol{\Omega}}(\frac{Du_1}{Dt}v_d+\mu(2\frac{\partial u_1}{\partial x}\frac{\partial v_d}{\partial x}+\frac{\partial u_1}{\partial y}\frac{\partial v_d}{\partial y})+\mu\frac{\partial u_2}{\partial x}\frac{\partial v_d}{\partial y}-p\frac{\partial v_d}{\partial x})d\boldsymbol{x}\\&=\int_{\Gamma_o}\{(2\mu\frac{\partial u_1}{\partial x}-p)n_x+\mu(\frac{\partial u_1}{\partial y}+\frac{\partial u_2}{\partial x})n_y\}v_d ds,\end{aligned} \tag{2.157a}$$

$$\begin{aligned}&-\int_{\boldsymbol{\Omega}}(\frac{Du_2}{Dt}v_l+\mu(2\frac{\partial u_2}{\partial y}\frac{\partial v_l}{\partial y}+\frac{\partial u_2}{\partial y}\frac{\partial v_l}{\partial y})+\mu\frac{\partial u_2}{\partial y}\frac{\partial v_l}{\partial x}-p\frac{\partial v_l}{\partial y})d\boldsymbol{x}\\&=\int_{\Gamma_o}\{(2\mu\frac{\partial u_2}{\partial y}-p)n_y+\mu(\frac{\partial u_1}{\partial y}+\frac{\partial u_2}{\partial x})n_x\}v_l ds,\end{aligned} \tag{2.157b}$$

or one can derive the following short forms,

$$\begin{aligned}&-\int_{\boldsymbol{\Omega}}(\frac{Du_1}{Dt}v_d+\mu\boldsymbol{\nabla}u_1\cdot\boldsymbol{\nabla}v_d+\mu(\frac{\partial u_1}{\partial x}\frac{\partial v_d}{\partial x}+\frac{\partial u_2}{\partial x}\frac{\partial v_d}{\partial y})-p\frac{\partial v_d}{\partial x})d\boldsymbol{x}\\&=\int_{\Gamma_o}\{(2\mu\frac{\partial u_1}{\partial x}-p)n_x+\mu(\frac{\partial u_1}{\partial y}+\frac{\partial u_2}{\partial x})n_y\}v_d ds,\end{aligned} \tag{2.158a}$$

$$\begin{aligned}&-\int_{\boldsymbol{\Omega}}(\frac{Du_2}{Dt}v_l+\mu\boldsymbol{\nabla}u_2\cdot\boldsymbol{\nabla}v_l+\mu(\frac{\partial u_1}{\partial y}\frac{\partial v_l}{\partial x}+\frac{\partial u_2}{\partial y}\frac{\partial v_l}{\partial y})-p\frac{\partial v_l}{\partial y})d\boldsymbol{x}\\&=\int_{\Gamma_o}\{(2\mu\frac{\partial u_2}{\partial y}-p)n_y+\mu(\frac{\partial u_1}{\partial y}+\frac{\partial u_2}{\partial x})n_x\}v_l ds.\end{aligned} \tag{2.158b}$$

By inspecting the RHS terms of the above two equations Eq(2.158), one can find the same values of drag and lift forces with those of Eq.(2.140a) and Eq.(1.140b) from the classical method times the test function and they will be the same if the value of the test functions equals unity at the interested boundary. By introducing the simple form of the stress tensor by using the gradient form which reads

$$\boldsymbol{\sigma} = -pI + 2\mu\boldsymbol{\nabla}\boldsymbol{u}. \tag{2.159}$$

Incorporate into the weak formulation Eq.(2.155) to get the following

$$-\int_{\boldsymbol{\Omega}}(\frac{Du_1}{Dt}v_d + 2\mu\boldsymbol{\nabla}u_1\cdot\boldsymbol{\nabla}v_d - p\frac{\partial v_d}{\partial x})d\boldsymbol{x} = \int_{\Gamma_o}\{(2\mu\frac{\partial u_1}{\partial x} - p)n_x + 2\mu\frac{\partial u_1}{\partial y}n_y\}v_d ds, \tag{2.160a}$$

$$-\int_{\boldsymbol{\Omega}}(\frac{Du_2}{Dt}v_l + 2\mu\boldsymbol{\nabla}u_2\cdot\boldsymbol{\nabla}v_l - p\frac{\partial v_l}{\partial y})d\boldsymbol{x} = \int_{\Gamma_o}\{(2\mu\frac{\partial u_2}{\partial y} - p)n_y + 2\mu\frac{\partial u_2}{\partial x}n_x\}v_l ds, \tag{2.160b}$$

readily, one can derive the following short forms

$$-\int_{\boldsymbol{\Omega}}(\frac{Du_1}{Dt}v_d + 2\mu\boldsymbol{\nabla}u_1\cdot\boldsymbol{\nabla}v_d - p\frac{\partial v_d}{\partial x})d\boldsymbol{x} = \int_{\Gamma_o}\{2\mu\frac{\partial u_1}{\partial \boldsymbol{n}} - pn_x\}v_d ds, \tag{2.161a}$$

$$-\int_{\boldsymbol{\Omega}}(\frac{Du_2}{Dt}v_l + 2\mu\boldsymbol{\nabla}u_2\cdot\boldsymbol{\nabla}v_l - p\frac{\partial v_l}{\partial y})d\boldsymbol{x} = \int_{\Gamma_o}\{2\mu\frac{\partial u_2}{\partial \boldsymbol{n}} - pn_y\}v_l ds. \tag{2.161b}$$

So too, by inspecting the RHS terms of the above two equations Eq.(2.161a) and Eq.(2.161b)), one can find the same values of drag and lift forces with those of Eq.(2.142) from the classical method for the simplified forms times the test function and already will be the same if the value of the test function equal unity at the interested boundary.
One can merge the two equation after recalling the total derivative to get the following vector form:

$$-\int_{\Omega}(\frac{\partial \boldsymbol{u}}{\partial t}\boldsymbol{v} + (\boldsymbol{u}\cdot\boldsymbol{\nabla}\boldsymbol{u})\boldsymbol{v} + 2\mu\boldsymbol{\nabla}\boldsymbol{u}\cdot\boldsymbol{\nabla}\boldsymbol{v} - p\boldsymbol{\nabla}\cdot\boldsymbol{v})d\boldsymbol{x} = \int_{\Gamma_o}\{2\mu\frac{\partial \boldsymbol{u}}{\partial \boldsymbol{n}} - p\boldsymbol{n}\}\cdot\boldsymbol{v}ds, \tag{2.162}$$

let us present in the following inner product form

$$-((\frac{\partial \boldsymbol{u}}{\partial t}, \boldsymbol{v}) + ((\boldsymbol{u}\cdot\boldsymbol{\nabla}\boldsymbol{u}), \boldsymbol{v}) + 2\mu(\boldsymbol{\nabla}\boldsymbol{u}, \boldsymbol{\nabla}\boldsymbol{v}) - (p, \boldsymbol{\nabla}\cdot\boldsymbol{v})) = (\mathsf{F}_{d,l}, \boldsymbol{v}), \tag{2.163}$$

This form has a significant property to use directly the primitive variables output to calculate the drag and lift forces. Keeping in mind, the other terms in the complete form in Eq.(2.158) will often be significant and should not be neglected at least if one wishes to wring the last drop of accuracy from the simulation. Comparing with Navier-Stokes equations, let us introduce the weak form in terms of u-p variables with the external force $\boldsymbol{f}$ which is written as follows:

$$(\frac{\partial \boldsymbol{u}}{\partial t}, \boldsymbol{v}) + ((\boldsymbol{u}\cdot\boldsymbol{\nabla}\boldsymbol{u}), \boldsymbol{v}) + 2\mu(\boldsymbol{\nabla}\boldsymbol{u}, \boldsymbol{\nabla}\boldsymbol{v}) - (p, \boldsymbol{\nabla}\cdot\boldsymbol{v}) = (\boldsymbol{f}, \boldsymbol{v}). \tag{2.164}$$

Compare the two forms Eq.(2.163) and Eq.(2.164) one can result the equivalence between the two forms if we multiplied the consistent force equation by minus sign. Therefore, the non-stationary form of Navier-Stokes equation is quite valid to calculate the approximated forces of drag and lift by using the consistent force method on the object's boundary. Any way, the two equations can be merged as follows:

$$(\frac{\partial \boldsymbol{u}}{\partial t}, \boldsymbol{v}) + ((\boldsymbol{u}\cdot\boldsymbol{\nabla}\boldsymbol{u}), \boldsymbol{v}) + 2\mu(\boldsymbol{\nabla}\boldsymbol{u}, \boldsymbol{\nabla}\boldsymbol{v}) - (p, \boldsymbol{\nabla}\cdot\boldsymbol{v}) - (\boldsymbol{f}, \boldsymbol{v}) = -(\mathsf{F}_{d,l}, \boldsymbol{v}). \tag{2.165}$$

Since Eq.(2.165) is meaningful for the velocity and pressure fields and is valid for the weak solution for a suitable spaces, and it can be readily employed for the computation of total drag and lift forces. To follow, the following assumptions should be taken into our account on the interested boundary Γ_o

$$v_d|_{\Gamma_o} = \begin{pmatrix} 1 \\ 0 \\ 0 \end{pmatrix}, \qquad \boldsymbol{v}_d|_{\partial\boldsymbol{\Omega}/\Gamma_o} = \begin{pmatrix} 0 \\ 0 \\ 0 \end{pmatrix} \tag{2.166}$$

$$v_l|_{\Gamma_o} = \begin{pmatrix} 0 \\ 1 \\ 0 \end{pmatrix}, \qquad v_l|_{\partial\boldsymbol{\Omega}/\Gamma_o} = \begin{pmatrix} 0 \\ 0 \\ 0 \end{pmatrix}. \tag{2.167}$$

So, the drag and lift forces have the following forms respectively

$$F_d = -((\frac{\partial \boldsymbol{u}}{\partial t}, v_d) + ((\boldsymbol{u}\cdot\boldsymbol{\nabla}\boldsymbol{u}), v_d) + 2\mu(\boldsymbol{\nabla}\boldsymbol{u}, \boldsymbol{\nabla} v_d) - (p, \boldsymbol{\nabla}\cdot v_d) - (\boldsymbol{f}, v_d)), \tag{2.168a}$$

$$F_l = -((\frac{\partial \boldsymbol{u}}{\partial t}, v_l) + ((\boldsymbol{u}\cdot\boldsymbol{\nabla}\boldsymbol{u}), v_l) + 2\mu(\boldsymbol{\nabla}\boldsymbol{u}, \boldsymbol{\nabla} v_l) - (p, \boldsymbol{\nabla}\cdot v_l) - (\boldsymbol{f}, v_l)). \tag{2.168b}$$

Let us recall and rewrite again equation Eq.(2.168) in the finite element sense, and suppose $\boldsymbol{v}_h$ the interpolation function of $\boldsymbol{v}$ for a suitable finite space, the approximated forces can be defined by

$$(\mathbf{F}_h, \boldsymbol{v}_h) = -((\frac{\partial \boldsymbol{u}_h}{\partial t}, \boldsymbol{v}_h) + ((\boldsymbol{u}_h\cdot\boldsymbol{\nabla}\boldsymbol{u}_h), \boldsymbol{v}_h) + 2\mu(\boldsymbol{\nabla}\boldsymbol{u}_h, \boldsymbol{\nabla}\boldsymbol{v}_h) - (p_h, \boldsymbol{\nabla}\cdot\boldsymbol{v}_h) - (\boldsymbol{f}_h, \boldsymbol{v}_h)). \tag{2.169}$$

Typically, Eq.(2.169) makes the computation of forces easier as well as it enables us to derive the error estimate for the calculated forces. In the case of stabilized finite element, indeed the stabilization terms make sense to get a significant accuracy for the approximated values unless if we detected the optimal stabilization parameters which practically and theoretically are not available.

2.11.3 Generalized Newtonian Fluid(Classical Method)

Let us follow the same steps by developing the nonlinear viscosity instead of constant viscosity to calculate the force components where the object immersed on an Non-Newtonian fluid. So, the stress tensor can be written in the following form:

$$\boldsymbol{\sigma} = -pI + \nu(\|\mathbf{D}\|, p)\mathbf{D}, \tag{2.170}$$

where $\mathbf{D} = \frac{1}{2}(\boldsymbol{\nabla}\boldsymbol{u} + \boldsymbol{\nabla}\boldsymbol{u}^T)$ and $\nu(\|\mathbf{D}\|, p)$ is the nonlinear viscosity which will be for the Bingham viscoplastic fluid $2\mu + \frac{\tau_s}{\|\mathbf{D}\|}$. Incorporate Eq.(2.170) into Eq.(2.137)and after simple calculations one can deduce the following expressions for the force components:

$$F_d = \int_{\Gamma_o} (\nu\frac{\partial u_1}{\partial x} - p)n_x + \frac{\nu}{2}(\frac{\partial u_1}{\partial y} + \frac{\partial u_2}{\partial x})n_y)ds, \tag{2.171a}$$

$$F_l = \int_{\Gamma_o} (\frac{\nu}{2}(\frac{\partial u_1}{\partial y} + \frac{\partial u_2}{\partial x})n_x + (\nu\frac{\partial u_2}{\partial y} - p)n_y)ds, \tag{2.171b}$$

$$F_n = \int_{\Gamma_o} (\nu(\frac{\partial u_1}{\partial x}n_x^2 + (\frac{\partial u_1}{\partial y} + \frac{\partial u_2}{\partial x})n_x n_y + \frac{\partial u_2}{\partial y}n_y^2) - p)ds, \tag{2.171c}$$

$$F_t = \int_{\Gamma_o} (\frac{\nu}{2}(2\frac{\partial u_1}{\partial x}t_x n_x + (\frac{\partial u_1}{\partial y} + \frac{\partial u_2}{\partial x})(t_x n_y + t_y n_x) + 2\frac{\partial u_2}{\partial y}t_y n_y))ds \tag{2.171d}$$

Remark: In order to simplify the previous forms, one can choose the gradient form instead the symmetric deformation form in the stress tensor equation which will read as follows:

$$\boldsymbol{\sigma} = -pI + \nu_G(\|\boldsymbol{\nabla} u\|, p)\boldsymbol{\nabla}\boldsymbol{u}, \tag{2.172}$$

where $\nu_G(\|\boldsymbol{\nabla u}\|, p)$ is the nonlinear viscosity with gradient form which will be read for Bingham viscoplastic fluid $2\mu + \frac{\tau_s}{\|\boldsymbol{\nabla u}\|}$. Therefore, the drag and lift force can be written in the following simplified forms as follows

$$F_d = \int_{\Gamma_o} (\nu_G(\frac{\partial u_1}{\partial x} n_x + \frac{\partial u_1}{\partial y} n_y) - p n_x) ds = \int_{\Gamma_o} (\nu_G \frac{\partial u_1}{\partial \boldsymbol{n}} - p n_x) ds, \tag{2.173a}$$

$$F_l = \int_{\Gamma_o} (\nu_G(\frac{\partial u_2}{\partial x} n_x + \frac{\partial u_2}{\partial y} n_y) - p n_y) ds = \int_{\Gamma_o} (\nu_G \frac{\partial u_2}{\partial \boldsymbol{n}} - p n_y) ds. \tag{2.173b}$$

Similarly, the same ideas can be used to compute the outward unit normal vector.

2.11.4 Generalized Newtonian Fluid(Volume Integral Formula)

So too, as mentioned before, the stress form used to describe the non-Newtonian fluid reads:

$$\boldsymbol{\sigma} = -pI + \nu(\|\mathbf{D}\|, p)\mathbf{D}, \qquad \mathbf{D} = \frac{1}{2}(\boldsymbol{\nabla u} + \boldsymbol{\nabla u}^T) \tag{2.174}$$

where $\nu(\|\mathbf{D}\|, p)$ is the nonlinear viscosity of the non-Newtonian fluid which will be for the Bingham viscoplastic fluid $2\mu + \frac{\tau_s}{\|\mathbf{D}\|}$. Assume that, $\boldsymbol{u} = (u \quad v)^T$, and $\boldsymbol{v} = (v_l \quad v_d)^T$ are the components in cartesian coordinate for velocity and test function respectively and $\frac{D\boldsymbol{u}}{Dt} = \frac{\partial \boldsymbol{u}}{\partial t} + \boldsymbol{u}.\boldsymbol{\nabla u}$ the total time derivative of the velocity field, after a simple calculation one can deduce in x and y directions in the following short forms:

$$\begin{aligned} &- \int_{\boldsymbol{\Omega}} (\frac{Du_1}{Dt} v_d + \frac{\nu}{2} \boldsymbol{\nabla} u_1 \cdot \boldsymbol{\nabla} v_d + \frac{\nu}{2}(\frac{\partial u_1}{\partial x}\frac{\partial v_d}{\partial x} + \frac{\partial u_2}{\partial x}\frac{\partial v_d}{\partial y}) - p\frac{\partial v_d}{\partial x}) d\boldsymbol{x} \\ &= \int_{\Gamma_o} \{(\nu \frac{\partial u_1}{\partial x} - p) n_x + \nu(\frac{\partial u_1}{\partial y} + \frac{\partial u_2}{\partial x}) n_y\} v_d ds, \end{aligned} \tag{2.175a}$$

$$\begin{aligned} &- \int_{\boldsymbol{\Omega}} (\frac{Du_2}{Dt} v_l + \frac{\nu}{2} \boldsymbol{\nabla} u_2 \cdot \boldsymbol{\nabla} v_l + \frac{\nu}{2}(\frac{\partial u_1}{\partial y}\frac{\partial v_l}{\partial x} + \frac{\partial u_2}{\partial y}\frac{\partial v_l}{\partial y}) - p\frac{\partial v_l}{\partial y}) d\boldsymbol{x} \\ &= \int_{\Gamma_o} \{(\nu \frac{\partial u_2}{\partial y} - p) n_y + \nu(\frac{\partial u_1}{\partial y} + \frac{\partial u_2}{\partial x}) n_x\} v_l ds. \end{aligned} \tag{2.175b}$$

By inspecting the RHS terms of the above two equations Eq.(2.175), one can find the same values of drag and lift forces with those of Eq(2.173) from the classical method times the test function and they will be the same if the value of the test functions equals unity at the interested boundary.

Remark: By Introducing the simple form of the stress tensor by using the gradient form which reads

$$\sigma = -pI + \nu_G(\|\boldsymbol{\nabla u}\|, p)\boldsymbol{\nabla u}, \tag{2.176}$$

where, $\nu_G(\|\boldsymbol{\nabla u}\|, p)$ is the nonlinear viscosity with gradient form which will be for Bingham viscoplastic fluid $2\mu + \frac{\tau_s}{\|\boldsymbol{\nabla u}\|}$. Incorporate Eq.(2.176) into the weak formulation to get the following

$$- \int_{\Omega} (\frac{Du_1}{Dt} v_d + \nu_G \boldsymbol{\nabla} u_1 \cdot \boldsymbol{\nabla} v_d - p\frac{\partial v_d}{\partial x}) d\boldsymbol{x} = \int_{\Gamma_o} \{(\nu_G \frac{\partial u_1}{\partial x} - p) n_x + \nu_G \frac{\partial u_1}{\partial y} n_y\} v_d ds, \tag{2.177a}$$

$$- \int_{\Omega} (\frac{Du_2}{Dt} v_l + \nu_G \boldsymbol{\nabla} u_2 \cdot \boldsymbol{\nabla} v_l - p\frac{\partial v_l}{\partial y}) d\boldsymbol{x} = \int_{\Gamma_o} \{(\nu_G \frac{\partial u_2}{\partial y} - p) n_y + \nu_G \frac{\partial u_2}{\partial x} n_x\} v_l ds. \tag{2.177b}$$

readily, one can derive the following short forms

$$-\int_{\boldsymbol{\Omega}}(\frac{Du_1}{Dt}v_d+\nu_G\boldsymbol{\nabla}u_1\cdot\boldsymbol{\nabla}v_d-p\frac{\partial v_d}{\partial x})d\boldsymbol{x}=\int_{\Gamma_o}\{\nu_G\frac{\partial u_1}{\partial \boldsymbol{n}}-pn_x\}v_d ds, \tag{2.178a}$$

$$-\int_{\boldsymbol{\Omega}}(\frac{Du_2}{Dt}v_l+\nu_G\boldsymbol{\nabla}u_2\cdot\boldsymbol{\nabla}v_l-p\frac{\partial v_l}{\partial y})d\boldsymbol{x}=\int_{\Gamma_o}\{\nu_G\frac{\partial u_2}{\partial \boldsymbol{n}}-pn_y\}v_l ds. \tag{2.178b}$$

So too, by inspecting the RHS terms of the above two equations Eq.(2.178)), one can find the same values of drag and lift forces with those of Eq.(2.173) from the classical method for the simplified forms times the test function and they will be the same if the value of the test functions equals unity at the interested boundary.
One can merge the two equations after recalling the total derivative to get the following vector form:

$$-\int_{\boldsymbol{\Omega}}(\frac{\partial \boldsymbol{u}}{\partial t}\boldsymbol{v}+(\boldsymbol{u}\cdot\boldsymbol{\nabla}\boldsymbol{u})\boldsymbol{v}+\nu_G\boldsymbol{\nabla}\boldsymbol{u}\cdot\boldsymbol{\nabla}\boldsymbol{v}-p\boldsymbol{\nabla}\cdot\boldsymbol{v})d\boldsymbol{x}=\int_{\Gamma_o}\{\nu_G\frac{\partial \boldsymbol{u}}{\partial \boldsymbol{n}}-p\boldsymbol{n}\}\cdot\boldsymbol{v}ds, \tag{2.179}$$

let us present them in the following inner product form

$$-((\frac{\partial \boldsymbol{u}}{\partial t},\boldsymbol{v})+((\boldsymbol{u}\cdot\boldsymbol{\nabla}\boldsymbol{u}),\boldsymbol{v})+(\nu_G\boldsymbol{\nabla}\boldsymbol{u},\boldsymbol{\nabla}\boldsymbol{v})-(p,\boldsymbol{\nabla}\cdot\boldsymbol{v}))=(\mathsf{F}_{d,l},\boldsymbol{v}), \tag{2.180}$$

So too, the significant property is to use directly the primitive variables output with nonlinear viscosity to calculate the drag and lift forces. Let us introduce the weak form of the Navier-Stokes equation with nonlinear viscosity for non-Newtonian fluid in terms of u-p variables and external force $\boldsymbol{f}$ which can be written as follows:

$$(\frac{\partial \boldsymbol{u}}{\partial t},\boldsymbol{v})+((\boldsymbol{u}\cdot\boldsymbol{\nabla}\boldsymbol{u}),\boldsymbol{v})+(\nu_G\boldsymbol{\nabla}\boldsymbol{u},\boldsymbol{\nabla}\boldsymbol{v})-(p,\boldsymbol{\nabla}\cdot\boldsymbol{v})=(\boldsymbol{f},\boldsymbol{v}), \tag{2.181}$$

compare the two forms Eq.(2.180) and Eq.(2.181), one can result the equivalence between the two forms if we multiplied the consistent force equation by minus sign. Therefore, the non-stationary form of navier-stokes equation with nonlinear viscosity is quite valid to calculate the approximated forces of drag and lift by using the consistent force method. Therefore, the two equations can be merged as follows:

$$(\frac{\partial \boldsymbol{u}}{\partial t},\boldsymbol{v})+((\boldsymbol{u}\cdot\boldsymbol{\nabla}\boldsymbol{u}),\boldsymbol{v})+(\nu_G\boldsymbol{\nabla}\boldsymbol{u},\boldsymbol{\nabla}\boldsymbol{v})-(p,\boldsymbol{\nabla}\cdot\boldsymbol{v})-(\boldsymbol{f},\boldsymbol{v})=-(\mathsf{F}_{d,l},\boldsymbol{v}), \tag{2.182}$$

so, one can use the following assumption to compute the forces on the interface between solid and fluid

$$v_d|_{\Gamma_o}=\begin{pmatrix}1\\0\\0\end{pmatrix},\qquad v_d|_{\partial\boldsymbol{\Omega}/\Gamma_o}=\begin{pmatrix}0\\0\\0\end{pmatrix} \tag{2.183}$$

$$v_l|_{\Gamma_o}=\begin{pmatrix}0\\1\\0\end{pmatrix},\qquad v_l|_{\partial\boldsymbol{\Omega}/\Gamma_o}=\begin{pmatrix}0\\0\\0\end{pmatrix}, \tag{2.184}$$

so, the drag and lift forces have the following forms respectively

$$F_d=-((\frac{\partial \boldsymbol{u}}{\partial t},v_d)+((\boldsymbol{u}\cdot\boldsymbol{\nabla}\boldsymbol{u}),v_d)+(\nu_G\boldsymbol{\nabla}\boldsymbol{u},\boldsymbol{\nabla}v_d)-(p,\boldsymbol{\nabla}\cdot v_d)-(\boldsymbol{f},v_d)), \tag{2.185a}$$

$$F_l=-((\frac{\partial \boldsymbol{u}}{\partial t},v_l)+((\boldsymbol{u}\cdot\boldsymbol{\nabla}\boldsymbol{u}),v_l)+(\nu_G\boldsymbol{\nabla}\boldsymbol{u},\boldsymbol{\nabla}v_l)-(p,\boldsymbol{\nabla}\cdot v_l)-(\boldsymbol{f},v_l)). \tag{2.185b}$$

2.12 Summary

This chapter handles the basic laws which have used in the stationary and nonstationary viscoplastic fluids. These laws have been started with the balance equations and the constitutive theory and end with

the mathematical aspects which are based on the existence and uniqness of the viscoplastic problems. The investigations of the numerical difficulties which arise from the nonlinearity and the non-differentiability have been presented with possible remedies for the implementation. The properties of Bingham fluids are exposed and proved particularly for the distribution of the pressure. The derivation of the drag and lift forces are obtained with several methods which may facilitate the programming part and accompanied with high accuracy in the calculations. Finally, this chapter highlights the necessary bases for the numerical simulation of the generalized Newtonian fluids and viscoplastic fluids.

3

Discretization Techniques for Viscoplastic Fluids

This chapter handles the flow problems with three different discretization approaches in the sense of accuracy and convergence for the Newtonian and generalized Newtonian problems particularly viscoplastic fluids problem. The study will be concerned in from the focusable point of the discretization techniques for the pressure spaces namely, constant global approach, local linear approach, and global linear approach which are represented by $\tilde{Q}_1Q_0$, Q_2P_1, and $Q_2P_1^{np}$ respectively.
The solution behavior and the efficiency of the solvers are investigated in the sense of error estimates. The produced numerical results are compared with well-known exact solutions for Newtonian fluid (Poiseuille and Stokes flows), the generalized Newtonian problems (shear thinning fluid, shear thickening) and viscoplastic fluid problems by using $\mathbf{L}^2$ and $\mathbf{H}^1$ norms for the primitive variables(velocity and pressure). We discuss the velocity-pressure approximations and their accuracy regarding the regular and the perturbed meshes for every flow case. The aim is, in the sense of coupled Newton-Multigrid solvers within the monolithic approach, to confirm the idea of global approach for the pressure element to be preferred with respect to the local approach for the calculation of the pressure in particular for the perturbed mesh. Special attention is paid for the flow of viscoplastic fluids in channel to prove numerically the dependence of the pressure field on the value of the yield stress, creating for instance null pressure space over the plug region when the yield stress is constant $\tau_s = const$.

3.1 Introduction

This chapter tackles the numerical matching between the finite element techniques and the flow problems in the case of the FEM discretization techniques. Three different discretization approaches and their numerical approximation properties on the quadrilateral meshes for different flow problems are introduced. These numerical properties refer to the mixed formulation of velocity and pressure. These techniques are provided by the finite elements $\tilde{Q}_1Q_0$,Q_2P_1 and $Q_2P_1^{np}$. The finite element space for Q_2P_1 is constructed starting with the given finite dimensional space of function on a square reference element which is then transformed to a space of functions on each convex quadrilateral element via a bilinear isomorphism of the square into the element. The compatible pressure space is represented by a linear space on the local(mapped) coordinates. For $Q_2P_1^{np}$, has the same construction with Q_2P_1 but the definition of pressure space differs by choosing the global approach(unmapped). In contrast, The finite element space for $\tilde{Q}_1Q_0$ is constructed starting with the given finite dimensional space of function on the real element for the velocity and pressure with constant value (see [177]). The elements satisfy the inf-sup conditions as well. The degradation of the convergence of Q_2P_1 due to the local approach for pressure as compared with $Q_2P_1^{np}$ and $\tilde{Q}_1Q_0$ as low order finite element with constant pressure approximation has already been proved. This means that, element $Q_2P_1^{np}$ has become as mandatory alternative for the flow problems with the others for the pressure approximation which has the second order accuracy for the regular mesh

and super convergence for the perturbed mesh.
The presented flow problems here have different parameter setting corresponding to different models. They are divided, as usual, into Newtonian and Non-Newtonian fluids to measure the approximation of the discretization techniques for a wide range of the flow problems. The Newtonian problems are represented by Poiseuille and Stokes flows. The Non-Newtonian problems are represented by shear thickening, shear thinning, and viscoplastic problems. The computational domains are a unit square with different dimension coordinates ($[0,1]\times[0,1]$ *and* $[-0.5,0.5]\times[-0.5,0.5]$). The general quadrilateral mesh can be created by perturbing the uniform mesh by shifting the nodes with 20% (see Fig.(3.1)).

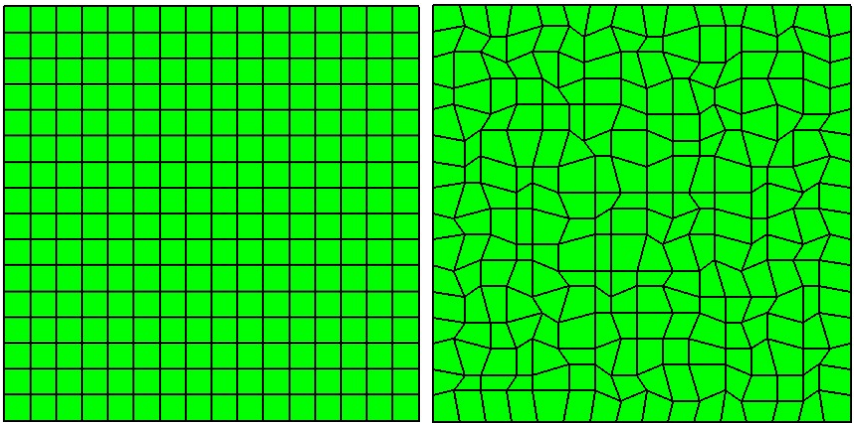

Fig. 3.1. Uniform mesh(left)and perturbed meshes(right) (16×16 elements)

3.2 Finite Element Approximations

Let $\boldsymbol{\Omega}\subset\mathbb{R}^2$ be a polygonal domain, and divide $\boldsymbol{\Omega}$ into finitely many subdomains. We will approximate the solution of such variational problem with functions which are polynomials on each subdomain. Firstly, let us expose general definitions used in the field of finite element theory.

Definition 3.2.1 *(see [29, 32])*
Let $\mathbf{T}_h=\{\mathcal{T}_i, i=1,...,n\}$ *be a partition of* $\boldsymbol{\Omega}$ *into quadrilaterals, where diam*$\mathcal{T}\le h$ *for all i=1,...,n. We call* $\mathbf{T}_h$ *a triangulation of* $\boldsymbol{\Omega}$ *if the following conditions are satisfied*

(a) $\bar{\boldsymbol{\Omega}}=\cup_{i=1}^{n}\mathcal{T}_i$,

(b) if $i\neq j$ *and* $\mathcal{T}_i\neq\mathcal{T}_j\neq\emptyset$ *then exactly one of the following two conditions is satisfied*

(i) $\mathcal{T}_i\cap\mathcal{T}_j$ *consists of exactly one point, and this point is a common vertex of* $\mathcal{T}_i$ *and* $\mathcal{T}_j$,

(ii) $\mathcal{T}_i\cap\mathcal{T}_j$ *is a common edge of* $\mathcal{T}_i$ *and* $\mathcal{T}_j$.

Definition 3.2.2 *(see [29, 32]) A finite element is a triple* $(\mathcal{T},\Pi_{\mathcal{T}},\Sigma_{\mathcal{T}})$ *with the following properties:*

(a) $\mathcal{T}$ *is a polyhedron in* $\mathbb{R}^2$,

(b) $\Pi_{\mathcal{T}}$ *is a subspace of* $C(\mathcal{T})$ *with finite dimension s,*

(c) $\Sigma_{\mathcal{T}}$ *is a set of s linearly independent functional on* $\Pi_{\mathcal{T}}$. *Each* $P\in\Pi_{\mathcal{T}}$ *is uniquely defined by the values of the functionals in* $\Sigma_{\mathcal{T}}$.

Since the functionals usually involve point evaluation of a function or of its derivatives at points in $\mathcal{T}$, we call these functionals interpolation conditions, and the set $\Pi_{\mathcal{T}}$ itself is called a finite element.

Definition 3.2.3 *(see [29, 32]) If there is a set of points which uniquely determines any function in the finite element space by its values at the given points, these points are called nodal points and the functionals that map the nodal points on the functions values are called (Lagrange type) degrees of freedom.*

Definition 3.2.4 *(Affine Families (see [29, 32]))*
Let $\mathbf{T}_h$ be a triangulation of $\boldsymbol{\Omega}$, and Let $\mathbf{V}_h$ be a family of finite elements for the partition $\mathbf{T}_h$. This family is called affine family if there exists a reference element $(\mathcal{T}_0, \Pi_0, \Sigma_0)$ such that for every $\mathcal{T} \in \mathbf{T}_h$ there exists an affine mapping $\mathbf{F}_{\mathcal{T}}(\boldsymbol{x}) = \mathbf{B}_{\mathcal{T}} + b_{\mathcal{T}}$, $\mathbf{B}_{\mathcal{T}} \in \mathbb{R}^{2\times 2}$, which has the following properties:

(a) $\mathbf{F}_{\mathcal{T}} : \mathcal{T}_0 \to \mathcal{T}$ and $\mathbf{F}_{\mathcal{T}}(\mathcal{T}_0) = \mathcal{T}$,

(b) For every $\boldsymbol{v} \in \mathbf{V}_h$, $\boldsymbol{v}|_{\mathcal{T}}(\boldsymbol{x}) = p(\mathbf{F}_{\mathcal{T}}^{-1}(\boldsymbol{x}))$ holds where $p \in \Pi_0$.

Definition 3.2.5 *(see[190])*
One calls the family of triangulation $\{\mathbf{T}_h\}$, $0 < h \leq 1$ quasiuniform if there exists a constant $k > 0$ such that $k.h \geq \rho_{\mathcal{T}} \quad \forall \in \mathbf{T}_h, \quad 0 < h \leq 1$, where $\rho_{\mathcal{T}}$ denotes the supremum of diameters of discs contained in $\mathcal{T}$.

3.2.1 Quadrilateral Nonconforming Finite Element ($\tilde{Q}_1 Q_0$)

Here, we expose an example for one of low order finite element families for the two/three dimensional fluid problem, namely the non-conforming rotated bilinear finite element (see [166, 177]). Typically, the family is defined for arbitrary order k which has stable inf-sup condition for $k \geq 2$ under a grid condition for the space $< 1, x, y, x^k - y^k >$. The element $\tilde{Q}_1 Q_0$ in [177] is the natural quadrilateral analogue of the well-known triangular finite element of Crouzeix-Raviart(see [59]). It prescribes the velocity and the pressure as a piecewise 'rotated' bilinear (reference) shape functions and piecewise constant respectively. The nodal values are prescribed as the mean values of the velocity vector over the element edges and the mean value of the pressure over the element (see Fig.3.2).
Let us assume $\boldsymbol{\Omega}$ to be convex polygonal and $\mathbf{T}_h$ be a regular decomposition of the domain $\boldsymbol{\Omega} \subset \mathbb{R}^2$ into (convex) quadrilateral denoted by $\mathcal{T}$ where the mesh parameter $h > 0$ describes the maximum diameter of the element of $\mathcal{T}$. Let $\psi_{\mathcal{T}} : \hat{\mathcal{T}} \to \mathcal{T}$ be the bilinear transformation for each $\mathcal{T} \in \mathbf{T}_h$ to the unit square. So, the family of $\tilde{Q}_1$ is defined by

$$\tilde{Q}_1 := \left\{ q \circ \psi_{\mathcal{T}}^{-1} : q \in \text{span} < 1, x, y, x^2 - y^2 > \right\}, \tag{3.1}$$

the degrees of freedom are determined by the following nodal functionals $\{F_{\Gamma}^{(a,b)}(\cdot), \Gamma \subset \partial \mathbf{T}_h\}$, with

(a) continuity at the mean, symbolized by

$$\mathbf{F}_{\Gamma}^{a} = |\Gamma|^{-1} \int_{\Gamma} \boldsymbol{v} d\gamma \tag{3.2}$$

and the corresponding shape functions $\boldsymbol{\psi} = [\psi_1, \psi_2, \psi_3, \psi_4]$ on the reference element $[-1, 1]^2$ can be deduced as follows:

$$\begin{aligned} \boldsymbol{\psi} = [&-\frac{3}{8}(x^2 - y^2) - \frac{1}{2}y + \frac{1}{4}, +\frac{3}{8}(x^2 - y^2) + \frac{1}{2}x + \frac{1}{4}, \\ &-\frac{3}{8}(x^2 - y^2) + \frac{1}{2}y + \frac{1}{4}, +\frac{3}{8}(x^2 - y^2) - \frac{1}{2}x + \frac{1}{4}]. \end{aligned} \tag{3.3}$$

(b) continuity at the midpoints of the edges/faces symbolized by

$$F_{\Gamma}^{b} = v(m_{\Gamma}) \quad (m_{\Gamma} \text{ midpoint of edge } \Gamma) \tag{3.4}$$

and the corresponding shape functions on the reference element $[-1,1]^2$ can be deduced as follows:

$$\begin{aligned}\boldsymbol{\psi} = [&-\frac{1}{4}(x^2-y^2) - \frac{1}{2}y + \frac{1}{4}, +\frac{1}{4}(x^2-y^2) + \frac{1}{2}x + \frac{1}{4},\\ &-\frac{1}{4}(x^2-y^2) + \frac{1}{2}y + \frac{1}{4}, +\frac{1}{4}(x^2-y^2) - \frac{1}{2}x + \frac{1}{4}].\end{aligned} \tag{3.5}$$

The discrete velocity is assumed to be continuous but there is no continuity on the pressure ,

$$\begin{aligned}\mathbf{W}_h^{a,b} := \{&\boldsymbol{v} \in \mathbf{L}^2(\boldsymbol{\Omega}_h), \boldsymbol{v} \in \tilde{Q}_1(\mathcal{T}), \forall \mathcal{T} \in \mathbf{T}_h, \boldsymbol{v} \text{ continuous with respect to all}\\ &\text{nodal functionals } \mathbf{F}_{\Gamma_{i,j}}^{a,b}(\cdot), \text{ and } \mathbf{F}_{\Gamma_{i0}}^{a,b}(\boldsymbol{v}) = 0, \forall \Gamma_{i0}\}\end{aligned} \tag{3.6}$$

$$\mathbf{V}_h = \mathbf{W}_h^{a,b} \times \mathbf{W}_h^{a,b} \tag{3.7}$$

$$\mathbf{L}_h^{a,b} := \{q_h \in \mathbf{L}_2(\boldsymbol{\Omega}_h), q_h \in Q_0(\mathcal{T}), \forall \mathcal{T} \in \mathbf{T}_h\}. \tag{3.8}$$

Here, $\Gamma_{i,j}$ denotes all inner edges sharing the two elements i and j, while Γ_{i0} denotes the boundary edges of $\partial\boldsymbol{\Omega}_h$. Clearly $\mathbf{W}_h^a \neq \mathbf{W}_h^b$, but for the corresponding triangular element $\mathbf{W}_h^a$ and $\mathbf{W}_h^b$ coincide.

Definition 3.2.6 *(Measure of mesh degeneration(σ_h)): For such element ($\mathcal{T} \in \mathbf{T}_h$), the measure of mesh degeneration is prescribed by σ_h which approximated by $\sigma_h \equiv max\{|\pi - \alpha_{\mathcal{T}}|, \mathcal{T} \in \mathbf{T}_h\}$. where $\alpha_{\mathcal{T}} \in (0,\pi)$ denotes the maximum angle enclosed between the normal unit vectors corresponding to any two opposite edges of $\mathcal{T}$ (see [177, 214]).*

Theorem 3.2.1 *(The approximation properties (see [177, 214])) For the interpolation operators $i_h = i_h^{(\frac{a}{b})}$, and $j_h : \mathbf{L}_0^2 \to \mathbf{L}_h$, there holds the error estimate*

$$\|\boldsymbol{v} - i_h\boldsymbol{v}\|_0 + h\,\|\boldsymbol{v} - i_h\boldsymbol{v}\|_h \leq ch(h+\sigma_h)\,\|\boldsymbol{v}\|_2\,, \quad \forall \boldsymbol{v} \in \mathbf{H}_0^1(\boldsymbol{\Omega}) \cap \mathbf{H}^2(\boldsymbol{\Omega}), \tag{3.9a}$$

$$\|q - j_h q\|_0 \leq ch\,\|q\|_1\,. \tag{3.9b}$$

Theorem 3.2.2 *(The stability condition (see [177, 214])) Let $q_h \in \mathbf{L}_h$ and $\boldsymbol{v}_h \in \mathbf{H}^{(\frac{a}{b})}$ be given, then one can get the following constrained stability condition*

$$\beta\,\|q_h\|_0 \leq \sup_{\boldsymbol{v}_h \in \mathbf{H}_h^{(\frac{a}{b})}} \left(\frac{c_h(q_h, \boldsymbol{v}_h)}{\|\boldsymbol{v}_h\|_h}\right) + c\sigma\,\|q_h\|_0 \tag{3.10}$$

whether $\sigma \equiv sup_{h>0}(\sigma_h)$ is sufficiently small, the general stability estimates hold.

Theorem 3.2.3 *Suppose that the preceding assumptions hold. Then, for $\mathbf{H}_h = \mathbf{H}_h^{(\frac{a}{b})}$ and if the quantity $\sigma \equiv sup_{h>0}(\sigma_h)$ is sufficiently small, the discrete Stokes problem has a unique solution $\{\boldsymbol{u}_h, p_h\} \in \mathbf{H}^{\frac{a}{b}} \times \mathbf{L}_h$, there holds*

$$\|\boldsymbol{u} - \boldsymbol{u}_h\|_h + \|p - p_h\|_0 \leq c(h+\sigma)(\|\boldsymbol{u}\|_2 + \|p\|_1), \tag{3.11a}$$

$$\|\boldsymbol{u} - \boldsymbol{u}_h\|_0 + \|p - p_h\|_{-1} \leq c(h+\sigma)^2(\|\boldsymbol{u}\|_2 + \|p\|_1). \tag{3.11b}$$

($\|.\|_{-1}$ denotes the norm of the dual space of $\mathbf{L}_0^2 \cap \mathbf{H}^1$)(see [177, 214]).

In [177, 214], a convergence analysis is given and computational results are reported, furthermore it is shown that $\mathbf{W}_h^a$ is less sensitive to mesh distortion than $\mathbf{W}_h^b$ when stokes problem is solved, both are stable w.r.t LBB condition .
In addition to, the stability condition holds for the pair $(\mathbf{V}_h^a, \mathbf{L}_h)$ from the uniform one with a constant β independent of the mesh's aspect ratio. In contrast, for the "midpoint oriented" finite element $\mathbf{V}_h^b$ the independence of the stability constant on the mesh aspect ratio is restricted with the modification of the bilinear form $\mathbf{B}(\cdot,\cdot)$ by its numerically integrated version.

$$(\mathbf{B}^{(b)} q_h, \boldsymbol{v}_h) \approx -\sum_{\mathcal{T}\in\mathbf{T}_h} q_h \sum_{\Gamma\subset\partial\mathcal{T}} \oint_{\Gamma} \boldsymbol{v}_h \cdot \boldsymbol{n}_{\Gamma}\, d\gamma \tag{3.12}$$

Furthermore, on general nonuniform meshes the bilinear transformations $\psi_{\mathcal{T}} : \hat{\mathcal{T}} \to \mathcal{T}$ are of another polynomial type than the shape functions on $\mathcal{T}$. In contrast to the parametric counterpart, let (ξ, η) be a local coordinate system obtained by joining the midpoints of the opposing faces of $\mathcal{T}$. Then, in the *nonparametric* case, set on each element$\mathcal{T}$

$$\tilde{Q}_1(\mathcal{T}) := \text{span} < 1, \xi, \eta, \xi^2 - \eta^2 >, \tag{3.13}$$

hence, we get the error estimate independent of σ_h

$$\|\boldsymbol{v} - i_h \boldsymbol{v}\|_0 + h\,\|\boldsymbol{v} - i_h \boldsymbol{v}\|_h \le c h^2\,\|\boldsymbol{v}\|_2\,, \quad \forall \boldsymbol{v} \in \mathbf{H}_0^1(\boldsymbol{\Omega}) \cap \mathbf{H}^2(\boldsymbol{\Omega}). \tag{3.14}$$

As a consequence the optimal order convergence estimates holds

$$\|\boldsymbol{u} - \boldsymbol{u}_h\|_h + \|p - p_h\|_0 \le c\,h\,\{\|\boldsymbol{u}\|_2 + \|p\|_1\}\,. \tag{3.15}$$

The main reported features of the rotated bilinear finite element can be summarized in the following two manifolds:

a) It is possible to construct a divergence-free (local) nodal-basis which allows the elimination of the pressure from the problem resulting in a positive definite algebraic system for the velocity unknown alone.

b) The reduced algebraic system can be solved efficiently by special adapted multigrid methods.

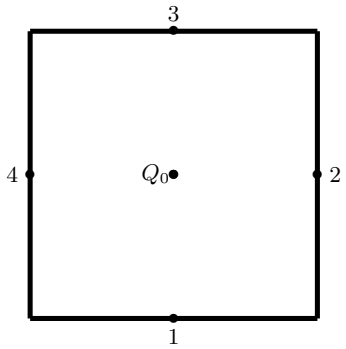

Fig. 3.2. $\tilde{Q}_1 Q_0$ Finite element 2D

3.2.2 Quadrilateral Conforming Finite Element ($Q_2P_1/Q_2P_1^{np}$)

Q_2P_1 is the lowest order of the quadrilateral finite element family $Q_kP_{k-1}(k \geq 2)$ and one of the most popular stokes elements used for flow problems. This element is discovered around a blackboard at the Banff Conference on Finite Elements in Flow Problems (see [26]). This element is a relatively late comer in the field; the reason for this is that using a P_1 pressure on a quadrilateral meshes is not a standard procedure. As it is reported in [26], and it appeared as a cure for the instability of the Q_2Q_1 element which appears quite naturally in the use of reduced integration penalty method. This last element is essentially related to the Q_1P_0 element and suffers the same problems even to a lesser extent. Another cure can be obtained by adding internal nodes(see [8, 25, 79, 91, 149]). This element is defined by introducing four corner node, all together with four additional mid side nodes and with a ninth node at the centroid as illustrated in the pictorial representation of the figure Fig.3.3. In this case, there are four vertex functions,

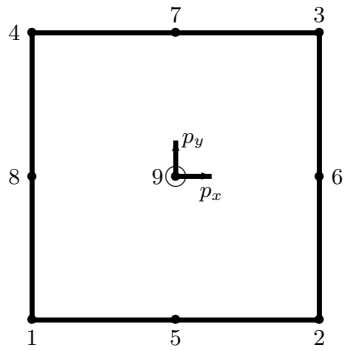

Fig. 3.3. Q2P1 Finite elements 2D

four edge functions, and one internal (or bubble) function in the element basis. The space approximation is the linear combination of the nine terms $\{1, x, y, xy, x^2, y^2, x^2y, xy^2, x^2y^2\}$. So, the space of Q2 is complete bilinear polynomial together with a bi-variate quadratic as well as all six terms of complete quadratic plus cubic terms x^2y and xy^2 and the single quadratic term (see [223]). It is clearly that, Q_2 approximation on rectangles is continuous and so is conforming for equation of viscoplastic fluid as well as the approximation which may be employed on arbitrary quadrilaterals through the use of the bilinear mapping. Q_2 tri-quadratic, the analogous approximation for 3D, has obviously twenty seven nodes, there are eight corner basis functions, twelve mid edge basis functions, six mid face basis functions and a single bubble function associated with the node at the centroid of the brick. The corresponding shape functions $\boldsymbol{\psi} = [\psi_1, .., \psi_9]$ on the reference element $[-1, 1] \times [-1, 1]$ can be deduced as follows:

$$\begin{aligned}\boldsymbol{\psi} = [&+\frac{1}{4}(1-x)(1-y)xy, -\frac{1}{4}(1+x)(1-y)xy, +\frac{1}{4}(1+x)(1+y)xy,\\ &-\frac{1}{4}(1-x)(1-y)xy, -\frac{1}{2}(1-x^2)(1-y)y, +\frac{1}{2}(1+x)(1-y^2)x,\\ &+\frac{1}{2}(1-x^2)(1+y)y, -\frac{1}{2}(1-x)(1-y^2)x, +(1-x^2)(1-y^2)].\end{aligned} \tag{3.16}$$

The mixed part of this element represents the pressure space which is defined on the general quadrilateral meshes as linear function for each element by two ways:

Global Approach (The Unmapped Pressure Approach P_1^{np})

Global approach contains (discontinuous) piecewise linear functions. The corresponding pressure space for P_1^{np}, is defined globally in the following linear form,

$$p_h = p_o + p_1(\boldsymbol{x}_1 - \boldsymbol{x}_0) + p_2(\boldsymbol{x}_2 - \boldsymbol{x}_0), \tag{3.17}$$

where, $\boldsymbol{x}_0 = (\boldsymbol{x}_1 + \boldsymbol{x}_2 + \boldsymbol{x}_3 + \boldsymbol{x}_4)/4$, and $\boldsymbol{x}_i, i = 1, 4$ are the global finite element vertices (see [191]).

Local Approach (The Mapped Pressure Approach P_1)

Local approach is built by considering three linear shape functions on the reference unit square and mapping them to the general elements like what is usually done for continuous finite elements. In this case the mapping from the reference element to the general element is bilinear but not affine, so that the two constructions are not equivalent. The corresponding pressure space for P_1, is defined locally in the following linear form,

$$p_h = p_o + p_1\xi + p_2\eta, \tag{3.18}$$

where, ξ and η are the local coordinates of the standard reference square $[-1, 1] \times [-1, 1]$. Both of them have the fact that , the space of pressure is discontinuous across internal element boundaries (see [191]).

The difference between Q_2P_1 and $Q_2P_1^{np}$ from the numerical point of view is for $Q_2P_1^{np}$, $\boldsymbol{v}_h$ satisfies the following

$$\int_{\boldsymbol{\Omega}} (\boldsymbol{\nabla} \cdot \boldsymbol{v}_h)(\boldsymbol{x}_i - \boldsymbol{x}_0) d\boldsymbol{x} = 0, \quad i = 1, 2, \tag{3.19}$$

but for Q_2P_1, $\boldsymbol{v}_h$ satisfies the following

$$\int_{\boldsymbol{\Omega}} (\boldsymbol{\nabla} \cdot \boldsymbol{v}_h)\xi d\boldsymbol{x} = 0, \tag{3.20a}$$

$$\int_{\boldsymbol{\Omega}} (\boldsymbol{\nabla} \cdot \boldsymbol{v}_h)\eta d\boldsymbol{x} = 0. \tag{3.20b}$$

.

The stability analysis of these approaches are presented in [8, 25, 79, 91, 149].

Theorem 3.2.4 *(Approximation properties of the rectangular elements (see [8]) Suppose $1 \leq p < \infty$ (and $p = \infty$). Let $\hat{S}$ be a finite dimensional subspace of $\mathbf{L}^p(\hat{\mathcal{T}})$, and r a nonnegative integer. The following conditions are equivalent:*

a). There is a constant C such that $\inf_{\boldsymbol{v} \in S_h} \|\boldsymbol{u} - \boldsymbol{v}\|_{\mathbf{L}^p(\boldsymbol{\Omega})} \leq Ch^{r+1}|\boldsymbol{u}|_{\mathbf{W}_p^{r+1}(\boldsymbol{\Omega})}$ for all $\boldsymbol{u} \in \mathbf{W}_p^{r+1}(\boldsymbol{\Omega})$.

b). $\inf_{\boldsymbol{v} \in S_h} \|\boldsymbol{u} - \boldsymbol{v}\|_{\mathbf{L}^p(\boldsymbol{\Omega})} = O(h^r)$ for all $\boldsymbol{u} \in P_r(\boldsymbol{\Omega})$.

c). $P_r(\hat{\mathcal{T}}) \subset \hat{S}$

Theorem 3.2.5 *(Approximation properties of the rectangular elements (see [8]) Suppose $1 \leq p < \infty$ (and $p = \infty$). Let $\hat{S}$ be a finite dimensional subspace of $\mathbf{L}^p(\hat{\mathcal{T}})$, and r a nonnegative integer. The following conditions are equivalent:*

a). There is a constant C such that $\inf_{\boldsymbol{v} \in \mathbf{S}_h} \|\boldsymbol{\nabla}_h(\boldsymbol{u} - \boldsymbol{v})\|_{\mathbf{L}^p(\boldsymbol{\Omega})} \leq Ch^r|\boldsymbol{u}|_{\mathbf{W}_p^{r+1}(\boldsymbol{\Omega})}$ for all $\boldsymbol{u} \in W_p^{r+1}(\boldsymbol{\Omega})$.

b). $\inf_{\boldsymbol{v} \in S_h} \|\boldsymbol{\nabla}_h(\boldsymbol{u} - \boldsymbol{v})\|_{\mathbf{L}^p(\boldsymbol{\Omega})} = O(h^{r-1}) \forall \boldsymbol{u} \in P_r(\boldsymbol{\Omega})$.

c). $P_r(\hat{\mathcal{T}}) \subset P_0(\hat{\mathcal{T}}) + \hat{S}$

Where $\hat{\mathcal{T}}$ is the reference element and $S_h = \{u : \boldsymbol{\Omega} \to \mathbb{R} | u_{\mathcal{T}} \in S(\mathcal{T}) \forall \mathcal{T} \in \mathbf{T}_h\}$ for the associated subspace $S(\mathcal{T}) = \{u : \mathcal{T} \to \mathbb{R} | \hat{u}_{\mathcal{T}} \in \hat{S}\}$ on arbitrary square $\mathcal{T}$ and for any smooth function $\boldsymbol{u} \in \mathbf{L}^1(\mathcal{T})$ where $\hat{\boldsymbol{u}} = \boldsymbol{u} \circ \mathbf{F}_{\mathcal{T}} \in \mathbf{L}^1(\mathcal{T})$ with a given subspace $\hat{S}$ of $\mathbf{L}^1(\hat{\mathcal{T}})$. P_r and Q_r are the spaces of polynomials at most degree r (see [8]).

The previous estimates can be extended readily for the general quadrilateral meshes, but the need to

construct a stronger condition on $\hat{\mathbf{V}}$(the finite dimensional space of shape function given on a reference element) is required namely that $\hat{\mathbf{V}} \supseteq \mathbf{Q}_r(\hat{\mathcal{T}})$, and with this condition the above estimates hold for any sequences of general quadrilateral meshes (see [49, 50, 91]). Therefore, the condition $\mathbf{V}_F(\mathcal{T}) \supseteq P_r(\mathcal{T})$ is necessary and sufficient to have that $\hat{\mathbf{V}} \supseteq \mathbf{Q}_r(\hat{\mathcal{T}})$ whenever $\mathbf{F}$ is a bilinear isomorphism of $\mathcal{T}$ onto a convex quadrilateral, where $\mathbf{V}_F(\mathcal{T}) = \{u : \mathcal{T} \to \mathbb{R} | \hat{u}_{\mathcal{T},\mathbf{F}} \in \hat{\mathbf{V}}\}$ and $\hat{u}_{\mathcal{T},\mathbf{F}} = \boldsymbol{u} \circ \mathbf{F}_{\mathcal{T}}$ (see [8]).
The choice of unmapped pressure approach has not been possible for the definition $\mathbf{V}_h \subset \mathbf{V}(= \mathbf{H}_0^1(\boldsymbol{\Omega})^2)$: without the use of the mapping $\mathbf{F}_{\mathcal{T}} : \hat{\mathcal{T}} \to \mathcal{T}$. It turns out that no continuity can be imposed from one element to the other. On the other hand functions in $\mathbf{Q}_h \subset \mathbf{Q}(= \mathbf{L}_0^2(\boldsymbol{\Omega}))$ need not to be continuous, in this case this choice is practical. The recent results show that choice of the unmapped pressure approach is actually the correct one which the approximation properties are concerned. It is proved that

$$\inf_{q \in Q^{(P_1)}} \|p - q\|_Q = O(h), \tag{3.21a}$$

$$\inf_{q \in Q^{(P_1^{np})}} \|p - q\|_Q = O(h^2). \tag{3.21b}$$

when the mesh sequence is regular and the solution p is smooth enough (see [25]). Therefore, the result presented so far confirms that one has to use the global approach to get the optimal approximation of the solution of the stokes problem. The stability result has been proved in [196] and achieved for the regular $\boldsymbol{u}$ and p the following:

$$\|\boldsymbol{u} - \boldsymbol{u}_h\|_{\mathbf{V}} + \|p - p_h\|_Q = O(h^2). \tag{3.22}$$

Regarding the stability of the mapped pressure approach in the sense that the inf-sup condition is satisfied, one can get the following (see [25]):

$$\|\boldsymbol{u} - \boldsymbol{u}_h\|_{\mathbf{V}} + \|p - p_h\|_Q = O(h). \tag{3.23}$$

3.2.3 Non-conforming Approximations

The finite element spaces $\mathbf{V}_h$ and P_h where we want to approximate the solution of the variational problem. They do not lie in the spaces $(\mathbf{H}^1(\boldsymbol{\Omega}))^2$ and in $\mathbf{L}^2(\boldsymbol{\Omega})$, respectively. Then we call the finite elements non-conforming finite elements. Our used example for non-conforming finite elements is the bilinear rotated finite element (RT element), where

$\mathbf{V}_h = \{\boldsymbol{v} : \boldsymbol{v}|_{\mathcal{T}} \in (Q_1)^2, \forall \mathcal{T} \in \mathbf{T}_h, \boldsymbol{v}$ is continuous at the midpoints of the edges and
$\boldsymbol{v} = 0 \quad$ at the midpoints along $\quad \partial\boldsymbol{\Omega}\}$,

$P_h = \{q : q|_{\mathcal{T}} \in Q_0, \forall \mathcal{T} \in \mathbf{T}_h\}$.

Since the element of $\mathbf{V}_h$(the discrete velocities) is not continuous on the common side of two adjacent quadrilateral (the continuity is required only in one point) the space $\mathbf{V}_h$ is not subspace of $(\mathbf{H}^1(\boldsymbol{\Omega}))^2$ and we can not define the bilinear forms as in the conforming one. Therefore, Let us assume

$$a(\boldsymbol{u}, \boldsymbol{v}) = \sum_{\mathcal{T} \in \mathbf{T}_h} \int_{\mathcal{T}} \boldsymbol{\nabla u} : \boldsymbol{\nabla v}, \tag{3.24a}$$

$$c(p, \boldsymbol{v}) = \sum_{\mathcal{T} \in \mathbf{T}_h} \int_{\mathcal{T}} p(\boldsymbol{\nabla} \cdot \boldsymbol{v}). \tag{3.24b}$$

In analogy with the norm $\|.\|_{1,\boldsymbol{\Omega}}$ of the space $\mathbf{V} = \mathbf{H}_0^1(\boldsymbol{\Omega})$, the natural candidate of the norm of the space $\mathbf{V}_h$ is

$$\boldsymbol{v}_h \to \|\boldsymbol{v}_h\|_h = (\sum_{\mathcal{T}\in\mathbf{T}_h} \|\boldsymbol{v}_h\|^2_{1,\mathcal{T}})^{1/2}, \tag{3.25}$$

From this assumption one can prove that for a family of spaces $\mathbf{V}_h$, the approximate bilinear forms are uniformly elliptic in the sense that

$$a_h(\boldsymbol{v}_h, \boldsymbol{v}_h) \geq \alpha \|\boldsymbol{v}_h\|^2_1, \quad \forall \alpha > 0, \boldsymbol{v}_h \in \mathbf{V}_h, \tag{3.26}$$

which is the case of the ellipticity condition is satisfied. Then by using the continuity and the coercivity assumptions, the following theorem is satisfied (see [49]).

Theorem 3.2.6 *(second Strang lemma) Consider a family of discrete problems for which the associated approximate bilinear forms are uniformly $\mathbf{V}_h$ elliptic, then there exists a constant C independent of the subspace $\mathbf{V}_h$ such that*

$$\|\boldsymbol{u} - \boldsymbol{u}_h\|_h \leq C(\inf_{\boldsymbol{v}_h\in\mathbf{V}_h} \|\boldsymbol{u} - \boldsymbol{v}_h\|_h + \sup_{\boldsymbol{w}_h\in\mathbf{V}_h} \frac{a_h(\boldsymbol{u}, w_h) - \boldsymbol{f}(\boldsymbol{w}_h)}{\|\boldsymbol{w}_h\|_h}). \tag{3.27}$$

The above error estimate shows the difference between the conforming and nonconforming methods from the second part of the RHS term. This term $a_h(\boldsymbol{u}, \boldsymbol{w}_h) - f(\boldsymbol{w}_h)$ is identically zero when $\mathbf{V}_h \subset \mathbf{V}$. The term $\sup_{\boldsymbol{w}_h\in\mathbf{V}_h}(\frac{a_h(\boldsymbol{u},\boldsymbol{w}_h)-\boldsymbol{f}(\boldsymbol{w}_h)}{\|\boldsymbol{w}_h\|_h})$ is called the consistency error term due to the 'non-conformity' of the method. Consequently, a sufficient condition for the convergence is the consistency condition :

$$\lim_{h\to 0} \sup_{\boldsymbol{w}_h\in\mathbf{V}_h} \frac{a_h(\boldsymbol{u}, \boldsymbol{w}_h) - \boldsymbol{f}_(\boldsymbol{w}_h)}{\|\boldsymbol{w}_h\|_h} = 0. \tag{3.28}$$

3.3 Korn's Inequality

This inequality guarantees the coerciveness of the bilinear form which is related to the weak formulations of problems in which forces are prescribed on a part of the boundary of the computational domain $\boldsymbol{\Omega}$. The first inequality (see [31, 129, 130, 166])states that there exists a positive constant C such that

$$\|\mathbf{D}(\boldsymbol{v})\|^2_0 \geq C \|\boldsymbol{v}\|_1, \tag{3.29}$$

for every $\boldsymbol{v} \in \mathbf{H}^1(\boldsymbol{\Omega})$ with homogenous Dirichlet boundary value on $\partial\boldsymbol{\Omega}$. The discrete analog reads

$$\sum_{\mathcal{T}\in\mathbf{T}_h} \|\mathbf{D}(\boldsymbol{v}_h)\|^2_{0,\mathcal{T}} \geq C_h \sum_{\mathcal{T}\in\mathbf{T}_h} \|\boldsymbol{v}_h\|_{1,\mathcal{T}}, \tag{3.30}$$

where $\mathbf{T}_h$ is a triangular of $\boldsymbol{\Omega}$ consisting of shape-regular elements $\mathcal{T}$ satisfying the usual compatibility conditions and C_h denotes the smallest constant for which the discrete version holds.
The classical Korn's inequality is involved in the following theorem

Theorem 3.3.1 *(see [163]) Let $d \geq 2$ and $\boldsymbol{\Omega} \in \mathbb{R}^d$ be open and bounded with Lipschitz boundary. Assume that the Dirichlet boundary has a positive surface measure. Then there exists $C > 0$ such that*

$$\|\mathbf{D}(\boldsymbol{v})\|^2_0 + \|\boldsymbol{v}\|^2_0 \geq C \|\boldsymbol{v}\|^2_1, \quad \boldsymbol{v} \in \mathbf{H}^1(\boldsymbol{\Omega}). \tag{3.31}$$

In lower order finite elements approximation with the symmetric deformation tensor formulations; the Korn's inequality is not fulfilled for instance $\tilde{Q}_1 Q_0$. The successful remedy to surmount this difficulty for a low order finite element methods is to use the interior penalty stabilized finite element methods

which referred as edge-oriented stabilization. The idea is to add a term to treat the jump across the interelementary boundaries via adding the following bilinear forms:

$$(\mathbf{J}, \boldsymbol{v}) = \gamma \sum_{Edge} \frac{1}{|E|} \int_E [\boldsymbol{u}][\boldsymbol{v}] ds \tag{3.32}$$

where γ is a free parameter and the definition of the jump of the function on an edge is given by

$$\boldsymbol{u} = \begin{cases} \boldsymbol{u}^+ \cdot \boldsymbol{n}^+ + \boldsymbol{u}^- \cdot \boldsymbol{n}^- & on \quad E_I, \\ \boldsymbol{u} \cdot \boldsymbol{n} & on \quad E_D, \\ 0 & on \quad E_N. \end{cases} \tag{3.33}$$

where E_I, E_D, and E_N are internal edges, Dirichlet boundary edges and Neumann boundary edges respectively, $\boldsymbol{n}$ is outward normal to the edge, and $(.)^+$ and $(.)^-$ indicate the value of generic quantity $(.)$ on the two elements sharing the same edge (see [101]). In the low order finite element, the classical Korn's inequality can be provided in the following way:

$$\|\mathbf{D}(\boldsymbol{v})\|_0^2 + \|\boldsymbol{v}\|_0^2 + \sum_E \frac{1}{|E|} \|[\boldsymbol{v}]_E\|_0^2 \geq C \|\boldsymbol{v}\|_1^2, \quad \boldsymbol{v} \in \mathbf{H}^1(\boldsymbol{\Omega}). \tag{3.34}$$

3.4 Finite Element Discretization for Newtonian Fluids Problem

3.4.1 Stokes Problem

Let us describe the stokes problem as a mixed problem and can be analyzed in the general framework as a mixed method. Stokes problem can be written as:

Find $\boldsymbol{u} \in \mathbf{H}_0^1(\boldsymbol{\Omega})$ and $p \in \mathbf{L}^2(\boldsymbol{\Omega})$ such that:

$$a(\boldsymbol{u}, \boldsymbol{v}) - c(p, \boldsymbol{v}) = (\boldsymbol{f}, \boldsymbol{v}), \tag{3.35a}$$

$$c(q, \boldsymbol{u}) = 0. \tag{3.35b}$$

The bilinear form a(.,.) is coercive, then the well-posedness of the mixed problem can be stated in the following theorem:

Theorem 3.4.1 *Let $\boldsymbol{f}$ be given in $\mathbf{H}^{-1}(\boldsymbol{\Omega})$. Then there exists a unique $(\boldsymbol{u}, p) \in \mathbf{H}_0^1 \times \mathbf{L}^2$ solution to the mixed problem which satisfies*

$$\|\boldsymbol{u}\|_{\mathbf{H}_0^1} + \|p\|_{\mathbf{L}^2} \leq C \|\boldsymbol{f}\|_{\mathbf{H}^{-1}}. \tag{3.36}$$

Let $\mathbf{T}_h$ be a triangulation of a given domain and let $\mathbf{V}_h \subset (\mathbf{H}_0^1)^2$ and $P_h \subset \mathbf{L}^2(\boldsymbol{\Omega})$ be finite element spaces. The spaces $\mathbf{V}_h$ and P_h are subspaces of $(\mathbf{H}_0^1(\boldsymbol{\Omega}))^2$ and $\mathbf{L}^2(\boldsymbol{\Omega})$ respectively, the bilinear forms are well defined on $\mathbf{V}_h \times \mathbf{V}_h$ and on $\mathbf{V}_h \times P_h$, and the discrete form of the stokes equations is the following:

Find $\boldsymbol{u}_h \in \mathbf{V}_h$ and $p_h \in P_h$ such that

$$a_h(\boldsymbol{u}_h, \boldsymbol{v}_h) - c_h(p_h, \boldsymbol{v}_h) = (\boldsymbol{f}, \boldsymbol{v}_h), \tag{3.37a}$$

$$c_h(q_h, \boldsymbol{u}_h) = 0. \tag{3.37b}$$

Since the bilinear form is coercive on $\mathbf{V}_h$, then there is no problem for the existence of solution $\{\boldsymbol{u}_h, p_h\}$ while it might have troubles with the uniqness of p (see [207]). The pressure can be determined only up to an additive constant, since the null space of the gradient operator is one dimensional and it contains only constant functions. Therefore, the space of the pressure in the variational formulation of stokes equation contains only the constant function $\{q \in \mathbf{L}^2(\boldsymbol{\Omega}) : c(\boldsymbol{v}, q) = 0 \forall \boldsymbol{v} \in (\mathbf{H}_0^1(\boldsymbol{\Omega}))^2)\}$, so the pressure is uniquely determined in $\mathbf{L}^2(\boldsymbol{\Omega})$. From the definitions of the gradient and divergence operators $\mathbf{B} : \boldsymbol{v} \to c(\boldsymbol{v}, .)$ and $\mathbf{B}^T : \boldsymbol{v} \to c(., q)$, one can obtain $\ker\mathbf{B}^T$ as one dimensional. In the case of the discrete problem, the following may happen if the discrete space $\ker\mathbf{B}^T$ contains non-constant functions, the pressure can not be determined uniquely in $P_h/\mathbb{R}$, as there are present 'energy-free' pressure. The following theorem explains the sufficient and necessary conditions for uniqueness and solvability of the discrete problem (see [34]).

Theorem 3.4.2 *Suppose that*

(i) the bilinear form a is coercive on the space $\mathbf{V}_{h,0} = \{\boldsymbol{v}_h \in \mathbf{V}_h : c_h(\boldsymbol{v}_h, q_h) = 0 \quad \forall q_h \in P_h\}$
i.e there exists $\alpha_h > 0$ *such that*

$$a_h(\boldsymbol{v}_h, \boldsymbol{v}_h) \geq \alpha_h \left\|\boldsymbol{v}_h\right\|_1^2 \quad \boldsymbol{v}_h \in \mathbf{V}_{h,0} \tag{3.38}$$

(ii) and with a constant $\beta_h > 0$

$$\sup_{\boldsymbol{v}_h \in \mathbf{V}_h} \frac{c_h(\boldsymbol{v}_h, q_h)}{\left\|\boldsymbol{v}_h\right\|_1} \geq \inf_{q_{0h} \in ker B_h^T} \left\|q_h + q_{0h}\right\|_{\mathbf{L}^2(\boldsymbol{\Omega})} = \beta_h \left\|q_h\right\|_{\mathbf{L}^2(\boldsymbol{\Omega})/ker B_h^T}, \tag{3.39}$$

holds for all $q_h \in P_h$*, then the discrete problem Eq.(3.37) is uniquely solvable in* $\mathbf{V}_h \times (P_h/ker\mathbf{B}_h^T)$*. Moreover, if* $\beta_h \geq \beta_0 > 0$ *holds with a constant* β_0 *independent of h, then the solution is stable and*

$$\left\|\boldsymbol{u} - \boldsymbol{u}_h\right\|_1 \leq c_1(\left\|\boldsymbol{u} - \boldsymbol{v}_h\right\|_1 + \inf_{q_h \in P_h} \left\|p - q_h\right\|_{\mathbf{L}^2(\boldsymbol{\Omega})}), \tag{3.40a}$$

$$\left\|p - p_h\right\|_{\mathbf{L}^2(\boldsymbol{\Omega})/ker\mathbf{B}_h^T} \leq c_2(\left\|\boldsymbol{u} - \boldsymbol{v}_h\right\|_1 + \inf_{q_h \in P_h} \left\|p - q_h\right\|_{\mathbf{L}^2(\boldsymbol{\Omega})}), \tag{3.40b}$$

where the constants c_1 *and* c_2 *are independent of h.*

The second condition is called the discrete inf-sup condition or LBB condition. This means that it is not possible to choose the spaces of velocity and pressure arbitrary. There are many standard techniques for the proof of LBB condition that can be applied to a large class of elements such as Fortin's trick (see [77, 78]), Verfurth's trick (see [219]), and Macroelement technique (see [196, 197, 198, 199]). A vital example for the conforming finite elements approximations of the Stokes problem is the Q_2P_1; the velocity and the pressure are approximated quadrilateralwise by biquadratic polynomial of degree 2 and linear function, respectively. The discrete velocities are continuous on the common edge of two adjacent quadrilaterals.

3.4.2 The Incompressibility Condition

It is typically accepted the fact that the main difficulty related to the incompressible flow equations in the pressure-velocity formulations is the treatment of the incompressibility constraint ($\boldsymbol{\nabla} \cdot \boldsymbol{u} = 0$). It includes the constraint on the velocity field which has to be divergence free. Various methods have been proposed in the frame of numerical works to cope with. These methods can be classified in three categories according to how the incompressibility has been treated.

(a) Method of mixed finite elements, which requires compatible spaces of velocity and pressure fields. These spaces can not be chosen arbitrarily. The necessary link is LBB condition. The resulting discrete system is coupled and indefinite which is still a challenging task to be solved.

(b) Method of divergence-free subspace velocity approximation in which the pressure is eliminated from the system, resulting in a well-behaved positive definite discrete system with smaller number of unknowns compared to a coupled formulation. However, the divergence free subspaces are not usually easy to construct and they involve tedious programming in general.

(c) Method of Pseudo-compressibility, the idea beyond this is supplemented by terms involving a pressure thereby giving it a similar appearance as the continuity in compressible flow models to be $\boldsymbol{\nabla} \cdot \boldsymbol{u} = \frac{p}{\bar{\lambda}}$ where $\bar{\lambda}$ is too large parameter such as artificial compressibility method and penalty method (see [18, 112, 176]). This substitution eliminates the pressure from the momentum equation. The idea from the computational point of view is very attractive but the presence of the penalty parameter may cause a loss of accuracy for the large values of λ and prevent the convergence to the actual solution for insufficiently large values.

3.5 The Finite Element Discretization for Generalized Newtonian Fluids Problem

3.5.1 Standard Form

We consider the discrete version of the generalized Newtonian problems which comes from the application of the finite element spatial discretization for the following system.

$$\frac{\partial \boldsymbol{u}}{\partial t} + \boldsymbol{u} \cdot \boldsymbol{\nabla} \boldsymbol{u} + \boldsymbol{\nabla} p = \boldsymbol{\nabla} \cdot \boldsymbol{\tau} + \boldsymbol{f} \quad in \quad \boldsymbol{\Omega} \times (0, T), \tag{3.41a}$$

$$\boldsymbol{\nabla} \cdot \boldsymbol{u} = 0 \quad in \quad \boldsymbol{\Omega} \times (0, T). \tag{3.41b}$$

According to the standard presentation of the finite element methods, we assume that $\mathbf{V}^h$, P^h the trial and test functions respectively. Then finite element formulation for the viscoplastic problem can be written as :
Given $\boldsymbol{f}$ find $\boldsymbol{u}_h \in \mathbf{V}_h$, $p_h \in P_h$ such that $\forall \boldsymbol{v}_h \in \mathbf{V}_h$, $\forall q_h \in P_h$ the following expression is satisfied:

$$\int_{\boldsymbol{\Omega}} \frac{\partial \boldsymbol{u}_h}{\partial t} \boldsymbol{v}_h + \int_{\boldsymbol{\Omega}} (\boldsymbol{u}_h \cdot \boldsymbol{\nabla} \boldsymbol{u}_h) \boldsymbol{v}_h + \int_{\boldsymbol{\Omega}} \mathbf{D}(\boldsymbol{v}_h) : \boldsymbol{\tau}(\boldsymbol{u}_h) + \int_{\boldsymbol{\Omega}} \boldsymbol{\nabla} p_h \boldsymbol{v}_h = \int_{\boldsymbol{\Omega}} \boldsymbol{f} \boldsymbol{v}_h \quad in \quad \boldsymbol{\Omega} \times (0, T), \tag{3.42a}$$

$$\int_{\boldsymbol{\Omega}} \boldsymbol{\nabla} \cdot \boldsymbol{u}_h q_h d\boldsymbol{\Omega} = 0 \quad in \quad \boldsymbol{\Omega} \times (0, T). \tag{3.42b}$$

The above equation can be further expanded by substituting the constitutive law in the place of stress tensor $\boldsymbol{\tau}$. Hence the final expression for the finite element formulation of the problem can be written as:

$$\int_{\boldsymbol{\Omega}} \frac{\partial \boldsymbol{u}_h}{\partial t} \boldsymbol{v}_h + \int_{\boldsymbol{\Omega}} (\boldsymbol{u}_h \cdot \boldsymbol{\nabla} \boldsymbol{u}_h) \boldsymbol{v}_h + \int_{\boldsymbol{\Omega}} \nu(\|\mathbf{D}\|) \mathbf{D}(\boldsymbol{u}_h) : \mathbf{D}(\boldsymbol{v}_h) - \int_{\boldsymbol{\Omega}} p_h \boldsymbol{\nabla} \cdot \boldsymbol{v}_h = \int_{\boldsymbol{\Omega}} \boldsymbol{f} \boldsymbol{v}_h \quad in \quad \boldsymbol{\Omega} \times (0, T), \tag{3.43a}$$

$$\int_{\boldsymbol{\Omega}} \boldsymbol{\nabla} \cdot \boldsymbol{u}_h q_h d\boldsymbol{\Omega} = 0 \quad in \quad \boldsymbol{\Omega} \times (0, T). \tag{3.43b}$$

For the Bingham viscoplastic problem, the relationship between the stress tensor $\boldsymbol{\tau}$ and the shear rate is represented only for the shear region which is $\|\mathbf{D}\| \neq 0$ representing the first definition in the constitutive law.

$$\int_{\boldsymbol{\Omega}|_{shear}} \frac{\partial \boldsymbol{u}_h}{\partial t}\boldsymbol{v}_h + \int_{\boldsymbol{\Omega}|_{shear}} (\boldsymbol{u}_h \cdot \boldsymbol{\nabla}\boldsymbol{u}_h)\boldsymbol{v}_h - \int_{\boldsymbol{\Omega}|_{shear}} p_h \boldsymbol{\nabla}\cdot\boldsymbol{v}_h +$$
$$\int_{\boldsymbol{\Omega}|_{shear}} (2\mu + \frac{\tau_s}{\|\mathbf{D}\|})\mathbf{D}(\boldsymbol{u}_h) : \mathbf{D}(\boldsymbol{v}_h) = \int_{\boldsymbol{\Omega}|_{shear}} \boldsymbol{f}\boldsymbol{v}_h \quad in \quad \boldsymbol{\Omega}|_{shear} \times (0,T), \tag{3.44a}$$
$$\int_{\boldsymbol{\Omega}} \boldsymbol{\nabla}\cdot\boldsymbol{u}_h q_h d\boldsymbol{\Omega} = 0 \quad in \quad \boldsymbol{\Omega} \times (0,T). \tag{3.44b}$$

The extended definition for these equation in the form of the finite element formulation using the second part of the constitutive law for the plug region/dead regions $\|\mathbf{D}\| = 0$ can be formulated as follows:

$$-\int_{\boldsymbol{\Omega}|_{plug}} p_h \boldsymbol{\nabla}\cdot\boldsymbol{v}_h = -\int_{\boldsymbol{\Omega}|_{plug}} \boldsymbol{\tau}_s : \mathbf{D}(\boldsymbol{v}_h) + \int_{\boldsymbol{\Omega}|_{plug}} \boldsymbol{f}\cdot\boldsymbol{v}_h \quad in \quad \boldsymbol{\Omega}|_{plug} \times (0,T). \tag{3.45}$$

But in our case we need to merge the two definition to cover the whole domain by one definition since it is difficult to detect the null shear rate space, so that by using the one of such regularization techniques we have

$$\int_{\boldsymbol{\Omega}} \frac{\partial \boldsymbol{u}_h}{\partial t}\boldsymbol{v}_h + \int_{\boldsymbol{\Omega}} (\boldsymbol{u}_h \cdot \boldsymbol{\nabla}\boldsymbol{u}_h)\boldsymbol{v}_h - \int_{\boldsymbol{\Omega}} p_h \boldsymbol{\nabla}\cdot\boldsymbol{v}_h +$$
$$\int_{\boldsymbol{\Omega}} (2\mu + \frac{\tau_s}{\sqrt{\epsilon^2 + \|\mathbf{D}\|^2}})\mathbf{D}(\boldsymbol{u}_h) : \mathbf{D}(\boldsymbol{v}_h) = \int_{\boldsymbol{\Omega}} \boldsymbol{f}\boldsymbol{v}_h \quad in \quad \boldsymbol{\Omega} \times (0,T), \tag{3.46a}$$
$$\int_{\boldsymbol{\Omega}} \boldsymbol{\nabla}\cdot\boldsymbol{u}_h q_h d\boldsymbol{\Omega} = 0 \quad in \quad \boldsymbol{\Omega} \times (0,T). \tag{3.46b}$$

3.5.2 Variational Form

Following [69], we use the variational inequality such that:
For $t \in (0,T)$, given $\boldsymbol{f}$ find $\boldsymbol{u}_h \in \mathbf{V}_h$, $p_h \in P_h$ such that $\forall \boldsymbol{v}_h \in \mathbf{V}_h$, $\forall q_h \in P_h$ the following expression is satisfied:

$$\int_{\boldsymbol{\Omega}} \frac{\partial \boldsymbol{u}_h}{\partial t}(\boldsymbol{v}_h - \boldsymbol{u}_h) + \int_{\boldsymbol{\Omega}} (\boldsymbol{u}_h \cdot \boldsymbol{\nabla}\boldsymbol{u}_h)(\boldsymbol{v}_h - \boldsymbol{u}_h) - \int_{\boldsymbol{\Omega}} p_h \boldsymbol{\nabla}\cdot(\boldsymbol{v}_h - \boldsymbol{u}_h) =$$
$$-\int_{\boldsymbol{\Omega}} \mathbf{D}(\boldsymbol{v}_h - \boldsymbol{u}_h) : \boldsymbol{\tau}(\boldsymbol{u}_h) + \int_{\boldsymbol{\Omega}} \boldsymbol{f}(\boldsymbol{v}_h - \boldsymbol{u}_h) \quad in \quad \boldsymbol{\Omega} \times (0,T), \tag{3.47a}$$
$$\int_{\boldsymbol{\Omega}} \boldsymbol{\nabla}\cdot\boldsymbol{u}_h q_h d\boldsymbol{\Omega} = 0 \quad in \quad \boldsymbol{\Omega} \times (0,T). \tag{3.47b}$$

For Bingham viscoplastic problem, by using the regularized stress tensor equation to define the whole domain, one can get

$$\int_{\boldsymbol{\Omega}} \frac{\partial \boldsymbol{u}_h}{\partial t}(\boldsymbol{v}_h - \boldsymbol{u}_h) + \int_{\boldsymbol{\Omega}} (\boldsymbol{u}_h \cdot \boldsymbol{\nabla}\boldsymbol{u}_h)(\boldsymbol{v}_h - \boldsymbol{u}_h) - \int_{\boldsymbol{\Omega}} p_h \boldsymbol{\nabla}\cdot(\boldsymbol{v}_h - \boldsymbol{u}_h) +$$
$$\tau_s(j(\boldsymbol{v}_h) - j(\boldsymbol{u}_h)) \geq \int_{\boldsymbol{\Omega}} \boldsymbol{f}(\boldsymbol{v}_h - \boldsymbol{u}_h) \quad in \quad \boldsymbol{\Omega} \times (0,T), \tag{3.48a}$$
$$\int_{\boldsymbol{\Omega}} \boldsymbol{\nabla}\cdot\boldsymbol{u}_h q_h d\boldsymbol{\Omega} = 0 \quad in \quad \boldsymbol{\Omega} \times (0,T). \tag{3.48b}$$

At this point for both forms the standard formulation of the finite element interpolation functions is introduced for primitive variables (velocity and pressure). Let $\phi_j/\psi_j : \boldsymbol{\Omega} \rightarrow \mathbb{R}$, j=1,...,$n_{\boldsymbol{u}/p}$ denote the prescribed $n_{\boldsymbol{u}/p}$ finite element interpolation functions for velocity and pressure together with the associated nodal points. Then finite dimensional subspaces can be represented respectively by:

$$\boldsymbol{u}_h = \sum_{j=1}^{n_{\boldsymbol{u}}} \boldsymbol{u}_j \phi_j, \qquad p_h = \sum_{j=1}^{n_p} p_j \psi_j. \tag{3.49}$$

Where $\boldsymbol{u}_j$ and p_j are the nodal velocities and pressures. The above equation represents the different order interpolation functions for velocity and pressure fields since we use different finite elements for velocity and pressure. By inserting those into the finite element formulation and in view of the arbitrariness of the parameters $\boldsymbol{u}_j$ and p_j representing the virtual nodal velocities and pressures respectively, a set of nonlinear equations is obtained which can be expressed in the following matrix form as:
find a vector $\boldsymbol{x} = (\boldsymbol{u}, p)$ of the nodal variables such that $\forall t \in (0, T)$ following system of evolution equations is satisfied

$$\mathbf{R}(\boldsymbol{x}) = 0. \tag{3.50}$$

The algebraic system of non-linear equations obtained in this way is then solved by an iterative methods. We have employed certain time stepping scheme within the Newton methods and multigrids as discussed in the next chapter.

3.6 Numerical Results for Newtonian Fluids

As already pointed out, we have considered three numerical tests for Newtonian fluids, each test has particular difficulties. Our first problem is Poiseuille flow which is classical but gives arise to interesting conclusions. The next is the Stokes flow but with linear pressure form and the last one is the stokes problem with nonlinear pressure form which are handled in [25].
Many of the researchers have reported that (e.g. [51, 72, 75, 191]) and the references therein, the finite element $Q_2P_1^{np}$ has an influence to be the potential candidate to be considered as the best for CFD equations in many applications particularly comparing with the element Q_2P_1 which is tested only for CFD problems in a few publications. As well as comparing with Q_2Q_1 (An eight-node velocity and four-node pressure) which has been used most frequently in the early development stage of the finite element method for flows. This element yielded inaccurate pressure as the Reynolds number was increased (see [115, 206]). In [128], the researchers have compared both finite elements in velocity-pressure integrated and the penalty approaches and reported that the two finite elements exhibited almost identical convergence rates for the example problem considered. Moreover, the penalty method with the pressure interpolation polynomials given in Eq.(3.18), was found to be numerically more stable and yielded more uniformly convergent solution than that with the pressure interpolation polynomials in the global one. The used pressure element was interpolated using the linear shape function defined on the triangular element which is contained inside the quadratic element, the three pressure nodes are located at the three Gauss points of the three point Gauss quadrature rule for the quadrilateral elements, the coordinates of the pressure nodes on the computational element are given as

$$\boldsymbol{\xi}_1 = (0, \sqrt{2}/\sqrt{3}), \tag{3.51a}$$

$$\boldsymbol{\xi}_2 = (1/\sqrt{2}, -1/\sqrt{6}), \tag{3.51b}$$

$$\boldsymbol{\xi}_3 = (1/\sqrt{2}, -1/\sqrt{6}). \tag{3.51c}$$

where, $\boldsymbol{\xi}_n = (\xi_n, \eta_n)$ and n=1,2,3 denote the pressure node numbers. The shape functions for each of the nodes are given as

$$\psi_1 = \frac{1}{3} + \frac{\sqrt{2}}{\sqrt{3}}\eta, \tag{3.52a}$$

$$\psi_2 = \frac{1}{3} - \frac{1}{\sqrt{2}}\xi - \frac{1}{\sqrt{6}}\eta, \tag{3.52b}$$

$$\psi_3 = \frac{1}{3} + \frac{1}{\sqrt{2}}\xi - \frac{1}{\sqrt{6}}\eta. \tag{3.52c}$$

In [155], it is reported that, the mapped pressure space results for the velocity about 30% better than the unmapped pressure one on the same grids. In [191], the following reported table(3.1) explains the comparison and characterization of the two finite elements. For the used grid, the first row presents the results for unmapped(global) and the second row presents the mapped(local) pressure and the third one gives the ratio between the local and the global approaches in percents. The norms $\|.\|_{sup}$ and $\|.\|_{\mathbf{L}^2}$ are the discrete analogs (in the nodes of the triangulation) of the sup-norm and the $\mathbf{L}^2$ norm respectively. The results from this table confirms that the local approach is better with decreasing of the stretching, it gives about 60% better results for the velocity for the mentioned problem. The following studies involved in [25] have given a light for the lack in the approximation properties for the space coming out from the local pressure approach and the numerical results within. Actually it shows that; the unmapped pressure space is better for the perturbed meshes as well as the mapped one is sub-optimally convergent. The used test problem is the Stokes problem with its corresponding exact solution to confirm that the use of the global choice is to be preferred with respect to the local choice with the mentioned percents in the following table(3.2) for the perturbed meshes. This table(3.2) shows that in the case of the square meshes the two approaches are equivalent and also shows us that the velocities converge with the correct rate which is the third order in $\mathbf{L}^2$ while the pressure superconverges with third order instead of the second order in $\mathbf{L}^2$ in contrast of the perturbed meshes(trapezoidal mesh), the behavior is perfectly different. Whenever the pressure is chosen locally then the sub-optimality of the method is evident, only first order in the $\mathbf{L}^2$ norm, but with respect to the global choice, it recovers the optimal second order accuracy. For the Newtonian fluids, we present two examples(Poiseuille flow and Stokes flow) to show the differences with the behavior of convergence among the three approaches.

Error	$\|\boldsymbol{u}-\boldsymbol{u}_h\|_{sup}$	$\|\boldsymbol{u}-\boldsymbol{u}_h\|_{\mathbf{L}^2}$	$\|\boldsymbol{u}-\boldsymbol{u}_h\|_{sup}$	$\|\boldsymbol{u}-\boldsymbol{u}_h\|_{\mathbf{L}^2}$	$\|\boldsymbol{u}-\boldsymbol{u}_h\|_{sup}$	$\|\boldsymbol{u}-\boldsymbol{u}_h\|_{\mathbf{L}^2}$	$\|\boldsymbol{u}-\boldsymbol{u}_h\|_{sup}$	$\|\boldsymbol{u}-\boldsymbol{u}_h\|_{\mathbf{L}^2}$
stretching ratio	1.27		0.51		0.25		0.05	
global pressure	3.52E-4	1.4E-4	5.32E-4	1.88E-4	3.81E-4	1.02E-4	3.87E-4	9.5E-5
local pressure	2.34E-4	1.07E-4	3.85E-4	1.46E-4	1.58E-4	3.8E-5	1.47E-4	3.0E-5
ratio	66.48	76.43	72.37	77.66	41.47	37.25	37.98	31.58

Table 3.1. Comparison between global pressure and local pressure approaches in [191].

Pressure	global				local			
Error	$\|\boldsymbol{u}-\boldsymbol{u}_h\|_{L^2}$	$\|p-p_h\|_{L^2}$	$\|\boldsymbol{u}-\boldsymbol{u}_h\|_{L^2}$	$\|p-p_h\|_{L^2}$	$\|\boldsymbol{u}-\boldsymbol{u}_h\|_{L^2}$	$\|p-p_h\|_{L^2}$	$\|\boldsymbol{u}-\boldsymbol{u}_h\|_{L^2}$	$\|p-p_h\|_{L^2}$
Mesh	uniform		trapizoid		uniform		trapizoid	
2×2	1.2E-3	1.2E-2	8.3E-4	1.0E-2	1.4E-3	1.6E-1	8.3E-4	1.0E-2
4×4	1.8E-4	3.3E-3	1.2E-4	1.3E-3	4.0E-4	9.1E-2	1.2E-4	1.3E-3
8×8	2.2E-5	5.5E-4	1.5E-5	1.7E-4	1.1E-4	3.9E-2	1.5E-5	1.7E-4
16×16	2.8E-6	1.2E-4	1.9E-6	2.1E-5	2.9E-5	1.8E-2	1.9E-6	2.1E-5
32×32	3.5E-7	2.6E-5	2.4E-7	2.6E-6	7.4E-6	9.0E-3	2.4E-7	2.6E-6

Table 3.2. Comparison between global pressure and local pressure approaches in [25].

3.6.1 Poiseuille Flow

The problem can be described briefly in such a way that a parabolic velocity profile is imposed at both the inlet and outlet of a rectangular channel. If H is the height of the channel, then the analytic solution of the Navier-Stokes equations is :

$$\boldsymbol{u} = (\frac{6y}{5H^2}(H-y), 0), \tag{3.53a}$$

$$p = \frac{-x}{H^2} + const. \tag{3.53b}$$

We test our approaches against the exact solution of Poiseuille solution for the plane flow in a channel for the used meshes and the discretizations which are the uniform and perturbed. We prescribe at the inlet and the outlet of the channel of unit length and unit width and use regular finite elements for a uniform triangulation refinement.

3.6.1.a Convergence Study for the Uniform and the Perturbed Meshes

As we expected the numerical solution for the uniform mesh is going with the sense of the theory of finite element for $\tilde{Q}_1Q_0$, the element converge with the expected order 2 for the velocity and one for its gradient and the pressure (see table(3.3)). For Q_2P_1 and $Q_2P_1^{np}$, the numerical solution coincides with the exact one up to the accuracy of the computer arithmetic, because of the finite element of the second order (see table(3.4) and table(3.5)).

The same is true for the irregular mesh of $\tilde{Q}_1Q_0$, therefore the irregular mesh has no bad influence on the behavior of the element and still preserves the 2^{nd} convergence for velocity and the 1^{st} for the gradient and the pressure (see table(3.3)).
In the case of Q_2P_1 the mapped pressure dropped down the optimal convergence to behave as the low order finite element $\tilde{Q}_1Q_0$ which has the 2^{nd} convergence for velocity and the 1^{st} for the gradient and the pressure. This refers to the bad influence of the mapped pressure on the convergence of the primitive variables. For the unmapped approach, the convergence still has the optimal property to the coincidence of the numerical exact one up to the accuracy of the computer arithmetic(see table(3.4) and table(3.5)). From Fig.(3.4), in all cases the pressure is described without distortion with respect to the perturbed mesh.

Mesh	*uniform*			*perturbed*		
Error	$\|\boldsymbol{u}-\boldsymbol{u}_h\|_{\mathbf{L}^2}$	$\|p-p_h\|_{\mathbf{L}^2}$	$\|\boldsymbol{u}-\boldsymbol{u}_h\|_{\mathbf{H}^1}$	$\|\boldsymbol{u}-\boldsymbol{u}_h\|_{\mathbf{L}^2}$	$\|p-p_h\|_{\mathbf{L}^2}$	$\|\boldsymbol{u}-\boldsymbol{u}_h\|_{\mathbf{H}^1}$
2×2	4.676616E-2	4.295899E-1	3.067336E-1	4.980101E-2	4.389876E-1	3.147061E-1
4×4	1.352814E-2(3.457)	1.923701E-1(2.233)	1.655566E-1(1.852)	1.573002E-2(3.166)	2.042393E-1(2.149)	1.787113E-1(1.761)
8×8	3.554409E-3(3.806)	8.994456E-2(2.138)	8.514705E-2(1.944)	4.699097E-3(3.475)	9.892158E-2(2.064)	9.514945E-2(1.878)
16×16	9.036021E-4(3.934)	4.381863E-2(2.052)	4.301634E-2(1.979)	1.214841E-3(3.868)	4.772691E-2(2.072)	4.871139E-2(1.953)
32×32	2.272177E-4(3.976)	2.172638E-2(2.020)	2.159202E-2(1.992)	3.098842E-4(3.920)	2.369003E-2(2.014)	2.469290E-2(1.972)
64×64	5.692546E-5(3.991)	1.083609E-2(2.000)	1.081258E-2(1.996)	7.845793E-5(3.949)	1.185708E-2(1.998)	1.241273E-2(1.989)
128×128	1.424322E-5(3.997)	5.414162E-3(2.000)	5.409757E-3(1.998)	1.976253E-5(3.970)	5.927987E-3(2.000)	6.230694E-3(1.992)
256×256	3.562049E-6(3.999)	2.706537E-3(2.000)	2.705644E-3(1.999)	4.964351E-6(3.981)	2.967733E-3(1.997)	3.123898E-3(1.994)

Table 3.3. *Poiseuille flow:* $\mathbf{L}^2/\mathbf{H}^1$ errors for $\tilde{Q}_1Q_0$ using grid $[0,1]\times[0,1]$.

3.6.2 Stokes Flow

The used domain is a unit square $[0,1]\times[0,1]$. On the boundary of this domain we impose homogenous boundary conditions $\boldsymbol{u}=0$ on $\partial\boldsymbol{\Omega}$ with the derived external forces $\boldsymbol{f}=(f1,f2)$. So that the analytic solution of Stokes equation with linear/nonlinear pressure forms can be written as follows

Mesh	*uniform*			*perturbed*		
Error	$\|\boldsymbol{u}-\boldsymbol{u}_h\|_{\mathbf{L}^2}$	$\|p-p_h\|_{\mathbf{L}^2}$	$\|\boldsymbol{u}-\boldsymbol{u}_h\|_{\mathbf{H}^1}$	$\|\boldsymbol{u}-\boldsymbol{u}_h\|_{\mathbf{L}^2}$	$\|p-p_h\|_{\mathbf{L}^2}$	$\|\boldsymbol{u}-\boldsymbol{u}_h\|_{\mathbf{H}^1}$
2×2	1.118317E-16	2.182354E-14	3.333415E-15	1.171911E-3	2.209861E-2	1.374668E-2
4×4	1.118317E-16	2.182354E-14	3.333415E-15	6.508008E-4(1.800)	1.820232E-2(1.214)	1.503308E-2(0.914)
8×8	1.118317E-16	2.182354E-14	3.333415E-15	1.611861E-4(4.037)	8.496304E-3(2.142)	7.004969E-3(2.146)
16×16	1.118317E-16	2.182354E-14	3.333415E-15	3.915460E-5(4.116)	4.236501E-3(2.005)	3.581325E-3(1.956)
32×32	1.118317E-16	2.182354E-14	3.333415E-15	1.141103E-5(3.431)	2.374492E-3(1.784)	2.051462E-3(1.745)
64×64	1.118317E-16	2.182354E-14	3.333415E-15	2.703178E-6(4.221)	1.142082E-3(2.079)	9.855188E-4(2.081)
128×128	1.118317E-16	2.182354E-14	3.333415E-15	7.125840E-7(3.793)	5.899803E-4(1.935)	5.134672E-4(1.919)
256×256	1.118317E-16	2.182354E-14	3.333415E-15	1.767095E-7(4.032)	2.959862E-4(1.993)	2.565737E-4(2.001)

Table 3.4. *Poiseuille flow:* $\mathbf{L}^2/\mathbf{H}^1$ errors for Q_2P_1 using grid $[0,1]\times[0,1]$.

Mesh	*uniform*			*perturbed*		
Error	$\|\boldsymbol{u}-\boldsymbol{u}_h\|_{\mathbf{L}^2}$	$\|p-p_h\|_{\mathbf{L}^2}$	$\|\boldsymbol{u}-\boldsymbol{u}_h\|_{\mathbf{H}^1}$	$\|\boldsymbol{u}-\boldsymbol{u}_h\|_{\mathbf{L}^2}$	$\|p-p_h\|_{\mathbf{L}^2}$	$\|\boldsymbol{u}-\boldsymbol{u}_h\|_{\mathbf{H}^1}$
2×2	1.154522E-16	2.146492E-14	2.906613E-15	2.19881E-16	6.734168E-15	4.016841E-15
4×4	1.154522E-16	2.146492E-14	2.906613E-15	2.19881E-16	6.734168E-15	4.016841E-15
8×8	1.154522E-16	2.146492E-14	2.906613E-15	2.19881E-16	6.734168E-15	4.016841E-15
16×16	1.154522E-16	2.146492E-14	2.906613E-15	2.19881E-16	6.734168E-15	4.016841E-15
32×32	1.154522E-16	2.146492E-14	2.906613E-15	2.19881E-16	6.734168E-15	4.016841E-15
64×64	1.154522E-16	2.146492E-14	2.906613E-15	2.19881E-16	6.734168E-15	4.016841E-15
128×128	1.154522E-16	2.146492E-14	2.906613E-15	2.19881E-16	6.734168E-15	4.016841E-15
256×256	1.154522E-16	2.146492E-14	2.906613E-15	2.19881E-16	6.734168E-15	4.016841E-15

Table 3.5. *Poiseuille flow:* $\mathbf{L}^2/\mathbf{H}^1$ errors for $Q_2P_1^{np}$ using grid $[0,1]\times[0,1]$.

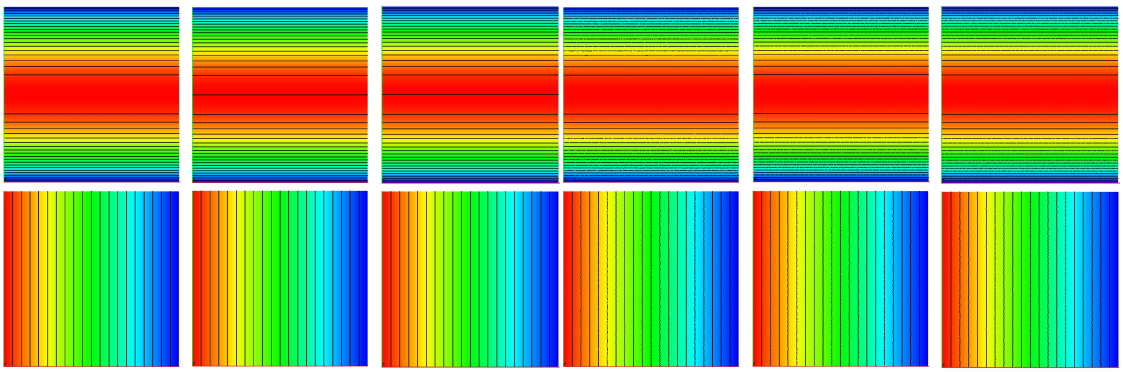

Fig. 3.4. *Poiseuille flow:* Velocity distributions for $\tilde{Q}_1Q_0$, Q_2P_1 and $Q_2P_1^{np}$ using uniform and perturbed meshes (top) and pressure distributions for $\tilde{Q}_1Q_0$, Q_2P_1 and $Q_2P_1^{np}$ using uniform and perturbed meshes (bottom) at level 256×256.

$$\boldsymbol{u} = [-2x^2y(1-x)^2(1-3y+2y^2), 2xy^2(1-y)^2(1-3x+2x^2)], \tag{3.54a}$$

$$[p_{linear}, p_{nonlinear}] = [x+y-1, cos(\pi x)cos(\pi y)]. \tag{3.54b}$$

3.6.2.a Convergence Study for the Uniform Mesh

From the depicted tables for the linear pressure and nonlinear pressure cases (see (table(3.6) to table(3.11)), our first attempt is to use the conforming and nonconforming finite element on the regular sense, as one can see the results are very good for both velocity and pressure. The smoothness of the pressure field for $\tilde{Q}_1Q_0$ is for the nonlinear pressure which is not a little bit defected and the velocity field is still satisfactory, the same is for the mapped/unmapped pressure approaches. The order of convergence

for the linear pressure and nonlinear pressure cases with the element $\tilde{Q}_1Q_0$ converges with the optimal and correct rates (second order for velocity and first order for its gradient and the pressure). On the other hand, the linear pressure case with the mapped and unmapped elements converges with the optimal and correct rates (third order for velocity and second order for the its gradient and the pressure respectively). For the nonlinear pressure, the behavior of the mapped and unmapped pressure which is completely different invites us to observe that the order of convergence for the low levels(level2-level6) has the order around 4 and at the higher levels (level7-level8) goes to the correct rate. It gives an indication that the smoothness and the upper/lower bound of pressure field affect the convergence of the velocity. Whereas for the pressure we have no gain to expect superconvergence but we expect the optimal second order convergence.

Mesh	*uniform*			*perturbed*		
Error	$\|\boldsymbol{u}-\boldsymbol{u}_h\|_{\mathbf{L}^2}$	$\|p-p_h\|_{\mathbf{L}^2}$	$\|\boldsymbol{u}-\boldsymbol{u}_h\|_{\mathbf{H}^1}$	$\|\boldsymbol{u}-\boldsymbol{u}_h\|_{\mathbf{L}^2}$	$\|p-p_h\|_{\mathbf{L}^2}$	$\|\boldsymbol{u}-\boldsymbol{u}_h\|_{\mathbf{H}^1}$
2×2	1.458269E-2	2.154930E-1	1.180573E-1	1.705428E-2	2.261305E-1	1.249899E-1
4×4	4.662576E-3(3.127)	1.063630E-1(2.026)	7.105395E-2(1.661)	5.667363E-3(3.009)	1.121998E-1(2.015)	7.625785E-2(1.639)
8×8	1.262958E-3(3.691)	5.211045E-2(2.041)	3.783777E-2(1.877)	1.742362E-3(3.252)	5.634321E-2(1.991)	4.248568E-2(1.794)
16×16	3.248191E-4(3.888)	2.573200E-2(2.025)	1.935353E-2(1.955)	4.506326E-4(3.866)	2.745926E-2(2.051)	2.178076E-2(1.950)
32×32	8.203030E-5(3.959)	1.279576E-2(2.011)	9.758129E-3(1.983)	1.176878E-4(3.829)	1.375119E-2(1.996)	1.116442E-2(1.950)
64×64	2.058322E-5(3.985)	6.385036E-3(2.004)	4.894607E-3(1.993)	2.997574E-5(3.926)	6.879868E-3(1.998)	5.636537E-3(1.980)
128×128	5.152986E-6(3.994)	3.190387E-3(2.001)	2.450406E-3(1.997)	7.533190E-6(3.979)	3.432935E-3(2.004)	2.827146E-3(1.993)
256×256	1.288966E-6(3.997)	1.594861E-3(2.000)	1.225857E-3(1.998)	1.896746E-6(3.971)	1.720173E-3(1.995)	1.418744E-3(1.992)

Table 3.6. *Stokes flow:* $\mathbf{L}^2/\mathbf{H}^1$ errors for $\tilde{Q}_1Q_0$ using grid $[0,1]\times[0,1]$ for the linear pressure form.

Mesh	*uniform*			*perturbed*		
Error	$\|\boldsymbol{u}-\boldsymbol{u}_h\|_{\mathbf{L}^2}$	$\|p-p_h\|_{\mathbf{L}^2}$	$\|\boldsymbol{u}-\boldsymbol{u}_h\|_{\mathbf{H}^1}$	$\|\boldsymbol{u}-\boldsymbol{u}_h\|_{\mathbf{L}^2}$	$\|p-p_h\|_{\mathbf{L}^2}$	$\|\boldsymbol{u}-\boldsymbol{u}_h\|_{\mathbf{H}^1}$
2×2	1.187110E-3	3.398331E-3	1.790120E-2	1.632885E-3	1.972924E-2	2.206107E-2
4×4	1.666263E-4(7.124)	4.023808E-4(8.445)	4.485897E-3(3.990)	3.871196E-4(4.218)	9.960029E-3(1.980)	9.098682E-3(2.424)
8×8	2.131971E-5(7.815)	4.630225E-5(8.690)	1.115958E-3(4.019)	9.413735E-5(4.112)	4.575729E-3(2.176)	4.086411E-3(2.226)
16×16	2.679891E-6(7.955)	5.580447E-6(8.297)	2.785507E-4(4.006)	2.369964E-5(3.972)	2.463525E-3(1.857)	2.115088E-3(1.932)
32×32	3.354514E-7(7.988)	6.902958E-7(8.084)	6.960896E-5(4.001)	6.118748E-6(3.873)	1.266284E-3(1.945)	1.097413E-3(1.927)
64×64	4.194595E-8(7.997)	8.605251E-8(8.021)	1.740043E-5(4.000)	1.467888E-6(4.168)	6.201449E-4(2.041)	5.341758E-4(2.054)
128×128	5.243698E-9(7.999)	1.074918E-8(8.005)	4.349993E-6(4.000)	3.811107E-7(3.851)	3.165545E-4(1.959)	2.750875E-4(1.941)
256×256	6.554764E-10(8.000)	1.343433E-9(8.001)	1.087491E-6(4.000)	9.345877E-8(4.077)	1.564570E-4(2.023)	1.358282E-4(2.025)

Table 3.7. *Stokes flow:* $\mathbf{L}^2/\mathbf{H}^1$ errors for Q_2P_1 using grid $[0,1]\times[0,1]$ for the linear pressure form.

Mesh	*uniform*			*perturbed*		
Error	$\|\boldsymbol{u}-\boldsymbol{u}_h\|_{\mathbf{L}^2}$	$\|p-p_h\|_{\mathbf{L}^2}$	$\|\boldsymbol{u}-\boldsymbol{u}_h\|_{\mathbf{H}^1}$	$\|\boldsymbol{u}-\boldsymbol{u}_h\|_{\mathbf{L}^2}$	$\|p-p_h\|_{\mathbf{L}^2}$	$\|\boldsymbol{u}-\boldsymbol{u}_h\|_{\mathbf{H}^1}$
2×2	1.187110E-3	3.398331E-3	1.790120E-2	1.468627E-3	5.564475E-3	2.007121E-2
4×4	1.666263E-4(7.124)	4.023808E-4(8.445)	4.485897E-3(3.990)	2.269163E-4(6.472)	1.282031E-3(4.340)	5.651285E-3(3.551)
8×8	2.131971E-5(7.815)	4.630225E-5(8.690)	1.115958E-3(4.019)	3.488055E-5(6.505)	2.648828E-4(4.840)	1.616614E-3(3.495)
16×16	2.679891E-6(7.955)	5.580447E-6(8.297)	2.785507E-4(4.006)	4.417930E-6(7.895)	6.908506E-5(3.834)	4.085463E-4(3.957)
32×32	3.354514E-7(7.988)	6.902958E-7(8.084)	6.960896E-5(4.001)	5.752545E-7(7.680)	1.699629E-5(4.064)	1.057473E-4(3.863)
64×64	4.194595E-8(7.997)	8.605251E-8(8.021)	1.740043E-5(4.000)	7.391026E-8(7.783)	4.242222E-6(4.006)	2.691804E-5(3.928)
128×128	5.243698E-9(7.999)	1.074918E-8(8.005)	4.349993E-6(4.000)	9.284606E-9(7.960)	1.117887E-6(3.794)	6.800197E-6(3.958)
256×256	6.554764E-10(8.000)	1.343434E-9(8.001)	1.087491E-6(4.000)	1.170535E-9(7.931)	2.784247E-7(4.015)	1.710802E-6(3.974)

Table 3.8. *Stokes flow:* $\mathbf{L}^2/\mathbf{H}^1$ errors for $Q_2P_1^{np}$ using grid $[0,1]\times[0,1]$ for the linear pressure form

3.6.2.b Convergence Study for the Perturbed Mesh

The depicted tables(3.6 to 3.11) for the perturbed meshes show that, the three discretizations are not equivalent in the sense of convergence behavior since the element $\tilde{Q}_1Q_0$ still preserves its super convergence which is second order for velocity and first order for the pressure and the gradient (see table(3.9)). Whereas, The convergence of the velocity is optimal and with the correct rate which is third order in $\mathbf{L}^2$ and second in $\mathbf{H}^1$ for unmapped approach and for Q_2P_1 the convergence behaves as the low order finite element in second order for velocity and first element for the pressure and the gradient or a bit better (see table(3.10)). Out of this, one can evolve that, the distorted mesh has a big influence on the behavior for the velocity and pressure. For $\tilde{Q}_1Q_0$ the behavior is going to be close to optimal which recovers the first and second order accuracy. If the pressure space is chosen locally Q_2P_1, then the suboptimality of the method is evident which oscillates around the fist order energy norm. On the other hand with unmapped approach one recovers the optimal second order accuracy. For the second choice of pressure; nonlinear pressure function, for $\tilde{Q}_1Q_0$ and the unmapped pressure approach (see table(3.11)) is going to the optimal order of convergence, but it could have the superconvergence at the lower levels with no expectation at the higher levels.

Mesh	*uniform*			*perturbed*		
Error	$\|\boldsymbol{u}-\boldsymbol{u}_h\|_{\mathbf{L}^2}$	$\|p-p_h\|_{\mathbf{L}^2}$	$\|\boldsymbol{u}-\boldsymbol{u}_h\|_{\mathbf{H}^1}$	$\|\boldsymbol{u}-\boldsymbol{u}_h\|_{\mathbf{L}^2}$	$\|p-p_h\|_{\mathbf{L}^2}$	$\|\boldsymbol{u}-\boldsymbol{u}_h\|_{\mathbf{H}^1}$
2×2	3.595238E-3	2.422839E-2	4.739255E-2	6.814065E-3	1.256411E-1	6.481039E-2
4×4	1.418134E-2(0.253)	2.946790E-1(0.0822)	2.179526E-1(0.2174)	1.512279E-2(0.450)	2.984173E-1(0.421)	2.137298E-1(0.303)
8×8	3.466944E-3(4.090)	1.569314E-1(1.877)	1.128279E-1(1.931)	4.608162E-3(3.281)	1.630588E-1(1.830)	1.198560E-1(1.783)
16×16	8.590557E-4(4.035)	7.973185E-2(1.968)	5.681027E-2(1.986)	1.264815E-3(3.643)	8.503157E-2(1.917)	6.433340E-2(1.863)
32×32	2.146101E-4(4.003)	4.002612E-2(1.992)	2.850021E-2(1.993)	3.392430E-4(3.728)	4.338921E-2(1.959)	3.345315E-2(1.923)
64×64	5.369191E-5(3.997)	2.003314E-2(1.998)	1.427508E-2(1.996)	8.690264E-5(3.903)	2.188169E-2(1.982)	1.696906E-2(1.971)
128×128	1.343164E-5(3.997)	1.001908E-2(1.999)	7.143957E-3(1.998)	2.188763E-5(3.970)	1.094218E-2(1.999)	8.513485E-3(1.993)
256×256	3.359229E-6(3.998)	5.009856E-3(2.000)	3.573604E-3(1.999)	5.497728E-6(3.981)	5.476648E-3(1.998)	4.267300E-3(1.995)

Table 3.9. *Stokes flow:* $\mathbf{L}^2/\mathbf{H}^1$ errors for $\tilde{Q}_1Q_0$ using grid $[0,1]\times[0,1]$ for the nonlinear pressure form.

Mesh	*uniform*			*perturbed*		
Error	$\|\boldsymbol{u}-\boldsymbol{u}_h\|_{\mathbf{L}^2}$	$\|p-p_h\|_{\mathbf{L}^2}$	$\|\boldsymbol{u}-\boldsymbol{u}_h\|_{\mathbf{H}^1}$	$\|\boldsymbol{u}-\boldsymbol{u}_h\|_{\mathbf{L}^2}$	$\|p-p_h\|_{\mathbf{L}^2}$	$\|\boldsymbol{u}-\boldsymbol{u}_h\|_{\mathbf{H}^1}$
2×2	1.187110E-3	3.227901E-1	1.790120E-2	3.390876E-3	3.340615E-1	4.613820E-2
4×4	2.294869E-3(0.5173)	1.174191E-1(2.749)	6.128969E-2(0.292)	2.106207E-3(1.609)	1.216761E-1(2.745)	5.525743E-2(0.835)
8×8	1.470860E-4(15.602)	3.048052E-2(3.852)	1.070977E-2(5.722)	3.869673E-4(5.442)	3.822849E-2(3.182)	1.807509E-2(3.057)
16×16	9.521767E-6(15.447)	7.619676E-3(4.000)	1.535329E-3(6.975)	7.434379E-5(5.205)	1.173314E-2(3.258)	6.973276E-3(2.592)
32×32	6.691897E-7(14.228)	1.902057E-3(4.006)	2.098042E-4(7.317)	2.105955E-5(3.530)	4.884878E-3(2.401)	3.780172E-3(1.844)
64×64	5.561513E-8(12.032)	4.752646E-4(4.002)	3.064757E-5(6.845)	5.005821E-6(4.207)	2.191417E-3(2.229)	1.827999E-3(2.067)
128×128	5.723292E-9(9.717)	1.187992E-4(4.000)	5.389081E-6(5.687)	1.304984E-6(3.835)	1.097408E-3(1.996)	9.454292E-4(1.933)
256×256	6.710421E-10(8.528)	2.969873E-5(4.000)	1.158469E-6(4.651)	3.268261E-7(3.992)	5.466795E-4(2.007)	4.739137E-4(1.994)

Table 3.10. *Stokes flow:* $\mathbf{L}^2/\mathbf{H}^1$ errors for Q_2P_1 using grid $[0,1]\times[0,1]$ for the nonlinear pressure form.

3.7 Numerical Results of Generalized Newtonian Fluids

Now, we show the results from the numerical experiments with various physical models for the proposed discretization and the solution behavior. The domain of calculations is a unit square with different dimensions $[0,1]\times[0,1]$ and $[-0.5,0.5]\times[-0.5,0.5]$ and the exact solution $(\boldsymbol{u},p)$ will be given for each case. The computations are provided for the the shear thickening fluids, shear thinning fluids (see Fig.3.5) and viscoplastic fluids. In the following sections, we will confirm on using the global approach for the pressure element to be preferred with respect to the local approach for the pressure element.

Mesh	*uniform*			*perturbed*		
Error	$\|\boldsymbol{u}-\boldsymbol{u}_h\|_{\mathbf{L}^2}$	$\|p-p_h\|_{\mathbf{L}^2}$	$\|\boldsymbol{u}-\boldsymbol{u}_h\|_{\mathbf{H}^1}$	$\|\boldsymbol{u}-\boldsymbol{u}_h\|_{\mathbf{L}^2}$	$\|p-p_h\|_{\mathbf{L}^2}$	$\|\boldsymbol{u}-\boldsymbol{u}_h\|_{\mathbf{H}^1}$
2×2	1.187110E-3	3.227901E-1	1.790120E-2	3.535451E-3	3.350032E-1	4.774431E-2
4×4	2.294869E-3(0.517)	1.174191E-1(2.749)	6.128969E-2(0.292)	2.063796E-3(1.713)	1.203394E-1(2.783)	5.554151E-2(0.859)
8×8	1.470860E-4(15.602)	3.048052E-2(3.852)	1.070977E-2(5.722)	2.522283E-4(8.182)	3.652626E-2(3.294)	1.411592E-2(3.934)
16×16	9.521767E-6(15.447)	7.619676E-3(4.000)	1.535329E-3(6.975)	2.844681E-5(8.866)	9.212208E-3(3.965)	3.197616E-3(4.414)
32×32	6.691897E-7(14.228)	1.902057E-3(4.006)	2.098042E-4(7.317)	3.835944E-6(7.415)	2.342961E-3(3.931)	8.124443E-4(3.935)
64×64	5.561513E-8(12.032)	4.752646E-4(4.002)	3.064757E-5(6.845)	4.851796E-7(7.906)	5.894995E-4(3.974)	2.070148E-4(3.924)
128×128	5.723292E-9(9.717)	1.187992E-4(4.000)	5.389081E-6(5.687)	6.097120E-8(7.957)	1.475417E-4(3.995)	5.123155E-5(4.040)
256×256	6.710421E-10(8.529)	2.969873E-5(4.000)	1.158469E-6(4.651)	7.760329E-9(7.856)	3.705648E-5(3.981)	1.309061E-5(3.913)

Table 3.11. *Stokes flow:* $\mathbf{L}^2/\mathbf{H}^1$ errors for $Q_2P_1^{np}$ using grid $[0,1]\times[0,1]$ for the nonlinear pressure form.

Mesh information			Q_2P_1	$\tilde{Q}_1Q_0$
Level	Elements	Vertices	Total unknowns	Total unknowns
1	4	9	62	28
2	16	25	210	96
3	64	81	770	352
4	256	289	2946	1344
5	1024	1089	11522	5248
6	4096	4225	45570	20736
7	16384	16641	181250	82432
8	65536	66049	722946	328704

Table 3.12. Coarse mesh and geometrical details for the 'Cavity Flow' configuration for the both elements $\tilde{Q}_1Q_0$ and Q_2P_1 on the different levels of mesh refinement.

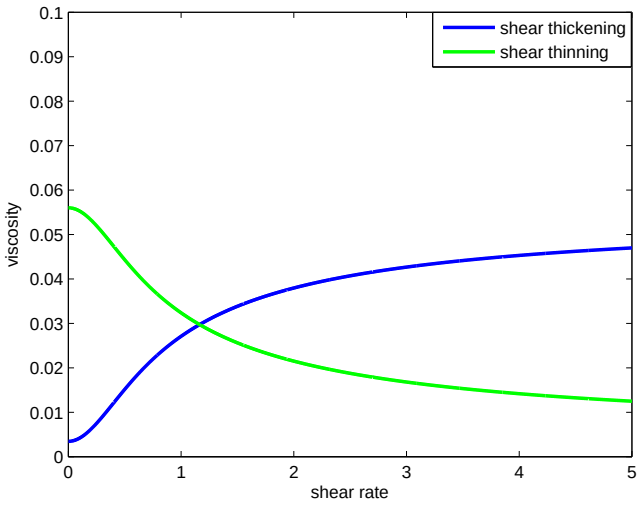

Fig. 3.5. Viscosity behavior for shear thickening and shear thinning fluids.

3.7.1 Shear Thickening Fluids

This section presents a numerical test for the first nonlinear problem, the general viscosity model is Carreau-Yasuda model (see [152])

$$\nu(\|\mathbf{D}\|) = \nu_\infty + (\nu_0 - \nu_\infty)(1 + (\lambda\,\|\mathbf{D}\|)^a)^{\frac{n-1}{a}}, \tag{3.55}$$

and obeying the shear thickening model with the associated parameters in the table(3.13)(see Fig.3.5): The assumed exact solution for the this problem is

fluid type	ν_0	ν_∞	λ	n	a
Shear Thickening	0.00345	0.056	1.902	0.22	2.

Table 3.13. *Shear Thickening parameters for Carreau-Yasuda model.*

$$\boldsymbol{u} = [ye^{5(x^2+y^2)}, -xe^{5(x^2+y^2)}], \tag{3.56a}$$

$$p(linear) = x + y - 1, \tag{3.56b}$$

$$p(nonlinear) = e^{(\frac{5}{4})} sin(2\pi x) sin(2\pi y). \tag{3.56c}$$

So now, we are dealing with a nonlinear finite element formulation where nonlinearity is engendered by the diffusive term. in order to get a converged solution on a given mesh, the nonlinear iteration runs until numerical convergence is attained to 10^{-8}, and the linear problem runs until numerical convergence is attained to 10^{-5}. Once the converged solution is attained, the error norms of the computed solution with respect to the exact solution are computed. We report the convergence rates in terms of $\mathbf{L}^2 - norm$ of velocity and pressure as well as $\mathbf{H}^1 - norm$ for velocity. The previous mesh figure(Fig.3.1) is designed in such a way that the coarser discretization is fully embedded in the refined discretization. The quadrilaterals are generated by bisecting the parents as mentioned above.

3.7.1.a Convergence Study for the Mesh $[0, 1] \times [0, 1]$

From the depicted tables (table(3.14) to table(3.19)) for the regular mesh either linear or nonlinear pressures, the theoretical prediction rates for the convergence are confirmed for the element type $\tilde{Q}_1 Q_0$. Surprisingly, the smoothness of the pressure field for $\tilde{Q}_1 Q_0$ is not defected and leaded to the velocity field is not satisfactory. Therefore, the non-smoothness of the velocity field for $\tilde{Q}_1 Q_0$ is not due the satisfactory or the failure of the LBB conditions but to the fact that we are using piecewise low degree polynomial in the element space. Consequently the highly nonlinear analytic velocity can not be produced efficiently even if we have good refinement. This case is a good striking case of the dependency of the approximation of velocity for the lower order finite element. To cure the piecewise lower order element, one should have the piecewise higher order approaches(quadratic approach at least). So the fields can be observed clearly from the depicted figures.
For $Q_2 P_1$ and $Q_2 P_1^{np}$, the velocity and pressure strike the optimal rates in the lower levels (third order convergence for the velocity and second order for pressure) until they reach fixed values without gaining due to the refinement. This means that the higher order elements hit the solution faster. The depicted tables (3.14 to 3.19) exhibit for $\tilde{Q}_1 Q_0$ that the optimal rates are not obtained at all for the velocity field which has more degradation due to the heterogeneity for the discretization. but the pressure still has the correct rate of convergence. While the mapped pressure approach has a big degradation due to the heterogeneity for the discretization.
The behavior is pretty similar to the low order finite element for the computed pressure. For unmapped approach the convergence is slightly achieved (third order in $\mathbf{L}^2$ and second order in $\mathbf{H}^1$ for the gradient and the pressure), therefore, the convergence rates for the velocity and pressure fields are still preserved in the norms considered for the unmapped approach.

3.7.1.b Convergence Study for the Mesh $[-0.5, 0.5] \times [-0.5, 0.5]$

In this case the behavior is quite different for the $\tilde{Q}_1 Q_0$, the velocity and pressure for linear and nonlinear pressure converge with the correct rate(second order in $\mathbf{L}^2$ and first order in $\mathbf{H}^2$ for the gradient and the

pressure). This indicates that, the choosing of the domain can recover the optimal accuracy. The same case for the Q_2P_1 and $Q_2P_1^{np}$, they reach the optimal accuracy at lower level till the fixed value at the high levels (see table(3.20) to table(3.25)). In this case the behavior is slightly different for the $\tilde{Q}_1Q_0$, the velocity and pressure for linear and nonlinear pressure converge approximately with the correct rate(second order in $\mathbf{L}^2$ and first order in $\mathbf{H}^1$ for the gradient and the pressure). The same case for the Q_2P_1 and $Q_2P_1^{np}$, they can be close to reach the optimal accuracy at certain level with decreasing till a fixed value at the high levels.

Mesh	*uniform*			*perturbed*		
Error	$\|\boldsymbol{u}-\boldsymbol{u}_h\|_{\mathbf{L}^2}$	$\|p-p_h\|_{\mathbf{L}^2}$	$\|\boldsymbol{u}-\boldsymbol{u}_h\|_{\mathbf{H}^1}$	$\|\boldsymbol{u}-\boldsymbol{u}_h\|_{\mathbf{L}^2}$	$\|p-p_h\|_{\mathbf{L}^2}$	$\|\boldsymbol{u}-\boldsymbol{u}_h\|_{\mathbf{H}^1}$
2×2	4.219048E-2	2.052816E-1	3.224218E-1	4.048540E-2	2.155475E-1	2.894239E-1
4×4	2.299276E-2(1.834)	1.027423E-1(1.998)	2.949801E-1(1.093)	2.709358E-2(1.494)	1.084055E-1(1.988)	3.108173E-1(0.931)
8×8	1.481327E-2(1.552)	5.125953E-2(2.004)	2.712463E-1(1.087)	1.713110E-2(1.581)	5.538471E-2(1.957)	2.994057E-1(1.038)
16×16	8.657031E-3(1.711)	2.556687E-2(2.004)	2.375312E-1(1.141)	1.035676E-2(1.654)	2.730731E-2(2.028)	2.636345E-1(1.135)
32×32	4.685417E-3(1.847)	1.276827E-2(2.002)	2.022294E-1(1.174)	5.478806E-3(1.890)	1.372112E-2(1.990)	2.260173E-1(1.166)
64×64	3.130938E-3(1.496)	6.380957E-3(2.001)	1.693431E-1(1.194)	3.546178E-3(1.545)	6.875347E-3(1.995)	1.881341E-1(1.201)
128×128	2.224867E-3(1.407)	3.189865E-3(2.000)	1.352285E-1(1.252)	2.465239E-3(1.438)	3.431394E-3(2.003)	1.492027E-1(1.260)
256×256	1.393330E-3(1.596)	1.594831E-3(2.000)	1.002032E-1(1.349)	1.582393E-3(1.557)	1.719526E-3(1.995)	1.115807E-1(1.337)

Table 3.14. *Shear thickening fluid:* $\mathbf{L}^2/\mathbf{H}^1$ errors for $\tilde{Q}_1Q_0$ using grid $[0,1]\times[0,1]$ for the linear pressure form.

Mesh	*uniform*			*perturbed*		
Error	$\|\boldsymbol{u}-\boldsymbol{u}_h\|_{\mathbf{L}^2}$	$\|p-p_h\|_{\mathbf{L}^2}$	$\|\boldsymbol{u}-\boldsymbol{u}_h\|_{\mathbf{H}^1}$	$\|\boldsymbol{u}-\boldsymbol{u}_h\|_{\mathbf{L}^2}$	$\|p-p_h\|_{\mathbf{L}^2}$	$\|\boldsymbol{u}-\boldsymbol{u}_h\|_{\mathbf{H}^1}$
2×2	1.224684E-3	1.851241E-5	1.794888E-2	3.577792E-2	1.775501E-2	4.511530E-1
4×4	1.706693E-4(7.175)	4.573132E-6(4.048)	4.511921E-3(3.978)	1.563589E-2(2.288)	9.575561E-3(1.854)	3.393578E-1(1.329)
8×8	3.589985E-5(4.754)	3.593126E-6(1.272)	1.200571E-3(3.758)	6.326278E-3(2.471)	4.500161E-3(2.127)	2.221751E-1(1.527)
16×16	2.928240E-5(1.226)	3.568502E-6(1.006)	5.246150E-4(2.288)	3.284858E-3(1.925)	2.441894E-3(1.842)	1.586839E-1(1.400)
32×32	2.918497E-5(1.003)	3.566626E-6(1.000)	4.502988E-4(1.165)	1.671275E-3(1.965)	1.260223E-3(1.937)	1.077327E-1(1.472)
64×64	2.918463E-5(1.000)	3.566489E-6(1.000)	4.452520E-4(1.011)	7.029883E-4(2.377)	6.172812E-4(2.041)	6.492267E-2(1.659)
128×128	2.918470E-5(1.000)	3.566485E-6(1.000)	4.449348E-4(1.000)	2.538549E-4(2.769)	3.153460E-4(1.957)	3.752876E-2(1.729)
256×256	2.918470E-5(1.000)	3.566479E-6(1.000)	4.449150E-4(1.000)	7.564985E-5(3.355)	1.559089E-4(2.022)	1.965586E-2(1.909)

Table 3.15. *Shear thickening fluid:* $\mathbf{L}^2/\mathbf{H}^1$ errors for Q_2P_1 using grid $[0,1]\times[0,1]$ for the linear pressure form.

Mesh	*uniform*			*perturbed*		
Error	$\|\boldsymbol{u}-\boldsymbol{u}_h\|_{\mathbf{L}^2}$	$\|p-p_h\|_{\mathbf{L}^2}$	$\|\boldsymbol{u}-\boldsymbol{u}_h\|_{\mathbf{H}^1}$	$\|\boldsymbol{u}-\boldsymbol{u}_h\|_{\mathbf{L}^2}$	$\|p-p_h\|_{\mathbf{L}^2}$	$\|\boldsymbol{u}-\boldsymbol{u}_h\|_{\mathbf{H}^1}$
2×2	1.224684E-3	1.851241E-5	1.794888E-2	1.509017E-3	2.639337E-5	2.015292E-2
4×4	1.706693E-4(7.175)	4.573132E-6(4.048)	4.511921E-3(3.978)	2.367002E-4(6.375)	7.208724E-6(3.661)	5.692891E-3(3.540)
8×8	3.589985E-5(4.754)	3.593126E-6(1.272)	1.200571E-3(3.758)	4.623754E-5(5.119)	3.848838E-6(1.873)	1.686182E-3(3.376)
16×16	2.928240E-5(1.226)	3.568502E-6(1.006)	5.246150E-4(2.288)	2.955779E-5(1.564)	3.582180E-6(1.074)	6.059601E-4(2.782)
32×32	2.918497E-5(1.003)	3.566626E-6(1.000)	4.502988E-4(1.165)	2.918806E-5(1.012)	3.567617E-6(1.004)	4.574280E-4(1.324)
64×64	2.918463E-5(1.000)	3.566489E-6(1.000)	4.452520E-4(1.011)	2.918452E-5(1.000)	3.566552E-6(1.000)	4.457345E-4(1.026)
128×128	2.918470E-5(1.000)	3.566485E-6(1.000)	4.449348E-4(1.000)	2.918482E-5(1.000)	3.566492E-6(1.000)	4.449680E-4(1.001)
256×256	2.918470E-5(1.000)	3.566479E-6(1.000)	4.449150E-4(1.000)	2.918494E-5(1.000)	3.566504E-6(1.000)	4.449206E-4(1.000)

Table 3.16. *Shear thickening fluid:* $\mathbf{L}^2/\mathbf{H}^1$ errors for $Q_2P_1^{np}$ using grid $[0,1]\times[0,1]$ for the linear pressure form.

3.7.2 Shear Thinning Fluids

This section presents a second numerical test for a nonlinear problem which is the shear thinning model, the general viscosity model is Carreau-Yasuda model (see [152])

$$\nu(\|\mathbf{D}\|) = \nu_\infty + (\nu_0 - \nu_\infty)(1 + (\lambda\|\mathbf{D}\|)^a)^{\frac{n-1}{a}} \tag{3.57}$$

Mesh	*uniform*			*perturbed*		
Error	$\|\boldsymbol{u}-\boldsymbol{u}_h\|_{\mathbf{L}^2}$	$\|p-p_h\|_{\mathbf{L}^2}$	$\|\boldsymbol{u}-\boldsymbol{u}_h\|_{\mathbf{H}^1}$	$\|\boldsymbol{u}-\boldsymbol{u}_h\|_{\mathbf{L}^2}$	$\|p-p_h\|_{\mathbf{L}^2}$	$\|\boldsymbol{u}-\boldsymbol{u}_h\|_{\mathbf{H}^1}$
2×2	7.677587E-3	3.341986E-1	5.665520E-2	9.529417E-3	3.407661E-1	7.097276E-2
4×4	3.345657E-2(0.229)	1.612354E-1(2.072)	4.380626E-1(0.129)	3.121882E-2(0.305)	1.621355E-1(2.101)	3.992272E-1(0.177)
8×8	2.134043E-2(1.567)	8.031864E-2(2.007)	4.050834E-1(1.081)	2.645783E-2(1.179)	8.829100E-2(1.836)	4.372316E-1(0.913)
16×16	1.244279E-2(1.715)	4.010926E-2(2.002)	3.485314E-1(1.162)	1.401119E-2(1.888)	4.356590E-2(2.026)	3.881040E-1(1.126)
32×32	6.802165E-3(1.829)	2.004581E-2(2.000)	2.890950E-1(1.205)	7.648159E-3(1.832)	2.190476E-2(1.988)	3.228874E-1(1.202)
64×64	4.748038E-3(1.432)	1.002125E-2(2.000)	2.375229E-1(1.217)	5.080083E-3(1.505)	1.095770E-2(1.999)	2.613667E-1(1.235)
128×128	3.704156E-3(1.281)	5.010253E-3(2.000)	1.884985E-1(1.260)	3.920987E-3(1.295)	5.472493E-3(2.002)	2.062353E-1(1.267)
256×256	2.671301E-3(1.386)	2.505061E-3(2.000)	1.413343E-1(1.333)	2.883080E-3(1.360)	2.740822E-3(1.996)	1.556708E-1(1.324)

Table 3.17. *Shear thickening fluid:* $\mathbf{L}^2/\mathbf{H}^1$ errors for $\tilde{Q}_1Q_0$ using grid $[0,1]\times[0,1]$ for the nonlinear pressure form.

Mesh	*uniform*			*perturbed*		
Error	$\|\boldsymbol{u}-\boldsymbol{u}_h\|_{\mathbf{L}^2}$	$\|p-p_h\|_{\mathbf{L}^2}$	$\|\boldsymbol{u}-\boldsymbol{u}_h\|_{\mathbf{H}^1}$	$\|\boldsymbol{u}-\boldsymbol{u}_h\|_{\mathbf{L}^2}$	$\|p-p_h\|_{\mathbf{L}^2}$	$\|\boldsymbol{u}-\boldsymbol{u}_h\|_{\mathbf{H}^1}$
2×2	1.224684E-3	1.124559E-1	1.794888E-2	3.213227E-2	1.167934E-1	3.949699E-1
4×4	1.108349E-2(0.110)	2.981793E-2(3.771)	3.230460E-1(0.055)	1.985790E-2(1.618)	3.345887E-2(3.490)	4.560332E-1(0.866)
8×8	2.699746E-3(4.105)	7.574675E-3(3.936)	1.327492E-1(2.433)	9.663020E-3(2.055)	1.210625E-2(2.763)	3.389713E-1(1.345)
16×16	2.822447E-4(9.565)	1.900929E-3(3.984)	3.222802E-2(4.119)	4.443207E-3(2.174)	4.745196E-3(2.551)	2.170602E-1(1.561)
32×32	3.230673E-5(8.736)	4.752494E-4(3.999)	4.465922E-3(7.216)	2.886712E-3(1.539)	2.263101E-3(2.096)	1.521708E-1(1.426)
64×64	2.920655E-5(1.106)	1.188518E-4(3.998)	7.204508E-4(6.198)	1.540700E-3(1.873)	1.079235E-3(2.096)	9.531949E-2(1.596)
128×128	2.918558E-5(1.000)	2.991205E-5(3.973)	4.506319E-4(1.598)	7.057695E-4(2.183)	5.476379E-4(1.970)	5.858414E-2(1.627)
256×256	2.918476E-5(1.000)	8.236780E-6(3.631)	4.450057E-4(1.012)	2.410625E-4(2.927)	2.725206E-4(2.009)	3.247077E-2(1.804)

Table 3.18. *Shear thickening fluid:* $\mathbf{L}^2/\mathbf{H}^1$ errors for Q_2P_1 using grid $[0,1]\times[0,1]$ for the nonlinear pressure form.

Mesh	*uniform*			*perturbed*		
Error	$\|\boldsymbol{u}-\boldsymbol{u}_h\|_{\mathbf{L}^2}$	$\|p-p_h\|_{\mathbf{L}^2}$	$\|\boldsymbol{u}-\boldsymbol{u}_h\|_{\mathbf{H}^1}$	$\|\boldsymbol{u}-\boldsymbol{u}_h\|_{\mathbf{L}^2}$	$\|p-p_h\|_{\mathbf{L}^2}$	$\|\boldsymbol{u}-\boldsymbol{u}_h\|_{\mathbf{H}^1}$
2×2	1.224684E-3	1.124559E-1	1.794888E-2	3.750400E-2	1.199832E-1	4.909743E-1
4×4	1.108349E-2(0.110)	2.981793E-2(3.771)	3.230460E-1(0.055)	1.632918E-2(2.296)	3.078636E-2(3.897)	3.859593E-1(1.272)
8×8	2.699746E-3(4.105)	7.574675E-3(3.936)	1.327492E-1(2.433)	5.304645E-3(3.078)	9.223627E-3(3.337)	2.173315E-1(1.775)
16×16	2.822447E-4(9.565)	1.900929E-3(3.984)	3.222802E-2(4.119)	1.253957E-3(4.230)	2.290831E-3(4.026)	9.498057E-2(2.288)
32×32	3.230673E-5(8.736)	4.752494E-4(3.999)	4.465922E-3(7.216)	2.043286E-4(6.137)	5.788084E-4(3.957)	3.267210E-2(2.907)
64×64	2.920655E-5(1.061)	1.188518E-4(3.998)	7.204508E-4(6.198)	3.772576E-5(5.416)	1.464162E-4(3.953)	9.185434E-3(3.556)
128×128	2.918558E-5(1.000)	2.991205E-5(3.973)	4.506319E-4(1.598)	2.929676E-5(1.287)	3.693490E-5(3.964)	2.348744E-3(3.910)
256×256	2.918476E-5(1.000)	8.236780E-6(3.631)	4.450057E-4(1.012)	2.918518E-5(1.003)	9.888793E-6(3.735)	7.329799E-4(3.204)

Table 3.19. *Shear thickening fluid:* $\mathbf{L}^2/\mathbf{H}^1$ errors for $Q_2P_1^{np}$ using grid $[0,1]\times[0,1]$ for the nonlinear pressure form.

Mesh	*uniform*			*perturbed*		
Error	$\|\boldsymbol{u}-\boldsymbol{u}_h\|_{\mathbf{L}^2}$	$\|p-p_h\|_{\mathbf{L}^2}$	$\|\boldsymbol{u}-\boldsymbol{u}_h\|_{\mathbf{H}^1}$	$\|\boldsymbol{u}-\boldsymbol{u}_h\|_{\mathbf{L}^2}$	$\|p-p_h\|_{\mathbf{L}^2}$	$\|\boldsymbol{u}-\boldsymbol{u}_h\|_{\mathbf{H}^1}$
2×2	1.127000E00	2.058629E-1	9.812302E00	1.127973E00	2.161057E-1()	9.798628E00
4×4	5.562785E-1(2.026)	2.359357E-1(0.872)	7.064762E00(1.388)	5.658529E-1(1.993)	2.674606E-1(0.808)	7.084801E00(1.383)
8×8	1.580610E-1(3.519)	8.961723E-2(2.632)	3.953628E00(1.786)	1.658353E-1(3.412)	1.050227E-1(2.546)	3.951880E00(1.792)
16×16	3.988200E-2(3.963)	3.196093E-2(2.804)	2.022337E00(1.955)	4.611249E-2(3.596)	3.414614E-2(3.075)	2.126654E00(1.858)
32×32	9.561379E-3(4.171)	1.351518E-2(2.364)	1.026317E00(1.970)	1.113975E-2(4.139)	1.582989E-2(2.157)	1.073144E00(1.981)
64×64	2.371198E-3(4.032)	6.462900E-3(2.091)	5.234604E-1(1.960)	2.930046E-3(3.801)	7.713070E-3(2.052)	5.634859E-1(1.904)
128×128	6.655729E-4(3.562)	3.199288E-3(2.020)	2.671875E-1(1.959)	8.386502E-4(3.493)	3.918746E-3(1.968)	2.941280E-1(1.915)
256×256	2.201485E-4(3.023)	1.595885E-3(2.004)	1.362393E-1(1.961)	2.806098E-4(2.988)	2.032937E-3(1.927)	1.565661E-1(1.878)

Table 3.20. *Shear thickening fluid:* $\mathbf{L}^2/\mathbf{H}^1$ errors for $\tilde{Q}_1Q_0$ using grid $[-0.5,0.5]\times[-0.5,0.5]$ for the linear pressure form.

with the associated parameters in the table(3.26) (see Fig.3.5):

The assumed exact solution for this problem is

$$\boldsymbol{u} = [ye^{5(x^2+y^2)}, -xe^{5(x^2+y^2)}], \tag{3.58a}$$

$$p(linear) = x + y - 1, \tag{3.58b}$$

$$p(nonlinear) = e^{(\frac{5}{4})}sin(2\pi x)sin(2\pi y). \tag{3.58c}$$

Mesh	*uniform*			*perturbed*		
Error	$\|\boldsymbol{u}-\boldsymbol{u}_h\|_{\mathbf{L}^2}$	$\|p-p_h\|_{\mathbf{L}^2}$	$\|\boldsymbol{u}-\boldsymbol{u}_h\|_{\mathbf{H}^1}$	$\|\boldsymbol{u}-\boldsymbol{u}_h\|_{\mathbf{L}^2}$	$\|p-p_h\|_{\mathbf{L}^2}$	$\|\boldsymbol{u}-\boldsymbol{u}_h\|_{\mathbf{H}^1}$
2×2	3.028911E-1	2.709032E-2	3.765881E00	3.074762E-1	3.709076E-2	3.812097E00
4×4	5.703167E-2(5.310)	7.426581E-3(3.647)	1.421301E00(2.649)	6.067049E-2(5.068)	1.569015E-2(2.364)	1.482532E00(2.571)
8×8	8.195207E-3(6.959)	1.384663E-3(5.363)	4.169822E-1(3.408)	9.406437E-3(6.449)	6.291658E-3(2.493)	4.542570E-1(3.263)
16×16	1.065734E-3(7.689)	1.846183E-4(7.500)	1.096497E-1(3.802)	1.631403E-3(5.765)	2.554704E-3(2.462)	1.462646E-1(3.105)
32×32	1.390451E-4(7.664)	2.289237E-5(8.064)	2.778806E-2(3.945)	3.124466E-4(5.221)	1.299105E-3(1.966)	4.793407E-2(3.051)
64×64	3.638625E-5(3.821)	8.142887E-6(2.811)	6.975351E-3(3.983)	9.266392E-5(3.371)	6.209770E-4(2.092)	2.157874E-2(2.221)
128×128	3.884357E-5(0.936)	7.668933E-6(1.061)	1.769000E-3(3.943)	3.963024E-5(2.338)	3.159892E-4(1.965)	1.088808E-2(1.981)
256×256	3.876910E-5(1.001)	7.662125E-6(1.000)	5.265376E-4(3.359)	3.144561E-5(1.260)	1.558516E-4(2.027)	5.416256E-3(2.010)

Table 3.21. *Shear thickening fluid:* $\mathbf{L}^2/\mathbf{H}^1$ errors for Q_2P_1 using grid $[-0.5,0.5]\times[-0.5,0.5]$ for the linear pressure form.

Mesh	*uniform*			*perturbed*		
Error	$\|\boldsymbol{u}-\boldsymbol{u}_h\|_{\mathbf{L}^2}$	$\|p-p_h\|_{\mathbf{L}^2}$	$\|\boldsymbol{u}-\boldsymbol{u}_h\|_{\mathbf{H}^1}$	$\|\boldsymbol{u}-\boldsymbol{u}_h\|_{\mathbf{L}^2}$	$\|p-p_h\|_{\mathbf{L}^2}$	$\|\boldsymbol{u}-\boldsymbol{u}_h\|_{\mathbf{H}^1}$
2×2	3.028911E-1	2.709032E-2	3.765881E00	3.072315E-1	3.196685E-2	3.808123E00
4×4	5.703167E-2(5.310)	7.426581E-3(3.647)	1.421301E00(2.649)	6.037675E-2(5.088)	1.223682E-2(2.612)	1.475567E00(2.580)
8×8	8.195207E-3(6.959)	1.384663E-3(5.363)	4.169822E-1(3.408)	9.066591E-3(6.659)	4.306091E-3(2.841)	4.435264E-1(3.326)
16×16	1.065734E-3(7.689)	1.846183E-4(7.500)	1.096497E-1(3.802)	1.445031E-3(6.273)	1.175192E-3(3.664)	1.359668E-1(3.262)
32×32	1.390451E-4(7.664)	2.289237E-5(8.064)	2.778806E-2(3.945)	1.983293E-4(7.286)	3.202205E-4(3.669)	3.601689E-2(3.775)
64×64	3.638625E-5(3.821)	8.142887E-6(2.811)	6.975351E-3(3.983)	4.252646E-5(4.663)	9.062294E-5(3.533)	9.988672E-3(3.605)
128×128	3.884357E-5(0.936)	7.668933E-6(1.061)	1.769000E-3(3.943)	3.220491E-5(1.320)	2.494162E-5(3.633)	2.493791E-3(4.005)
256×256	3.876910E-5(1.001)	7.662125E-6(1.000)	5.265376E-4(3.359)	3.196239E-5(1.007)	9.834791E-6(2.536)	6.823067E-4(3.654)

Table 3.22. *Shear thickening fluid:* $\mathbf{L}^2/\mathbf{H}^1$ errors for $Q_2P_1^{np}$ using grid $[-0.5,0.5]\times[-0.5,0.5]$ for the linear pressure form.

Mesh	*uniform*			*perturbed*		
Error	$\|\boldsymbol{u}-\boldsymbol{u}_h\|_{\mathbf{L}^2}$	$\|p-p_h\|_{\mathbf{L}^2}$	$\|\boldsymbol{u}-\boldsymbol{u}_h\|_{\mathbf{H}^1}$	$\|\boldsymbol{u}-\boldsymbol{u}_h\|_{\mathbf{L}^2}$	$\|p-p_h\|_{\mathbf{L}^2}$	$\|\boldsymbol{u}-\boldsymbol{u}_h\|_{\mathbf{H}^1}$
2×2	1.126233E00	8.456539E-2	9.807468E00	1.128943E00	4.401035E-1	9.806843E00
4×4	5.934944E-1(1.897)	1.052475E00(0.080)	7.643182E00(1.283)	6.062912E-1(1.862)	1.068256E00(0.412)	7.601098E00(1.290)
8×8	1.725199E-1(3.440)	5.549636E-1(1.896)	4.455073E00(1.715)	1.924455E-1(3.150)	5.849565E-1(1.826)	4.529656E00(1.678)
16×16	4.927649E-2(3.501)	2.792549E-1(1.987)	2.500120E00(1.781)	6.059577E-2(3.175)	3.023941E-1(1.934)	2.691389E00(1.683)
32×32	1.900817E-2(2.592)	1.398117E-1(1.997)	1.444771E00(1.730)	2.254045E-2(2.688)	1.516450E-1(1.994)	1.574750E00(1.709)
64×64	1.097944E-2(1.731)	6.994054E-2(1.999)	8.471429E-1(1.705)	1.228698E-2(1.834)	7.653341E-2(1.981)	9.546765E-1(1.649)
128×128	3.855058E-3(2.848)	3.497704E-2(1.999)	3.639995E-1(2.327)	7.585680E-3(1.619)	3.825868E-2(2.000)	5.738722E-1(1.663)
256×256	2.634139E-3(1.463)	1.748705E-2(2.000)	2.253046E-1(1.615)	4.640394E-3(1.634)	1.918771E-2(1.993)	3.480513E-1(1.648)

Table 3.23. *Shear thickening fluid:* $\mathbf{L}^2/\mathbf{H}^1$ errors for $\tilde{Q}_1Q_0$ using grid $[-0.5,0.5]\times[-0.5,0.5]$ for the nonlinear pressure form.

Mesh	*uniform*			*perturbed*		
Error	$\|\boldsymbol{u}-\boldsymbol{u}_h\|_{\mathbf{L}^2}$	$\|p-p_h\|_{\mathbf{L}^2}$	$\|\boldsymbol{u}-\boldsymbol{u}_h\|_{\mathbf{H}^1}$	$\|\boldsymbol{u}-\boldsymbol{u}_h\|_{\mathbf{L}^2}$	$\|p-p_h\|_{\mathbf{L}^2}$	$\|\boldsymbol{u}-\boldsymbol{u}_h\|_{\mathbf{H}^1}$
2×2	3.028911E-1	1.126912E00	3.765881E00	3.467055E-1	1.164378E00	4.383107E00
4×4	1.226551E-1(2.469)	4.026565E-1(2.798)	3.141302E00(1.198)	1.313512E-1(2.639)	4.486721E-1(2.595)	3.261454E00(1.343)
8×8	1.492679E-2(8.217)	1.058347E-1(3.804)	7.740977E-1(4.058)	2.785755E-2(4.715)	1.354598E-1(3.312)	1.124682E00(2.899)
16×16	2.235368E-3(6.677)	2.658077E-2(3.981)	1.768355E-1(4.377)	8.898176E-3(3.130)	4.221095E-2(3.209)	4.696541E-1(2.394)
32×32	2.021613E-4(11.057)	6.638839E-3(4.003)	3.789254E-2(4.666)	3.947928E-3(2.253)	1.692642E-2(2.493)	2.490476E-1(1.885)
64×64	3.645322E-5(5.545)	1.658859E-3(4.002)	7.811256E-3(4.851)	2.183041E-3(1.808)	7.725846E-3(2.190)	1.462436E-1(1.703)
128×128	3.204765E-5(1.137)	4.147233E-4(3.999)	1.817062E-3(4.298)	9.823395E-4(2.222)	3.859650E-3(2.001)	8.409539E-2(1.739)
256×256	3.196778E-5(1.002)	1.039523E-4(3.989)	5.065288E-4(3.587)	3.913598E-4(2.510)	1.906204E-3(2.024)	4.700716E-2(1.789)

Table 3.24. *Shear thickening fluid:* $\mathbf{L}^2/\mathbf{H}^1$ errors for Q_2P_1 using grid $[-0.5,0.5]\times[-0.5,0.5]$ for the nonlinear pressure form.

Similarly with the previous shear thickening case; the nonlinear iteration and the linear iteration run until numerical convergence is attained to 10^{-8} and 10^{-5} respectively. Once the converged solution is attained, the error norms of the computed solution with respect to the exact solution are computed. It is reported the convergence rates in terms of $\mathbf{L}^2-norm$ of velocity and pressure as well as $\mathbf{H}^1-norm$ for velocity. The previous figures are designed in such a way that the coarser discretization is fully embedded in the refined discretization. The significant difference between this case and the previous one is only in

Mesh	*uniform*			*perturbed*		
Error	$\|\boldsymbol{u}-\boldsymbol{u}_h\|_{\mathbf{L}^2}$	$\|p-p_h\|_{\mathbf{L}^2}$	$\|\boldsymbol{u}-\boldsymbol{u}_h\|_{\mathbf{H}^1}$	$\|\boldsymbol{u}-\boldsymbol{u}_h\|_{\mathbf{L}^2}$	$\|p-p_h\|_{\mathbf{L}^2}$	$\|\boldsymbol{u}-\boldsymbol{u}_h\|_{\mathbf{H}^1}$
2×2	3.028911E-1	1.126912E00	3.765881E00	3.492358E-1	1.167038E00	4.409872E00
4×4	1.226551E-1(2.469)	4.026565E-1(2.798)	3.141302E00(1.198)	1.199745E-1(2.910)	4.379501E-1(2.664)	3.085155E00(1.429)
8×8	1.492679E-2(8.217)	1.058347E-1(3.804)	7.740977E-1(4.058)	1.986140E-2(6.040)	1.248091E-1(3.509)	9.123804E-1(3.381)
16×16	2.235368E-3(6.677)	2.658077E-2(3.981)	1.768355E-1(4.377)	4.029412E-3(4.929)	3.207268E-2(3.891)	2.832551E-1(3.221)
32×32	2.021613E-4(11.057)	6.638839E-3(4.003)	3.789254E-2(4.666)	9.079869E-4(4.437)	8.172465E-3(3.924)	9.532576E-2(2.971)
64×64	2.021613E-4(5.545)	6.638839E-3(4.002)	3.789254E-2(4.851)	1.976861E-4(4.593)	2.050573E-3(3.985)	3.445892E-2(3.445)
128×128	3.204765E-5(1.137)	4.147233E-4(3.999)	1.817062E-3(4.298)	3.818839E-5(5.176)	5.142597E-4(3.987)	1.071474E-2(3.216)
256×256	3.196778E-5(1.002)	1.039523E-4(3.989)	5.065288E-4(3.587)	3.194857E-5(1.195)	1.290264E-4(3.985)	2.871199E-3(3.731)

Table 3.25. *Shear thickening fluid:* $\mathbf{L}^2/\mathbf{H}^1$ errors for $Q_2P_1^{np}$ using grid $[-0.5,0.5]\times[-0.5,0.5]$ for the nonlinear pressure form.

fluid type	ν_0	ν_∞	λ	n	a
Shear Thinning	0.056	0.00345	1.902	0.22	2.

Table 3.26. *Shear Thinning parameters for Carreau-Yasuda model*

the value of the viscosity μ_∞ which has a corresponding bigger Reynolds number. Therefore, this invite us to observe the behavior of the different techniques.

3.7.2.a Convergence study for the Uniform Meshes $[0,1]\times[0,1]$ and $[-0.5,0.5]\times[-0.5,0.5]$

From the depicted table (see table(3.27) to table(3.38)), the theoretical prediction rates for the convergence are confirmed for all the considered element types. The smoothness of the pressure field for the nonlinear pressure is not a little bit defected and the velocity field is still satisfactory which has a significant difference from the corresponding shear thickening one.

3.7.2.b Convergence study for the Perturbed Meshes $[0,1]\times[0,1]$ and $[-0.5,0.5]\times[-0.5,0.5]$

The depicted tables exhibit that (see table(3.27) to table(3.38)) the optimal rates are obtained for the velocity field and pressure for $\tilde{Q}_1Q_0$. For The computed pressure in the mapped approach the convergence suboptimal due to the heterogeneity for the discretization for the mapped pressure approach. Generally, all fields are slightly different from the regular but better from the corresponding shear thickening. However, the full convergence for each field has the full dependence on the element space and the chosen domain dimensions.

Mesh	*uniform*			*perturbed*		
Error	$\|\boldsymbol{u}-\boldsymbol{u}_h\|_{\mathbf{L}^2}$	$\|p-p_h\|_{\mathbf{L}^2}$	$\|\boldsymbol{u}-\boldsymbol{u}_h\|_{\mathbf{H}^1}$	$\|\boldsymbol{u}-\boldsymbol{u}_h\|_{\mathbf{L}^2}$	$\|p-p_h\|_{\mathbf{L}^2}$	$\|\boldsymbol{u}-\boldsymbol{u}_h\|_{\mathbf{H}^1}$
2×2	3.660411E-2	2.058296E-1	2.800318E-1	3.568659E-2	2.160036E-1	2.550993E-1
4×4	1.683996E-2(2.173)	1.030322E-1(1.997)	2.273001E-1(1.232)	2.005220E-2(1.779)	1.084799E-1(1.991)	2.403147E-1(1.061)
8×8	6.847584E-3(2.459)	5.134153E-2(2.006)	1.712604E-1(1.327)	9.236605E-3(2.170)	5.530951E-2(1.961)	1.932904E-1(1.243)
16×16	2.353242E-3(2.909)	2.558913E-2(2.006)	1.189906E-1(1.439)	3.148886E-3(2.933)	2.728452E-2(2.027)	1.316026E-1(1.468)
32×32	7.201060E-4(3.267)	1.277249E-2(2.003)	7.577283E-2(1.570)	3.148886E-3(2.933)	2.728452E-2(2.027)	1.316026E-1(1.468)
64×64	2.044878E-4(3.521)	6.381483E-3(2.001)	4.433526E-2(1.709)	3.062602E-4(3.341)	6.877435E-3(1.993)	5.313147E-2(1.640)
128×128	5.517554E-5(3.706)	3.189861E-3(2.000)	2.430955E-2(1.823)	8.692871E-5(3.523)	3.436296E-3(2.001)	3.059206E-2(1.736)
256×256	1.453663E-5(3.795)	1.594786E-3(2.000)	1.278480E-2(1.901)	2.408379E-5(3.609)	1.724070E-3(1.993)	1.709404E-2(1.789)

Table 3.27. *Shear thinning fluid:* $\mathbf{L}^2/\mathbf{H}^1$ errors for $\tilde{Q}_1Q_0$ using grid $[0,1]\times[0,1]$ for the linear pressure form.

Mesh	*uniform*			*perturbed*		
Error	$\|\boldsymbol{u}-\boldsymbol{u}_h\|_{\mathbf{L}^2}$	$\|p-p_h\|_{\mathbf{L}^2}$	$\|\boldsymbol{u}-\boldsymbol{u}_h\|_{\mathbf{H}^1}$	$\|\boldsymbol{u}-\boldsymbol{u}_h\|_{\mathbf{L}^2}$	$\|p-p_h\|_{\mathbf{L}^2}$	$\|\boldsymbol{u}-\boldsymbol{u}_h\|_{\mathbf{H}^1}$
2×2	1.258166E-3	2.744039E-4	1.801935E-2	9.476571E-3	1.817644E-2	1.211233E-1
4×4	1.707305E-4(7.369)	3.131831E-5(8.761)	4.505915E-3(3.999)	3.370791E-3(2.811)	9.653114E-3(1.883)	7.668729E-2(1.579)
8×8	2.160649E-5(7.901)	4.447693E-6(7.041)	1.118515E-3(4.028)	8.860916E-4(3.804)	4.520504E-3(2.135)	3.812886E-2(2.011)
16×16	3.359417E-6(6.431)	3.506306E-6(1.268)	2.804128E-4(3.988)	2.316010E-4(3.825)	2.444594E-3(1.849)	2.064239E-2(1.847)
32×32	2.031401E-6(1.653)	3.504018E-6(1.000)	7.609246E-5(3.685)	5.995468E-5(3.862)	1.259907E-3(1.940)	1.075907E-2(1.918)
64×64	2.003028E-6(1.014)	3.504571E-6(1.000)	3.529141E-5(2.156)	1.453828E-5(4.123)	6.172692E-4(2.041)	5.248578E-3(2.049)
128×128	2.002540E-6(1.000)	3.504615E-6(1.000)	3.100938E-5(1.138)	4.229850E-6(3.837)	3.153404E-4(1.957)	2.694397E-3(1.948)
256×256	2.002530E-6(1.000)	3.504618E-6(1.000)	3.072197E-5(1.009)	2.201780E-6(1.921)	1.559002E-4(2.022)	1.331706E-3(2.023)

Table 3.28. *Shear thinning fluid:* $\mathbf{L}^2/\mathbf{H}^1$ errors for Q_2P_1 using grid $[0,1]\times[0,1]$ for the linear pressure form.

Mesh	*uniform*			*perturbed*		
Error	$\|\boldsymbol{u}-\boldsymbol{u}_h\|_{\mathbf{L}^2}$	$\|p-p_h\|_{\mathbf{L}^2}$	$\|\boldsymbol{u}-\boldsymbol{u}_h\|_{\mathbf{H}^1}$	$\|\boldsymbol{u}-\boldsymbol{u}_h\|_{\mathbf{L}^2}$	$\|p-p_h\|_{\mathbf{L}^2}$	$\|\boldsymbol{u}-\boldsymbol{u}_h\|_{\mathbf{H}^1}$
2×2	1.258166E-3	2.744039E-4	1.801935E-2	1.542540E-3	4.077450E-4	2.020888E-2
4×4	1.707305E-4(7.369)	3.131831E-5(8.761)	4.505915E-3(3.999)	2.387110E-4(6.462)	8.137110E-5(5.010)	5.695267E-3(3.548)
8×8	2.160649E-5(7.901)	4.447693E-6(7.041)	1.118515E-3(4.028)	3.640625E-5(6.556)	1.788502E-5(4.549)	1.627946E-3(3.498)
16×16	3.359417E-6(6.431)	3.506306E-6(1.268)	2.804128E-4(3.988)	4.982477E-6(7.306)	5.885423E-6(3.038)	4.124302E-4(3.947)
32×32	2.031401E-6(1.653)	3.504018E-6(1.000)	7.609246E-5(3.685)	2.090757E-6(2.383)	3.694814E-6(1.592)	1.108477E-4(3.720)
64×64	2.003028E-6(1.014)	3.504571E-6(1.000)	3.529141E-5(2.156)	2.004183E-6(1.043)	3.516654E-6(1.050)	4.095341E-5(2.706)
128×128	2.002540E-6(1.000)	3.504615E-6(1.000)	3.100938E-5(1.138)	2.002564E-6(1.000)	3.505485E-6(1.003)	3.145742E-5(1.301)
256×256	2.002530E-6(1.000)	3.504618E-6(1.000)	3.072197E-5(1.009)	2.002530E-6(1.000)	3.504672E-6(1.000)	3.075104E-5(1.023)

Table 3.29. *Shear thinning fluid:* $\mathbf{L}^2/\mathbf{H}^1$ errors for $Q_2P_1^{np}$ using grid $[0,1]\times[0,1]$ for the linear pressure form.

Mesh	*uniform*			*perturbed*		
Error	$\|\boldsymbol{u}-\boldsymbol{u}_h\|_{\mathbf{L}^2}$	$\|p-p_h\|_{\mathbf{L}^2}$	$\|\boldsymbol{u}-\boldsymbol{u}_h\|_{\mathbf{H}^1}$	$\|\boldsymbol{u}-\boldsymbol{u}_h\|_{\mathbf{L}^2}$	$\|p-p_h\|_{\mathbf{L}^2}$	$\|\boldsymbol{u}-\boldsymbol{u}_h\|_{\mathbf{H}^1}$
2×2	6.961924E-3	3.341986E-1	5.308481E-2	8.385142E-3	3.408259E-1	6.331576E-2
4×4	2.612691E-2(0.266)	1.632764E-1(2.046)	3.490769E-1(0.152)	2.504202E-2(0.3348)	1.638412E-1(2.080)	3.221615E-1(0.196)
8×8	1.223370E-2(2.135)	8.099437E-2(2.015)	2.770167E-1(1.260)	1.563196E-2(1.602)	8.876493E-2(1.845)	2.993263E-1(1.076)
16×16	4.386935E-3(2.788)	4.027281E-2(2.011)	1.915539E-1(1.446)	5.861890E-3(2.666)	4.370184E-2(2.031)	2.196354E-1(1.362)
32×32	1.329222E-3(3.300)	2.007477E-3(20.061)	1.205056E-1(1.589)	1.885315E-3(3.109)	2.192393E-2(1.993)	1.416017E-1(1.551)
64×64	3.724068E-4(3.569)	1.002533E-3(2.002)	6.999857E-2(1.721)	5.446038E-4(3.461)	1.096350E-2(1.999)	8.447275E-2(1.676)
128×128	9.970667E-5(3.735)	5.010719E-3(0.2001)	3.826279E-2(1.721)	1.517460E-4(3.588)	5.479547E-3(2.000)	4.807524E-2(1.757)
256×256	2.601547E-5(3.832)	2.505081E-3(2.000)	2.010233E-2(1.903)	4.117638E-5(3.685)	2.746580E-3(1.995)	2.651472E-2(1.813)

Table 3.30. *Shear thinning fluid:* $\mathbf{L}^2/\mathbf{H}^1$ errors for $\tilde{Q}_1Q_0$ using grid $[0,1]\times[0,1]$ for the nonlinear pressure form.

Mesh	*uniform*			*perturbed*		
Error	$\|\boldsymbol{u}-\boldsymbol{u}_h\|_{\mathbf{L}^2}$	$\|p-p_h\|_{\mathbf{L}^2}$	$\|\boldsymbol{u}-\boldsymbol{u}_h\|_{\mathbf{H}^1}$	$\|\boldsymbol{u}-\boldsymbol{u}_h\|_{\mathbf{L}^2}$	$\|p-p_h\|_{\mathbf{L}^2}$	$\|\boldsymbol{u}-\boldsymbol{u}_h\|_{\mathbf{H}^1}$
2×2	1.258166E-3	1.124564E-1	1.801935E-2	7.793640E-3	1.168958E-1	9.616319E-2
4×4	3.034570E-3(0.414)	2.999855E-2(3.748)	9.644552E-2(0.186)	5.583831E-3(1.395)	3.372479E-2(3.466)	1.375215E-1(0.699)
8×8	2.135587E-4(14.209)	7.594819E-3(3.949)	1.615167E-2(5.971)	1.859474E-3(3.002)	1.212378E-2(2.781)	8.014855E-2(1.715)
16×16	1.451141E-5(14.716)	1.901183E-3(3.994)	2.286127E-3(7.065)	4.082743E-4(4.554)	4.748103E-3(2.553)	3.670352E-2(2.183)
32×32	2.207293E-6(6.574)	4.752498E-4(4.000)	3.072600E-4(7.440)	1.036735E-4(3.938)	2.262239E-3(2.098)	1.881628E-2(1.950)
64×64	2.002528E-6(1.102)	1.188502E-4(3.998)	5.186327E-5(5.924)	2.533190E-5(4.092)	1.078941E-3(2.096)	9.137949E-3(2.059)
128×128	2.002460E-6(1.000)	2.990480E-5(3.974)	3.137756E-5(1.652)	6.778333E-6(3.737)	5.474313E-4(1.970)	4.677222E-3(1.953)
256×256	2.002525E-6(1.000)	8.210198E-6(3.642)	3.072782E-5(1.021)	2.568976E-6(2.638)	2.724600E-4(2.009)	2.330456E-3(2.007)

Table 3.31. *Shear thinning fluid:* $\mathbf{L}^2/\mathbf{H}^1$ errors for Q_2P_1 using grid $[0,1]\times[0,1]$ for the nonlinear pressure form.

3.7.3 Bingham Viscoplastic Fluids

Finally, we consider the flow of viscoplastic fluid in channel which has a special treatment to measure the behavior of velocity and pressure with respect to the following exact solution which depends on the linearization of the pressure over the whole domain (see [3, 27, 36, 53, 63, 99, 104, 164, 195, 205]).

$$\boldsymbol{u} = (u, 0),\ p = -x + c, \tag{3.59}$$

where

Mesh	*uniform*			*perturbed*		
Error	$\|\boldsymbol{u}-\boldsymbol{u}_h\|_{\mathbf{L}^2}$	$\|p-p_h\|_{\mathbf{L}^2}$	$\|\boldsymbol{u}-\boldsymbol{u}_h\|_{\mathbf{H}^1}$	$\|\boldsymbol{u}-\boldsymbol{u}_h\|_{\mathbf{L}^2}$	$\|p-p_h\|_{\mathbf{L}^2}$	$\|\boldsymbol{u}-\boldsymbol{u}_h\|_{\mathbf{H}^1}$
2×2	1.258166E-3	1.124564E-1	1.801935E-2	1.131722E-2	1.202099E-1	1.506312E-1
4×4	3.034570E-3(0.4146)	2.999855E-2(3.748)	9.644552E-2(0.186)	4.420422E-3(2.5602)	3.099121E-2(3.878)	1.139420E-1(1.322)
8×8	2.135587E-4(14.209)	7.594819E-3(3.949)	1.615167E-2(5.971)	7.941099E-4(5.5665)	9.244050E-3(3.352)	4.111526E-2(2.771)
16×16	1.451141E-5(14.716)	1.901183e-3(3.994)	2.286127e-3(7.065)	8.709524E-5(9.117)	2.293121E-3(4.031)	9.379934E-3(4.383)
32×32	2.207293E-6(6.574)	4.752498E-4(4.000)	3.072600E-4(7.440)	1.144685E-5(7.608)	5.789009E-4(3.961)	2.297850E-3(4.082)
64×64	2.002528E-6(1.102)	1.188502E-4(3.998)	5.186327E-5(5.924)	2.480103E-6(4.615)	1.464095E-4(3.954)	5.990484E-4(3.835)
128×128	2.002460E-6(1.000)	2.990480E-5(3.974)	3.137756E-5(1.652)	2.011006E-6(1.233)	3.692706E-5(3.964)	1.524306E-4(3.930)
256×256	2.002525E-6(1.000)	8.210198E-6(3.642)	3.072782E-5(1.021)	2.002659E-6(1.004)	9.866228E-6(3.742)	4.860959E-5(3.135)

Table 3.32. *Shear thinning fluid:* $\mathbf{L}^2/\mathbf{H}^1$ errors for $Q_2P_1^{np}$ using grid $[0,1]\times[0,1]$ for the nonlinear pressure form.

Mesh	*uniform*			*perturbed*		
Error	$\|\boldsymbol{u}-\boldsymbol{u}_h\|_{\mathbf{L}^2}$	$\|p-p_h\|_{\mathbf{L}^2}$	$\|\boldsymbol{u}-\boldsymbol{u}_h\|_{\mathbf{H}^1}$	$\|\boldsymbol{u}-\boldsymbol{u}_h\|_{\mathbf{L}^2}$	$\|p-p_h\|_{\mathbf{L}^2}$	$\|\boldsymbol{u}-\boldsymbol{u}_h\|_{\mathbf{H}^1}$
2×2	1.138128E00	2.052296E-1	9.857493E00	1.137723E00	2.154619E-1	9.840242E00
4×4	6.387038E-1(1.781)	2.509600E-1(0.8178)	7.388681E00(1.334)	6.403540E-1(1.776)	2.779592E-1(0.775)	7.376374E00(1.334)
8×8	2.119137E-1(3.014)	9.636838E-2(2.604)	4.370816E00(1.690)	2.301111E-1(2.782)	1.073771E-1(2.588)	4.397310E00(1.677)
16×16	6.551910E-2(3.234)	3.284348E-2(2.934)	2.257865E00(1.935)	7.265619E-2(3.167)	3.519952E-2(3.050)	2.434281E00(1.806)
32×32	1.647424E-2(3.977)	1.343558E-2(2.444)	1.072733E00(2.104)	1.915311E-2(3.793)	1.468481E-2(2.397)	1.177880E00(2.066)
64×64	3.551075E-3(4.639)	6.425463E-3(2.091)	5.159669E-1(2.079)	4.321699E-3(4.431)	6.963498E-3(2.108)	5.849859E-1(2.013)
128×128	8.082410E-4(4.393)	3.192563E-3(2.012)	2.596838E-1(1.986)	9.735196E-4(4.439)	3.440944E-3(2.023)	2.875427E-1(2.034)
256×256	3.129038E-4(2.583)	1.595034E-3(2.001)	1.335320E-1(1.944)	3.322740E-4(2.929)	1.722958E-3(1.997)	1.476912E-1(1.946)

Table 3.33. *Shear thinning fluid:* $\mathbf{L}^2/\mathbf{H}^1$ errors for $\tilde{Q}_1Q_0$ using grid $[-0.5,0.5]\times[-0.5,0.5]$ for the linear pressure form.

Mesh	*uniform*			*perturbed*		
Error	$\|\boldsymbol{u}-\boldsymbol{u}_h\|_{\mathbf{L}^2}$	$\|p-p_h\|_{\mathbf{L}^2}$	$\|\boldsymbol{u}-\boldsymbol{u}_h\|_{\mathbf{H}^1}$	$\|\boldsymbol{u}-\boldsymbol{u}_h\|_{\mathbf{L}^2}$	$\|p-p_h\|_{\mathbf{L}^2}$	$\|\boldsymbol{u}-\boldsymbol{u}_h\|_{\mathbf{H}^1}$
2×2	3.410424E-1	1.475805E-2	3.870885E00	3.413442E-1	2.373213E-2	3.923560E00
4×4	6.417521E-2(5.324)	4.922231E-3(2.998)	1.425459E00(2.715)	6.891256E-2(4.953)	1.123662E-2(2.112)	1.499918E00(2.615)
8×8	8.354923E-3(7.681)	4.980438E-4(9.883)	4.171748E-1(3.416)	1.013008E-2(6.802)	4.655718E-3(2.413)	4.677721E-1(3.206)
16×16	1.071521E-3(7.797)	5.811988E-5(8.569)	1.096694E-1(3.803)	1.697724E-3(5.966)	2.309917E-3(2.015)	1.556035E-1(3.006)
32×32	2.750307E-4(3.896)	1.510156E-5(3.848)	2.786138E-2(3.936)	3.872427E-4(4.384)	1.265433E-3(1.825)	6.064449E-2(2.565)
64×64	2.475448E-4(1.111)	1.331317E-5(1.134)	7.265227E-3(3.834)	2.292020E-4(1.689)	6.154753E-4(2.056)	2.580571E-2(2.350)
128×128	2.474159E-4(1.000)	1.327153E-5(1.003)	2.690105E-3(2.700)	2.405101E-4(0.953)	3.157780E-4(1.949)	1.310366E-2(1.969)
256×256	2.474343E-4(1.000)	1.326976E-5(1.000)	2.093985E-3(1.284)	2.410591E-4(0.997)	1.562946E-4(2.020)	6.646037E-3(1.971)

Table 3.34. *Shear thinning fluid:* $\mathbf{L}^2/\mathbf{H}^1$ errors for Q_2P_1 using grid $[-0.5,0.5]\times[-0.5,0.5]$ for the linear pressure form.

Mesh	*uniform*			*perturbed*		
Error	$\|\boldsymbol{u}-\boldsymbol{u}_h\|_{\mathbf{L}^2}$	$\|p-p_h\|_{\mathbf{L}^2}$	$\|\boldsymbol{u}-\boldsymbol{u}_h\|_{\mathbf{H}^1}$	$\|\boldsymbol{u}-\boldsymbol{u}_h\|_{\mathbf{L}^2}$	$\|p-p_h\|_{\mathbf{L}^2}$	$\|\boldsymbol{u}-\boldsymbol{u}_h\|_{\mathbf{H}^1}$
2×2	3.410424E-1	1.475805E-2	3.870885E00	3.380067E-1	1.598085E-2	3.894660E00
4×4	6.417521E-2(5.324)	4.922231E-3(2.998)	1.425459E00(2.715)	6.767099E-2(4.994)	5.761138E-3(2.773)	1.481830E00(2.628)
8×8	8.354923E-3(7.681)	4.980438E-4(9.883)	4.171748E-1(3.416)	9.451927E-3(7.159)	9.641459E-4(5.975)	4.458260E-1(3.323)
16×16	1.071521E-3(7.797)	5.811988E-5(8.569)	1.096694E-1(3.803)	1.498188E-3(6.308)	2.194270E-4(4.393)	1.368676E-1(3.257)
32×32	2.750307E-4(3.896)	1.510156E-5(3.848)	2.786138E-2(3.936)	3.092352E-4(4.844)	5.633287E-5(3.895)	3.632401E-2(3.768)
64×64	2.475448E-4(1.111)	1.331317E-5(1.134)	7.265227E-3(3.834)	2.476888E-4(1.248)	1.915913E-5(2.940)	1.027145E-2(3.536)
128×128	2.474159E-4(1.000)	1.327153E-5(1.000)	2.690105E-3(2.700)	2.471899E-4(1.002)	1.377394E-5(1.391)	3.231597E-3(3.178)
256×256	2.474343E-4(1.000)	1.326976E-5(1.000)	2.093985E-3(1.284)	2.473586E-4(0.999)	1.329977E-5(1.035)	2.145121E-3(1.506)

Table 3.35. *Shear thinning fluid:* $\mathbf{L}^2/\mathbf{H}^1$ errors for $Q_2P_1^{np}$ using grid $[-0.5,0.5]\times[-0.5,0.5]$ for the linear pressure form.

$$u=\begin{cases}\dfrac{1}{8}[(1-2\tau_s)^2-(1-2\tau_s-2y)^2] & \text{if} \quad 0\le y<\dfrac{1}{2}-\tau_s,\\ \dfrac{1}{8}(1-2\tau_s)^2 & \text{if} \quad \dfrac{1}{2}-\tau_s\le y\le\dfrac{1}{2}+\tau_s,\\ \dfrac{1}{8}[(1-2\tau_s)^2-(2y-2\tau_s-1)^2] & \text{if} \quad \dfrac{1}{2}+\tau_s<y<1.\end{cases} \tag{3.60}$$

With yield stress value $\tau_s=0.25$.
Here we present this numerical example for Bingham fluid to create an idea about the behavior of pressure

Mesh	*uniform*			*perturbed*		
Error	$\|\boldsymbol{u}-\boldsymbol{u}_h\|_{\mathbf{L}^2}$	$\|p-p_h\|_{\mathbf{L}^2}$	$\|\boldsymbol{u}-\boldsymbol{u}_h\|_{\mathbf{H}^1}$	$\|\boldsymbol{u}-\boldsymbol{u}_h\|_{\mathbf{L}^2}$	$\|p-p_h\|_{\mathbf{L}^2}$	$\|\boldsymbol{u}-\boldsymbol{u}_h\|_{\mathbf{H}^1}$
2×2	1.137560E00	8.456539E-2	9.853397E00	1.138306E00	4.404449E-1	9.847180E00
4×4	6.829124E-1(1.665)	1.057254E00(0.080)	8.276918E00(1.190)	6.879239E-1(1.654)	1.072393E00(0.4107)	8.169900E00(1.205)
8×8	2.278247E-1(2.997)	5.582381E-1(1.893)	5.302726E00(1.560)	2.553716E-1(2.693)	5.880010E-1(1.823)	5.426456E00(1.505)
16×16	1.043389E-1(2.183)	2.800708E-1(1.993)	3.317365E00(1.598)	1.284197E-1(1.988)	3.038572E-1(1.935)	3.740789E00(1.450)
32×32	5.913204E-2(1.764)	1.399549E-1(2.001)	2.150002E00(1.543)	7.443383E-2(1.725)	1.517860E-1(2.001)	2.499549E00(1.496)
64×64	3.135678E-2(1.885)	6.997353E-2(2.000)	1.412989E00(1.521)	4.170821E-2(1.784)	7.651475E-2(1.983)	1.689754E00(1.479)
128×128	1.287051E-2(2.436)	3.498370E-2(2.000)	8.995821E-1(1.570)	1.765456E-2(2.362)	3.821124E-2(2.002)	1.080560E00(1.563)
256×256	4.228305E-3(3.043)	1.748891E-2(2.000)	5.432532E-1(1.655)	5.978153E-3(2.953)	1.914378E-2(1.996)	6.652389E-1(1.624)

Table 3.36. *Shear thinning fluid:* $\mathbf{L}^2/\mathbf{H}^1$ errors for $\tilde{Q}_1Q_0$ using grid $[-0.5,0.5]\times[-0.5,0.5]$ for the nonlinear pressure form.

Mesh	*uniform*			*perturbed*		
Error	$\|\boldsymbol{u}-\boldsymbol{u}_h\|_{\mathbf{L}^2}$	$\|p-p_h\|_{\mathbf{L}^2}$	$\|\boldsymbol{u}-\boldsymbol{u}_h\|_{\mathbf{H}^1}$	$\|\boldsymbol{u}-\boldsymbol{u}_h\|_{\mathbf{L}^2}$	$\|p-p_h\|_{\mathbf{L}^2}$	$\|\boldsymbol{u}-\boldsymbol{u}_h\|_{\mathbf{H}^1}$
2×2	3.410424E-1	1.126683E00	3.870885E00	1.412812E00	1.164963E00	1.766873E01
4×4	1.099603E00(0.3102)	4.026433E-1(2.798)	2.283606E01(0.1695)	1.175286E00(1.202)	4.482656E-1(2.598)	2.446919E01(0.7221)
8×8	6.860767E-2(16.027)	1.066360E-1(3.775)	2.044208E00(11.171)	1.898157E-1(6.191)	1.358317E-1(3.300)	4.172779E00(5.864)
16×16	2.359525E-3(29.076)	2.659275E-2(4.010)	2.977954E-1(6.864)	2.995607E-2(6.336)	4.235927E-2(3.206)	1.277259E00(3.267)
32×32	2.836276E-4(8.319)	6.638816E-3(4.005)	4.748469E-2(6.271)	7.160115E-3(4.183)	1.696674E-2(2.496)	6.210466E-1(2.056)
64×64	2.473766E-4(1.146)	1.658891E-3(4.002)	8.831634E-3(5.376)	1.491006E-3(4.802)	7.727434E-3(2.195)	2.991193E-1(2.076)
128×128	2.474116E-4(0.999)	4.148625E-4(3.998)	2.765114E-3(3.193)	2.867744E-4(5.199)	3.861051E-3(2.001)	1.544415E-1(1.936)
256×256	2.474342E-4(0.999)	1.045047E-4(3.969)	2.095538E-3(1.319	1.686421E-4(1.700)	1.906856E-3(2.024)	7.738762E-2(1.995)

Table 3.37. *Shear thinning fluid:* $\mathbf{L}^2/\mathbf{H}^1$ errors for Q_2P_1 using grid $[-0.5,0.5]\times[-0.5,0.5]$ for the nonlinear pressure form.

Mesh	*uniform*			*perturbed*		
Error	$\|\boldsymbol{u}-\boldsymbol{u}_h\|_{\mathbf{L}^2}$	$\|p-p_h\|_{\mathbf{L}^2}$	$\|\boldsymbol{u}-\boldsymbol{u}_h\|_{\mathbf{H}^1}$	$\|\boldsymbol{u}-\boldsymbol{u}_h\|_{\mathbf{L}^2}$	$\|p-p_h\|_{\mathbf{L}^2}$	$\|\boldsymbol{u}-\boldsymbol{u}_h\|_{\mathbf{H}^1}$
2×2	3.410424E-1	1.126683E00	3.870885E00	1.474711E00	1.167803E00	1.837326E01
4×4	1.099603E00(0.3102)	4.026433E-1(2.798)	2.283606E01(0.1695)	1.047386E00(1.408)	4.385711E-1(2.662)	2.212849E01(0.830)
8×8	6.860767E-2(16.027)	1.066360E-1(3.775)	2.044208E00(11.171)	1.073303E-1(9.758)	1.254313E-1(3.496)	2.750289E00(8.045)
16×16	2.359525E-3(29.076)	2.659275E-2(4.010)	2.977954E-1(6.864)	9.027883E-3(11.888)	3.209173E-2(3.908)	6.237486E-1(4.09)
32×32	2.836276E-4(8.319)	6.638816E-3(4.005)	4.748469E-2(6.271)	8.577134E-4(10.525)	8.171131E-3(3.927)	1.642697E-1(3.797)
64×64	2.473766E-4(1.146)	1.658891E-3(4.002)	8.831634E-3(5.376)	2.355240E-4(3.641)	2.048027E-3(3.989)	4.382748E-2(3.748)
128×128	2.474116E-4(0.999)	4.148625E-4(3.998)	2.765114E-3(3.193)	2.414982E-4(0.975)	5.136310E-4(3.987)	1.148773E-2(3.815)
256×256	2.474342e-4(0.999)	1.045047E-4(3.969)	2.095538E-3(1.319)	2.460251E-4(0.981)	1.292741E-4(3.973)	3.563980E-3(3.223)

Table 3.38. *Shear thinning fluid:* $\mathbf{L}^2/\mathbf{H}^1$ errors for $Q_2P_1^{np}$ using grid $[-0.5,0.5]\times[-0.5,0.5]$ for the nonlinear pressure form.

in one dimensional Bingham flow and to give another scope about the prediction for the behavior of pressure as well as the numerical behavior for element under the regularization parameter ϵ in comparison with the analytical solution. From the depicted tables(3.40 and 3.41) the low order finite element loses its property of convergence when the value of ϵ approaches one and goes the natural optimal behavior of convergence when ϵ is close to zero. In this case the high order finite elements are different. The norms are fixed at every ϵ after certain level which means the numerical solution is reached at this level, so we gain no more but the norms decrease gradually with decreasing regularization parameter.
One can observe that the pressure has no gain with decreasing of ϵ which means the norms are not able to decrease with the decreasing of ϵ and always fixed. This indicates that the linear pressure for the exact pressure is predicted incorrectly which leads us to create another idea about the behavior of the pressure. This idea should be based on the yield stress value. To test the influence of the yield stress value(τ_s) on the pressure error estimates($\mathbf{L}^2$-error and $\mathbf{H}^1$-error) for the Bingham fluid at different values of regularization parameter(ϵ) and mesh size(h). Let us set the boundary conditions to be Dirichlet at the inlet and DO NOTHING at the outlet for the gradient form to get the following results (see table(3.39)):

The results which can be evolved from the table(3.39) are:

	$\|p-p_h\|_{\mathbf{L}^2}$	$\|p-p_h\|_{\mathbf{H}^1}$	$\|p-p_h\|_{\mathbf{L}^2}$	$\|p-p_h\|_{\mathbf{H}^1}$
$\tau_s = 0.0$	1.520830E-13	1.195168E-12		
		$h = 1/20$		
τ_s	$\epsilon = 10^{-3}$		$\epsilon = 10^{-4}$	
0.001	1.116018E-7	7.278083E-6	3.414335E-7	2.121368E-5
0.01	8.758298E-5	5.949762E-3	1.620420E-4	1.055898E-2
0.1	5.069186E-3	1.896491E-1	4.258504E-3	1.731343E-1
0.4	8.125401E-2	1.075701E00	6.343204E-2	1.001301E00
		$h = 1/40$		
τ_s	$\epsilon = 10^{-3}$		$\epsilon = 10^{-4}$	
0.001	6.920631E-7	9.467591E-5	3.748435E-7	4.801995E-5
0.01	2.985680E-5	4.061566E-3	4.571764E-5	6.180068E-3
0.1	5.125886E-3	2.353337E-1	4.052771E-3	2.076018E-1
0.4	7.936582E-2	1.258224E00	6.340927E-2	1.165174E00
		$h = 1/80$		
τ_s	$\epsilon = 10^{-3}$		$\epsilon = 10^{-4}$	
0.001	9.810040E-7	2.636342E-4	7.692089E-7	1.928347E-4
0.01	5.479722E-5	1.068717E-2	3.904419E-5	9.071861E-3
0.1	5.079381E-3	2.796408E-1	3.960689E-3	2.503833E-1
0.4	7.921253E-2	1.372576E00	6.329500E-2	1.312911E00

Table 3.39. *Bingham flow in channel:* $\mathbf{L}^2/\mathbf{H}^1$ errors for pressure using Q_2P_1 at different values of yield stress ($\tau_s = 10^{-3}, 10^{-2}, 10^{-1}, 0.4$).

(1) The influence of regularization parameter and mesh size are much more fragile with respect to the influence of yield stress value on the pressure numerical calculation for Bingham fluid.

(2) The convergence rate could be of third order of τ_s in $\mathbf{L}^2$ and second order of τ_s in $\mathbf{H}^1$ which provides inaccurate and unstable pressure solution at higher value yield stress.

(3) The same influence on the pressure can take place for the shear stress, shear rate and also viscosity, since their numerical calculations depend mainly on the yield stress value.

These calculations give us the predicted numerical behavior of the pressure which can be sketched from Fig.3.6 to Fig.3.10 and Fig.3.11.

Elements	$\tilde{Q}_1Q_0$			Q_2P_1			$Q_2P_1^{np}$		
Errors	$\|\boldsymbol{u}-\boldsymbol{u}_h\|_{\mathbf{L}^2}$	$\|p-p_h\|_{\mathbf{L}^2}$	$\|\boldsymbol{u}-\boldsymbol{u}_h\|_{\mathbf{H}^1}$	$\|\boldsymbol{u}-\boldsymbol{u}_h\|_{\mathbf{L}^2}$	$\|p-p_h\|_{\mathbf{L}^2}$	$\|\boldsymbol{u}-\boldsymbol{u}_h\|_{\mathbf{H}^1}$	$\|\boldsymbol{u}-\boldsymbol{u}_h\|_{\mathbf{L}^2}$	$\|p-p_h\|_{\mathbf{L}^2}$	$\|\boldsymbol{u}-\boldsymbol{u}_h\|_{\mathbf{H}^1}$
$\epsilon = 10^{-1}$									
2x2	6.256396E-3	1.584572E-1	7.322182E-2	4.442295E-3	6.651154E-2	3.775577E-2	4.442295E-3	6.561154E-2	3.775577E-2
4x4	3.932215E-3(1.591)	9.989349E-2(1.586)	4.470624E-2(1.637)	2.888636E-3(1.537)	9.011845E-2(0.738)	2.883854E-2(1.309)	2.888636E-3(1.537)	9.011845E-2(0.738)	2.883854E-2(1.309)
8x8	3.110987E-3(1.264)	8.820159E-2(1.132)	3.402723E-2(1.313)	2.857074E-3(1.011)	8.906132E-2(1.011)	2.889129E-2(0.998)	2.857074E-3(1.011)	8.906132E-2(1.011)	2.889129E-2(0.998)
16x16	2.917639E-3(1.066)	8.792556E-2(1.003)	3.033679E-2(1.121)	2.855734E-3(1.000)	8.876478E-2(1.003)	2.893028E-2(0.998)	2.855734E-3(1.000)	8.876478E-2(1.003)	2.893028E-2(0.998)
32x32	2.871095E-3(1.016)	8.843745E-2(0.994)	2.929818E-2(1.035)	2.855712E-3(1.000)	8.872259E-2(1.000)	2.893663E-2(0.998)	2.855712E-3(1.000)	8.872259E-2(1.000)	2.893663E-2(0.998)
64x64	2.859556E-3(1.004)	8.863930E-2(0.997)	2.902844E-2(1.009)	2.855715E-3(1.000)	8.871789E-2(1.000)	2.893734E-2(1.000)	2.855715E-3(1.000)	8.871747E-2(1.000)	2.893734E-2(1.000)
128x128	2.856675E-3(1.001)	8.869716E-2(0.999)	2.896023E-2(1.002)	2.855716E-3(1.000)	8.871747E-2(1.000)	2.893740E-2(1.000)	2.855716E-3(1.000)	8.871747E-2(1.000)	2.893740E-2(1.000)
256x256	2.855956E-3(1.000)	8.871230E-2(0.999)	2.894312E-2(1.000)	2.855716E-3(1.000)	8.871743E-2(1.000)	2.893741E-2(1.000)	2.855716E-3(1.000)	8.871743E-2(1.000)	2.893741E-2(1.000)
$\epsilon = 10^{-2}$									
2x2	6.289975E-3	1.463450E-1	7.176738E-2	3.990220E-3	6.004970E-2	3.452452E-2	3.990220E-3	6.004970E-2	3.452452E-2
4x4	2.592363E-3(2.426)	1.150618E-1(1.271)	3.720109E-2(1.929)	5.075842E-4(1.754)	5.621443E-2(1.068)	5.520552E-3(6.253)	5.075842E-4(1.754)	5.621443E-2(1.068)	5.520552E-3(6.253)
8x8	8.082549E-4(3.207)	6.255720E-2(1.839)	2.112163E-2(1.761)	5.195547E-4(0.977)	5.726508E-2(0.981)	7.031666E-3(0.781)	5.195547E-4(0.977)	5.726508E-2(0.981)	7.031666E-3(0.781)
16x16	5.413759E-4(1.493)	5.640152E-2(1.109)	1.179940E-2(1.790)	5.045525E-4(1.029)	5.619094E-2(1.019)	7.016094E-3(1.002)	5.045525E-4(1.029)	5.619094E-2(1.019)	7.016094E-3(1.002)
32x32	5.113537E-4(1.058)	5.594857E-2(1.008)	8.438116E-3(1.398)	5.032551E-4(1.002)	5.605989E-2(1.002)	6.976386E-3(1.005)	5.032551E-4(1.002)	5.605989E-2(1.002)	6.978386E-3(1.005)
64x64	5.050761E-4(1.012)	5.596534E-2(0.999)	7.364975E-3(1.145)	5.032082E-4(1.000)	5.606254E-2(1.000)	6.974584E-3(1.000)	5.032082E-4(1.000)	5.606254E-2(1.000)	6.974584E-3(1.000)
128x128	5.036596E-4(1.002)	5.602817E-2(0.998)	7.075537E-3(1.040)	5.032092E-4(1.000)	5.606561E-2(0.999)	6.974156E-3(1.000)	5.032092E-4(1.000)	5.606561E-2(0.999)	6.974156E-3(1.000)
256x256	5.033206E-4(1.000)	5.605523E-2(0.999)	6.999651E-3(1.010)	5.032096E-4(1.000)	5.606551E-2(1.000)	6.974126E-3(1.000)	5.032096E-4(1.000)	5.606551E-2(1.000)	6.974126E-3(1.000)
$\epsilon = 10^{-3}$									
2x2	6.308244E-3	1.469785E-1	7.155200E-2	4.042736E-3	7.950745E-2	3.486620E-2	4.042736E-3	7.950745E-2	3.486620E-2
4x4	2.231318E-3(2.827)	1.566248E-1(0.938)	3.614345E-2(1.979)	5.110308E-5(28.738)	3.496618E-2(2.273)	9.329350E-4(37.372)	5.110308E-5(28.738)	3.496618E-2(2.273)	9.329350E-4(37.372)
8x8	5.022538E-4(4.442)	5.994477E-2(2.612)	2.061175E-2(1.753)	5.301892E-5(0.963)	4.312988E-2(0.810)	1.040902E-3(0.896)	5.301892E-5(0.963)	4.312988E-2(0.810)	1.040902E-3(0.896)
16x16	1.407617E-4(3.568)	4.297567E-2(1.394)	1.042023E-2(1.978)	6.070004E-5(0.8735)	4.212593E-2(1.023)	1.246095E-3(0.835)	6.070004E-5(0.8735)	4.212593E-2(1.023)	1.246095E-3(0.835)
32x32	6.541930E-5(2.151)	4.035554E-2(1.064)	5.301816E-3(1.965)	5.952553E-5(1.019)	4.191533E-2(1.005)	1.348964E-3(0.9237)	6.070004E-5(1.019)	4.212593E-2(1.005)	1.246095E-3(0.9237)
64x64	5.859392E-5(1.116)	4.138835E-2(0.975)	2.841854E-3(1.865)	5.838635E-5(1.019)	4.190132E-2(1.000)	1.333018E-3(1.012)	5.838635E-5(1.019)	4.190132E-2(1.000)	1.333018E-3(1.012)
128x128	5.838899E-5(1.003)	4.175872E-2(0.991)	1.828524E-3(1.554)	5.834382E-5(1.000)	4.195602E-2(0.998)	1.327233E-3(1.004)	5.834382E-5(1.000)	4.195602E-2(0.998)	1.327233E-3(1.004)
256x256	5.835013E-5(1.000)	4.190111E-2(0.996)	1.468616E-3(1.245)	5.834031E-5(1.000)	4.198989E-2(0.999)	1.326833E-3(1.000)	5.834031E-5(1.000)	4.198989E-2(0.999)	1.326833E-3(1.000)
$\epsilon = 10^{-4}$									
2x2	6.308529E-3	1.469863E-1	7.154909E-2	4.043965E-3	7.987018E-2	3.487433E-2	4.043965E-3	7.987018E-2	3.487433E-2
4x4	2.184766E-3(2.887)	1.719144E-1(0.885)	3.608559E-2(1.982)	5.347667E-6(756.211)	3.511240E-2(2.274)	1.000024E-4(348.734)	5.347667E-6(756.211)	3.511240E-2(2.274)	1.000024E-4(348.734)
8x8	4.838069E-4(4.515)	5.996705E-2(2.866)	2.056792E-2(1.754)	5.282573E-6(1.012)	4.273933E-2(0.821)	1.248916E-4(0.8007)	5.282573E-6 (1.012)	4.273933E-2(0.821)	1.248916E-4(0.8007)
16x16	1.196968E-4(4.041)	4.165045E-2(1.439)	1.028845E-2(1.999)	5.642644E-6(0.936)	4.028807E-2(1.060)	1.481283E-4(0.8431)	5.642644E-6 (0.936)	4.028807E-2(1.060)	1.481283E-4(0.8431)
32x32	3.051736E-5(3.922)	3.818925E-2(1.090)	5.130966E-3(2.005)	6.221081E-6(0.907)	3.959339E-2(1.017)	1.611600E-4(0.9191)	6.221081E-6 (0.907)	3.959339E-2(1.017)	1.611600E-4(0.9191)
64x64	1.006809E-5(3.031)	3.802632E-2(1.004)	2.566747E-3(1.999)	6.545888E-6(0.950)	3.948121E-2(1.002)	1.799085E-4(0.8958)	6.545888E-6 (0.950)	3.948121E-2(1.002)	1.799085E-4(0.8958)
128x128	6.621453E-6(1.520)	3.852228E-2(0.987)	1.291809E-3(1.986)	6.466429E-6(1.012)	3.949520E-2(0.999)	1.911995E-4(0.9409)	6.466429E-6 (1.012)	3.949520E-2(0.999)	1.911995E-4(0.9409)
256x256	6.406059E-6(1.033)	3.929316E-2(0.980)	6.632371E-4(1.947)	6.410718E-6(1.008)	3.951589E-2(0.999)	1.897036E-4(1.007)	6.410718E-6 (1.008)	3.951589E-2(0.999)	1.897036E-4(1.007)
$\epsilon = 10^{-5}$									
2x2	6.308532E-3	1.469863E-1	7.154906E-3()	4.043978E-3	7.987385E-2()	3.487441E-2	4.043978E-3	7.987385E-2	3.487441E-2
4x4	2.179416E-3(2.894)	1.742969E-1(0.843)	3.608441E-2(0.1983)	5.371774E-7()	3.514582E-2(2.272)	1.006428E-5()	5.371770E-7()	3.514582E-2(2.272)	1.006428E-5
8x8	4.821782E-4(4.519)	5.997359E-2(2.906)	2.056406E-2(1.754)	5.309666E-7(1.011)	4.276339E-2(0.8219)	1.270743E-5(0.792)	5.309666E-7(1.011)	4.276339E-2(0.8219)	1.270743E-5(0.792)
16x16	1.182497E-4(4.077)	4.151917E-2(1.444)	1.027724E-2(2.000)	5.612741E-7(0.946)	4.027201E-2(1.061)	1.551651E-5(0.819)	5.612741E-7(0.946)	4.027201E-2(1.061)	1.551651E-5(0.819)
32x32	2.885912E-5(4.097)	3.801796E-2(1.092)	5.120012E-3(2.007)	5.934664E-7(0.945)	3.953273E-2(1.018)	1.813115E-5(0.8558)	5.934664E-7(0.945)	3.953273E-2(1.018)	1.813115E-5(0.8558)
64x64	7.217540E-6(3.998)	8.780438E-2(0.433)	2.554942E-3(2.004)	6.201919E-7(0.956)	3.916852E-2(1.009)	2.041271E-5(0.8882)	6.201919E-7(0.956)	3.916852E-2(1.009)	2.041271E-5(0.8882)
128x128	1.976306E-6(3.652)	3.809465E-2(2.304)	1.276664E-3(2.001)	6.459938E-7(0.960)	3.898871E-2(1.004)	2.118198E-5(0.963)	6.459938E-7(0.960)	3.898871E-2(1.004)	2.118198E-5(0.963)
256x256	8.354747E-7(2.365)	3.843507E-2(0.9911)	6.385859E-4(1.999)	6.591133E-7(0.980)	3.903359E-2(0.998)	2.288229E-5(0.9257)	6.591133E-7(0.980)	3.903359E-2(0.998)	2.288229E-5(0.9257)

Table 3.40. *Bingham flow in channel:* $\mathbf{L}^2/\mathbf{H}^1$ errors for $\tilde{Q}_1Q_0$, Q_2P_1 and $Q_2P_1^{np}$ using uniform grid $[0,1]\times[0,1]$ at $\tau_s = 0.25$.

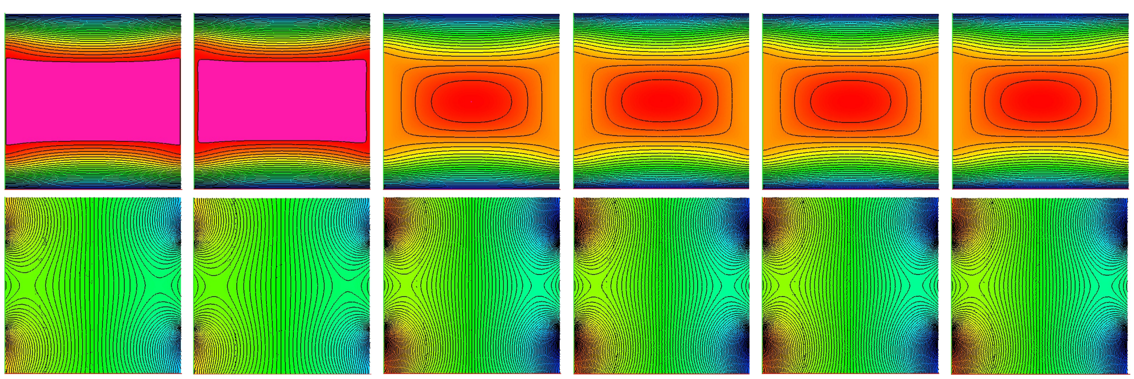

Fig. 3.6. *Bingham flow in channel:* Velocity distributions for $\tilde{Q}_1Q_0$, Q_2P_1 and $Q_2P_1^{np}$ (top) and pressure distributions for $\tilde{Q}_1Q_0$, Q_2P_1 and $Q_2P_1^{np}$ (bottom) using uniform and perturbed meshes $[0,1]\times[0,1]$ at 256×256, $\epsilon = 10^{-1}$ and $\tau_s = 0.25$.

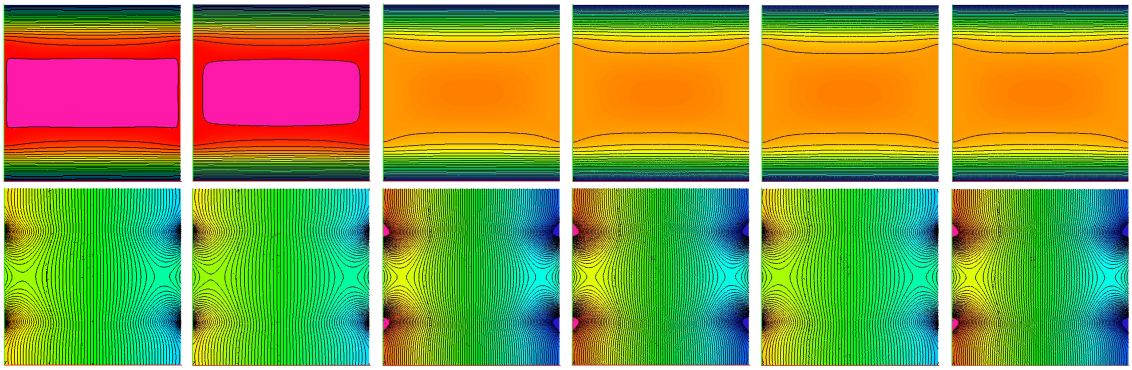

Fig. 3.7. *Bingham flow in channel:* Velocity distributions for $\tilde{Q}_1Q_0$, Q_2P_1 and $Q_2P_1^{np}$ (top) and pressure distributions for $\tilde{Q}_1Q_0$, Q_2P_1 and $Q_2P_1^{np}$ (bottom) using uniform and perturbed meshes $[0,1]\times[0,1]$ at 256×256, $\epsilon = 10^{-2}$ and $\tau_s = 0.25$.

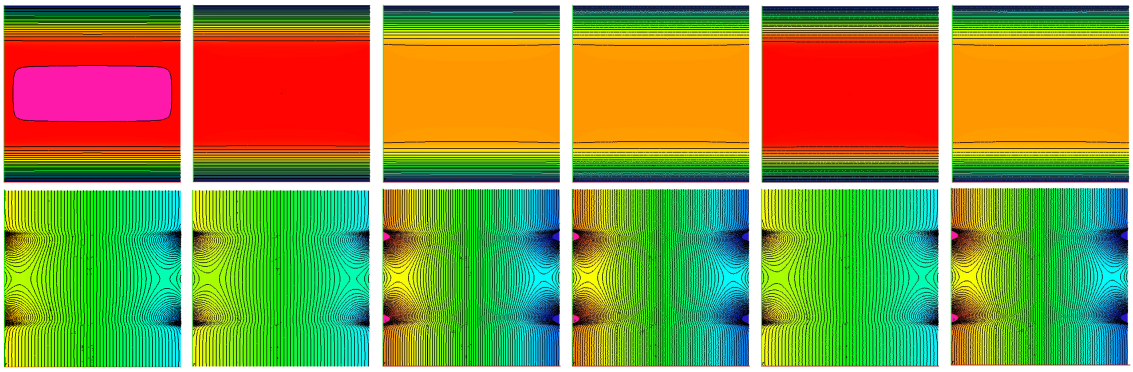

Fig. 3.8. *Bingham flow in channel:* Velocity distributions for $\tilde{Q}_1Q_0$, Q_2P_1 and $Q_2P_1^{np}$ (top) and pressure distributions for $\tilde{Q}_1Q_0$, Q_2P_1 and $Q_2P_1^{np}$ (bottom) using uniform and perturbed meshes $[0,1]\times[0,1]$ at 256×256, $\epsilon = 10^{-3}$ and $\tau_s = 0.25$.

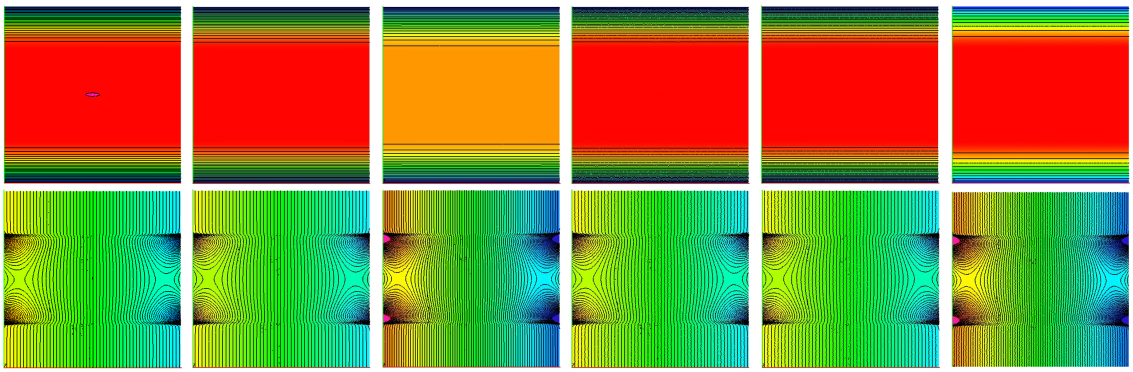

Fig. 3.9. *Bingham flow in channel:* Velocity distributions for $\tilde{Q}_1Q_0$, Q_2P_1 and $Q_2P_1^{np}$ (top) and pressure distributions for $\tilde{Q}_1Q_0$, Q_2P_1 and $Q_2P_1^{np}$ using uniform and perturbed meshes $[0,1]\times[0,1]$ at 256×256, $\epsilon = 10^{-4}$ and $\tau_s = 0.25$.

Elements		$\tilde{Q}_1Q_0$			Q_2P_1			$Q_2P_1^{np}$	
Errors	$\lVert\boldsymbol{u}-\boldsymbol{u}_h\rVert_{\mathbf{L}^2}$	$\lVert p-p_h\rVert_{\mathbf{L}^2}$	$\lVert\boldsymbol{u}-\boldsymbol{u}_h\rVert_{\mathbf{H}^1}$	$\lVert\boldsymbol{u}-\boldsymbol{u}_h\rVert_{\mathbf{L}^2}$	$\lVert p-p_h\rVert_{\mathbf{L}^2}$	$\lVert\boldsymbol{u}-\boldsymbol{u}_h\rVert_{\mathbf{H}^1}$	$\lVert\boldsymbol{u}-\boldsymbol{u}_h\rVert_{\mathbf{L}^2}$	$\lVert p-p_h\rVert_{\mathbf{L}^2}$	$\lVert\boldsymbol{u}-\boldsymbol{u}_h\rVert_{\mathbf{H}^1}$
$\epsilon=10^{-1}$									
2x2	6.441406E-3	1.630374E-1	6.950600E-2	4.461705E-3	6.873304E-2	3.935597E-2	4.458798E-3	6.832050E-2	3.930839E-2
4x4	3.996302E-3(1.611)	1.042279E-1(1.564)	4.556020E-2(1.525)	2.881932E-3(1.548)	9.397227E-2(0.7314)	2.867716E-2(1.372)	2.885913E-3(1.545)	9.334640E-2(0.7319)	2.867319E-2(1.370)
8x8	3.137963E-3(1.273)	8.920191E-2(1.168)	3.504870E-2(1.299)	2.858854E-3(1.008)	8.928686E-2(1.0525)	2.881642E-2(0.995)	2.859281E-3(1.009)	8.931305E-2(1.045)	2.880871E-2(0.995)
16x16	2.935766E-3(1.068)	8.748068E-2(1.019)	3.123852E-2(1.122)	2.855750E-3(1.001)	8.879750E-2(1.005)	2.891452E-2(0.996)	2.855698E-3(1.001)	8.879579E-2(1.005)	2.891124E-2(0.996)
32x32	2.874648E-3(1.021)	8.823765E-2(0.991)	2.949096E-2(1.059)	2.855726E-3(1.000)	8.872473E-2(1.000)	2.893265E-2(0.999)	2.855711E-3(1.000)	8.872393E-2(1.000)	2.893156E-2(0.999)
64x64	2.860749E-3(1.004)	8.855797E-2(0.996)	2.909870E-2(1.013)	2.855717E-3(1.000)	8.871862E-2(1.000)	2.893636E-2(0.999)	2.855714E-3(1.000)	8.871844E-2(1.000)	2.893611E-2(0.999)
128x128	2.857066E-3(1.001)	8.867008E-2(0.998)	2.898024E-2(1.004)	2.855717E-3(1.000)	8.871751E-2(1.000)	2.893709E-2(1.000)	2.855715E-3(1.000)	8.871753E-2(1.000)	2.893702E-2(1.000)
256x256	2.856063E-3(1.000)	8.870440E-2(0.999)	2.894872E-2(1.001)	2.855716E-3(1.000)	8.871744E-2(1.000)	2.893733E-2(1.000)	2.855716E-3(1.000)	8.871745E-2(1.000)	2.893731E-2(1.000)
$\epsilon=10^{-2}$									
2x2	6.481482E-3	1.530410E-1	6.839668E-2	4.005796E-3	6.438525E-2	3.592071E-2	4.002542E-3	6.251450E-2	3.588501E-2
4x4	2.775667E-3(2.335)	1.175963E-1(1.301)	3.867713E-2(1.768)	7.555916E-4(5.301)	9.491784E-2(1.377)	8.245241E-3(4.356)	7.590063E-4(5.273)	9.446016E-2(0.661)	8.231319E-3(4.359)
8x8	9.557096E-4(2.904)	6.154041E-2(1.910)	2.304851E-2(1.678)	5.544898E-4(1.362)	5.985487E-2(1.075)	7.845083E-3(1.051)	5.541332E-4(1.369)	5.971177E-2(1.581)	7.835665E-3(1.050)
16x16	5.635960E-4(1.695)	5.543353E-2(1.110)	1.276791E-2(1.805)	5.059748E-4(1.095)	5.629410E-2(1.063)	7.052738E-3(1.112)	5.059818E-4(1.095)	5.632435E-2(1.060)	7.049526E-3(1.111)
32x32	5.145520E-4(1.095)	5.528618E-2(1.002)	8.957362E-3(1.425)	5.033686E-4(1.005)	5.608821E-2(1.003)	6.973527E-3(1.011)	5.033430E-4(1.005)	5.608326E-2(1.004)	6.972025E-3(1.011)
64x64	5.057991E-4(1.017)	5.569596E-2(0.992)	7.534640E-3(1.188)	5.032178E-4(1.000)	5.606148E-2(1.000)	6.973438E-3(1.000)	5.032131E-4(1.000)	5.606211E-2(1.000)	6.973058E-3(0.999)
128x128	5.038558E-4(1.003)	5.593084E-2(0.995)	7.124062E-3(1.057)	5.032110E-4(1.000)	5.606515E-2(0.999)	6.973706E-3(1.000)	5.032095E-4(1.000)	5.606555E-2(0.999)	6.973596E-3(0.999)
256x256	5.033719E-4(1.001)	5.602744E-2(0.998)	7.012942E-3(1.015)	5.032099E-4(1.000)	5.606540E-2(1.000)	6.974011E-3(1.000)	5.032095E-4(1.000)	5.606552E-2(1.000)	6.973981E-3(0.999)
$\epsilon=10^{-3}$									
2x2	6.500957E-3	1.539863E-1	6.821757E-2	4.021613E-3	7.470875E-2	3.605959E-2	4.008508E-3	7.366928E-2	3.595755E-2
4x4	2.463085E-3(2.639)	1.545084E-1(0.996)	3.779591E-2(1.804)	2.508607E-4(16.031)	1.618888E-1(0.4615)	5.295230E-3(6.809)	2.505447E-4(15.999)	1.612325E-1(0.456)	5.271495E-3(6.821)
8x8	6.847694E-4(3.597)	5.966001E-2(2.589)	2.276826E-2(1.660)	1.638624E-4(1.530)	5.536880E-2(2.923)	4.173859E-3(1.268)	1.633805E-4(1.533)	5.510104E-2(2.926)	4.159007E-3(1.267)
16x16	1.773827E-4(3.860)	4.184734E-2(1.425)	1.130225E-2(2.014)	7.349606E-5(2.229)	4.307263E-2(1.285)	1.800068E-3(2.318)	7.351177E-5(2.222)	4.305900E-2(1.279)	1.790096E-3(2.323)
32x32	7.490450E-5(2.368)	3.957699E-2(1.057)	6.000789E-3(1.883)	6.149341E-5(1.195)	4.212987E-2(1.022)	1.458681E-3(1.234)	6.149287E-5(1.195)	4.210922E-2(1.022)	1.452996E-3(1.232)
64x64	5.985624E-5(1.251)	4.070899E-2(0.972)	3.224087E-3(1.861)	5.848808E-5(1.051)	4.187556E-2(1.006)	1.343456E-3(1.085)	5.849201E-5(1.051)	4.189392E-2(1.005)	1.341889E-3(1.082)
128x128	5.860124E-5(1.021)	4.158115E-2(0.979)	1.984274E-3(1.624)	5.835027E-5(1.002)	4.196210E-2(0.997)	1.327322E-3(1.012)	5.835079E-5(1.002)	4.196008E-2(0.998)	1.326874E-3(1.011)
256x256	5.839245E-5(1.003)	4.184729E-2(0.993)	1.523079E-3(1.302)	5.834064E-5(1.000)	4.199155E-2(0.999)	1.326776E-3(1.000)	5.834078E-5(1.000)	4.199165E-2(0.999)	1.326658E-3(1.000)
$\epsilon=10^{-4}$									
2x2	6.501348E-3	1.540009E-1	6.821488E-2	4.024200E-3	7.586033E-2	3.608460E-2	4.009700E-3	7.472220E-2	3.597152E-2
4x4	2.422137E-3(2.684)	1.696407E-1(0.907)	3.773448E-2(1.807)	1.730055E-4(23.260)	1.774986E-1(0.553)	5.471158E-3(6.595)	1.721792E-4(23.287)	1.765242E-1(0.423)	5.447069E-3(6.603)
8x8	6.693740E-4(3.618)	5.975318E-2(2.839)	2.278535E-2(1.656)	1.434918E-4(1.205)	6.299672E-2(1.204)	4.206971E-3(1.300)	1.432237E-4(1.202)	6.298645E-2(2.802)	4.192433E-3(1.299)
16x16	1.592971E-4(4.202)	4.004388E-2(1.492)	1.120380E-2(2.033)	2.802821E-4(0.512)	4.358394E-2(1.445)	1.298038E-3(3.241)	2.811371E-5(5.094)	4.359499E-2(1.444)	1.281301E-3(3.272)
32x32	4.494515E-5(3.544)	3.767756E-2(1.062)	5.868756E-3(1.909)	1.158146E-5(24.200)	4.056617E-2(1.074)	5.483892E-4(2.367)	1.155320E-5(2.433)	4.050651E-2(1.076)	5.314253E-4(2.411)
64x64	1.335551E-5(3.365)	3.742174E-2(1.006)	2.976394E-3(1.971)	7.358774E-6(1.573)	3.952251E-2(1.026)	2.826905E-4(1.939)	7.359931E-6(1.569)	3.956555E-2(1.023)	2.742980E-4(1.937)
128x128	7.124687E-6(1.874)	3.832832E-2(0.976)	1.498445E-3(1.986)	6.534119E-6(1.126)	3.951436E-2(1.000)	2.088590E-4(1.353)	6.535297E-6(1.126)	3.950906E-2(1.001)	2.059018E-4(1.332)
256x256	6.471674E-6(1.100)	3.916520E-2(0.978)	7.662700E-4(1.955)	6.414985E-6(1.018)	3.952886E-2(0.999)	1.923882E-4(1.085)	6.415465E-6(1.018)	3.952653E-2(0.999)	1.915556E-4(1.0749)
$\epsilon=10^{-5}$									
2x2	6.501352E-3	1.540011E-1	6.821486E-2	4.024231E-3	7.587612E-2	3.608492E-2	4.009715E-3	7.473572E-2	3.597169E-2
4x4	2.454294E-3(2.649)	2.004375E-1(0.768)	3.768270E-2(1.810)	1.685712E-4(23.872)	1.800208E-1(0.421)	5.526486E-3(6.529)	1.676538E-4(23.916)	1.790234E-1(0.4175)	5.500147E-3(6.540)
8x8	6.691547E-4(3.667)	7.042982E-2(2.845)	2.211199E-2(1.704)	1.432746E-4(1.176)	6.465191E-2(2.784)	4.269965E-3(1.294)	1.431559E-4(1.1711)	6.476694E-2(2.764)	4.258711E-3(1.291)
16x16	1.581692E-4(4.230)	4.069768E-2(1.730)	1.104121E-2(2.002)	2.453616E-5(5.839)	4.731096E-2(1.366)	1.366670E-3(3.124)	2.467126E-5(5.8025)	4.726526E-2(1.370)	1.351239E-3(3.151)
32x32	4.344952E-5(3.640)	3.765197E-2(1.080)	5.778980E-3(1.910)	6.510835E-6(3.768)	4.240552E-2(1.115)	5.346693E-4(2.556)	6.438698E-6(3.831)	4.229349E-2(1.117)	5.166353E-4(2.615)
64x64	1.111550E-5(3.908)	3.721886E-2(1.011)	2.937532E-3(1.967)	1.901460E-6(3.424)	3.960106E-2(1.070)	1.983905E-4(2.695)	1.881121E-6(3.422)	3.966502E-2(1.066)	1.861246E-4(2.775)
128x128	2.907832E-6(3.822)	3.783143E-2(0.9838)	1.478855E-3(1.986)	8.553508E-7(2.223)	3.906583E-2(1.013)	8.399180E-5(2.362)	8.533509E-7(2.204)	3.906794E-2(1.015)	7.618808E-5(2.443)
256x256	9.793501E-7(2.969)	3.854973E-2(0.9814)	7.476597E-4(1.978)	6.868443E-7(1.245)	3.910008E-2(0.999)	4.470702E-5(1.878)	6.869199E-7(1.2423)	3.909505E-2(0.999)	4.083351E-5(1.865)

Table 3.41. *Bingham flow in channel:* $\mathbf{L}^2/\mathbf{H}^1$ errors for $\tilde{Q}_1Q_0$, Q_2P_1 and $Q_2P_1^{np}$ using perturbed grid $[0,1]\times[0,1]$ at $\tau_s=0.25$.

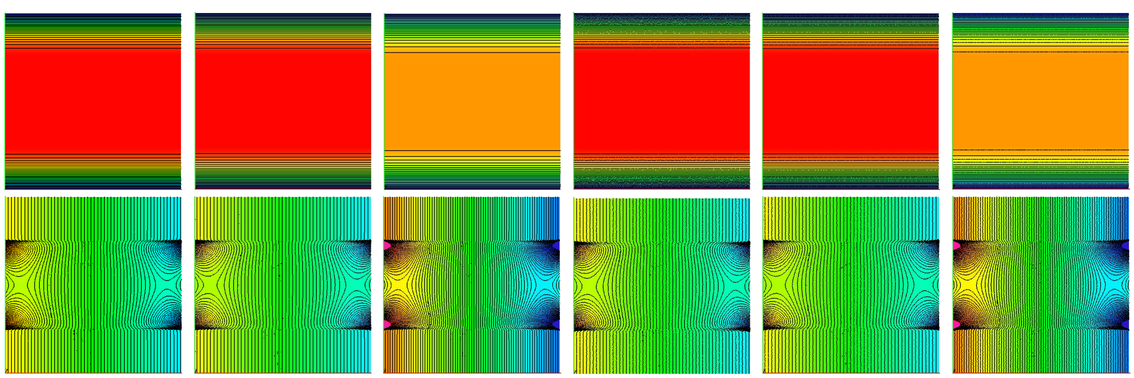

Fig. 3.10. *Bingham flow in channel:* Velocity distributions for $\tilde{Q}_1Q_0$, Q_2P_1 and $Q_2P_1^{np}$ (top) and pressure distributions for $\tilde{Q}_1Q_0$, Q_2P_1 and $Q_2P_1^{np}$ (bottom) using uniform and perturbed meshes $[0,1]\times[0,1]$ at 256×256, $\epsilon=10^{-5}$ and $\tau_s=0.25$.

3.8 Summary

This chapter handles three possible discretization techniques with low and high order spaces for different problems. The definition of the pressure is performed by using three different definitions from the spaces of interested elements; the global constant approach, the local linear approach and the global linear approach. All of them satisfy the inf-sup condition. The above tables and figures show the resulting approximation properties with respect to the measured $\mathbf{L}^2$ and $\mathbf{H}^1$ norms on the different refinement

levels. The results from these tables are quite prototypical for the Newtonian and Non-Newtonian fluids and one can observe the following:
It is concluded that the $\tilde{Q}_1Q_0$ does not give the exact solution for the velocity for the Poiseuille flow, since the velocity space does contain the exact solution. Unfortunately, this comes from the pressure space definition which is far from the real space definition. Moreover, the discrete incompressibility condition $(q_h, \boldsymbol{\nabla}.\boldsymbol{u}_h) = 0, \forall\, q_h \in Q_h$ is too weak as it leads to the so-called compressible element and may lead to very poor results. Therefore, the solution is to enforce the incompressibility which drops down the real behavior of the velocity. To enhance the doing of this element, one can follows the similar well-known case for $Q_2^8P_0$ and Q_2P_1 to enrich the velocity by adding an internal node and by using the linear pressure. This enhancement will satisfy naturally the inf-sup condition. However, one sometimes does not care for this enriching case which is not always valuable due to the extra cost with small gain.
The presented theoretical results imply the global approach (unmapped pressure approach) can be third order accurate for the regular mesh and second order accurate in the case of general quadrilateral meshes but the mapped one can not be second order accurate because of the lack in the approximation properties of the mapped linear finite element.
As it is expected the $Q_2P_1^{np}$ is more accurate for the considered linear/nonlinear problems, which means the $\tilde{Q}_1Q_0$ approach requires approximately 5-20 times more grids points, particularly for the nonlinear flow problems. On the other hand, the Q_2P_1 may have a major drawback which is the computational cost but it no so clear since a coarser mesh is sufficient to get the exact solution which has been showed in our calculations.
The use of stabilization in case of lower order finite element leads to the reduction of the order of errors to (could be or less) $h^{\frac{3}{2}}$ for the FEM edge oriented stabilization for the nonlinear flow problems (or $h^{\frac{3}{2}}$ for streamline diffusion and h for FEM Upwinding [187]). In contrast to the order of h^3 to the central $Q_2P_1^{np}$ the general quadrilateral meshes which make the reliability of the comparison, is still under investigation for the Newtonian and Non-Newtonian Flows. The element $\tilde{Q}_1Q_0$ approach requires about 1 or 2 further levels of grid refinement to produce a comparable accuracy as the quadratic Q_2P_1 ansatz for linear and nonlinear pressure problems and regular or distorted meshes.
The behavior of the pressure in the viscoplastic fluids is not uniformly linear as it was expected before (see Fig.3.11), and the value depends on the value of the yield stress. This creates a non-uniform distribution over the flow domain. The pressure has jumps on the interfacial boundaries among the viscoplastic fluid regimes. However, at the zero value of the yield stress; the viscoplastic equation is turned to the Navier-Stokes equations and the pressure has linear distribution over the whole domain.

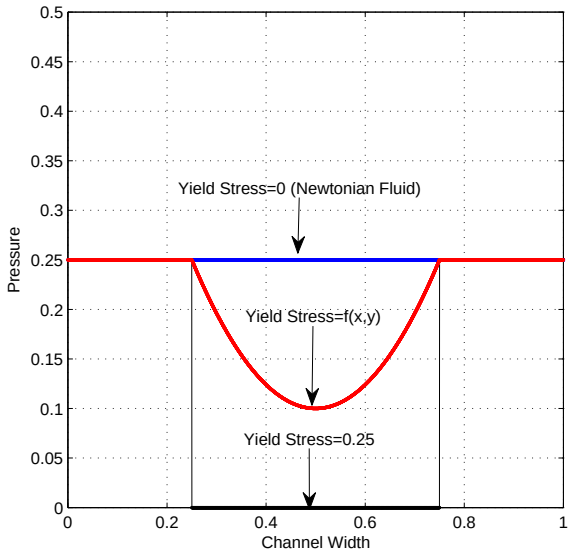

Fig. 3.11. Pressure cut line over the width of channel for the Newtonian fluid and the viscoplastic fluid

4

Newton and Multigrid Processes for Viscoplastic Fluids

A comparison between different discretization techniques(global constant pressure($\tilde{Q}_1Q_0$), local linear pressure(Q_2P_1), and global linear pressure($Q_2P_1^{np}$) approaches) with respect to the accuracy of benchmark parameters (energy norm, drag and lift forces) and the total cost are considered. The coupled Newton-multigrid processes for different discrete saddle point problems corresponding to the different flow models are tested due to the variation of the problem parameters. Particular concerning is to expose the nonlinear/linear solvers algorithms that used as outer/inner in the solution process for the nonlinear fluids problems arising from the the discretization aspects. It turns out that the domain fitted higher order finite element methods are in general most accurate and inexpensive. In addition to multigrid method in connection with cell oriented Vanka smoother has been confirmed to be the efficient linear solver for highly nonlinear problems arising from the nonlinear viscosity models. Finally, the solvers are analyzed for different problems in the sense of the accuracy, the convergence and the cost for all problems.

4.1 Introduction

The numerical studies of the benchmark problems have been analyzed for incompressible Navier-Stokes equation in such a way that they compute the benchmark parameters e.g. drag, lift and energy norm[118]. In this study we present different discretizations to cope with different flow models to be compared the results in the sense of accuracy for the global constant pressure approach, local linear pressure approach and global linear pressure approach which are represented by the $\tilde{Q}_1Q_0$, Q_2P_1, and $Q_2P_1^{np}$ respectively. The most accurate results might be computed with isoparametric higher order finite element $Q_2P_1^{np}$ (see [120, 118]). The nonlinear difficulties arisen from the discrete saddle point problems can be treated by using Newton-Multigrid process. The remedies are based on calculating the Frechet derivative for the nonlinear terms to construct the Jacobian matrix for different discretizations on different grid levels. our main aspect is to analyze the numerical behavior of the coupled solver for different spaces from the accuracy, efficiency, and robustness of the coupled solvers.
The governing equation for the nonlinear flow model problem can be overwritten as follows:

$$\frac{\partial \boldsymbol{u}}{\partial t} + \boldsymbol{u}\cdot\boldsymbol{\nabla}\boldsymbol{u} - \boldsymbol{\nabla}\cdot\nu(\|\mathbf{D}\|)\mathbf{D}(\boldsymbol{u}) + \boldsymbol{\nabla}p = \boldsymbol{f} \quad in \quad \boldsymbol{\Omega}\times(0,T), \tag{4.1a}$$

$$\boldsymbol{\nabla}\cdot\boldsymbol{u} = 0 \quad in \quad \boldsymbol{\Omega}\times(0,T), \tag{4.1b}$$

$$\boldsymbol{u}(\boldsymbol{x},t) = \boldsymbol{u}^o \quad on \quad \partial\boldsymbol{\Omega}\times(0,T), \tag{4.1c}$$

$$\boldsymbol{u}(\boldsymbol{x},0) = \boldsymbol{u}_o \quad in \quad \boldsymbol{\Omega} \tag{4.1d}$$

$$\tag{4.1e}$$

Where $\boldsymbol{\Omega}$ is the domain and $\partial\boldsymbol{\Omega}$ is the boundary with outward normal $\boldsymbol{n}$. Let us recall the weak form of suitable finite spaces after dropping down the unsteady term. Let $\mathbf{T}_h$ be a decomposition of $\boldsymbol{\Omega}$ into

quadrilaterals and $h_{\mathcal{T}}$ is the diameter of the mesh cell $\mathcal{T}$. The finite element spaces are denoted by V_h for the velocity and Q_h for the pressure. The strong relation for such pairs of finite element spaces is involved in the study which fulfills LBB conditions to guarantee the unique solvability of the discrete system i.e. there exists a constant β independent of the triangulation such that:

$$\inf_{q_h \in Q_h} \sup_{\boldsymbol{v}_h \in \mathbf{V}_h} \frac{(\boldsymbol{\nabla} \cdot \boldsymbol{v}_h, q_h)}{\|\boldsymbol{v}_h\|_{V_h} \|q_h\|_{Q_h}} \geq \beta > 0. \tag{4.2}$$

The standard Galerkin approximation of the system of equation reads as follows:

$$b(\boldsymbol{u}_h, \boldsymbol{u}_h, \boldsymbol{v}_h) + a(\boldsymbol{u}_h, \boldsymbol{v}_h) - c(p_h, \boldsymbol{v}_h) = (\boldsymbol{f}, \boldsymbol{v}_h), \tag{4.3a}$$

$$c(q_h, \boldsymbol{u}_h) = 0. \tag{4.3b}$$

For lower finite element spaces, the convection might be stabilized for the convection dominated problem. Let us denote the stabilization function ($\mathbf{J}$) of which $\mathbf{J}_{up}$, $\mathbf{J}_{sd}$ and $\mathbf{J}_{eo}$ for the corresponding stabilization Upwinding, streamline diffusion and edge oriented stabilization respectively. Therefore, the standard Galerkin system might be overwritten as follows:

$$b(\boldsymbol{u}_h, \boldsymbol{u}_h, \boldsymbol{v}_h) + a(\boldsymbol{u}_h, \boldsymbol{v}_h) + (\mathbf{J}_h, \boldsymbol{v}_h) - c(p_h, \boldsymbol{v}_h) = (\boldsymbol{f}, \boldsymbol{v}_h), \tag{4.4a}$$

$$c(q_h, \boldsymbol{u}_h) = 0. \tag{4.4b}$$

where,

$$a(\boldsymbol{u}, \boldsymbol{v}) = \int_{\boldsymbol{\Omega}} \nu(\|\mathbf{D}\|)\mathbf{D}(\boldsymbol{u}) : \mathbf{D}(\boldsymbol{v}) d\boldsymbol{x}, \tag{4.5a}$$

$$b(\boldsymbol{u}, \boldsymbol{v}, \boldsymbol{w}) = \int_{\boldsymbol{\Omega}} u_i v_{j,i} w_j d\boldsymbol{x}, \tag{4.5b}$$

$$c(q, \boldsymbol{v}) = \int_{\boldsymbol{\Omega}} q \boldsymbol{\nabla} \cdot \boldsymbol{v} d\boldsymbol{x}. \tag{4.5c}$$

After applying this discretization, a system of residual equation can be obtained and represented by the following nonlinear function :

$$\mathbf{R}(\boldsymbol{x}) = b(\boldsymbol{u}_h, \boldsymbol{u}_h, \boldsymbol{v}_h) + a(\boldsymbol{u}_h, \boldsymbol{v}_h) + (\mathbf{J}_{\cdot}, \boldsymbol{v}_h) - c(p_h, \boldsymbol{v}_h) - (\boldsymbol{f}, \boldsymbol{v}_h), \tag{4.6}$$

where ν is the viscosity in case of regularized form (ν_ϵ) but ϵ notation is dropped down for simplicity.

4.2 Stabilization Techniques

For the lower order finite element discretizations, the Galerkin standard finite element discretization may lead to a severe numerical behavior or the in-solvability of the discrete problem. It comes from either the dominant convective term or the lack of coerciveness in the deformation formulation of the nonlinear viscosity problems or by using small values for regularization parameter in the viscoplastic problems. The preliminary remedy is to stabilize the badly physical behavior by using the stabilizers or adding such terms. These stabilizers have the ability to treat the nonphysical oscillations from the central discretizations and the dropping of the ellipticity or the unbounded values. The schemes of stabilizations which have been successfully to remedy these are FEM upwinding, FEM streamline diffusion, algebraic FEM-FCT, FEM-TVD and edge oriented stabilizations (see [31, 35, 38, 111, 123, 132, 134, 133, 143, 159, 186, 188, 201, 208, 211, 216, 217]).

4.2.1 Upwinding

The main idea is investigated in [186, 188] for non-conforming finite element spaces of lowest order for the convection dominated problem to introduce new edge-central lumping regions and special lumping operators with convergence in the energy norm of order $O(hLog(h))$ (see [214]). This type of stabilization is used only in connection with finite element spaces $\tilde{Q}_1Q_0$ and $P_1^{nc}P_0$. The alternative discrete convective operator has the following form

$$\mathbf{J}_{up}(\boldsymbol{u},\boldsymbol{v},\boldsymbol{w}) = \sum_l \sum_k \oint_{\Gamma_{lk}} \boldsymbol{u}.\boldsymbol{n}_{lk} d\gamma (1-\lambda_{lk}(\boldsymbol{u})(\boldsymbol{v}(m_k)-\boldsymbol{v}(m_l))\boldsymbol{v}(m_l) \tag{4.7}$$

where λ_{lk} is the weighting function which is based on the local Reynolds number $Re_{\mathcal{T}}$ on each cell $\mathcal{T}$ and reads as follows:

$$\lambda_{lk}(\boldsymbol{u}) = \begin{cases} \dfrac{1+2\delta^* Re_{\mathcal{T}}}{2(1+\delta^* Re_{\mathcal{T}})} & \text{if} \quad Re_{\mathcal{T}} \geq 0, \\ \dfrac{1}{2(1-\delta^* Re_{\mathcal{T}})} & \text{if} \quad Re_{\mathcal{T}} < 0, \end{cases} \tag{4.8}$$

where δ^* is a free parameter, and $h_{\mathcal{T}}$ is the local mesh parameter on each cell $\mathcal{T}$, and $Re_{\mathcal{T}}$ is the local Reynolds number which reads as follows:

$$Re_{\mathcal{T}} = \frac{\|\boldsymbol{u}\|_\infty h_{\mathcal{T}}}{\mu}, \tag{4.9}$$

where $\|.\|_\infty$ is maximum norm on the element $\mathcal{T}$.
The choosing of the free parameter δ^* is not usually a delicated task since it is not optimized with the flow models. It leads to a significant effect on the accuracy. This parameter is used in our calculation to be small and at most 0.1.

4.2.2 Streamline Diffusion

This stabilizer is introduced in [35, 111] and followed by [123] and analyzed for the incompressible Navier-Stokes equation in [143, 208]. The idea is to stabilize the convective term by using an additional term which represents an additional coercivity in the local flow direction. This stabilizer reads as follows:

$$\mathbf{J}_{sd}(\boldsymbol{u},\boldsymbol{v},\boldsymbol{w}) = \sum_{\mathcal{T}\in\mathbf{T}_h} \delta_{\mathcal{T}} \int_{\mathcal{T}} (\boldsymbol{u}\cdot\boldsymbol{\nabla}\boldsymbol{u})(\boldsymbol{u}\cdot\boldsymbol{\nabla}\boldsymbol{v}) d\boldsymbol{x}, \tag{4.10}$$

where $\delta_{\mathcal{T}}$ is the local damping parameter or the streamline diffusion parameter. Choosing the value $\delta_{\mathcal{T}}$ in [214] is based on the local Reynolds($Re_{\mathcal{T}}$) number and the local mesh size ($h_{\mathcal{T}}$) to obtain the following form:

$$\delta_{\mathcal{T}} = \delta^* \frac{h_{\mathcal{T}}}{\|\boldsymbol{u}_\infty\|} \frac{2Re_{\mathcal{T}}}{1+Re_{\mathcal{T}}}, \tag{4.11}$$

but in [120] the parameter is introduced as $h_{\mathcal{T}}^2$. The drawback for the first definition of $\delta_{\mathcal{T}}$ is the relation with the choice the free parameter δ^* in an optimized way to avoid the inaccuracy behavior. In our case it is adaptive to have the unity. The convergence in the streamline diffusion norm is of order $O(h^{\frac{3}{2}})$ for $\tilde{Q}_1Q_0$ on rectangular shape- regular tensor product meshes which is quite close to the estimate of the conforming case (see [166, 201]).

4.2.3 Edge Oriented Stabilization

In general, the choice of lower order elements i.e. $(\tilde{Q}_1 Q_0)$ for certain problems is not purely optimal, since there are two severely well-known numerical situations for low order nonconforming finite elements which may arise the lack of coercivity for symmetric deformation tensor formulation (see [31]), and the treatment of pure transport problem. These can be handled by the proposed jump stabilizer in the discrete problem in [37, 38, 39, 40, 68, 101, 122, 215]. Therefore, to cure the inherited numerical instability by using the proposed jump stabilizers which act only on the velocity $\boldsymbol{u}$ in the momentum equations. This leads us to gather up the proposed stabilization kernels in the following forms.

$$\mathbf{J}_{eo1} = \sum_{\text{edge E}} \frac{\gamma\nu}{|E|} \int_E [\boldsymbol{u}][\boldsymbol{v}] ds, \tag{4.12a}$$

$$\mathbf{J}_{eo2} = \sum_{\text{edge E}} \gamma |E|^{\alpha} \int_E [\boldsymbol{\nabla u}][\boldsymbol{\nabla v}] ds, \tag{4.12b}$$

$$\mathbf{J}_{eo3} = \sum_{\text{edge E}} \gamma |E|^{\alpha} \int_E [\boldsymbol{n} \cdot \boldsymbol{\nabla u}][\boldsymbol{n} \cdot \boldsymbol{\nabla v}] ds, \tag{4.12c}$$

$$\mathbf{J}_{eo4} = \sum_{\text{edge E}} \gamma |E|^{\alpha} \int_E [\boldsymbol{t} \cdot \boldsymbol{\nabla u}][\boldsymbol{t} \cdot \boldsymbol{\nabla v}] ds, \tag{4.12d}$$

$$\mathbf{J}_{eo5} = \sum_{\text{edge E}} \gamma |E|^{\alpha} \int_E [(\boldsymbol{t} \cdot \boldsymbol{\nabla u}) \cdot \boldsymbol{n}][(\boldsymbol{t} \cdot \boldsymbol{\nabla v}) \cdot \boldsymbol{n}] ds, \tag{4.12e}$$

$$\mathbf{J}_{eo6} = \sum_{\text{edge E}} \gamma |E|^{2} \int_E [\boldsymbol{\nabla} \cdot \boldsymbol{u}][\boldsymbol{\nabla} \cdot \boldsymbol{v}] ds, \tag{4.12f}$$

$$\mathbf{J}_{eo7} = \sum_{\text{edge E}} \frac{\gamma\nu}{|E|} \int_E [\boldsymbol{n} \cdot \boldsymbol{u}][\boldsymbol{n} \cdot \boldsymbol{v}] ds. \tag{4.12g}$$

The choice of the kernel is strongly associated with the treated numerical problem, i.e. the kernel J_{eo1} is introduced in [101, 122] for convection dominated problem to improve the accuracy as with conforming streamline diffusion FEM method to fulfill the coercivity condition in the discrete problem. The kernels J_{eo2}, J_{eo3}, J_{eo4} and J_{eo5} are introduced in [37, 38, 39, 68] to stabilize the convection dominated problem. The kernel J_{eo6} is introduced in [40] to capture the numerical instability arising from the incompressibility condition. The last kernel is introduced in [38] to control the nonconformity arising from the pressure term in Darcy's law.
However, the essential kernels for the presented problem which is used to stabilize because of the lack of coercivity condition in the deformation tensor form is

$$\mathbf{J}_{eo1} = \sum_{\text{edge E}} \frac{\gamma\nu}{h_E} \int_E [\boldsymbol{u}][\boldsymbol{v}] ds, \tag{4.13a}$$

$$\mathbf{J}_{eo2} = \sum_{\text{edge E}} \max(\gamma\nu h_E, \gamma^* h_E^2) \int_E [\boldsymbol{\nabla u}][\boldsymbol{\nabla v}] ds. \tag{4.13b}$$

where h_E is length of the element edge, ν whether it can be equal the viscosity(μ) or the regularized effective viscosity(ν_ϵ). γ and γ^* are free parameters. The optimal choice for the parameters γ and γ^* has not been accurately recognized yet. Clearly, the accuracy of the results is quite sensitive to the choice of the free parameters. In viscoplastic fluid, the behavior of convergence of the solver is quite associated to the relation between the free parameter of the introduced kernel and viscoplastic flow parameters (ϵ, τ_s, Re). The value of γ and γ^* are accompanied strongly with the decreasing of ϵ or increasing of τ_s and

Re. However, in the present study, we optimize from the experience with the viscoplastic work that the accuracy must be preserved for the computing parameters in connection with the kernel parameters and the viscoplastic flow parameters as follows:

(a) if $\frac{\epsilon}{\tau_s Re} < 10^{-3}$ then γ and $\gamma^* \leq 0.5$
(b) if $\frac{\epsilon}{\tau_s Re} \geq 10^{-3}$ then $\gamma \propto \frac{1}{(\epsilon)^{1/4}}$ and $\gamma^* \propto \frac{1}{(\epsilon)^{1/2}}$.

For the presented work we have preferred to work with the second kernel $\mathbf{J}_{eo2}(\mathbf{J})$, since in the finest meshes the first kernel $\mathbf{J}_{eo1}$ has a big weight which leads us to pay more attention to adapt the kernel parameters. The second kernel reads in the discrete form

$$\mathbf{J}_h = \sum_{\text{edge E}} \max(\gamma \nu h_E, \gamma^* h_E^2) \int_E [\boldsymbol{\nabla} \boldsymbol{u}_h][\boldsymbol{\nabla} \boldsymbol{v}_h] ds. \tag{4.14}$$

The work with edge oriented stabilization kernel might increase the stencil of the matrix since the FEM basis functions and the basis of the kernels do not have a common local support. This might be a way to choose the reduced integration such as mid point rule to have different amount of additional memory requirements (see [166]).
The addition of the stabilization allows us to rewrite the equations with the associated ellipticity and LBB conditions in the following compact form:

$$b(\boldsymbol{u}_h, \boldsymbol{u}_h, \boldsymbol{v}_h) + \bar{a}(\boldsymbol{u}_h, \boldsymbol{v}_h) - c(p_h, \boldsymbol{v}_h) = (\boldsymbol{f}, \boldsymbol{v}_h), \tag{4.15a}$$
$$c(q_h, \boldsymbol{u}_h) = 0, \tag{4.15b}$$
$$\bar{a}(\boldsymbol{u}_h, \boldsymbol{v}_h) \geq c \left\| \boldsymbol{u}_h \right\| \left\| \boldsymbol{v}_v \right\|, \tag{4.15c}$$
$$\inf_{q_h \in Q_h} \sup_{\boldsymbol{v}_h \in \mathbf{V}_h} \frac{(\boldsymbol{\nabla} \cdot \boldsymbol{v}_h, q_h)}{\left\| \boldsymbol{v}_h \right\|_{V_h} \left\| q_h \right\|_{Q_h}} \geq \beta. \tag{4.15d}$$

where,

$$\bar{a}(\boldsymbol{u}_h, \boldsymbol{v}_h) = a(\boldsymbol{u}_h, \boldsymbol{v}_h) + (\mathbf{J}_h, \boldsymbol{v}_h) \tag{4.16}$$

This leads us to update the equation of the residual in the discrete form to get

$$\mathbf{R}(\boldsymbol{x}) = b(\boldsymbol{u}_h, \boldsymbol{u}_h, \boldsymbol{v}_h) + \bar{a}(\boldsymbol{u}_h, \boldsymbol{v}_h) - c(p_h, \boldsymbol{v}_h) - (\boldsymbol{f}, \boldsymbol{v}_h) \simeq 0, \tag{4.17}$$

4.3 Saddle Point Problem

Saddle point forms arise in many scientific applications specially CFD and CSM problems, where the mixed finite element method is probably one of the most prominent. There is a great variety of solution and preconditioning methods for the saddle point problems coming from the fluid fields. Typically, the general form for the saddle point problem can be written in the following forms

$$\boldsymbol{A}\boldsymbol{x} = \mathbf{b} \quad \text{or} \quad \begin{pmatrix} \mathbf{A} & \mathbf{B} \\ \mathbf{B}^T & \mathbf{C}_s \end{pmatrix} \begin{pmatrix} \boldsymbol{u} \\ p \end{pmatrix} = \begin{pmatrix} \boldsymbol{f} \\ g \end{pmatrix}, \tag{4.18}$$

where $\boldsymbol{A} = \begin{pmatrix} \mathbf{A} & \mathbf{B} \\ \mathbf{B}^T & \mathbf{C}_s \end{pmatrix}$, $\boldsymbol{x} = \begin{pmatrix} \boldsymbol{u} \\ p \end{pmatrix}$ and $\mathbf{b} = \begin{pmatrix} \boldsymbol{f} \\ g \end{pmatrix}$.
In the case of stable finite element pairs the matrix $\mathbf{C}_s = 0$, therefore we have under this condition the standard saddle point problem. The most popular solution techniques described to solve this the

standard form are the decoupled methods and coupled methods. In the other side we can describe briefly the preconditioners which accelerate the solution procedures.
For the decoupled methods which decouple the two unknown vectors $\boldsymbol{u}$ and p and reduce the solution of the overall system to the solution of the smaller subsystems. So that the matrix $\boldsymbol{A}$ can be decomposed to the following:

$$\boldsymbol{A} = \begin{pmatrix} \mathbf{I} & 0 \\ \mathbf{B}^T\mathbf{A}^{-1} & \mathbf{I} \end{pmatrix} \begin{pmatrix} \mathbf{A} & \mathbf{B} \\ 0 & \mathbf{S} \end{pmatrix}, \tag{4.19}$$

where $\mathbf{S} = \mathbf{B}^T\mathbf{A}^{-1}\mathbf{B}$ is the pressure schur complement of the matrix $\boldsymbol{A}$. The overall system can be reduced to the following smaller two subsystems:

$$\mathbf{S}p = \mathbf{B}^T\mathbf{A}^{-1}\boldsymbol{f}, \tag{4.20a}$$

$$\mathbf{A}\boldsymbol{u} = \boldsymbol{f} - \mathbf{B}p. \tag{4.20b}$$

From Eq.(4.20a) the inverse of the Schur complement matrix is not easy to compute as a result the iterative method is successful to be perform. This iteration is called the classical Uzawa algorithm and this case is called pressure Schur complement(PSC).
For the coupled method we solve the system in one form which is:

$$\begin{pmatrix} \mathbf{A} & \mathbf{B} \\ \mathbf{B}^T & 0 \end{pmatrix} \begin{pmatrix} \boldsymbol{u} \\ p \end{pmatrix} = \begin{pmatrix} \boldsymbol{f} \\ \boldsymbol{g} \end{pmatrix}. \tag{4.21}$$

This system can be solved iteratively by the following technique

$$\boldsymbol{x}^{n+1} = \boldsymbol{x}^n - \omega^n\mathbf{C}^{-1}(\boldsymbol{A}(\boldsymbol{x}^n)\boldsymbol{x}^n - \boldsymbol{b}), \tag{4.22}$$

where $\omega^n \in (0, 1]$ is a damping parameter which has to be chosen appropriately and $\mathbf{C}$ is a suitable preconditioning matrix. Then, the updated solution could be written with the residual in the following form:

$$\boldsymbol{x}^{n+1} = \boldsymbol{x}^n - \omega^n\mathbf{C}^{-1}\mathbf{R}(\boldsymbol{x}^n), \tag{4.23}$$

where $\mathbf{R}(\boldsymbol{x}^n) = \boldsymbol{A}(\boldsymbol{x}^n)\boldsymbol{x}^n - \boldsymbol{b}$ is the defect(the residual). In this study, this equation represents the core of the introduced coupled solver with relaxation parameter ω^n which is the nonlinear solver and the linear solver to solve the preconditioning. In the nonlinear solver iteration, the iteration should be repeated until $\|\delta\boldsymbol{x}\| = \left\|\boldsymbol{x}^{n+1} - \boldsymbol{x}^n\right\|$ equals the stopping criteria. In other words; the ratio between two residual should be small enough and can be represented by the following condition

$$\frac{\left\|\mathbf{R}(\boldsymbol{x}^{n+1})\right\|}{\|\mathbf{R}(\boldsymbol{x}^n)\|} \leq \omega^n \frac{\left\|\boldsymbol{x}^{n+1}\right\|}{\|\boldsymbol{x}^n\|} \tag{4.24}$$

4.4 Nonlinear Solver

4.4.1 Fixed Point Defect Correction Method

Many nonlinear problems are naturally employing a fixed point iteration strategy. This algorithm represents the easiest way to linearize the nonlinear problem. This strategy might be considered as a simple way to linearize the nonlinear equations and it is relatively easy to be implemented. Nonlinear viscosity models have strongly nonlinear terms as engendered by the diffusion and convective terms. However, the task herein is to employ the strategy to linearize our nonlinear problem which is involved by the stabilization terms. So, the linearized form can be written in the primitive variables as:

$$\boldsymbol{u}^n \cdot \boldsymbol{\nabla}\boldsymbol{u} - \boldsymbol{\nabla} \cdot \nu(\|\mathbf{D}^n\|)\mathbf{D}(\boldsymbol{u}) + \sum_E \max(\gamma h_E, \gamma^* h_E^2) \int_E \nu(\|\mathbf{D}^n\|)[\boldsymbol{\nabla}\boldsymbol{u}]\boldsymbol{\nabla} + \boldsymbol{\nabla} p = \boldsymbol{f} \quad in \quad \boldsymbol{\Omega}, \tag{4.25a}$$

$$\boldsymbol{\nabla} \cdot \boldsymbol{u} = 0 \qquad in \quad \boldsymbol{\Omega}. \tag{4.25b}$$

The basic nonlinear iteration due to the fixed point linearization is

$$\boldsymbol{x}^{n+1} = \boldsymbol{x}^n - \omega^n \mathbf{C}^{-1}\mathbf{R}(\boldsymbol{x}^n), \tag{4.26}$$

where ω^n is damping parameter and $\mathbf{C}$ is a suitable preconditioning matrix to accelerate the solution behavior. The appropriate preconditioning matrix might be chosen as a part or the whole from the following form (see [214]).

$$\mathbf{C} = \begin{pmatrix} \mathbf{A} & \mathbf{B} \\ \mathbf{B}^T & 0 \end{pmatrix} \tag{4.27}$$

where $\mathbf{A}$ represents the following term;

$$\mathbf{A} = (\boldsymbol{u}^n \cdot \boldsymbol{\nabla}\boldsymbol{u}, \boldsymbol{v}) + \int_{\boldsymbol{\Omega}} \nu(\|\mathbf{D}^n\|)[\mathbf{D}(\boldsymbol{u}) : \mathbf{D}(\boldsymbol{v})] + \sum_E \max(\gamma h_E, \gamma^* h_E^2) \int_E \nu(\|\mathbf{D}^n\|)[\boldsymbol{\nabla}\boldsymbol{u}][\boldsymbol{\nabla}\boldsymbol{v}]. \tag{4.28}$$

This method is very effective for low and moderate Reynolds numbers, but the main drawback is the rate of convergence which might be linear at the most. Then, it takes a greater number of iterations to converge. However, this method can be described by the following algorithm:

---

given $\boldsymbol{x}^o$ *as initial value*
Do while $\boldsymbol{d}^n \leq TOL$
defect: $\boldsymbol{d}^n = \mathbf{R}(\boldsymbol{x}^n)$
correction step: $\delta\boldsymbol{x}^n = \mathbf{C}^{-1}(\boldsymbol{x}^n)\boldsymbol{d}^n$
updating step: $\boldsymbol{x}^{n+1} = \boldsymbol{x}^n - \omega^n \delta\boldsymbol{x}^n$
end

The fruitful part of the fixed method is simple to program and has a large region of convergence. The un-delicated part is linearly to converge and the rate of convergence is pretty slow. Therefore, it is always used as good start for the fast nonlinear solvers, for instance Newton method and quasi-Newton method.

4.4.2 Newton Method

Newton method is characterized by the fact that it is quadratically converging process. Therefore, once it converges it requires only a few iterations. A typical disadvantage of Newton method is usually that a good initial solution is required which is considered the most cumbersome part of this method. One can use the result of some few fixed point iterations, a so-called continuation method to start with or one level above. For the Newtonian fluids, the former would be very efficient as a starting value merely at low Reynolds numbers but appear to be ineffective at large Reynolds numbers. The two later has been suggested for a large Reynolds number problems to start with a small Reynolds number , compute the solution and use this solution as an initial guess for a larger Reynolds number.
For the viscoplastic fluid, the former is usually a good starting for the Newton process, but the main drawback is that the starting value is associated with the values of characterizing viscoplastic parameters(Reynolds number(Re), the yield stress(τ_s) and the regularization parameter(ϵ)). The second is roughly ineffective due to the dependency and severalty of the characterizing viscoplastic parameters. To start with a high value of ϵ to speed up the convergence of Newton process for the lower values could work only at the small values of τ_s, similarly, to start with a low value of τ_s to compute at higher values

could work only at high values of ϵ. While the later is quite prominent to get a quick results.
However, to apply Newton method, the derivative of the function $\mathbf{R}$ is required which can be calculated numerically by using central finite difference or analytically by applying Frechet derivative on the nonlinear function $\mathbf{R}$. In fact, the analytical Jacobian matrix for a large and complicated problem is usually difficult and error-prone, even with the help of symbolic differentiation, especially as the complexity increases. In this sense, the finite difference approach proves to be an efficient way to compute the derivatives and has the advantage that one needs only the residual function $\mathbf{R}(\boldsymbol{x})$ as a 'black box'.
Let us express the Newton method in its continuous form for the considered nonlinear terms in a separate way by applying Frechet derivative to get the following:

$$(\boldsymbol{u}\cdot\boldsymbol{\nabla}\boldsymbol{u},\boldsymbol{v}) = (\boldsymbol{u}^n\cdot\boldsymbol{\nabla}\boldsymbol{u},\boldsymbol{v}) + (\boldsymbol{u}\cdot\boldsymbol{\nabla}\boldsymbol{u}^n,\boldsymbol{v}), \tag{4.29a}$$

$$(\boldsymbol{u}\cdot\boldsymbol{\nabla}\boldsymbol{u})(\boldsymbol{u}\cdot\boldsymbol{\nabla}\boldsymbol{v}) = (\boldsymbol{u}^n\cdot\boldsymbol{\nabla}\boldsymbol{u}^n)(\boldsymbol{u}\cdot\boldsymbol{\nabla}\boldsymbol{v}) + (\boldsymbol{u}^n\cdot\boldsymbol{\nabla}\boldsymbol{u})(\boldsymbol{u}^n\cdot\boldsymbol{\nabla}\boldsymbol{v}) + (\boldsymbol{u}\cdot\boldsymbol{\nabla}\boldsymbol{u}^n)(\boldsymbol{u}^n\cdot\boldsymbol{\nabla}\boldsymbol{v}), \tag{4.29b}$$

$$\nu(\|\boldsymbol{\nabla}\boldsymbol{u}^n\|)[\boldsymbol{\nabla}\boldsymbol{u}:\boldsymbol{\nabla}\boldsymbol{v}] = \nu^n(\|\boldsymbol{\nabla}\boldsymbol{u}\|)[\boldsymbol{\nabla}\boldsymbol{u}:\boldsymbol{\nabla}\boldsymbol{v}] + \frac{\partial\nu^n(\|\boldsymbol{\nabla}\boldsymbol{u}\|)}{\partial\|\boldsymbol{\nabla}\boldsymbol{u}\|^2}[\boldsymbol{\nabla}\boldsymbol{u}^n:\boldsymbol{\nabla}\boldsymbol{u}][[\boldsymbol{\nabla}\boldsymbol{u}^n:\boldsymbol{\nabla}\boldsymbol{v}], \tag{4.29c}$$

$$\nu^n(\|\mathbf{D}\|)[\mathbf{D}(\boldsymbol{u}):\mathbf{D}(\boldsymbol{v})] = \nu^n[\mathbf{D}(\boldsymbol{u}):\mathbf{D}(\boldsymbol{v})] + \frac{\partial\nu^n(\|\mathbf{D}\|)}{\partial\|\mathbf{D}\|^2}[\mathbf{D}(\boldsymbol{u}^n):\mathbf{D}(\boldsymbol{u})][\mathbf{D}(\boldsymbol{u}^n):\mathbf{D}(\boldsymbol{v})]. \tag{4.29d}$$

Where $\nu^n = \nu(\|\mathbf{D}(\boldsymbol{u}^n)\|)$ and $\mathbf{D}^n = \mathbf{D}(\boldsymbol{u}^n)$. However, the continuous Newton method might simply be written for the primitive variable in the following form:

$$\begin{array}{l}(\boldsymbol{u}^n\cdot\boldsymbol{\nabla}\boldsymbol{u},\boldsymbol{v}) + \delta_c(\boldsymbol{u}\cdot\boldsymbol{\nabla}\boldsymbol{u}^n,\boldsymbol{v})\\ + \int_{\boldsymbol{\Omega}}(\nu^n[\mathbf{D}(\boldsymbol{u}):\mathbf{D}(\boldsymbol{v})] + \delta_d\nu^n_{\|\mathbf{D}\|^2}[\mathbf{D}^n:\mathbf{D}(\boldsymbol{u})][\mathbf{D}(\boldsymbol{u}^n):\mathbf{D}(\boldsymbol{v})])\\ + \sum_E \max(\gamma\nu h_E,\gamma^* h_E^2)\int_E[\boldsymbol{\nabla}\boldsymbol{u}][\boldsymbol{\nabla}\boldsymbol{v}] + (\boldsymbol{\nabla}p,\boldsymbol{v}) = (\boldsymbol{f},\boldsymbol{v}) \quad in \quad \boldsymbol{\Omega}.\end{array} \tag{4.30}$$

The basic nonlinear iteration due to the Newton linearization is:

$$\boldsymbol{x}^{n+1} = \boldsymbol{x}^n - \omega^n\mathbf{C}^{-1}\mathbf{R}(\boldsymbol{x}^n), \tag{4.31}$$

where ω^n is damping parameter which has to be appropriately chosen from (0,1] and $\mathbf{C}$ is the Jacobian preconditioning matrix, which can be written in the following continuous form:

$$\mathbf{C} = \begin{pmatrix}\mathbf{A} + \delta_c(\boldsymbol{u}\cdot\boldsymbol{\nabla}\boldsymbol{u}^n,\boldsymbol{v}) + \delta_d\int_{\boldsymbol{\Omega}}\nu^n_{\|\mathbf{D}\|^2}[\mathbf{D}^n:\mathbf{D}(\boldsymbol{u})][\mathbf{D}^n:\mathbf{D}(\boldsymbol{v})] & \mathbf{B}\\ \mathbf{B}^T & 0\end{pmatrix}, \tag{4.32}$$

where ν^n represents the regularized velocity $\nu(\|\mathbf{D}(\boldsymbol{u}^n)\|,\epsilon)$, $\nu_{\|\mathbf{D}\|^2} = \frac{\partial\nu}{\partial\|\mathbf{D}\|^2}$, δ_c and δ_d are free parameters to switch between Newton and fixed point method which must be chosen from $[0,1]$. Therefore, the corresponding values for fixed point are zeros and for full Newton are ones. $\mathbf{A}$ represents the fixed point terms;

$$\mathbf{A} = (\boldsymbol{u}^n\cdot\boldsymbol{\nabla}\boldsymbol{u},\boldsymbol{v}) + \nu^n[\mathbf{D}(\boldsymbol{u}):\mathbf{D}(\boldsymbol{v})] + \sum_E \max(\gamma\nu h_E,\gamma^* h_E^2)\int_E \nu(\|\mathbf{D}^n\|)[\boldsymbol{\nabla}\boldsymbol{u}][\boldsymbol{\nabla}\boldsymbol{v}]. \tag{4.33}$$

On the other hand, the Jacobian can be approximated by using finite differences as

$$\frac{\partial\mathbf{R}(\boldsymbol{x}^n)}{\partial\boldsymbol{x}}|_{ij} \approx \frac{\mathbf{R}_i(\boldsymbol{x}^n + \varepsilon\boldsymbol{e}_j) - \mathbf{R}_i(\boldsymbol{x}^n - \varepsilon\boldsymbol{e}_j)}{2\varepsilon}, \tag{4.34}$$

where $\boldsymbol{e}_j$ is column j of the identity matrix and ε is a suitable step length. A straight forward implementation of the above equation requires computing $\mathbf{R}(\boldsymbol{x}^n + \varepsilon\boldsymbol{e}_j)$ for each j, i.e NEQ evaluations of $\mathbf{R}$ at displacements from $\boldsymbol{x}$. From the view of numerical sense, it would be easier to use by applying the finite

difference technique(central) for Newton method in particular for the highly nonlinear problems. So, the preconditioning matrix is:

$$\mathbf{C} = [\frac{\partial \mathbf{R}(\boldsymbol{x}^n)}{\partial \boldsymbol{x}}]_{ij}. \tag{4.35}$$

To solve the previous nonlinear system with the preconditioning matrix '$\mathbf{C}^{-1}$', and the initial guess $\boldsymbol{x}^o$, one can compute the sequence iterates $\boldsymbol{u}$ to satisfy the following Newton iterative algorithm,

---

given $\boldsymbol{x}^o$ *as initial value*
Do while $\boldsymbol{d}^n \leq TOL$, *n=0,..*
defect: $\boldsymbol{d}^n = \mathbf{R}(\boldsymbol{x}^n)$,
correction step: $\delta \boldsymbol{x}^n = \mathbf{C}^{-1}(\boldsymbol{x}^n)\boldsymbol{d}^n$,
updating step: $\boldsymbol{x}^{n+1} = \boldsymbol{x}^n - \omega^n \delta \boldsymbol{x}^n$.
end

Here, $\boldsymbol{x}^o$ is the initial value of the solution vector $\boldsymbol{x}^{n+1}$. It is known that if the initial value is close to the exact solution and the Jacobian is invertible then the Newton Process will converge quadratically. Thus, $\left\|\mathbf{R}(\boldsymbol{x}^{n+1})\right\| \leq c \left\|\mathbf{R}(\boldsymbol{x}^n)\right\|^2$. The most costly part of the Newton iteration is the solving of the Newton correction step.

4.4.3 Preconditioning Matrix

To explore the concept of preconditioning in Fixed Point Method, choose the matrix $\mathbf{C}^{-1}$ to apply it on the residual to have the increment. The core idea of preconditioning is to accelerate the convergence with a Krylov subspace method. The idea to construct $\mathbf{C}$ comes from two strategies:
The first strategy is Algebraic Preconditioning Strategy which means, one can derive the matrix $\mathbf{C}$ from the global matrix independently about the mesh and problem characteristics. The second strategy is the Problem Based Preconditioners for instance, the poplar choices for the preconditioning $\mathbf{C}$ for Navier-Stokes equations (see [214]).
Regarding The first strategy, the most famous ones for this type are Jacobi, Gauss-Seidel and incomplete factorization.
The preconditioner is chosen to be the diagonal of the global matrix in Jacobi preconditioning. While this preconditioner is very cheap to construct, it only reduces the number of iteration by a small amount when comparatively with sophisticated techniques. However, Jacobi preconditioner performs effectively, when the matrix coefficient is diagonally dominant.
In Gaus-Seidel preconditioning, the preconditioner is chosen to be the difference between the diagonal and the lower triangular matrix. This preconditioner is usually effective, but it is pretty dependent on the ordering of unknowns in the system, which means if the matrix is poorly ordered, then it converges slowly.
The core idea of the third one which is ILU preconditioner is to ignore any fill-in that occurs with a certain tolerance. the fruitful advantage for these methods is to choose purely algebraically. Probably, the choice of the fill tolerance in the realistic problem can be a hard quantity to determine. The drawback of this method is not scalable, and there is difficulty with implementation however, it is very useful as smoother in multigrid techniques.

4.5 Multigrid Techniques

The core steps of the multigrid techniques are to smooth the defect, restrict it to a coarser grid, compute a defect correction, and prolongate it back to update the iteration vector. The problem now is, the coarse grid correction is actually based on a different configuration since it is computed on a larger domain. Hence, the coarse grid correction cannot be optimal and might even be harmful for the convergence process. The higher the number of levels in the grid hierarchy, the greater the difference in size between the domain on the finest grid and that on the coarsest grid will be. consequently, we have to expect that the convergence behavior of the multigrid solver is not level independent, i.e., one of the most important properties of the typical multigrid methods is lost. Furthermore, standard multigrid theory does not fully apply such that convergence can not be guaranteed. However, the main features of multigrid method are the smoothing on the current grid and error correction on a coarser grid. The smoothing step has the effect of damping out the oscillatory part of the error and the smooth part of the error can then be accurately corrected on the coarser grid. In [121], it was discussed five sufficient conditions [$\mathbf{H}1 - \mathbf{H}5$], which allow us to conclude that some standard multigrid solvers for quite general discretizations of mixed problems converge at optimal convergence rates. Their considerations include non-nested discretizations and even discretization with different finite element ansatz functions on different levels. We will outline in the following sections a multigrid approach for the proposed finite elements $\tilde{Q}_1 Q_0$ and $Q_2 P_1$ which are presented in the previous chapter. For the multigrid analysis, we will apply the general framework which develops in [214] for our problem. For the sake of completeness, we will repeat some of the argument used in [166].

4.5.1 Multigrid Discretization

let $\mathbf{T}$ denote the coarse macro triangulation. The finer macro triangulations $\mathbf{T}_k, k \geq 1$, are obtained by successive regular refinement for the parent quadrilaterals. Note that the mesh size of $\mathbf{T}_k$ is just the half of the mesh size of $\mathbf{T}_{k-1}$. Let $\mathbf{V}_k$, and Q_k denote the spaces $\mathbf{V}_h^k$ and Q_h^{k-1} with respect to the triangulation $\mathbf{T}_k$, noting that the sequences of velocity spaces $\{V_k^d\}_{k\geq 0}$ and the sequences $\{Q_k\}_{k\geq 0}$ of pressure spaces are non-nested. This causes by the non-nested triangulations which are, however, derived from the nested macro triangulations (see [137]).

4.5.2 Matrix Representation

Let $\{\phi_{k,i} : i \in I_k\}$ and $\{\psi_{k,j} : j \in J_k\}$ be bases of the spaces $\mathbf{V}_k^d$ and Q_k, respectively, where I_k, J_k denote the corresponding index sets. The solution $(\boldsymbol{u}_h, p_h)$ of the problem with $\mathbf{V}_h^k$ and Q_h^{k-1} based on the triangulation $\mathbf{T}_h = \mathbf{T}_k$ will be denoted by $(\boldsymbol{u}_k, p_k)$. The unique representations

$$\boldsymbol{u}_k = \sum_{i\in I_k} u_{k,i}\phi_{k,i}, \qquad p_k = \sum_{j\in J_k} p_{k,j}\psi_{k,j}, \tag{4.36}$$

define the finite element isomorphisms $\Phi_k : \mathbf{U}_k \to \mathbf{V}_k^d$, $\Psi_k : P_k \to Q_k$ between the vector spaces $\mathbf{U}_k = R^{dim V_k^d}$, $P_k = R^{dim Q_k}$ of the coefficient vectors $\boldsymbol{u}_k = (u_{k,i})_{i\in I_k}$, $p_k = (p_{k,j})_{j\in J_k}$ and the finite element spaces $\mathbf{V}_k^d$, and Q_k, respectively. Let a_k be the bilinear form a_h based on $\mathbf{T}_h = \mathbf{T}_k$. We introduce the finite element matrices A_k and B_k having the entries $a_{k,ij} = a_k(\phi_{k,j}, \phi_{k,i})$ and $b_{k,ij} = b(\psi_{k,i}, \phi_{k,j})$. Now the discrete problem is equivalent in such level 'k' to

$$\begin{pmatrix} \mathbf{A}_k + \mathbf{J}_k & \mathbf{B}_k \\ \mathbf{B}_k^T & 0 \end{pmatrix} \begin{bmatrix} \boldsymbol{u}_k \\ p_k \end{bmatrix} = \begin{bmatrix} \boldsymbol{f}_k \\ g_k \end{bmatrix}. \tag{4.37}$$

with $\boldsymbol{f}_{k,i} = (\boldsymbol{f}, \phi_{k,i})$ and $\boldsymbol{g}_{k,i} = (\boldsymbol{g}, \psi_{k,i})$. Note that $\mathbf{A}_k$ is not symmetric matrix. We will use in the vector spaces $\mathbf{U}_k$ and P_k the usual Euclidean norms scaled by suitable factors such that the following norm equivalences

$$\mathbf{C}^{-1} \|v_k\|_{\mathbf{U}_k} \leq \|\boldsymbol{v}_{hk}\|_0 \leq C \|\boldsymbol{v}_k\|_{\mathbf{U}_k}, \quad \forall \boldsymbol{v}_{hk} \in \mathbf{V}_k^d, \tag{4.38a}$$

$$\mathbf{C}^{-1} \|q_k\|_{P_k} \leq \|q_{hk}\|_0 \leq C \|q_k\|_{P_k}, \quad \forall q_{hk} \in Q_k. \tag{4.38b}$$

are satisfied with a constant C which is independent of both the mesh and the level of refinement (see [137]).

4.5.3 Smoothers

For smoothing the error of an approximate solution of the previous saddle point equation which can be transformed to

$$\boldsymbol{A}\boldsymbol{x} = \mathbf{b}, \tag{4.39}$$

where $\boldsymbol{x}^n$ here refers to the previous iteration solution. Assume here we have the basic iteration, which is

$$\boldsymbol{x}^{n+1} = \boldsymbol{x}^n - \omega^n \mathbf{C}^{-1}(\boldsymbol{A}(\boldsymbol{x}^n)\boldsymbol{x}^n - \mathbf{b}). \tag{4.40}$$

The smoothing properties of the previous equation can be studied with different choices of the matrix $\mathbf{C}$. Therefore, we study the iterative schemes as smoothers in coupled multigrid methods. On each level of a coupled multigrid method, a system of a saddle point form has to be solved approximately. The smoother used to damp the highly oscillating error modes of these systems.

4.5.3.a The Vanka Type Smoother

Vanka type smoother is originally proposed by Vanka in [218] for finite difference schemes, is considered as block Gauss-Seidel methods. For the nonconforming $\tilde{Q}_1 Q_0$ finite element discretizations, these are eight velocity degrees of freedom and one pressure degree of freedom, thus in each element a 9×9 linear system of equations have to be solved. But in case of biquadratic conforming finite element $Q_2 P_1$ discretizations these are 18×18 velocity degree of freedom and three pressure degrees of freedom, thus in each element a 21×21 linear system of equations has to be solved too. However, let us denote the block of the matrix $\mathbf{A}$ which is connected with the degrees of freedom of element $\mathcal{T}$ by $\mathbf{A}_\mathcal{T}$ i.e the intersection of the rows and columns of $\mathbf{A}$ with the global indices of $(\boldsymbol{u}, p)$. So that, the generated matrix will be,

$$\begin{pmatrix} \mathbf{A}_\mathcal{T} + \mathbf{J}_\mathcal{T} & \mathbf{B}_\mathcal{T} \\ \mathbf{B}_\mathcal{T}^T & 0 \end{pmatrix}. \tag{4.41}$$

In addition to, when we defined the diagonal matrix of $\mathbf{A}_\mathcal{T}$ in the way $\mathbf{D}_\mathcal{T} = diag(\mathbf{A}_\mathcal{T})$, the form of the element matrix will be

$$\boldsymbol{D}_\mathcal{T} = \begin{pmatrix} \mathbf{D}_\mathcal{T} + \mathbf{J}_\mathcal{T} & \mathbf{B}_\mathcal{T} \\ \mathbf{B}_\mathcal{T}^T & 0 \end{pmatrix}. \tag{4.42}$$

From that point, we can define two kind of Vanka smoother which are full Vanka smoother and diagonal Vanka smoother(see [166]).

(1) Full Vanka Smoother

The full or stabilized Vanka smoother computes in each element the updated velocity and pressure values by the following iteration

$$\begin{bmatrix} \boldsymbol{u}^{n+1} \\ p^{n+1} \end{bmatrix} = \begin{bmatrix} \boldsymbol{u}^{n} \\ p^{n} \end{bmatrix} - \omega^n \boldsymbol{A}_{\mathcal{T}}^{-1} \left(\boldsymbol{A}_{\mathcal{T}} \begin{bmatrix} \boldsymbol{u}^{n} \\ p^{n} \end{bmatrix} - \begin{bmatrix} \boldsymbol{f}^{n} \\ g^{n} \end{bmatrix} \right). \tag{4.43}$$

(2) Diagonal Vanka Smoother

The Diagonal Vanka smoother computes in each element the updated velocity and pressure values by the following iteration

$$\begin{bmatrix} \boldsymbol{u}^{n+1} \\ p^{n+1} \end{bmatrix} = \begin{bmatrix} \boldsymbol{u}^{n} \\ p^{n} \end{bmatrix} - \omega^n \boldsymbol{D}_{\mathcal{T}}^{-1} \left(\boldsymbol{D}_{\mathcal{T}} \begin{bmatrix} \boldsymbol{u}^{n} \\ p^{n} \end{bmatrix} - \begin{bmatrix} \boldsymbol{f}^{n} \\ g^{n} \end{bmatrix} \right). \tag{4.44}$$

4.5.3.b Vanka Variants

Vanka variant is the method to choose the subregions to build the local system (see [166]).

(1) The Cell-Based Vanka smoother

In this case the patches $\boldsymbol{\Omega}_i$ may consist only one element($\mathcal{T}$) which means the global stiffness matrix. This global matrix is restricted to the single quadrilaterals of the mesh and the corresponded algebraic system has to be solved (see [166]). The necessary calculations can be calculated for this variant in the following:

$$\boldsymbol{r}_{\mathcal{T}}^{n} = \boldsymbol{A}_{\mathcal{T}}(\boldsymbol{x}^n)\boldsymbol{x}_{\mathcal{T}}^{n} - \boldsymbol{f}_{\mathcal{T}}^{n}, \quad \text{local residual,} \tag{4.45a}$$

$$\delta\boldsymbol{x}_{\mathcal{T}}^{n} = \boldsymbol{A}_{\mathcal{T}}^{-1}\boldsymbol{r}_{\mathcal{T}}^{n}, \quad \text{local correction,} \tag{4.45b}$$

$$\boldsymbol{x}_{\mathcal{T}}^{n+1} = \boldsymbol{x}_{\mathcal{T}}^{n} - \omega^n \delta\boldsymbol{x}_{\mathcal{T}}^{n}, \quad \text{update of global solution.} \tag{4.45c}$$

Here, ω^n is the relaxation parameter. The most essential feature of this smoother is its flexibility to solve the $n \times n$ saddle point systems arising from the mixed formulation. Of course, this feature makes it very attractive from an point of view of implementation as it can be applied to arbitrary coupled equation systems without deeper knowledge about the underlying problem. The relaxation parameter ω^n is different from the global damping in the multigrid method. This parameter is used to relax the local correction and in our case it is always in (0,1].

(2) The Patch-Based Vanka Smoother

The idea of the patch-based is to loop over such group of elements in the mesh instead of all element (see [166]). In [202] the smoothing is done by a loop over all pressure points p_i. To each p_i, a patch consisting of the cells having p_i in common, is associated. This approach has some disadvantages which are
1) the local systems are larger than the previous one
2) the overlapping of the patches which results some increasing computational cost.
The same procedure to calculate the updated velocity can be applied here but instead of element; it will be the patch(pat).

$$\boldsymbol{r}_{pat}^{n} = \boldsymbol{A}_{pat}(\boldsymbol{x}^n)\boldsymbol{x}_{pat}^{n} - \boldsymbol{f}_{pat}^{n}, \quad \text{local residual,} \tag{4.46a}$$

$$\delta\boldsymbol{x}_{pat}^{n} = \boldsymbol{A}_{pat}^{-1}\boldsymbol{r}_{pat}^{n}, \quad \text{local correction,} \tag{4.46b}$$

$$\boldsymbol{x}_{pat}^{n+1} = \boldsymbol{x}_{pat}^{n} - \omega^n \delta\boldsymbol{x}_{pat}^{n}, \quad \text{update of global solution.} \tag{4.46c}$$

(3) The Edge Oriented Vanka Smoother

This smoother is relatively used for the lower order nonconforming finite element method to incorporate the full jump into the preconditioning step by using the edge oriented patch $\boldsymbol{\Omega}_{E,i}$ (see [166]). This will

keep the size of the local problem small and the full jump matrix $\mathbf{J}$ will be used for the preconditioning steps. The extension of the matrix for $\tilde{Q}_1 Q_0$ to support the jump term leads to a 5×5 FEM matrix block of the type

$$\begin{pmatrix} \mathbf{A}_{\mathcal{T}} + \mathbf{J}_{\mathcal{T}} & \mathbf{B}_{\mathcal{T}} \\ \mathbf{B}_{\mathcal{T}}^T & 0 \end{pmatrix} \tag{4.47}$$

To keep the size of the local problem small, the element matrix is disassembled to its edge contributions,

$$\boldsymbol{A}_{\mathcal{T}} = \sum_{i=1}^{m} \boldsymbol{A}_{\mathcal{T}}^{E_i}, \tag{4.48}$$

where $\boldsymbol{A}_{\mathcal{T}}^{E_i}$ is the contribution of the edge E_i to $\boldsymbol{A}_{\mathcal{T}}$ and m is the number of the edges on the cell $\mathcal{T}$. The edge stiffness matrix may contain the contribution of all elements

$$\boldsymbol{A}^{E_i} = \sum_{\mathcal{T} \in \boldsymbol{\Omega}_i} \boldsymbol{A}_{\mathcal{T}}^{E_i} = \boldsymbol{A}_{\boldsymbol{\Omega}_i}^{E_i}. \tag{4.49}$$

Then, one basic iteration can be described as follows

$$\begin{bmatrix} \boldsymbol{u}^{n+1} \\ p^{n+1} \end{bmatrix} = \begin{bmatrix} \boldsymbol{u}^{n} \\ p^{n} \end{bmatrix} - \omega^n \sum_{i \in I} [\boldsymbol{A}_{\boldsymbol{\Omega}_i}^{E_i}]^{-1} \left(\sum_{i \in I} \boldsymbol{A}_{\boldsymbol{\Omega}_i}^{E_i} \begin{bmatrix} \boldsymbol{u}^{n} \\ p^{n} \end{bmatrix} - \begin{bmatrix} \boldsymbol{f}^{n} \\ g^{n} \end{bmatrix} \right). \tag{4.50}$$

Where I is the total number of internal edges. This blocking strategy is different from that used in [189] to generate isotropic subdomains for stabilizing strong mesh anisotropy. Indeed, for the edge oriented patches the number of block matrices depends on the number of edges and not on the number of patches itself.

(4)Pressure Schur Complement Smoother

The well-known pressure schur complement scheme is the SIMPLE algorithm by Patankar and Spalding [169]. The idea of pressure schur complement (PSC) matrix is obtained by elimination of the velocity first, then deduction of the equation for the pressure which acts as Lagrange multiplier for the incompressibility constraint for the saddle point problem. In fact, if the operator $\mathbf{A}$ is singular, the velocity can be expressed as

$$\boldsymbol{u} = (\mathbf{A} + \mathbf{J})^{-1}(\mathbf{Res}_{\boldsymbol{u}} - \mathbf{B}p), \tag{4.51}$$

and plugged into the discretized continuity equation

$$\mathbf{B}^T \boldsymbol{u} = \mathbf{Res}_p, \tag{4.52}$$

which gives the scalar Schur Complement equation for the pressure

$$\mathbf{B}^T(\mathbf{A} + \mathbf{J})^{-1}\mathbf{B}p = \mathbf{B}^T(\mathbf{A} + \mathbf{J})^{-1}\mathbf{Res}_{\boldsymbol{u}} + \mathbf{Res}_p. \tag{4.53}$$

Where $\mathbf{Res}_{\boldsymbol{u}}$ and $\mathbf{Res}_p$ are the global defects. This idea can be applied in the sense of the local approach which is called local pressure Schur complement approach. This approach is a generalization of the Vanka smoother which acts directly in the element level and is embedded into outer block Jacobi/Gauss-Seidel iteration (see [166]).

(5)Braess-Sarazin Smoother

Braess and Sarazin in [30] studied Stokes equations for pressure Schur complement schemes as smoothers in coupled multigrid methods. This smoother is introduced to improve the well-known pressure Schur complement(SIMPLE algorithm) in [169]. In the case of the Braess-Sarazin smoother the pressure iteration is updated by the current pressure and velocity iterates, but in SIMPLE algorithm the updated pressure iteration depends only on the current pressure iterate, which leads to poor smoothing property (see [30, 169] for details).

4.5.4 Restriction and Prolongation

The multigrid method requires inter-grid transfer operators, but for nonconforming finite element approximations the finite element space of coarser level is not a subspace of the finite element space on a finer level: $\mathbf{V}_{k-1} \nsubseteq \mathbf{V}_k$. Therefore, the natural injection does not work and the restriction I_k^{k-1} from $\mathbf{V}_k$ to $\mathbf{V}_{k-1}$ must explicitly be constructed. This leads to what is known as non-nested multigrid methods. A simple scheme like piecewise linear interpolation and $\mathbf{L}^2$-projection operator are popular candidates. The choice of each of these operators can have an immense effects on convergence rates.

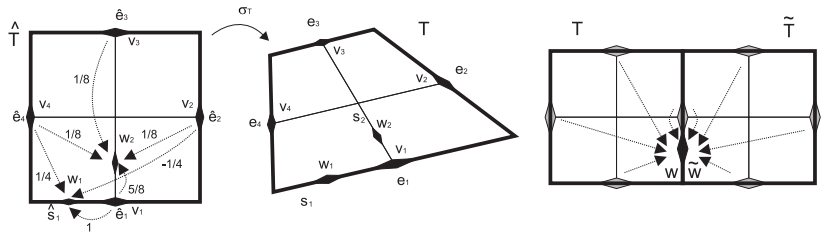

Fig. 4.1. Configuration for local grid transfer operators (from [131]).

4.5.4.a Adaptive Prolongation for $\tilde{Q}_1$

The adaptive prolongation for the rotated $\tilde{Q}_1$ element calculates on all fine edges the corresponding interpolated values due to the given function $\boldsymbol{v}_{2h}$ which is defined via the coefficient $v_i, i = 1, .., 4$ (see [166]). Let us introduce the Aspect-Ratio (AR): the ratio of largest to smallest dimension in an element, for instance one may use the following definition (for further details see [125, 126]).

$$AR = \max\left(\frac{\|m_3 - m_1\|}{\|m_4 - m_2\|}, \frac{\|m_3 - m_1\|}{\|m_4 - m_2\|}\right), \tag{4.54}$$

where $\|.\|$ is the Euclidean norm and $m_i, i = 1, .., 4$ are the midpoints of the quadrilateral element (see Fig.4.1). Then, define the following options for the interpolation operator (see [214]),

1. **Full interpolation:** If $AR \leq AR_0$ the full interpolation is used which reads:
   (a) mean-value on edges as degrees of freedom (d.o.f.)
   $$w_1 = v_1 + \tfrac{1}{4}v_2 + \tfrac{1}{4}v_4 \quad , \quad w_2 = \tfrac{5}{8}v_1 + \tfrac{1}{8}(v_2 + v_3 + v_4)$$
   (b) midpoint on edges as d.o.f.
   $$w_1 = \tfrac{15}{16}v_1 - \tfrac{3}{16}v_2 - \tfrac{1}{16}v_3 + \tfrac{5}{16}v_4 \quad , \quad w_2 = \tfrac{9}{16}v_1 + \tfrac{3}{16}v_2 + \tfrac{1}{16}v_3 + \tfrac{3}{16}v_4$$
2. **Constant interpolation:** If $AR > AR_0$ simply use the constant interpolation which reads:
   $$w_1 = v_1 \quad , \quad w_2 = v_1$$

For the values belonging to the 'macro' edges w_1 (for instance in Fig.4.1 one may take a mean-value by

(a) Simple averaging
$$\frac{w + \tilde{w}}{2} \tag{4.55}$$

(b) Weighted averaging

$$\frac{1}{|\mathcal{T}|+|\tilde{\mathcal{T}}|}(|\mathcal{T}|w+|\tilde{\mathcal{T}}|\tilde{w}). \tag{4.56}$$

It is recorded in [214] that AR_0 should belong to the interval $(10, 100)$. For more numerical investigation we refer to [131].

4.5.4.b Adaptive Prolongation for Q_2

In the conforming finite elements, the natural injection can be applied for the restriction operator, and the prolongation operator can be applied by constructing the biquadratic interpolation. Consider the

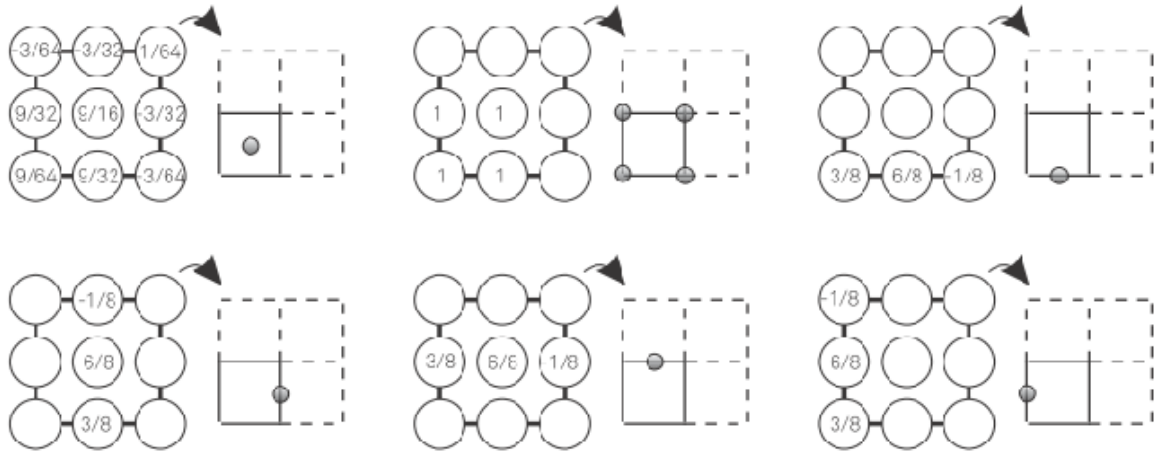

Fig. 4.2. Q2 Prolongation with biquadratic interpolation(see [60]).

macroelement on coarse level say (2h level) and the corresponding refined one is h level, which produced by the classical refinement process (see Fig.4.2). The biquadratic interpolation can be constructed in such a way that to calculate on all fine edges the corresponding interpolating values due to the given function u_{2h} via the coefficients $[u1_h, ..., u9_h]$ in the following way:

$$\begin{aligned}
&[u1_h, ..., u9_h] = [u1_{2h}, u2_{2h}, u3_{2h}, u4_{2h}, \frac{3}{8}u1_{2h} - \frac{1}{8}u2_{2h} + \frac{6}{8}u5_{2h},\\
&\frac{3}{8}u5_{2h} - \frac{1}{8}u7_{2h} + \frac{6}{8}u9_{2h}, -\frac{1}{8}u6_{2h} + \frac{3}{8}u8_{2h} + \frac{6}{8}u9_{2h}, \frac{3}{8}u1_{2h} - \frac{1}{8}u4_{2h} + \frac{6}{8}u8_{2h},\\
&\frac{9}{64}u1_{2h} + \frac{3}{64}u2_{2h} + \frac{1}{64}u3_{2h} - \frac{3}{64}u4_{2h} + \frac{9}{32}u5_{2h} - \frac{3}{32}u6_{2h} - \frac{3}{32}u7_{2h} + \frac{9}{32}u8_{2h} + \frac{9}{16}u9_{2h}].
\end{aligned} \tag{4.57a}$$

4.5.5 Coarse Grid Discretization and Solver

The multigrid algorithm requires an approximation of the fundamental matrix $\boldsymbol{A}$ on the coarse grid denoted by $\bar{\boldsymbol{A}}$. There are basically two ways to choose $\bar{\boldsymbol{A}}$ which are

(i) Discretization coarse grid approximation which is obtained by discretization by the fundamental problem

(ii) Galerkin coarse grid approximation which can be written in the following form

$$\bar{\boldsymbol{A}} = \bar{\mathbf{R}}\boldsymbol{A}\bar{\mathbf{P}}. \tag{4.58}$$

The matrices $\bar{\mathbf{R}}$ and $\bar{\mathbf{P}}$ are the restriction and prolongation operators which are very sparse and have almost a rather irregular sparsity pattern.
Galerkin coarse grid approximation will be useful only if $\bar{\boldsymbol{A}}$ is not much larger than $\boldsymbol{A}$, otherwise the important property of MG, that computing work is proportional to the number of unknowns may get lost. Although the discretization coarse grid approximation seems more straightforward. However, it generally believed that Galerkin coarse grid approximation has some more advantages which can be highlighted in the following items:

(a) On such very coarse grids 'discretization coarse grid approximation' may be unreliable if the coefficients are variable, because these coefficients are sampled in very few points (see [224]). The situation can be remedied by not sampling the coefficients pointwise on the coarse grids, but taking suitable averages. This is, however, precisely that Galerkin coarse grid approximation does accurately and automatically. For the same reason Galerkin coarse approximation is to be used for the interface problems(discontinuous coefficients), in this case the danger of pointwise sampling of coefficients is most obvious.

(b) Galerkin coarse approximation is purely algebraic in nature; no use in made of the underlying differential equation. This requires an input matrix and a right hand side (see [224]).

(c) The material programming such as construction of material matrices and integration in space are merely necessary on the finest grid (see [144]).

(d) This discretization requires only information of the element formulation which means practically it has to be programmed only once (see [144]).

4.5.6 Multigrid Algorithm

In case of viscoplastic problem, the linearization and discretization lead to a large saddle point problem which can be rewritten in the following manner

$$\boldsymbol{A}_n\boldsymbol{x}_n = \boldsymbol{f}_n. \tag{4.59}$$

Let us assume the existence of a hierarchy of levels $k = 1, ..., n$ associated with the triangulation $\mathbf{T}_{h_k}$ with mesh size h_k. On each level k the matrix $\boldsymbol{A}_k$ and the right-hand side $\boldsymbol{f}_k$ need to be assembled, the two level algorithm of multigrid linear solver is described as follows (see [214, 166]):
The k^{th} level iteration $MG(k, \boldsymbol{z}_0, \boldsymbol{g})$ of the multigrid algorithm with initial guess $\boldsymbol{z}_0$ yields an approximation to $\boldsymbol{z}_k$, the solution of

$$\boldsymbol{A}_k\boldsymbol{z} = \boldsymbol{g} \tag{4.60}$$

One step can be described in the following way:
For $k = 1$ on the coarsest level, the direct solver is used

$$MG(1, \boldsymbol{z}_0, \boldsymbol{g}) = \boldsymbol{A}_1^{-1}\boldsymbol{g}. \tag{4.61}$$

- Smoothing step $k > 1$: let $\boldsymbol{z}_l \in \mathbf{V}_l (1 \le l \le m)$ be defined by

$$\boldsymbol{z}_l = \boldsymbol{z}_{l-1} + {\Lambda_k}^{-1}(\boldsymbol{g} - \boldsymbol{A}_k\boldsymbol{z}_{l-1}) \;\; 1 \le l \le m \tag{4.62}$$

  where $\rho(\Lambda_k) \le Ch_k^{-2}$.

- Correction step: Let $\tilde{\boldsymbol{g}} = I_k^{k-1}(\boldsymbol{g} - \boldsymbol{A}_k \boldsymbol{z}_m)$ and let $\boldsymbol{g}_i \in \mathbf{V}_{k-1}$ be defined as

$$\begin{aligned} \boldsymbol{g}_0 &= 0 \\ \boldsymbol{g}_i &= MG(k-1, \boldsymbol{g}_{i-1}, \tilde{\boldsymbol{g}}) \;\; 1 \leq i \leq p. \end{aligned} \tag{4.63}$$

Final output

$$MG(k, \boldsymbol{z}_0, \boldsymbol{g}) = \boldsymbol{z}_m + I_{k-1}^k \boldsymbol{g}_p. \tag{4.64}$$

The efficiency of the multigrid solver mainly depends on the efficiency of its components which are

(a) the matrix-vector multiplication routines for the operators $\boldsymbol{A}_k, k \leq n$,

(b) the smoothers on finer levels and the coarse grid solver,

(c) the grid transfer operators: the prolongation I_{k-1}^k and the restriction I_k^{k-1}.

4.5.7 Multigrid Cycles

There are several structures to describe one iteration step in the multigrid method called multigrid cycles. The famous cycles are $\mathbf{V}_cycle$, $\mathbf{F}_cycle$ and $\mathbf{W}_cycle$ (see Fig.4.3). So let us mention the algorithm for every

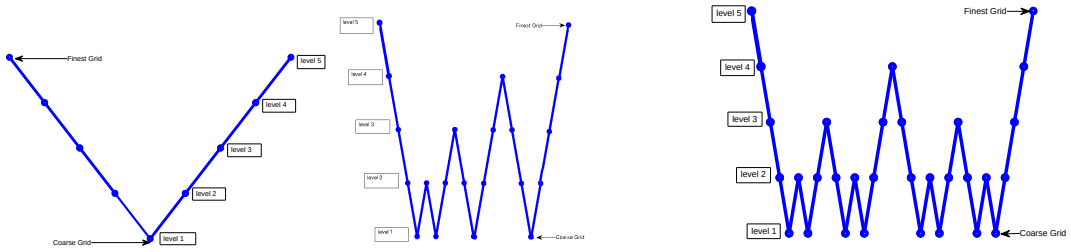

Fig. 4.3. Structure of multigrid $\mathbf{V}_{cycle}$, $\mathbf{F}_{cycle}$ and $\mathbf{W}_{cycle}$ for 5 levels.

cycle as the following.

$\mathbf{V}_{cycle}$ algorithm:

Given: $\boldsymbol{g} \in \mathbf{V}_k$, $\boldsymbol{z}_0 \in \mathbf{V}_k$ and the output of the algorithm is $MG_{\mathbf{V}}(k, \boldsymbol{g}, \boldsymbol{z}_k, m)$ where k=1,..,n the numbers of hierarchy levels, m is the number of presmoothing or postsmoothing steps and $\boldsymbol{z}_k$ is the approximated solution vector of the following linear equation

$$\boldsymbol{A}_k \boldsymbol{z} = \boldsymbol{g} \tag{4.65}$$

- **The coarse grid solution** $k = 1$
  $MG(1, \boldsymbol{g}, \boldsymbol{z}_0, m) = \boldsymbol{A}_1^{-1} \boldsymbol{g}$

- **Presmoothing step** $k \geq 2$**:**
  DO j=1,m
  $\boldsymbol{z}_j = \boldsymbol{z}_{j-1} + \Lambda_k{}^{-1} (\boldsymbol{g} - \boldsymbol{A}_k \boldsymbol{z}_{j-1})$
  END DO
  where $\rho(\Lambda_k) \leq C h_k^{-2}$.

- **Correction step:**
  $\boldsymbol{z}_{m+1} = \mathbf{I}_k^{k-1} MG(k-1, \mathbf{I}_k^{k-1}(\boldsymbol{g} - \boldsymbol{A}_k \boldsymbol{z}_m), 0, m)$

- **Postsmoothing step** $k \geq 2$**:**
  DO j=m,2m+1
  $\boldsymbol{z}_j = \boldsymbol{z}_{j-1} + \Lambda_k{}^{-1} (\boldsymbol{g} - \boldsymbol{A}_k \boldsymbol{z}_{j-1})$
  END DO

- **Final Output:**
  $MG(k, \boldsymbol{g}, \boldsymbol{z}_0, m) = \boldsymbol{z}_{2m+1}$.

$\mathbf{F}_{cycle}$ algorithm:

Given: $\boldsymbol{g} \in \mathbf{V}_k$, $\boldsymbol{z}_0 \in \mathbf{V}_k$ and the output of the algorithm is $MG_{\mathbf{F}}(k, \boldsymbol{g}, \boldsymbol{z}_k, m)$ where k=1,..,n the numbers of hierarchy levels, m is the number of presmoothing or postsmoothing steps and $\boldsymbol{z}_k$ is the approximated solution vector of the following linear equation

$$\boldsymbol{A}_k \boldsymbol{z} = \boldsymbol{g} \tag{4.66}$$

- **The coarse grid solution** $k = 1$
  $MG(1, \boldsymbol{g}, \boldsymbol{z}_0, m) = \boldsymbol{A}_1^{-1} \boldsymbol{g}$

- **Presmoothing step** $k \geq 2$**:**
  DO j=1,m
  $\boldsymbol{z}_j = \boldsymbol{z}_{j-1} + \Lambda_k{}^{-1} (\boldsymbol{g} - \boldsymbol{A}_k \boldsymbol{z}_{j-1})$
  END DO
  where $\rho(\Lambda_k) \leq C h_k^{-2}$.

- **Correction step:**
  $\boldsymbol{z}_{m+\frac{1}{2}} = \mathbf{I}_k^{k-1} MG(k-1, \mathbf{I}_k^{k-1}(\boldsymbol{g} - \boldsymbol{A}_k \boldsymbol{z}_m), 0, m)$
  $\boldsymbol{z}_{m+1} = \boldsymbol{z}_m + \mathbf{I}_k^{k-1} MG(k-1, \mathbf{I}_k^{k-1}(\boldsymbol{g} - \boldsymbol{A}_k \boldsymbol{z}_m), \boldsymbol{z}_{m+\frac{1}{2}}, m)$

- **Postsmoothing step** $k \geq 2$**:**
  DO j=m,2m+1
  $\boldsymbol{z}_j = \boldsymbol{z}_{j-1} + \Lambda_k{}^{-1} (\boldsymbol{g} - \boldsymbol{A}_k \boldsymbol{z}_{j-1})$
  END DO

- **Final Output:**
  $MG(k, \boldsymbol{g}, \boldsymbol{z}_0, m) = \boldsymbol{z}_{2m+1}$.

$\mathbf{W}_{cycle}$ algorithm:

Given: $\boldsymbol{g} \in \mathbf{V}_k$, $\boldsymbol{z}_0 \in \mathbf{V}_k$ and the output of the algorithm is $MG_{\mathbf{W}}(k, \boldsymbol{g}, \boldsymbol{z}_k, m)$ where k=1,..,n the numbers of hierarchy levels, m is the number of presmoothing or postsmoothing steps and $\boldsymbol{z}_k$ is the approximated solution vector of the following linear equation

$$\boldsymbol{A}_k \boldsymbol{z} = \boldsymbol{g} \tag{4.67}$$

- **The coarse grid solution** $k = 1$
  $MG(1, \boldsymbol{g}, \boldsymbol{z}_0, m) = \boldsymbol{A}_1^{-1} \boldsymbol{g}$

- **Presmoothing step** $k \geq 2$**:**
  DO j=1,m
  $\boldsymbol{z}_j = \boldsymbol{z}_{j-1} + \Lambda_k{}^{-1} (\boldsymbol{g} - \boldsymbol{A}_k \boldsymbol{z}_{j-1})$
  END DO
  where $\rho(\Lambda_k) \leq C h_k^{-2}$.

- **Correction step:**
  $\boldsymbol{z}_{m+\frac{1}{2}} = \mathbf{I}_k^{k-1} MG(k-1, \mathbf{I}_k^{k-1}(\boldsymbol{g} - \boldsymbol{A}_k \boldsymbol{z}_m), 0, m)$
  $\boldsymbol{z}_{m+\frac{3}{4}} = \mathbf{I}_k^{k-1} MG(k-1, \mathbf{I}_k^{k-1}(\boldsymbol{g} - \boldsymbol{A}_k \boldsymbol{z}_m), \boldsymbol{z}_{m+\frac{1}{2}}, m)$
  $\boldsymbol{z}_{m+1} = \boldsymbol{z}_m + \mathbf{I}_k^{k-1} MG(k-1, \mathbf{I}_k^{k-1}(\boldsymbol{g} - \boldsymbol{A}_k \boldsymbol{z}_m), \boldsymbol{z}_{m+\frac{3}{4}}, m)$

- **Postsmoothing step** $k \geq 2$**:**
  DO j=m,2m+1
  $\boldsymbol{z}_j = \boldsymbol{z}_{j-1} + \Lambda_k{}^{-1} (\boldsymbol{g} - \boldsymbol{A}_k \boldsymbol{z}_{j-1})$
  END DO

- **Final Output:**
  $MG(k, \boldsymbol{g}, \boldsymbol{z}_0, m) = \boldsymbol{z}_{2m+1}$.

4.6 Numerical Experiments

In this section, we present some results from a different numerical experiments associated to different physical models. The computational domains will be a unit channel, unit square cavity, and rectangular channel geometry with an obstacle(cylinder benchmark). For the unit square channel and the cylinder benchmark, we prescribe natural boundary conditions which lead to the well-known outflow boundary condition $(\boldsymbol{\tau} - p).\boldsymbol{n} = 0$ (see [103]) as well as on the boundaries, we prescribe no-slip conditions on the walls and on the obstacle. We aim for every numerical experiment to analyze the behavior of the coupled processes Newton and multigrid for three different discretization techniques to give highlighting about the flexibility, robustness and the efficiency of the coupled solvers. More precisely, for such discretization technique, Newton-multigrid process have been realized to show much more robust behavior with respect to a huge nonlinear systems for low order and high order finite elements. Therefore, we will analyze the behavior of convergence for the non-trivial flow configuration based on the constant constant and linear/nonlinear viscosity problems against the modeling error and the discretization error.

Element.	$\tilde{Q}_1Q_0$				Q_2P_1				$Q_2P_1^{np}$			
level	*Pois.*	*Stok.*	*S.Thin*	*S.Thick*	*Pois.*	*Stok.*	*S.Thin*	*S.Thick*	*Pois.*	*Stok.*	*S.Thin*	*S.Thick*
uniform												
2x2	4/9	3/5	3/7	4/11	1/1	3/4	2/5	3/6	1/1	2/4	2/5	3/6
4x4	2/2	2/2	4/4	4/4	1/1	2/2	2/2	2/2	1/1	2/2	2/2	2/2
8x8	2/2	2/2	4/4	5/7	1/1	2/2	2/2	2/2	1/1	1/1	2/2	2/2
16x16	3/3	3/3	4/5	6/8	1/1	2/2	2/2	2/3	1/1	1/1	2/2	2/2
32x32	2/3	3/4	4/5	7/11	1/1	2/2	2/3	2/3	1/1	1/1	2/3	2/3
64x64	2/3	3/5	4/5	9/24	1/1	3/4	2/3	2/4	1/1	1/1	2/3	2/4
128x128	2/3	3/5	3/4	9/21	1/1	3/4	2/4	2/4	1/1	1/1	2/4	2/4
256x256	2/3	3/5	3/4	7/10	1/1	3/4	2/3	2/4	1/1	1/1	2/3	2/4
perturbed												
2x2	3/8	3/5	4/9	4/10	2/6	2/4	3/6	65/80	1/1	2/4	2/4	3/7
4x4	2/2	2/2	4/4	5/5	2/2	2/2	3/3	63/63	1/1	2/2	2/2	2/2
8x8	2/2	2/2	4/4	5/7	2/2	1/1	3/3	61/61	1/1	2/2	2/2	2/2
16x16	3/3	3/3	4/5	6/8	2/2	1/1	3/3	33/33	1/1	2/2	2/2	2/2
32x32	2/3	3/4	4/5	8/12	2/2	1/1	3/4	16/17	1/1	2/2	2/2	2/3
64x64	2/3	3/5	3/4	10/24	1/1	1/1	3/4	9/10	1/1	2/2	2/3	2/4
128x128	2/3	3/5	3/4	9/15	1/1	1/1	3/4	6/6	1/1	2/2	2/4	2/4
256x256	2/3	3/5	3/4	8/12	1/1	1/1	3/4	5/6	1/1	1/1	2/4	2/4

Table 4.1. *The exact solution tests:* Newton-multigrid efficiency for the linear pressure problem and different flow models using the uniform grid $[0,1] \times [0,1]$.

4.6.1 The Exact Solution Tests

The first test presents the efficiency of the coupled solver for the known exact solution configuration fluid tests like, Poiseuille flow(Pois), Stokes flow(Stok), shear thinning flow(S.Thin), shear thickening flow(S.Thick) and the channel Bingham viscoplastic flow which have the previous prescribed linear pressure form. Table(4.1) shows us that the robustness of the coupled solvers for the Newtonian and Non-Newtonian fluids with slightly increasing for the stabilized constant global approach and local linear approach due to the mesh disturbance for the nonlinear flow models. In contrast with the global linear approach which is employed without any stabilization which seems to be dominant in the accuracy and robustness of the coupled solvers. For viscoplastic flow, the following analytical solution describes the flow in channel or between two parallel plates:

$$\boldsymbol{u} = (u, 0),\ p = -x + c, \tag{4.68}$$

where

$$u = \begin{cases} \dfrac{1}{8}[(1-2\tau_s)^2 - (1-2\tau_s-2y)^2] & \text{if } 0 \le y < \dfrac{1}{2} - \tau_s, \\ \dfrac{1}{8}(1-2\tau_s)^2 & \text{if } \dfrac{1}{2} - \tau_s \le y \le \dfrac{1}{2} + \tau_s, \\ \dfrac{1}{8}[(1-2\tau_s)^2 - (2y-2\tau_s-1)^2] & \text{if } \dfrac{1}{2} + \tau_s < y < 1. \end{cases} \tag{4.69}$$

For this equation, the boundary conditions are set to be Dirichlet at the inlet(left) and the outlet(right) to avoid flow overlapping for the deformation form. The solution shows that the plug region is $\frac{1}{2} - \tau_s \le y \le \frac{1}{2} + \tau_s$ which has a constant velocity. In our calculations we choose the yield stress value 0.25 to align the mesh with the plug region. The number of nonlinear iteration and number of the total number of multigrid sweeps can be seen according to the table(4.2).
In the agreement with our assumption for the performance of the Newton-multigrid processes, both of them are robust with respect to the parameter ϵ for the uniform mesh. But in the case of the unstructured mesh the number of inner iteration or multigrid iterations increases when ϵ approaches zero, and on the

other hand Newton process may lose the quadratic convergence to obtain super linear convergence. The influence of the modeling error due to regularization on the nonlinear solver efficiency is dominated over the influence of discretization error, and it has so strong influence if the parameter approaches zero which makes Newton process has the same behavior of the fixed point process.

Mesh	*uniform*			*perturbed*			*uniform*			*perturbed*		
Element	$\tilde{Q}_1Q_0$	Q_2P_1	$Q_2P_1^{np}$	$\tilde{Q}_1Q_0$	Q_2P_1	$Q_2P_1^{np}$	$\tilde{Q}_1Q_0$	Q_2P_1	$Q_2P_1^{np}$	$\tilde{Q}_1Q_0$	Q_2P_1	$Q_2P_1^{np}$
$\boldsymbol{\epsilon = 10^{-2}}$							$\boldsymbol{\epsilon = 10^{-3}}$					
2x2	8/18	9/20	9/20	8/18	8/18	9/21	10/22	10/24	10/24	10/24	10/26	10/22
4x4	9/9	10/10	10/10	10/10	8/8	8/8	19/19	13/13	13/13	21/21	20/20	20/20
8x8	12/12	8/8	8/8	13/13	8/8	8/8	11/11	7/7	7/7	13/13	12/13	12/13
16x16	14/14	8/8	8/8	13/13	8/8	8/8	20/21	11/11	11/11	19/19	12/12	12/12
32x32	10/11	6/7	6/7	12/13	9/10	9/10	25/29	9/10	9/10	25/26	11/11	11/11
64x64	8/22	4/5	4/5	11/13	8/10	8/10	18/30	5/8	5/8	21/25	11/15	11/15
128x128	6/39	3/4	3/4	10/12	8/12	8/12	8/34	4/4	4/4	13/17	8/13	8/13
256x256	4/44	3/4	3/4	9/11	7/11	7/11	5/50	4/4	4/4	11/16	8/17	8/17
$\boldsymbol{\epsilon = 10^{-4}}$							$\epsilon = 10^{-5}$					
2x2	10/22	10/24	10/24	10/24	10/26	10/23	10/22	10/24	10/24	10/24	10/26	10/23
4x4	38/39	18/18	18/18	41/43	37/38	36/37	56/73	23/29	23/29	51/96	51/68	49/66
8x8	11/16	10/10	10/10	21/27	18/18	18/18	12/125	10/15	10/15	36/122	24/30	26/31
16x16	20/21	10/10	10/10	30/32	20/20	20/20	19/61	10/10	10/10	51/68	36/40	35/39
32x32	24/29	8/8	8/8	28/29	17/17	17/17	23/39	9/9	9/9	261/261	26/28	27/29
64x64	21/61	7/8	7/8	27/30	15/19	15/19	21/66	6/6	6/6	546/546	88/92	16/18
128x128	13/124	5/9	5/9	19/27	11/23	11/23	12/168	5/8	5/8	648/648	101/112	52/64
256x256	6/53	4/8	4/8	50/60	10/30	10/30	9/245	7/13	7/13	1049/1049	75/102	39/77

Table 4.2. *The exact solution tests:* Numerical efficiency for $\tilde{Q}_1Q_0$, Q_2P_1 and $Q_2P_1^{np}$ using grid $[0,1]\times[0,1]$ at $\epsilon = 10^{-2}$, 10^{-3}, 10^{-4} and 10^{-5} for Bingham flow in channel.

4.6.2 Stationary Fluids in Lid-Driven Cavity

Driven cavity benchmark represents a common benchmark test case for incompressible CFD codes. Here, we test the total accuracy of the discretization techniques from the numerical approximated solution for the Newtonian fluids at different Reynolds numbers. The total accuracy of the approximation is to evaluate the energy norm of each discretization which is calculated by using $E = \frac{1}{2}\|\boldsymbol{u}\|^2$ as well as the numerical efficiency NNL/NMG. Every simulation is performed on the a unit square with uniformly refined from the uniform or perturbed coarse meshes. The computational domain is considered as a unit square $\boldsymbol{\Omega} = [0,1]^2$, with the absence of the external forces $\mathbf{f} = 0$. The boundary conditions are represented by the horizontal motion of the upper lid with constant unit speed, and homogenous Dirichlet boundary conditions on the rest of the part of the boundary. The solution has a non-physical singular behavior in the upper corners, definitely for the pressure; However the problem still serves as a standard benchmark for the CFD codes.

4.6.2.a Stationary Newtonian Fluids in Lid-Driven Cavity

This numerical test is used to investigate the behavior of the discretization techniques and the coupled solver due to the influence of Reynolds number. Therefore, we started to use Stokes and the cases of Reynolds numbers 1 and 100. The table(4.4) shows us that the cost is slightly increased with the increasing of the Reynolds number in particular for the unstructured mesh. But the global performance of coupled solver seems quite efficient with super priority for the global linear approach. In addition to the convergence behavior of multigrid is stable with the refinement in both cases Stokes or Navier-Stokes, the instability for unstructured mesh could be slightly observed (see [166]).

Level	*Elements*	*Vertices*	*Midpoints*	$DOF(\tilde{Q}_1Q_0)$	$DOF(Q_2P_1)$
level1	4	9	12	28	62
level2	16	25	40	96	210
level3	64	81	144	352	770
level4	256	289	544	1344	2946
level5	1024	1089	2112	5248	11522
level6	4096	4225	8320	20736	45570
level7	16384	16641	33024	82432	181250
level8	65536	66049	131584	328704	722946

Table 4.3. Degrees of Freedom of $\tilde{Q}_1Q_0$ and Q_2P_1 for driven cavity benchmark.

Mesh	*uniform*						*perturbed*					
Element	$\tilde{Q}_1Q_0$		Q_2P_1		$Q_2P_1^{np}$		$\tilde{Q}_1Q_0$		Q_2P_1		$Q_2P_1^{np}$	
T.Accuracy	*E.norm*	*Eff.*	*E.norm*	*Eff.*	*E.norm*	*Eff.*	*E.norm*	*Eff.*	*E.norm*	*Eff.*	*E.norm*	*Eff.*
Stokes												
2×2	5.004334E-2	3/5	4.253090E-2	3/6	4.253090E-2	3/6	5.159701E-2	3/5	4.171281E-2	3/5	4.168894E-2	3/5
4×4	3.836863E-2	2/2	3.371020E-2	2/2	3.371020E-2	2/2	3.941876E-2	2/2	3.370958E-2	2/2	3.376016E-2	2/2
8×8	3.504583E-2	2/2	3.224440E-2	2/2	3.224440E-2	2/2	3.497080E-2	2/2	3.216819E-2	2/2	3.215661E-2	2/2
16×16	3.401521E-2	2/2	3.252278E-2	2/3	3.252278E-2	2/3	3.405629E-2	2/2	3.252178E-2	2/2	3.252206E-2	2/2
32×32	3.369968E-2	2/3	3.294239E-2	2/3	3.294239E-2	2/3	3.370217E-2	2/3	3.294777E-2	2/3	3.294688E-2	2/3
64×64	3.360897E-2	2/3	3.322886E-2	2/3	3.322886E-2	2/3	3.360754E-2	2/3	3.322861E-2	2/3	3.322876E-2	2/3
128×128	3.358403E-2	2/3	3.339350E-2	2/3	3.339350E-2	2/3	3.358409E-2	2/3	3.339316E-2	2/3	3.339319E-2	2/3
256×256	3.357731E-2	2/3	3.348184E-2	2/3	3.348184E-2	2/3	3.357769E-2	2/3	3.348183E-2	2/3	3.348184E-2	2/3
Re=1												
2×2	5.004191E-2	4/8	4.253052E-2	3/6	4.253090E-2	3/6	5.166454E-2	4/8	4.171272E-2	4/7	4.168315E-2	4/7
4×4	3.836678E-2	3/3	3.370962E-2	2/2	3.370987E-2	2/2	3.943332E-2	3/3	3.370975E-2	3/3	3.375840E-2	3/3
8×8	3.504522E-2	3/3	3.224405E-2	2/2	3.224414E-2	2/2	3.497224E-2	3/3	3.216845E-2	2/2	3.215658E-2	2/2
16×16	3.401505E-2	3/3	3.252261E-2	3/4	3.252263E-2	3/4	3.405666E-2	3/3	3.252143E-2	3/4	3.252162E-2	3/4
32×32	3.369964E-2	3/4	3.294232E-2	3/4	3.294232E-2	3/4	3.370238E-2	3/4	3.294769E-2	2/3	3.294679E-2	3/4
64×64	3.360897E-2	3/4	3.322883E-2	2/3	3.322883E-2	2/3	3.360758E-2	3/4	3.322859E-2	2/3	3.322873E-2	2/3
128×128	3.358404E-2	3/4	3.339349E-2	2/3	3.339349E-2	2/3	3.358412E-2	3/4	3.339315E-2	2/3	3.339318E-2	2/3
256×256	3.357732E-2	2/3	3.348185E-2	2/2	3.348185E-2	2/3	3.357770E-2	3/5	3.348184E-2	2/3	3.348184E-2	2/3
Re=100												
2×2	5.074105E-2	4/9	4.156019E-2	5/14	4.245138E-2	4/10	4.963553E-2	4/9	3.981362E-2	5/13	3.949039E-2	5/13
4×4	3.618938E-2	4/4	3.117050E-2	4/4	3.182817E-2	4/4	3.561541E-2	4/4	3.101300E-2	4/4	3.184744E-2	4/4
8×8	3.323081E-2	3/3	3.039193E-2	4/4	3.077927E-2	3/3	3.163827E-2	4/4	3.026685E-2	4/4	3.084242E-2	4/4
16×16	3.365523E-2	3/4	3.182878E-2	3/4	3.199915E-2	3/4	3.297186E-2	3/4	3.173915E-2	3/4	3.195827E-2	3/4
32×32	3.414965E-2	3/5	3.299938E-2	3/4	3.305564E-2	3/4	3.394525E-2	3/5	3.298375E-2	3/5	3.305952E-2	3/5
64×64	3.435510E-2	3/5	3.368939E-2	3/4	3.370541E-2	3/4	3.428100E-2	3/5	3.368277E-2	3/4	3.370592E-2	3/4
128×128	3.441966E-2	2/3	3.405849E-2	2/2	3.406278E-2	2/2	3.440101E-2	3/5	3.405640E-2	2/2	3.406250E-2	2/2
256×256	3.443752E-2	2/3	3.424898E-2	2/2	3.425009E-2	2/2	3.443311E-2	2/3	3.424851E-2	2/2	3.425011E-2	2/2

Table 4.4. *Newtonian flow in driven cavity:* Energy norm and numerical efficiency using grid $[0,1]\times[0,1]$ for different discretizations for stokes and Navier-Stokes at Re=1, 100.

4.6.2.b Stationary Shear Thickening and Shear Thinning Fluids in Lid-Driven Cavity

This experiment shows the behavior of the coupled solver for the case of non-Newtonian fluid. Here, we employ the shear thickening and shear thinning models (see Fig.4.4) for the viscosity function (see [152])

$$\nu(\|\mathbf{D}\|) = \nu_\infty + (\nu_0 - \nu_\infty)(1 + (\lambda\|\mathbf{D}\|)^a)^{\frac{n-1}{a}}, \tag{4.70}$$

with the following associated parameters.

Since, in the case of the steady state flow the nonlinearity of the convective term is quite moderate comparing with the nonlinear viscosity function. In this case, we consider the flow is quite slow, then the influence of the convective term is ignored and the nonlinear viscosity is a unique source of the nonlinearity. The corresponding table(4.5) shows us the behavior of the coupled solver for different discretization techniques. As expected, the coupled solver expose a better nonlinear convergence for the structured and unstructured meshes and the corresponding linear sweeps behavior which is significantly better in both

Mesh	*uniform*						*perturbed*					
Element	$\tilde{Q}_1Q_0$		Q_2P_1		$Q_2P_1^{np}$		$\tilde{Q}_1Q_0$		Q_2P_1		$Q_2P_1^{np}$	
T.Accuracy	*E.norm*	*Eff.*	*E.norm*	*Eff.*	*E.norm*	*Eff.*	*E.norm*	*Eff.*	*E.norm*	*Eff.*	*E.norm*	*Eff.*
shear thickening												
2×2	5.341102E-2	4/8	4.671931E-2	5/9	4.671931E-2	5/9	5.217944E-2	4/10	4.610593E-2	6/12	4.611526E-2	6/12
4×4	4.250727E-2	5/5	3.904365E-2	4/4	3.904365E-2	4/4	4.277653E-2	5/5	3.901938E-2	5/5	3.904443E-3	5/5
8×8	4.097291E-2	5/5	3.800934E-2	4/4	3.800934E-2	4/4	4.066994E-2	5/5	3.796581E-2	4/4	3.796045E-3	4/4
16×16	3.993243E-2	5/5	3.841616E-2	4/4	3.841616E-2	4/4	3.998919E-2	5/5	3.841528E-2	4/4	3.841178E-3	4/4
32×32	3.957362E-2	5/5	3.881175E-2	4/4	3.881175E-2	4/4	3.956109E-2	5/5	3.881545E-2	5/5	3.881436E-2	5/5
64×64	3.942999E-2	5/5	3.906269E-2	4/4	3.906269E-2	4/4	3.942539E-2	5/5	3.906192E-2	5/6	3.906201E-2	5/6
128×128	3.938132E-2	5/5	3.920480E-2	3/3	3.920480E-2	3/3	3.938287E-2	5/6	3.920463E-2	5/7	3.920463E-2	5/7
256×256	3.936739E-2	5/5	3.928113E-2	3/3	3.928113E-2	3/3	3.936835E-2	5/7	3.928112E-2	5/9	3.928112E-2	5/9
shear thinning												
2×2	4.870935E-2	4/10	3.738914E-2	4/11	3.738914E-2	4/9	4.765398E-2	4/9	3.586148E-2	4/8	3.585932E-2	4/8
4×4	3.453570E-2	4/4	2.380914E-2	5/5	2.380914E-2	5/5	3.488445E-2	4/4	2.425220E-2	5/5	2.426588E-2	5/5
8×8	2.498514E-2	5/5	1.884616E-2	5/5	1.884616E-2	5/5	2.439737E-2	5/5	1.835444E-2	5/5	1.835065E-2	5/5
16×16	2.084902E-2	5/5	1.819327E-2	5/5	1.819327E-2	5/5	2.092063E-2	5/5	1.819629E-2	5/5	1.819815E-2	5/5
32×32	1.949934E-2	5/6	1.833784E-2	5/5	1.833784E-2	5/5	1.944323E-2	5/5	1.837027E-2	5/5	1.837170E-2	5/5
64×64	1.911524E-2	5/5	1.857262E-2	5/5	1.857262E-2	5/5	1.909212E-2	5/6	1.857732E-2	5/6	1.857761E-2	5/6
128×128	1.901357E-2	5/5	1.875386E-2	4/4	1.875386E-2	4/4	1.900765E-2	5/6	1.875297E-2	5/6	1.875311E-2	5/6
256×256	1.898605E-2	5/5	1.886298E-2	4/4	1.886298E-2	4/4	1.898296E-2	5/5	1.886283E-2	5/5	1.886288E-2	5/5

Table 4.5. *Shear thickening and shear thinning flows in driven cavity:* Energy norm and numerical efficiency using grid $[0,1] \times [0,1]$ for different discretizations for shear thickening and shear thinning fluids.

fluid type	ν_0	ν_∞	λ	n	a
Shear Thickening	0.00345	0.056	1.902	0.22	2,
Shear Thinning	0.056	0.00345	1.902	0.22	2.

Table 4.6. Shear thickening/thinnig parameters

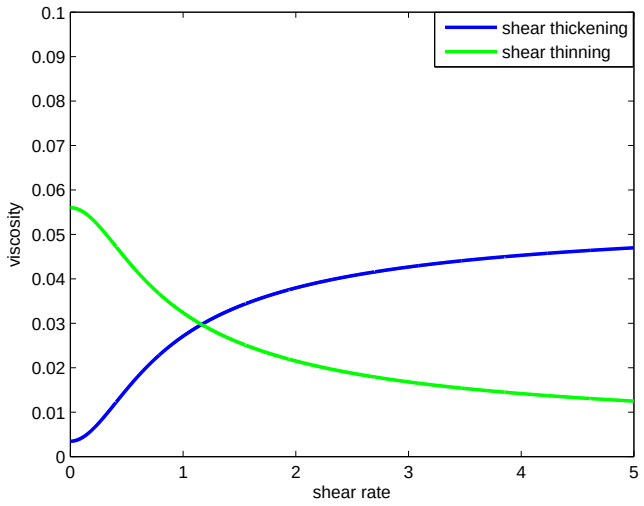

Fig. 4.4. Viscosity behavior for shear thickening and shear thinning fluids

the stabilized case and the unstabilized case.
In the stabilized case, we choose the stabilization parameters γ and ν for the edge oriented stabilization on each edge. The value of γ is 0.01 and the viscosity is constant and equals to the corresponding ν_∞ for each case. The difference among the discretizations is quite invisible and the behavior of the coupled solver looks the same for the structured mesh. One can observe that, the results for nonlinear viscosity problems are quite similar as those for the Newtonian problem for the structured and unstructured meshes. For the

performed multigrid process for the constant global approach is slightly sensitive to the mesh disturbance but robust against the variation in the mesh width, in contradiction with the global linear approach which is strongly stable due to the disturbance and the width variations.

4.6.2.c Stationary Viscoplastic Fluids in Lid-Driven Cavity

Mesh	*uniform*						*perturbed*					
Element	$\tilde{Q}_1Q_0$		Q_2P_1		$Q_2P_1^{np}$		$\tilde{Q}_1Q_0$		Q_2P_1		$Q_2P_1^{np}$	
Total accuracy	*E.norm.*	*Eff.*	*E.norm*	*Eff.*	*E.norm*	*Eff.*	*E.norm*	*Eff.*	*E.norm*	*Eff.*	*E.norm*	*Eff.*
$\epsilon = 10^{-1}$												
2x2	4.988893E-2	6/14	4.065350E-2	6/14	4.06535E-2	6/14	5.009792E-2	6/13	3.949389E-2	5/10	3.948554E-2	5/11
4x4	3.833261E-2	5/5	3.158572E-2	4/4	3.158572E-2	4/4	3.876395E-2	5/5	3.161334E-2	4/4	3.164207E-2	4/4
8x8	3.414338E-2	5/5	3.037576E-2	4/4	3.037576E-2	4/4	3.439311E-2	5/5	3.030160E-2	4/4	3.029405E-2	4/4
16x16	3.267321E-2	4/4	3.073505E-2	4/4	3.073505E-2	4/4	3.265290E-2	5/5	3.072618E-2	5/5	3.072715E-2	5/5
32x32	3.212386E-2	4/4	3.119341E-2	4/4	3.119341E-2	4/4	3.212727E-2	5/6	3.119734E-2	4/4	3.119700E-2	4/4
64x64	3.194877E-2	4/8	3.150391E-2	4/4	3.150391E-2	4/4	3.193671E-2	5/6	3.150334E-2	4/5	3.150349E-2	4/5
128x128	3.189631E-2	4/19	3.168127E-2	4/4	3.168127E-2	4/4	3.189859E-2	5/7	3.168093E-2	4/6	3.168097E-2	4/6
$\epsilon = 10^{-2}$												
2x2	4.986322E-2	7/7	4.059643E-2	7/7	4.059643E-2	7/7	5.007311E-2	6/6	3.942130E-2	7/16	3.941372E-2	7/7
4x4	3.828911E-2	5/5	3.151508E-2	5/5	3.151508E-2	5/5	3.871869E-2	5/5	3.155466E-2	5/5	3.158401E-2	5/5
8x8	3.410249E-2	6/6	3.033380E-2	6/6	3.033380E-2	6/6	3.435443E-2	6/6	3.025630E-2	5/5	3.024950E-2	5/5
16x16	3.264105E-2	5/5	3.069897E-2	6/6	3.069897E-2	6/6	3.262034E-2	6/6	3.068961E-2	6/6	3.069045E-2	6/6
32x32	3.209214E-2	6/7	3.116023E-2	5/5	3.116023E-2	5/5	3.209444E-2	8/8	3.116360E-2	6/6	3.116329E-2	6/6
64x64	3.191640E-2	6/18	3.147119E-2	5/5	3.147119E-2	5/5	3.190392E-2	7/8	3.147119E-2	7/8	3.147058E-2	7/8
128x128	3.186402E-2	5/29	3.164899E-2	5/5	3.164899E-2	5/5	3.186620E-2	9/11	3.164864E-2	8/12	3.164864E-2	8/12
$\epsilon = 10^{-3}$												
2x2	4.986295E-2	8/8	4.059555E-2	9/9	4.059555E-2	9/9	5.007284E-2	7/7	3.942033E-2	10/10	3.941277E-2	10/10
4x4	3.828860E-2	5/5	3.151366E-2	6/6	3.151366E-2	6/6	3.871813E-2	5/5	3.155344E-2	7/7	3.158280E-2	8/8
8x8	3.410180E-2	6/6	3.033294E-2	8/8	3.033294E-2	8/8	3.413580E-2	7/7	3.025535E-2	11/11	3.024855E-2	14/14
16x16	3.264054E-2	7/7	3.069812E-2	6/6	3.069812E-2	6/6	3.261991E-2	7/7	3.068920E-2	8/8	3.068991E-2	12/12
32x32	3.209181E-2	8/8	3.115981E-2	7/7	3.115981E-2	7/7	3.209420E-2	12/12	3.116313E-2	9/9	3.116281E-2	13/13
64x64	3.191577E-2	17/24	3.147071E-2	15/16	3.147071E-2	15/16	3.190336E-2	23/24	3.146994E-2	12/14	3.147007E-2	16/17
128x128	3.186354E-2	12/42	3.164850E-2	16/18	3.164850E-2	16/18	3.186575E-2	20/34	3.164815E-2	14/70	3.164818E-2	14/70

Table 4.7. *Bingham flow in driven cavity:* Energy norm and numerical efficiency using the uniform and perturbed meshes $[0,1] \times [0,1]$ for different discretizations and different regularization parameters at $\tau_s = 0.25$ for Bingham fluid.

This test is developed to examine the robustness of the coupled solver. The accuracy is measured by the energy norm against the modeling error and the discretization error. In this case we did not use the fixed point linearization techniques, since it has linearly convergence leading to the huge cost of the simulation process but is normally stable due to the perturbation from the mesh and the regularization. Our alternative is the continuous Newton solver which has been performed without damping. As the well-known behavior about Newton process the ratio between the residual on k^{th} level and residual on $k^{th} - 1$ should be quadratic value, taking in our mind the starting solution to be close to the solution point which in our experiment comes from the solution of the previous level. Therefore, we use 2 fixed point iterations at most to switch to Newton at the beginning with a given tolerance being $5.0E-3$ to avoid to run away for Newton method. The table(4.7) show that the total accuracy of the mapped and the unmapped approaches for the regular mesh have better results than the constant approach. For the distorted mesh the mapped and the unmapped approaches have the similar total accuracy, but the constant approach is influenced. This unsurpassable degree of accuracy for the constant and mapped approaches are dependent on the relaxation parameter of the edge oriented stabilization and the topology of the computational domain. One can observe that in tables(4.8 and 4.9), the influence of the discretization error is quite negligible with respect to the influence of the modeling error for $10^{-1} \leq \epsilon \leq 10^{-3}$. On the other hand, the energy norm exhibits that, the influence of the modeling error can be totaly neglected after 10^{-3}, since the value of the energy norm does not change for structured and the unstructured mesh. In the counterpart, The effect of the regularization parameter is not fragile on the behavior of Newton process which may lose the quadratic convergence when ϵ approaches zero.

Yield Value			$\tau_s = 0.5$				$\tau_s = 1$					
Element	$\widetilde{Q}_1Q_0$		Q_2P_1		$Q_2P_1^{np}$		$\widetilde{Q}_1Q_0$		Q_2P_1		$Q_2P_1^{np}$	
Total accuracy	*E.norm.*	*Eff.*	*E.norm*	*Eff.*	*E.norm*	*Eff.*	*E.norm*	*Eff.*	*E.norm*	*Eff.*	*E.norm*	*Eff.*
$\epsilon = 10^{-1}$												
2x2	4.896293E-2	7/16	3.968711E-2	7/15	3.968711E-2	7/15	4.746542E-2	5/12	3.824834E-2	4/4	3.824834E-2	4/4
4x4	3.723287E-2	7/7	3.006178E-2	5/5	3.006178E-2	5/5	3.555561E-2	5/5	2.773441E-2	5/5	2.773441E-2	5/5
8x8	3.269835E-2	6/6	2.884435E-2	5/5	2.884435E-2	5/5	3.037853E-2	6/6	2.639439E-2	5/5	2.639439E-2	5/5
16x16	3.122226E-2	6/6	2.922495E-2	5/5	2.922495E-2	5/5	2.886049E-2	6/6	2.679114E-2	5/6	2.679114E-2	5/6
32x32	3.067380E-2	5/7	2.970674E-2	5/5	2.970674E-2	5/5	2.832741E-2	5/6	2.730620E-2	5/6	2.730620E-2	5/6
64x64	3.049668E-2	5/14	3.003469E-2	4/4	3.003469E-2	4/4	2.814101E-2	5/13	2.765806E-2	5/6	2.765806E-2	5/6
128x128	3.044441E-2	5/29	3.022131E-2	4/4	3.022131E-2	4/4	2.808851E-2	5/26	2.765806E-2	4/5	2.765806E-2	4/5
$\epsilon = 10^{-2}$												
2x2	4.890849E-2	8/8	3.955916E-2	10/10	3.955916E-2	10/10	4.734292E-2	7/17	3.795553E-2	7/7	3.795553E-2	7/7
4x4	3.714010E-2	7/7	2.990349E-2	6/6	2.990349E-2	6/6	3.537700E-2	5/5	2.747876E-2	7/7	2.747876E-2	7/7
8x8	3.261337E-2	7/7	2.875491E-2	6/6	2.875491E-2	6/6	3.024681E-2	9/9	2.621525E-2	7/7	2.621525E-2	7/7
16x16	3.115669E-2	7/7	2.915551E-2	8/8	2.915551E-2	8/8	2.873656E-2	8/9	2.666064E-2	8/9	2.666064E-2	8/9
32x32	3.061087E-2	9/11	2.964134E-2	6/6	2.964134E-2	6/6	2.821573E-2	9/17	2.719720E-2	7/9	2.719720E-2	7/9
64x64	3.043279E-2	6/25	2.997107E-2	6/6	2.997107E-2	6/6	2.802756E-2	8/55	2.754670E-2	6/7	2.754670E-2	6/7
128x128	3.038019E-2	6/45	3.015750E-2	6/6	3.015750E-2	6/6	2.798127E-2	8/55	2.774321E-2	6/6	2.774321E-2	6/6
$\epsilon = 10^{-3}$												
2x2	4.890792E-2	8/8	3.955670E-2	10/10	3.955670E-2	10/10	4.734158E-2	9/9	3.794517E-2	10/25	3.794517E-2	10/25
4x4	3.713887E-2	5/5	2.989876E-2	5/5	2.989876E-2	5/5	3.537362E-2	6/6	2.746745E-2	22/22	2.746745E-2	22/22
8x8	3.261131E-2	6/6	2.875285E-2	8/8	2.875285E-2	8/8	3.024738E-2	10/10	2.620665E-2	34/34	2.620665E-2	34/34
16x16	3.115532E-2	7/7	2.915368E-2	10/10	2.915368E-2	10/10	2.872785E-2	11/15	2.665496E-2	11/12	2.665496E-2	11/12
32x32	3.060962E-2	13/24	2.964003E-2	9/11	2.964003E-2	9/11	2.821254E-2	15/15	2.719402E-2	13/43	2.719402E-2	13/43
64x64	3.043137E-2	11/114	2.996973E-2	10/22	2.996973E-2	10/22	2.802434E-2	12/271	2.754380E-2	10/19	2.754380E-2	10/19
128x128	3.037885E-2	12/248	3.015621E-2	9/14	3.015621E-2	9/14	2.797157E-2	11/635	2.774035E-2	10/17	2.774035E-2	10/17

Table 4.8. *Bingham flow in driven cavity:* Energy norm and numerical efficiency using the uniform mesh $[0,1] \times [0,1]$ for different discretizations and different regularization parameters at $\tau_s = 0.5$ and $\tau_s = 1.0$ for Bingham fluid.

Yield value			$\tau_s = 5$				$\tau_s = 10$					
Element	$\widetilde{Q}_1Q_0$		Q_2P_1		$Q_2P_1^{np}$		$\widetilde{Q}_1Q_0$		Q_2P_1		$Q_2P_1^{np}$	
Total accuracy	*E.norm.*	*Eff.*	*E.norm*	*Eff.*	*E.norm*	*Eff.*	*E.norm*	*Eff.*	*E.norm*	*Eff.*	*E.norm*	*Eff.*
$\epsilon = 10^{-1}$												
2x2	4.376160E-2	6/14	3.461515E-2	5/12	3.461515E-2	5/12	4.338570E-2	8/17	3.413796E-2	6/13	3.413796E-2	6/13
4x4	2.995563E-2	10/10	2.172977E-2	6/6	2.172977E-2	6/6	2.725653E-2	16/16	2.082197E-2	6/6	2.082197E-2	6/6
8x8	2.199208E-2	9/9	1.748922E-2	7/7	1.748922E-2	7/7	1.904773E-2	14/14	1.399005E-2	8/10	1.399005E-2	8/10
16x16	2.005370E-2	7/10	1.786177E-2	7/8	1.786177E-2	7/8	1.588973E-2	9/12	1.366051E-2	8/11	1.366051E-2	8/11
32x32	1.948361E-2	7/21	1.840508E-2	6/9	1.840508E-2	6/9	1.523858E-2	9/26	1.418152E-2	8/12	1.418152E-2	8/12
64x64	1.928949E-2	6/55	1.878824E-2	6/7	1.878824E-2	6/7	1.501845E-2	7/70	1.453999E-2	6/9	1.453999E-2	6/9
128x128	1.924355E-2	5/93	1.899138E-2	6/7	1.899138E-2	6/7	1.495064E-2	6/199	1.472826E-2	7/9	1.472826E-2	7/9
$\epsilon = 10^{-2}$												
2x2	4.333900E-2	11/25	3.352000E-2	7/7	3.352000E-2	7/7	4.305047E-2	30/72	3.341820E-2	5/5	3.341820E-2	5/5
4x4	3.025998E-2	18/18	2.132382E-2	13/13	2.132382E-2	13/13	2.747821E-2	40/40	2.064115E-2	17/21	2.064115E-2	17/21
8x8	2.183020E-2	19/21	1.709503E-2	13/22	1.709503E-2	13/22	1.867611E-2	52/54	1.355706E-2	14/22	1.355706E-2	14/22
16x16	1.986892E-2	16/31	1.766311E-2	12/21	1.766311E-2	12/21	1.570546E-2	36/50	1.339447E-2	10/29	1.339447E-2	10/29
32x32	1.932837E-2	14/83	1.827324E-2	10/17	1.827324E-2	10/17	1.509695E-2	32/85	1.404612E-2	12/25	1.404612E-2	12/25
64x64	1.913455E-2	10/89	1.864252E-2	10/15	1.864252E-2	10/15	1.487502E-2	20/274	1.439925E-2	12/21	1.439925E-2	12/21
128x128	1.907530E-2	10/293	1.884056E-2	8/11	1.884056E-2	8/11	1.480808E-2	14/375	1.458490E-2	10/17	1.458490E-2	10/17
$\epsilon = 10^{-3}$												
2x2	4.333095E-2	29/29	3.335420E-2	12/12	3.335420E-2	12/12	4.338278E-2	29/29	3.334189E-2	7/7	3.334189E-2	7/7
4x4	2.987667E-2	56/60	2.129195E-2	24/24	2.129195E-2	24/24	2.897199E-2	109/111	2.060652E-2	31/31	2.060652E-2	31/31
8x8	2.170386E-2	38/62	1.707229E-2	16/40	1.707229E-2	16/40	1.896900E-2	163/223	1.352766E-2	37/82	1.352766E-2	37/82
16x16	1.983956E-2	42/190	1.766390E-2	15/71	1.766390E-2	15/71	1.585550e-2	98/260	1.337971E-2	20/102	1.337971E-2	20/102
32x32	1.933501E-2	45/775	1.827686E-2	12/48	1.827686E-2	12/48	1.512280e-2	96/489	1.404993E-2	19/51	1.404993E-2	19/51
64x64	1.913675E-2	66/303	1.864844E-2	12/42	1.864844E-2	12/42	div	div	1.440594E-2	15/53	1.440594E-2	15/53
128x128	1.907941E-2	703/703	1.884634E-2	16/43	1.884634E-2	16/43	div	div	1.459374E-2	14/90	1.459374E-2	14/90

Table 4.9. *Bingham flow in driven cavity:* Energy norm and numerical efficiency using the uniform mesh $[0,1] \times [0,1]$ for different discretizations and different regularization parameters at $\tau_s = 5$ and $\tau_s = 10$ for Bingham fluid.

4.6.3 Stationary Fluids Around A Cylinder

Flow around a cylinder(see [216]) is a well-known benchmark developed in 1995 for the priority research program " Flow Simulation on Performance Computers " under the auspices of the DFG (the german research association) (see Fig.4.5). For the 2D case the geometry of the domain is prescribed by the rectangular domain 0.41 m height and 2.2 m long. The diameter of the cylinder is 0.1 m and the coordinates of center is (0.2,0.2). The following definitions are introduced to compute the following numbers and values. The Reynolds number can be defined by the following

$$Re = \frac{U_m D}{\mu} \tag{4.71}$$

where U_m is the mean velocity which is $\int_0^H u(y)dy$ and D is the diameter. u(y) is the inflow velocity which has

$$u(y) = \frac{4U_m y(H-y)}{H^2} \tag{4.72}$$

for the height H and $U_m = 0.3$. The Strouhal number is defined as

$$St = \frac{Df}{U_m} \tag{4.73}$$

where f is the frequency of the separation. The length of the circulation is $L_a = x_r - x_e$ where $x_e = 0.25$ is the x-component of the end of the cylinder and x_r is the x-coordinate of the end of the circulation area. As a further reference value, the pressure difference Δp can be computed which equals to the pressure difference between the front and end points of the cylinder. So, the pressure difference is obtained by the following:

$$\Delta p = p(x_a, y_a) - p(x_e, y_e). \tag{4.74}$$

where, the front point (x_a, y_a) and end point (x_e, y_e) are (0.15,0.2) and (0.25,0.2) respectively. The drag (F_d) and lift (F_l) forces can readily be calculated from the surface integration of the normal component of the shear stress tensor τ_s over the surface of the obstacle for the horizontal x and y direction respectively. The corresponding drag $\mathbf{C}_d$ and lift $\mathbf{C}_l$ coefficients can be computed from the following forms:

$$C_d = \frac{2F_d}{\rho U_m^2 D}, \qquad C_l = \frac{2F_l}{\rho U_m^2 D}. \tag{4.75}$$

In the governing equation, as we mentioned, shear stress formulation $\boldsymbol{\tau}$ has the symmetric part of deformation tensor $\mathbf{D} = (\boldsymbol{\nabla u} + \boldsymbol{\nabla u}^T)/2$, this leads to the failure of Korn inequality for lower order finite elements like $\tilde{Q}_1 Q_0$. The edge oriented stabilization is used to stabilize the bilinear form to satisfy Korn inequality. Most of researchers have reported such results to demonstrate and confirm the efficiency of the proposed stabilization, particulary the performance of the multigrid solver (see [217]), comparing with different stabilization techniques unlike, upwinding and streamline diffusion. In this case we used the edge oriented stabilization for global constant pressure approach, to compare with the central difference approach for the mapped linear or unmapped linear pressures approaches.
Firstly, our test cases will be for the laminar flow to avoid the complexity of the flow models. Drag force, lift force and the efficiency of the coupled solvers have to be computed in order to measure the ability to produce quantitatively accurate results and confirm the efficiency of the proposed solvers for the Newtonian and Non-Newtonian fluids. Afterwards we will go further to analyze and answer some decisive questions about the influence of the modeling error and the discretization error on the accuracy of the results.

D.O.F	*Elements*	*Vertices*	*Midpoints*	$DOF(\tilde{Q}_1 Q_0)$	$DOF(Q_2 P_1)$
level1	130	156	286	702	1534
level2	520	572	1092	2704	5928
level3	2080	2184	4264	10608	23296
level4	8320	8528	16848	42016	92352
level5	33280	33696	66976	167232	367744
level6	133120	133952	267072	667264	1467648
level7	532480	534144	1066624	2665728	5863936

Table 4.10. Degrees of Freedom of $\tilde{Q}_1 Q_0$ and $Q_2 P_1$ for cylinder benchmark.

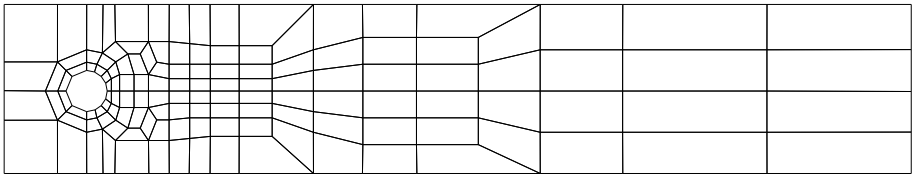

Fig. 4.5. Coarse mesh for the cylinder benchmark.

4.6.3.a Stationary Newtonian Fluids Around A Cylinder

Calculation of drag and lift forces are investigated analytically for the spherical particle in infinite Newtonian fluid under the creeping flow to obtain a compact form for the drag coefficient $C_d = \frac{24}{Re}$ (see [23, 52, 153, 105, 141]). Many monographs have handled numerically the drag and lift calculations to investigate the difference between the numerical and analytical approach and to measure the accuracy of the numerical results (see [74, 203, 204]).
In this section we present our numerical results for 2D Navier-stokes equation to investigate the accuracy of the discretization techniques and the efficiency of the coupled solver comparing them with the computational results in [28, 118, 120, 216, 214].
From the first look, to compare with several discretizations with respect to the accuracy of the computed benchmark parameters, one can observe that, the higher order finite elements are in general most accurate. This numerical comparison shows a drawback of the performance of the edge oriented stabilization in area of the low order finite elements and its influence on the accuracy of the results which is critical for the real simulation. It is found from the depicted table(4.11) that for $\tilde{Q}_1Q_0$ at Re=1 the minimum deviation of the numerical result at mesh 256×256 for the drag and lift values are $7.6 \times 10^{-3}\%$ and 2.1837% and corresponding values for Q_2P_1 are $2.227 \times 10^{-4}\%$ and 2.1694% respectively. In the second case at Re=20($\mu = 10^{-3}$) for $\tilde{Q}_1Q_0$ are 0.0430% and 0.4299% for Q_2P_1 are $3.5846 \times 10^{-4}\%$ and 0.075% respectively. The second complementary part is for efficiency of the coupled solver, comparing with others. This shows that the coupled Newton-multigrid process proves to be the significant for incompressible Navier-Stokes equation.

4.6.3.b Stationary Generalized Newtonian Fluids Around A Cylinder

In contrast to the voluminous computational works used to investigate drag and lift in Newtonian fluid, the computational work for drag and lift used to analyze the effect of nonlinear viscosity for Non-Newtonian fluids is still in its embryonic stage and under research (see [47]). The behavior of the particles(sphere or cylinder) in Non-Newtonian fluids have been studied recently by several researchers by using theoretical and computational investigations. In [14, 22, 47, 81] the authors have shown the drag and lift computations for several Non-Newtonian models. In [109] the boundary effect on the drag acting on a rigid particle is investigated with Carreau model. In [178] it is investigated with analytical way the movement of the spherical bubble and a rigid particle in an infinite Carreau fluid under the condition of creeping flow. For more details see [47, 48, 110, 170, 182, 194] and the references therein. For DFG cylinder benchmark configuration, We have a priority to compute the drag and lift for Carreau shear thickening and Carreau shear thinning with the following associated parameters(see table(4.12)). The absence of referenced values in this case enforces us to compare different discretizations to depict the average values for the introduced flow model besides the behavior of the coupled solvers in case of Non-Newtonian fluid. From the depicted table(4.13), the drag and lift values converge at fixed numbers of digits which result in very finest mesh.

Element		$\tilde{Q}_1Q_0$			Q_2P_1			$Q_2P_1^{np}$	
T.Accuracy	*drag*	*lift*	*Eff.*	*drag*	*lift*	*Eff.*	*drag*	*lift*	*Eff.*
Re=1									
level1	2.487516E3	1.972023E1	4/76	3.014473E3	2.774158E1	4/97	3.016468E3	2.779520E1	4/97
level2	2.911622E3	2.620460E1	3/7	3.110103E3	2.962368E1	2/3	3.110290E3	2.962849E1	2/3
level3	3.077545E3	2.904993E1	3/5	3.134128E3	3.004975E1	2/3	3.134138E3	3.004999E1	2/3
level4	3.125612E3	2.989672E1	3/5	3.140308E3	3.015881E1	2/3	3.140309E3	3.015882E1	2/3
level5	3.138180E3	3.012022E1	3/5	3.141891E3	3.018662E1	2/3	3.141891E3	3.018662E1	2/3
level6	3.141362E3	3.017701E1	2/3	3.142292E3	3.019366E1	2/3	3.142292E3	3.019366E1	2/3
level7	3.142160E3	3.019126E1	2/3	3.142393E3	3.019543E1	2/3	3.142393E3	3.019543E1	2/3
Re=20									
level1	5.886096E00	2.143208E-2	20/456	5.528999E00	5.311195E-3	6/238	5.604949E00	5.330656E-3	6/243
level2	5.698060E00	1.196719E-2	6/11	5.545640E00	9.037125E-3	3/7	5.547962E00	9.017241E-3	3/7
level3	5.786442E00	7.246277E-2	4/7	5.567122E00	1.042543E-2	3/5	5.547962E00	1.042687E-2	3/5
level4	5.671266E00	8.655240E-2	4/7	5.576081E00	1.056494E-2	3/5	5.576077E00	1.056506E-2	3/5
level5	5.609892E00	9.945187E-3	3/5	5.578650E00	1.060381E-2	2/3	5.578650E00	1.060381E-2	2/3
level6	5.588327E00	1.042512E-2	3/5	5.579313E00	1.061503E-3	2/3	5.579313E00	1.061503E-2	2/3
level7	5.581909E00	1.056439E-2	2/3	5.579480E00	1.061796E-2	2/3	5.579480E00	1.061796E-2	2/3

Table 4.11. *Newtonian flow around a cylinder:* Drag, lift and numerical efficiency for different discretizations at Re=1 (Reference value of drag = 3142.4, Reference value of lift= 30.865) and Re=20 (Reference value of drag = 5.5795, Reference value of lift=0.01061) for Newtonian fluid.

fluid type	ν_0	ν_∞	λ	n	a
Shear Thickening	0.00345	0.056	1.902	0.22	2,
Shear Thinning	0.056	0.00345	1.902	0.22	2.

Table 4.12. Shear thickening/thinnig parameters.

However, it is possible to define reference values which allow a clear assessment of the results obtained with higher and lower finite element spaces. We can obtain the reference values by taking them at the finest level with the fixed similar digits or by extrapolating the results which we consider accurate. But in our case we choose the former selection. Therefore, for shear thickening model one can consider the reference values for drag and lift are 136.58 ± 0.01 and 1.3712 ± 0.01 respectively and for shear thinning 47.76 ± 0.01 and 0.4438 ± 0.0001 respectively. The counterpart is the efficiency of the solver which can be computed by iteration cost, the behavior is quite similar to the Newtonian flow which associates a significant robustness of the coupled solver for the nonlinear models.

4.6.3.c Stationary Bingham Viscoplastic Fluids Around A Cylinder

Relatively needless to say that, a few works have been devoted to solve analytically the motion of viscoplastic fluid around an obstacle (sphere/cylinder), even in the creeping flow regime. The first work was done by Yoshioka et al in [228] for spherical shape and in [229] for cylindrical shape co-operating with (see [226, 227, 230, 231]). The authors have used the stress and velocity variational principles to obtain approximate upper and lower bounds on drag coefficients for the creeping motion of a sphere in a Bingham viscoplastic fluids. The numerical results for the spherical shape has been confirmed in a good agreement with the analytical ones due to Yoshioka et al in [19], but surprisingly with a major difference or disagreement in the predicted shape of the sheared zones in these two works. On the other hand, some of the researchers have a contribution for flow around sphere (see [5, 6, 9, 10, 117, 139, 140, 154, 175]) and with an additional conditions 'for instance wall effects'(see [24, 62]) and to predict an empirical value for drag and with the rang of Bingham number $0 \leq B_n = \frac{\tau_s D}{\mu U} \leq 1000$ in [24] to be $\delta C_d = a(B_n)^b$ where δC_d is the difference between Bingham fluid and Newtonian fluid($\tau_s = 0$) where D is the diameter of the sphere and U is the infinite flow velocity.
Regarding the experimental and numerical results for the cylindrical shape, the contributive works are to

Element	$\tilde{Q}_1Q_0$			Q_2P_1			$Q_2P_1^{np}$		
T.Accuracy	*drag*	*lift*	*Eff.*	*drag*	*lift*	*Eff.*	*drag*	*lift*	*Eff.*
s.thickening									
level1	1.456852E2	1.351800E00	5/119	1.319678E2	1.206470E00	17/321	1.320283E2	1.208802E00	17/326
level2	1.359454E2	1.333428E00	5/6	1.352235E2	1.337650E00	4/4	1.352292E2	1.337927E00	4/4
level3	1.355833E2	1.356328E00	5/6	1.362087E2	1.364789E00	4/4	1.362089E2	1.364768E00	4/4
level4	1.361925E2	1.365874E00	5/6	1.364865E2	1.369800E00	4/4	1.364865E2	1.369791E00	4/4
level5	1.364663E2	1.369591E00	4/4	1.365592E2	1.370929E00	4/5	1.365592E2	1.370928E00	4/5
level6	1.365520E2	1.370801E00	4/5	1.365778E2	1.371186E00	3/3	1.365592E2	1.371186E00	3/3
level7	1.365757E2	1.371175E00	4/5	1.365825E2	1.371278E00	3/3	1.365825E2	1.371278E00	3/3
s.thinning									
level1	5.795529E1	2.670679E-1	5/145	4.658142E1	3.776375E-1	6/159	4.661289E1	3.781424E-1	6/155
level2	4.901668E1	3.732135E-1	5/8	4.744784E1	4.343042E-1	4/4	4.745228E1	4.343290E-1	4/4
level3	4.760757E1	4.221035E-1	5/8	4.766654E1	4.420653E-1	4/4	4.766678E1	4.420743E-1	4/4
level4	4.761361E1	4.377557E-1	4/6	4.773629E1	4.434635E-1	4/5	4.773630E1	4.434637E-1	4/5
level5	4.770458E1	4.423480E-1	4/6	4.775558E1	4.437919E-1	3/3	4.775558E1	4.437919E-1	3/3
level6	4.774461E1	4.435146E-1	4/6	4.776058E1	4.438737E-1	3/3	4.776058E1	4.438737E-1	3/3
level7	4.775740E1	4.438049E-1	4/6	4.776185E1	4.438942E-1	3/3	4.776185E1	4.438942E-1	3/3

Table 4.13. *Shear thickening and shear thinning flow around a cylinder:* drag, lift and numerical efficiency for different discretizations for shear thickening and shear thinning fluids.

provide an approximated size and shape of the fluid-like and solid like zones in the vicinity of the cylinder boundary gathered by the qualitative influence of yield stress (see [62, 180, 209, 210, 236]). A few trails to predict the values of the drag coefficient have drawn for instance in [158, 229]. In [158], the author tried to predict an empirical value for drag coefficient for a cylindrical shape with the following normalized form $(1 + aB_n)^b$ to fit the numerical results for the corresponding geometry configuration (where a, b are fitting parameters which can be found by performing a non-linear regression analysis on the simulation results in the rang $0 \leq B_n \leq 1000$ for every geometry).
For the DFG cylinder benchmark, our aim is two-folded; the first is to compare the discretization techniques with respect to the accuracy against the modeling error and the discretization error for the computed benchmark parameters which might be drag and lift forces as well as to prove the efficiency and robustness of coupled solvers for the saddle point problem evolved from the viscoplastic equations. The second is the priority to compute the benchmark parameters for flow around cylinder in viscoplastic medium. The way to choose the computed benchmark parameters as references is based on which could be from the computed from higher order finite element discretization at the finest level 'global linear pressure approach' or by extrapolating the results from lower order and higher order finite elements. We might choose the first one as most accurate for the previous results.
From the depicted tables(4.15, 4.16 and 4.17), we have provided the values of drag and lift for different values of yield stress $\frac{1}{4}, \frac{1}{2}, 1$ to observe easily incremental increasing corresponding to the incremental increasing in the yield stress value. This observation is already mentioned in viscoplastic papers to prove the validity of the scheme. For each value for yield stress, the numerical values of drag and lift converges with a certain order of convergence which is decreasing at the finer levels and at lower values of regularization parameter to certain constant fixed values. These values can be overwritten in the following table(4.14). Surprisingly, the values of the lift are decreasing in contrast with the value of drag by increasing the yield

Yield Stress	$\frac{1}{4}$	$\frac{1}{2}$	1
drag	3321.55	3501.08	3859.89
lift	30.73	30.65	29.34

Table 4.14. Drag and lift values at level 8 for the corresponding yield stress.

stress value which is confirming the resistance property for the yield stress. The influence of the modeling error is reduced rapidly by decreasing the value of regularization parameter after 10^{-3} with relative error

10^{-3}% and 2% for drag and lift respectively for each value of yield stress. Therefore, the calculation of the benchmark parameter with loosely speaking is meaningless after 10^{-4} which consumes time from the numerical point of the view. The difference of the computed drag and lift to the different discretization techniques is a bit fragile but needless to say the most accurate parameters are computed with high order finite element.

To investigate the efficiency of the introduced solver for the saddle point problem obtained by the high order finite elements and the stabilized low order non-conforming finite element, the strong effect comes from the modeling error which destroys the behavior of the Newton process starting from 10^{-3}. After this value Newton process is behaved as fixed point method, and the gain to have low cost is rare particular at the fine grid, since the damping is not applied. It is observed from the computation that the used Tolerance (TOL) to switch for the Newton process from the resulted fixed point iteration which is usually at most 2 iterations influenced by the viscoplastic parameters, particularly, the regularization parameter(ϵ) which has a catastrophic effect on the convergence of Newton process. That means, at the smaller value of ($\leq 10^{-3}$), the Newton process is not helpful to speed up the convergence, i.e., the fixed point iteration and the Newton iteration have the same behavior in the sense of the convergence.

One can notice that, the starting value(tolerance) should be less and less than the value of the ϵ to obtain the convergence behavior for the Newton process, and taking into the account the action of τ_s and mesh size(h) which render the convergence process harder at the higher and lower values respectively. On the other hand, the table expose that the use of multigrid increases robustness of the solver considerably as a preconditioner with at high number of pre-smoothing and post-smoothing. Altogether, for the low order and high order finite elements discretizations the Newton-Multigrid might be considered the robust solver for the viscoplastic flow.

Element		$\tilde{Q}_1Q_0$			Q_2P_1			$Q_2P_1^{np}$	
T.Accuracy	*drag*	*lift*	*Eff.*	*drag*	*lift*	*Eff.*	*drag*	*lift*	*Eff.*
$\epsilon = 1.0E-1$									
level1	2.884442E3	2.333230E1	7/150	3.210867E3	2.906308E1	6/146	3.212485E3	2.909658E1	6/181
level2	3.154032E3	2.831101E1	6/7	3.290132E3	3.021593E1	5/5	3.290300E3	3.022011E1	5/5
level3	3.274129E3	2.989576E1	6/6	3.312745E3	3.054096E1	4/4	3.312753E3	3.054801E1	4/4
level4	3.308857E3	3.052150E1	5/6	3.318965E3	3.063360E1	4/5	3.318965E3	3.063369E1	4/5
level5	3.318022E3	3.062727E1	4/7	3.321003E3	3.066589E1	3/4	3.321003E3	3.066590E1	3/4
level7	3.320946E3	3.066558E1	4/32	3.321108E3	3.066757E1	3/4	3.321108E3	3.066757E1	3/4
$\epsilon = 1.0E-2$									
level1	2.884736E3	2.326333E1	9/178	3.211267E3	2.922626E1	13/356	3.218822E3	2.926039E1	13/354
level2	3.154405E3	2.836245E1	9/9	3.290563E3	3.025238E1	13/13	3.290731E3	3.025589E1	13/13
level3	3.274583E3	2.986777E1	8/8	3.313176E3	3.058295E1	12/13	3.313184E3	3.058417E1	12/13
level4	3.309296E3	3.056189E1	8/12	3.319404E3	3.066730E1	10/10	3.319405E3	3.066741E1	10/10
level5	3.318466E3	3.065815E1	7/23	3.321033E3	3.069278E1	7/7	3.321033E3	3.069278E1	7/7
level6	3.320801E3	3.069028E1	7/50	3.321447E3	3.069832E1	5/5	3.321447E3	3.069832E1	5/5
level7	3.321389E3	3.069808E1	6/48	3.321550E3	3.070007E1	4/4	3.321551E3	3.070007E1	4/4
$\epsilon = 1.0E-3$									
level1	2.884743E3	2.326956E1	10/202	3.211287E3	2.925773E1	26/581	3.212900E3	2.928898E1	24/580
level2	3.154407E3	2.837362E1	17/20	3.290562E3	3.026974E1	36/37	3.290731E3	3.027289E1	36/37
level3	3.274588E3	2.987501E1	23/41	3.313180E3	3.061435E1	36/41	3.313188E3	3.061567E1	36/41
level4	3.309300E3	3.058663E1	18/68	3.319408E3	3.069728E1	34/40	3.319408E3	3.069739E1	34/40
level5	3.318470E3	3.068754E1	20/119	3.321037E3	3.072317E1	26/30	3.321037E3	3.072318E1	26/30
level6	3.320806E3	3.072062E1	17/230	3.321451E3	3.072856E1	19/21	3.321451E3	3.072856E1	19/21
level7	3.321393E3	3.072863E1	22/144	3.321555E3	3.073030E1	10/11	3.321555E3	3.073030E1	10/11

Table 4.15. *Bingham flow around a cylinder:* Drag, lift and numerical efficiency for different discretizations at $\tau_s = 0.25$ for Bingham fluid.

Element	$\tilde{Q}_1Q_0$			Q_2P_1			$Q_2P_1^{np}$		
T.Accuracy	*drag*	*lift*	*Eff.*	*drag*	*lift*	*Eff.*	*drag*	*lift*	*Eff.*
$\epsilon = 1.0E-1$									
level1	3.039168E3	2.285431E1	9/182	3.383991E3	2.964564E1	8/244	3.385713E3	2.968540E1	8/249
level2	3.323628E3	2.847612E1	7/7	3.467717E3	3.058300E1	6/6	3.467893E3	3.058780E1	6/6
level	3.450764E3	3.002788E1	7/7	3.491260E3	3.084837E1	5/5	3.491269E3	3.084951E1	5/5
level4	3.487127E3	3.081335E1	6/8	3.497711E3	3.091678E1	4/4	3.497712E3	3.091689E1	4/4
level5	3.496703E3	3.090739E1	6/23	3.499396E3	3.094014E1	3/3	3.499396E3	3.094015E1	3/3
level6	3.499147E3	3.093751E1	5/32	3.499824E3	3.094524E1	3/3	3.499824E3	3.094524E1	3/3
level7	3.499763E3	3.094483E1	5/72	3.499933E3	3.094673E1	3/4	3.499933E3	3.094673E1	3/4
$\epsilon = 1.0E-2$									
level1	3.039838E3	2.232640E1	24/458	3.384910E3	2.973738E1	21/726	3.386641E3	2.979109E1	21/748
level2	3.324635E3	2.828230E1	24/25	3.468789E3	3.047451E1	22/23	3.468965E3	3.048038E1	22/23
level	3.451929E3	2.969039E1	23/27	3.492337E3	3.069578E1	16/17	3.492346E3	3.069706E1	16/17
level4	3.488238E3	3.063808E1	19/27	3.498834E3	3.071450E1	14/14	3.498835E3	3.071464E1	14/14
level5	3.497833E3	3.070359E1	15/76	3.500524E3	3.073702E1	10/10	3.500524E3	3.073703E1	10/10
level6	3.500275E3	3.073449E1	11/104	3.500950E3	3.073844E1	5/5	3.500954E3	3.073844E1	5/5
level7	3.500892E3	3.073846E1	9/76	3.501062E3	3.073987E1	6/7	3.501062E3	3.073987E1	6/7
$\epsilon = 1.0E-3$									
level1	3.039861E3	2.222489E1	62/752	3.384936E3	2.975511E1	36/1213	3.386670E3	2.980884E1	36/1120
level2	3.324692E3	2.797284E1	66/76	3.468817E3	3.033272E1	65/74	3.468993E3	3.033865E1	65/74
level	3.451974E3	2.939987E1	70/104	3.492351E3	3.062831E1	54/68	3.492360E3	3.062916E1	54/68
level4	3.488264E3	3.048286E1	71/131	3.498852E3	3.062856E1	52/54	3.498853E3	3.062868E1	52/54
level5	3.497854E3	3.060053E1	54/172	3.500542E3	3.065315E1	42/46	3.500542E3	3.065315E1	42/46
level6	3.500291E3	3.064905E1	52/386	3.500973E3	3.065339E1	29/32	3.500973E3	3.065338E1	29/32
level7	3.500911E3	3.065375E1	37/310	3.501081E3	3.065538E1	13/17	3.501081E3	3.065538E1	13/17

Table 4.16. *Bingham flow around a cylinder:* Drag, lift numerical efficiency for different discretizations at $\tau_s = 0.5$ for Bingham fluid.

4.7 Influence of Perturbation on the Solvers for Bingham Viscoplastic Fluids Problem

As a concrete test to observe the influence of the starting solution in the behavior of the solver, we have chosen two cases, the first one is the zero starting solution and the second is from one level above. It is observed that from the depicted tables(4.18, 4.19 and 4.20) for different discretizations the number of iterations for the linear and nonlinear solver are going to increase with the perturbation of the mesh due to the changing of the nodes at different ratios, but in the other hand the zero staring solution is already fixed for all ratios which means the starting is the same for all perturbations. For this reason, we have the same behavior of the solver at different ratios for the perturbed mesh (see table 4.21).

4.8 Summary

This chapter presents numerical studies of several flow models for different configuration defining benchmarks problems. The first aim is to exhibit a comparison of several finite element discretizations with respect to accuracy of the benchmarks parameters regarding energy norms, drag force and lift force. The second is to highlight the robustness, flexibility and efficiency of the coupled solver for non-stabilized and stabilized finite elements for several flow models. The results of the benchmark parameters are quite similar for the discretizations which confirm the idea of success of multigrid evolved from the efficient smoother. The results from the benchmarks parameters which have been computed with different finite elements are very promising for the real problems modeled by the deformation tensor. The accurate values for benchmark parameters evolved from known models with known results assist us for a clear

Element	$\tilde{Q}_1Q_0$			Q_2P_1			$Q_2P_1^{np}$		
T.Accuracy	*drag*	*lift*	*Eff.*	*drag*	*lift*	*Eff.*	*drag*	*lift*	*Eff.*
$\epsilon = 1.0E-1$									
level1	3.347616E3	2.161004E1	12/294	3.729504E3	3.009552E1	12/403	3.729504E3	3.014773E1	12/383
level2	3.662419E3	2.861036E1	10/11	3.822180E3	3.124086E1	8/8	3.822380E3	3.124638E1	8/8
level3	3.893299E3	3.059597E1	9/10	3.847634E3	3.165687E1	6/6	3.847644E3	3.165799E1	6/6
level4	3.842976E3	3.151227E1	8/20	3.854494E3	3.169732E1	5/5	3.854495E3	3.169735E1	5/5
level5	3.853368E3	3.164983E1	7/27	3.856310E3	3.170611E1	4/5	3.856310E3	3.170611E1	4/5
level6	3.856029E3	3.169689E1	6/45	3.856768E3	3.170974E1	4/5	3.856768E3	3.170974E1	4/5
level7	3.856699E3	3.71—-E1	5/66	3.856884E3	3.171079E1	3/4	3.856884E3	3.171079E1	3/5
$\epsilon = 1.0E-2$									
level1	3.321007E3	1.976797E1	27/27	3.731770E3	2.929552E1	23/23	3.733694E3	2.938541E1	23/23
level2	3.659166E3	2.690309E1	22/30	3.825225E3	2.990691E1	20/23	3.825425E3	2.991692E1	20/23
level	3.805780E3	2.867008E1	24/50	3.850633E3	3.028865E1	15/17	3.850642E3	3.029055E1	15/17
level4	3.845927E3	3.013134E1	15/70	3.857461E3	3.038229E1	11/13	3.857462E3	3.038232E1	11/13
level5	3.856384E3	3.023809E1	12/160	3.859299E3	3.038351E1	7/9	3.859299E3	3.038348E1	7/9
level6	3.859009E3	3.037258E1	10/331	3.859754E3	3.039010E1	6/7	3.859754E3	3.039010E1	6/7
level7	3.859685E3	3.038526E1	13/389	3.859871E3	3.038865E1	7/9	3.859871E3	3.038865E1	7/9
$\epsilon = 1.0E-3$									
level1	3.321000E3	1.937934E1	54/957	3.731933E3	2.834682E1	38/38	3.733852E3	2.846255E1	38/38
level2	3.659401E3	2.571132E1	53/100	3.825359E3	2.902317E1	150/150	3.825559E3	2.903283E1	150/150
level	3.806026E3	2.718188E1	45/197	3.850760E3	2.926056E1	253/253	3.850769E3	2.926226E1	253/253
level4	3.846117E3	2.888466E1	30/323	3.857604E3	2.932861E1	337/337	3.857604E3	2.932864E1	337/337
level5	3.856549E3	2.912118E1	25/447	3.859441E3	2.932933E1	285/285	3.859441E3	2.932929E1	285/285
level6	3.859147E3	2.931023E1	49/504	3.859895E3	2.934029E1	307/307	3.859895E3	2.934029E1	307/307

Table 4.17. *Bingham flow around a cylinder:* Drag, lift and numerical efficiency for different discretizations at $\tau_s = 1.0$ for Bingham fluid.

Perturbation	0%	5%	10%	15%	20%
*level*5					
$\|\boldsymbol{u} - \boldsymbol{u}_h\|_{\mathbf{L}^2}$	6.579984E-5	6.640359E-5	6.809965E-5	7.093351E-5	7.497943E-5
$\|p - p_h\|_{\mathbf{L}^2}$	4.045852E-2	4.044963E-2	4.030536E-2	4.005135E-2	3.971159E-2
$\|\boldsymbol{u} - \boldsymbol{u}_h\|_{\mathbf{H}^1}$	5.273610E-3	5.320178E-3	5.446232E-3	5.647091E-3	5.914822E-3
NN/MG	24/26	24/26	24/26	24/26	24/25
*level*6					
$\|\boldsymbol{u} - \boldsymbol{u}_h\|_{\mathbf{L}^2}$	5.862734E-5	5.872007E-5	5.895735E-5	5.933933E-5	5.986674E-5
$\|p - p_h\|_{\mathbf{L}^2}$	4.139677E-2	4.133230E-2	4.118435E-2	4.097375E-2	4.072607E-2
$\|\boldsymbol{u} - \boldsymbol{u}_h\|_{\mathbf{H}^1}$	2.835983E-3	2.859625E-3	2.928498E-3	3.041033E-3	3.193277E-3
NN/MG	18/25	18/21	19/23	20/24	21/25
*level*7					
$\|\boldsymbol{u} - \boldsymbol{u}_h\|_{\mathbf{L}^2}$	5.839306E-5	5.840695E-5	5.844880E-5	5.851618E-5	5.860501E-5
$\|p - p_h\|_{\mathbf{L}^2}$	4.176000E-2	4.175070E-2	4.171647E-2	4.165985E-2	4.158367E-2
$\|\boldsymbol{u} - \boldsymbol{u}_h\|_{\mathbf{H}^1}$	1.827316E-3	1.836392E-3	1.864406E-3	1.911452E-3	1.977432E-3
NN/MG	8/24	9/11	11/14	12/16	13/17
*level*8					
$\|\boldsymbol{u} - \boldsymbol{u}_h\|_{\mathbf{L}^2}$	5.835063E-5	5.835333E-5	5.836155E-5	5.837487E-5	5.839296E-5
$\|p - p_h\|_{\mathbf{L}^2}$	4.190127E-2	4.190130E-2	4.189260E-2	4.187485E-2	4.184770E-2
$\|\boldsymbol{u} - \boldsymbol{u}_h\|_{\mathbf{H}^1}$	1.468422E-3	1.471547E-3	1.481284E-3	1.497915E-3	1.521581E-3
NN/MG	5/38	7/9	8/10	10/15	11/16

Table 4.18. $\mathbf{L}^2/\mathbf{H}^1$ errors and numerical efficiency for $\tilde{Q}_1Q_0$ at different perturbations for Bingham flow in channel at $\tau_s = 0.25$ and $\epsilon = 10^{-3}$ with starting solution from the previous level.

assessment for values the benchmark parameters to have them as reference values for the models. These models might have doubted full results. The nonlinear viscosity problems have treated successfully in

Perturbation	0%	5%	10%	15%	20%
*level*5					
$\|\boldsymbol{u}-\boldsymbol{u}_h\|_{\mathbf{L}^2}$	5.952553E-5	5.970788E-5	6.011667E-5	6.071102E-5	6.149341E-5
$\|p-p_h\|_{\mathbf{L}^2}$	4.191533E-2	4.194773E-2	4.199146E-2	4.204802E-2	4.212987E-2
$\|\boldsymbol{u}-\boldsymbol{u}_h\|_{\mathbf{H}^1}$	1.348964E-3	1.361084E-3	1.382049E-3	1.409488E-3	1.458681E-3
NN/MG	9/10	10/11	10/10	11/11	11/11
*level*6					
$\|\boldsymbol{u}-\boldsymbol{u}_h\|_{\mathbf{L}^2}$	5.838635E-5	5.839163E-5	5.840803E-5	5.843709E-5	5.848808E-5
$\|p-p_h\|_{\mathbf{L}^2}$	4.190132E-2	4.189372E-2	4.188627E-2	4.187959E-2	4.187556E-2
$\|\boldsymbol{u}-\boldsymbol{u}_h\|_{\mathbf{H}^1}$	1.333018E-3	1.334939E-3	1.337343E-3	1.338863E-3	1.343456E-3
NN/MG	5/8	6/9	8/11	9/12	11/15
*level*7					
$\|\boldsymbol{u}-\boldsymbol{u}_h\|_{\mathbf{L}^2}$	5.834382E-5	5.834420E-5	5.834515E-5	5.834696E-5	5.835027E-5
$\|p-p_h\|_{\mathbf{L}^2}$	4.195602E-2	4.195691E-2	4.195821E-2	4.195991E-2	4.196210E-2
$\|\boldsymbol{u}-\boldsymbol{u}_h\|_{\mathbf{H}^1}$	1.327233E-3	1.327616E-3	1.327722E-3	1.327226E-3	1.327322E-3
NN/MG	4/4	6/8	7/10	8/12	8/13
*level*8					
$\|\boldsymbol{u}-\boldsymbol{u}_h\|_{\mathbf{L}^2}$	5.834031E-5	5.834032E-5	5.834035E-5	5.834042E-5	5.834064E-5
$\|p-p_h\|_{\mathbf{L}^2}$	4.198989E-2	4.199049E-2	4.199155E-2	4.199097E-2	4.199155E-2
$\|\boldsymbol{u}-\boldsymbol{u}_h\|_{\mathbf{H}^1}$	1.326833E-3	1.326927E-3	1.326776E-3	1.326955E-3	1.326776E-3
NN/MG	4/4	5/7	6/10	7/12	8/17

Table 4.19. $\mathbf{L}^2/\mathbf{H}^1$ errors and numerical efficiency for Q_2P_1 at different perturbations for Bingham flow in channel at $\tau_s = 0.25$ and $\epsilon = 10^{-3}$ with starting solution from the previous level.

Perturbation	0%	5%	10%	15%	20%
*level*5					
$\|\boldsymbol{u}-\boldsymbol{u}_h\|_{\mathbf{L}^2}$	5.952553E-5	5.970870E-5	6.011700E-5	6.070980E-5	6.149287E-5
$\|p-p_h\|_{\mathbf{L}^2}$	4.191533E-2	4.193850E-2	4.197508E-2	4.202732E-2	4.210922E-2
$\|\boldsymbol{u}-\boldsymbol{u}_h\|_{\mathbf{H}^1}$	1.348964E-3	1.360697E-3	1.380473E-3	1.406066E-3	1.452996E-3
NN/MG	9/10	10/11	10/10	11/11	11/11
*level*6					
$\|\boldsymbol{u}-\boldsymbol{u}_h\|_{\mathbf{L}^2}$	5.838635E-5	5.839176E-5	5.840858E-5	5.843864E-5	5.849201E-5
$\|p-p_h\|_{\mathbf{L}^2}$	4.190132E-2	4.189776E-2	4.189478E-2	4.189288E-2	4.189392E-2
$\|\boldsymbol{u}-\boldsymbol{u}_h\|_{\mathbf{H}^1}$	1.333018E-3	1.334823E-3	1.336886E-3	1.337893E-3	1.341889E-3
NN/MG	5/8	6/9	8/11	9/12	11/15
*level*7					
$\|\boldsymbol{u}-\boldsymbol{u}_h\|_{\mathbf{L}^2}$	5.834382E-5	5.834424E-5	5.834527E-5	5.834722E-5	5.835079E-5
$\|p-p_h\|_{\mathbf{L}^2}$	4.195602E-2	4.195629E-2	4.195703E-2	4.195826E-2	4.196008E-2
$\|\boldsymbol{u}-\boldsymbol{u}_h\|_{\mathbf{H}^1}$	1.327233E-3	1.327584E-3	1.327598E-3	1.326960E-3	1.326874E-3
NN/MG	4/4	6/8	7/10	8/12	8/13
*level*8					
$\|\boldsymbol{u}-\boldsymbol{u}_h\|_{\mathbf{L}^2}$	5.834031E-5	5.834033E-5	5.834039E-5	5.834050E-5	5.834078E-5
$\|p-p_h\|_{\mathbf{L}^2}$	4.198989E-2	4.199038E-2	4.199084E-2	4.199125E-2	4.199165E-2
$\|\boldsymbol{u}-\boldsymbol{u}_h\|_{\mathbf{H}^1}$	1.326833E-3	1.326919E-3	1.326923E-3	1.326733E-3	1.326658E-3
NN/MG	4/4	5/7	6/10	7/12	8/17

Table 4.20. $\mathbf{L}^2/\mathbf{H}^1$ errors and numerical efficiency for $Q_2P_1^{np}$ at different perturbations for Bingham flow in channel at $\tau_s = 0.25$ and $\epsilon = 10^{-3}$ with starting solution from the previous level.

the sense of the discretization and solvers. The results that evolved from the numerical efficiency for different discretizations and the behavior of the coupled solvers for $Q_2P_1^{np}$ are most accurate and might be preferable than $\tilde{Q}_1Q_0$. This indicates that the discretization and the solver can be treated as one part. So, the higher order finite elements can be conceived of the potential for linear/nonlinear flow models. The stabilized finite element spaces usually have a big drawback to cope with the highly nonlinear prob-

Perturbations	0%	5%	10%	15%	20%
$\tilde{Q}_1Q_0$	21/40	21/27	21/28	21/28	21/29
Q_2P_1	17/25	17/25	17/26	17/26	17/26
$Q_2P_1^{np}$	17/25	17/25	17/26	17/26	17/26

Table 4.21. Behavior of the solvers for $\tilde{Q}_1Q_0$, Q_2P_1, and $Q_2P_1^{np}$ at different perturbations for Bingham flow in channel with $\tau_s = 0.25$, $\epsilon = 10^{-3}$, $h = \frac{1}{64}$ and zero staring solution

lems to fulfill Korn's inequality in the sense of the deformation tensor form altogether with the variation of the problem parameters. This requires increasing the ability of the stabilization by increasing/decreasing the jump coefficient γ (free parameter) which has a straightforward effect on the accuracy of the benchmarks parameters. For instance for the approach of edge oriented stabilization, the free parameter γ has been increased from 0.01 to 0.5 with increasing the Reynolds number from 1 to 10^2 or decreasing the regularization parameter from 10^{-1} to 10^{-3}. This leads surprisingly to disappointed results shifting away the accuracy of solution.
On the other hand the Newton process is necessary to cope with the nonlinear viscosity problems to avoid unreliable cost in the solution process. Coupled with multigrid solver it shows an elegant flexible behavior for different flow models. In the viscoplastic flow, the incapability of the Newton process is quite natural to have the same behavior of fixed point at low values of ϵ, h and high values for τ_s and Re which turn out the problem as a tolerance dependent.
In Navier-Stokes equation the convergence of Newton method is dependent of the Reynolds number (Re) and the mesh size(h). In [127, 42] the researchers expected the behavior of radius of convergence as the following way $\rho \propto \frac{1}{Re}$. In the viscoplastic case, the observation for the numbers of nonlinear iterations for the Newton Process is in fact dependent on the regularization parameter and yield stress value. This dependence makes the convergence hard for the lower values of the former and higher for the later values respectively. In that case, the behavior of fixed point and Newton is similar which means we could not able to get the quadratic convergence even if we are using the adaptive Newton strategy; and the accuracy of the linear solver to that required for the nonlinear solver (see [4, 106, 107, 234]). From the done calculations one can confirm the following relation between the radius of convergence of Newton process ρ and the viscoplastic parameters (τ_s, Re, h, ϵ)

$$\rho \propto \frac{\epsilon h}{\tau_s Re}, \tag{4.76}$$

which leads to the prepaid tolerance formula

$$TOL \leq \frac{\epsilon h}{\tau_s Re}. \tag{4.77}$$

Therefore as a result of what mentioned above, the comparison between the two processes fixed point and Newton process to treat the nonlinear viscoplastic problem can be outlined in the following table(4.22):

No	Process	Newton Process	Fixed Point Process
1	Convergence	quadratic	linear
2	R. of Convergence	parameter dependent(Re, ϵ, τ_s, h)	larger than Newton Process
3	Cost	few iterations	many iterations
4	Starting Value	good starting value	arbitrary starting value
5	Tolerance	parameter dependent(Re, ϵ, τ_s, h)	arbitrary
6	Perturbation	dependent (if step 4 from one level)	dependent(if step 4 from one level)

Table 4.22. Comparison between Newton and Fixed Point for viscoplastic problems

5

Monolithic Approach for Stationary Viscoplastic Fluids

Numerical techniques to cope with the numerical difficulties for stationary Bingham viscoplastic fluids are presented. Bingham constitutive equation is used with an appropriate modification proposed by Bercovier-Engelman or bi-viscous model coupled with generalized Navier-Stokes equations to obtain a quasi-fully description for Bingham viscoplastic problem. The nonlinearity is treated by using the continuous Newton method calculated by the Frechet derivative for the nonlinear viscosity. The use of LBB-stable higher order conforming finite elements with unmapped pressure approach is employed to have accurate and robust discretization techniques and lower finite elements can be a candidate but with stabilization in case of symmetric deformation form. The resulting nonlinear discretized algebraic system is solved in a monolithic way in the frame of continuous Newton method. The resulting linear subproblems in each nonlinear iterations are treated by a geometric multigrid approach which is adapted to the quadrilateral conforming elements with local multilevel pressure complement smoothers. Three different benchmarks are studied to predict the behavior of the viscoplastic fluids. The main contribution is to show the ability of monolithic approach to handle such highly nonlinear problem with high accuracy and robustness and to predict the flow behavior in cases of appearance of unyielded flow regimes and the distribution of the pressure over the flow domain for all suggested benchmarks.

5.1 Introduction

The definition of generalized Newtonian fluids is characterized by the nonlinearities of their flow curves and featured particularly by the nonlinear viscosity which may depend on the second invariant of the deformation rate tensor($\|\mathbf{D}\|$) (see [48]). The importance of the generalized non-Newtonian fluids lies on the dependence of a variety of industrial applications on their fluidity properties. The motivation towards the theoretical and numerical simulation to predict the medium behavior has been increased during last decades. To date, a huge number of monographs is devoted to simulate quantitively and qualitatively these fluids which are based on the numerical simulation and theoretical investigation. The general form governing the incompressible behavior of these fluids can be written as

$$\frac{\partial \boldsymbol{u}}{\partial t} + \boldsymbol{u} \cdot \boldsymbol{\nabla} \boldsymbol{u} + \boldsymbol{\nabla} p = \boldsymbol{\nabla} \cdot \boldsymbol{\tau} + \boldsymbol{f}, \qquad \boldsymbol{\nabla} \cdot \boldsymbol{u} = 0, \qquad in \quad \boldsymbol{\Omega} \times [0, T], \tag{5.1}$$

for a given force $\boldsymbol{f}$ and the deviatoric part of the stress tensor ($\boldsymbol{\tau}$). The corresponding function for the shear stress is represented by a constitutive equation which gives a complete form to describe such behavior of the fluid. The corresponding nonlinear viscosity function (ν) can be used as primary categorical factor for the classification of fluids. Therefore, such fluids are divided into the following parts due to the relation between the effective viscosity and the symmetric part of deformation tensor: shear-thinning fluids(pseudo-plastic), viscoplastic fluids and shear thickening fluid(dilatant fluid). Our interest here is

restricted to viscoplastic fluids that possess the yield stress property. These fluids occur naturally or industrially as a diverse as greases, slurries, doughs, fresh concrete, and toothpaste. As for an exclusive industrial examples which explain the viscoplasticity behavior from experimental observation, are the wire drawing and the double base-propellants processes. The propellant materials are used for propulsion in guns and rockets. A process used in manufacturing is called solvent incorporation process. The composition is nitrocellulose(NC) plasticized with various amounts of nitroglycerine(NG), with a small amount of added stabilizer to form a dough. The dough is extruded through dies of various shapes and sizes. The process is seen to exhibit a behavior similar to Herschel-Bulkey fluids (see [43]). Others exhibit such viscoplastic behavior like colloidal suspensions (see [54]), and drilling fluids (see [11]).
Our study is going to use the simplest models that describe the viscoplastic behavior which is called Bingham model and reads as follows

$$\boldsymbol{\tau} = \begin{cases} (2\mu + \frac{\boldsymbol{\tau}_s}{\|\mathbf{D}\|})\mathbf{D}(\boldsymbol{u}) \text{ if} & \|\mathbf{D}\| \neq 0, \\ \leq \boldsymbol{\tau}_s \text{ if} & \|\mathbf{D}\| = 0, \end{cases} \tag{5.2}$$

or equivalently:

$$\mathbf{D}(u) = \begin{cases} \frac{1}{2\mu}(1 - \frac{\tau_s}{\|\boldsymbol{\tau}\|})\boldsymbol{\tau} \text{ if} & \|\boldsymbol{\tau}\| > \tau_s, \\ 0 \text{ if} & \|\boldsymbol{\tau}\| \leq \tau_s. \end{cases} \tag{5.3}$$

This model is characterized by a flow curve which is a straight line having an intercept τ_s on the shear stress axis. The shear stress must be exceeded over the yield condition to commence the flow, and the excess is linearly proportional to the shear rate . Typically, the fluid response after yield is taken to be linear in the deformation rate so the material may be viewed as a complicated generalized Newtonian fluid. Three crucial differences are noticed theoretically between Bingham viscoplastic fluids and Newtonian fluids namely nonuniform distribution of pressure, the existence of unyielded zones and the cessation phenomenon (see [44, 71, 113, 167]).
Naturally, Bingham viscoplastic materials have received an extensive attention by many mathematicians and CFD researchers began by Shwedov [192] who was the first to release the idea of yield stress. Later Bingham [21] presented the flow shear diagram resulting roughly a linear relation between stress and strain to fully prescribe the nature of plastic flow. Extensive mathematical studies were carried out by Oldroyd [165] and Prager [172] who established two extremum principles for the flow of Bingham material in which inertial terms can be neglected. Mosolov and Maisnikov, in three subsequent articles [160, 161, 162] for the unidirectional flow problem(cylindrical and simply connected cross-section) have resulted that there always exists at least one nucleus in the domain moving like a solid at a constant speed. Furthermore, the existence of the rigid zones is considered in flow and it is shown that they exist for domains with corner points.
Many researchers have followed and devoted their efforts to solve the problem to predict the flow regimes inside the domain. Glowinski [95] developed a variational approach to solve numerically the steady state problem in a cylindrical duct with rectangular cross-section. The depicted figures have given a prediction about the plug flow region but there is no mention about the dead ones. Huilgol [114] found an inner plug flow region together with areas of no flow near the corners for a L-shaped pipe. Taylor and Wilson [205] solved the problem using finite difference and multigrid techniques resulting that there are areas within the duct where the flow is stationary.
Fortin [76] solved directly the problem in a lid driven cavity using six node triangular finite element and duality type methods but the incompressibility condition is satisfied only approximately. Similar numerical studies have been carried out by Bercovier and Engelman [17] using a nine node iso-parametric Lagrangian element with a penalty approach for the continuity equation and the regularized constitutive equation resulting in a better prediction for the different zones inside the flow for a four values of the yield stress(2.5, 5, 7.5, 10). Mitsoulis et al. [158] studied for a higher values of yield stress showing in an elementary way the growth of the unyielded zones due to the increasing of the threshold value.
Adachi and Yoshioka [1] analyzed the creeping flow a Bingham fluid past a cylinder by using the variational principles. They provided an approximate location of the yielded/unyielded surfaces computed

analytically for a single Bingham number and reported the drag coefficient for a wide range of the dimensionless Bingham number. In [24, 15, 236, 158] they solved the problem numerically by using the proposed constitutive equation by Papanastasiou. For such case they presented the different flow regimes in a long with the drag coefficient for a wide range of Bingham number. In a different treatment with the problem, Roquet and Saramito [180] used the augmented Lagrangian method and a mixed finite element method to exhibit the categories of the flow zones and to analyze shear stress behavior when the cylinder gets close to the wall. Jay et al. [62, 210] presented finite element modeling involved regularizing Herschel-Bulkely model proposed by Papanastasiou to explore systemically the effect of the yield stress value and the shear thinning index on the kinematic field and the drag.

5.2 Mathematical Difficulties in Bingham Viscoplastic Problem

Before introducing the monolithic approach to simulate the Bingham viscoplastic problem, we wish to underline the main mathematical difficulties involved in as well as their treatments. The nature of Bingham constitutive law for modeling the flow of viscoplastic fluids is exhibited two main mathematical difficulties which require a special treatment and various modifications of the traditional handling concepts. These are included in the combination of the raised by nonlinearity, and the non-differentiability which can be read easily from the constitutive model

$$\boldsymbol{\tau} = \begin{cases} (2\mu + \frac{\tau_s}{\|\mathbf{D}\|})\mathbf{D}(\boldsymbol{u}) \text{ if} & \|\mathbf{D}\| \neq 0, \\ \leq \boldsymbol{\tau}_s \text{ if} & \|\mathbf{D}\| = 0, \end{cases} \tag{5.4}$$

with the nonlinear viscosity

$$\nu(\|\mathbf{D}\|) = 2\mu + \frac{\tau_s}{\|\mathbf{D}\|}, \tag{5.5}$$

and normally with an additional peculiar numerical treatment for the incompressibility constraint. The fundamental question of interest for both mathematician and CFD researchers is, what are the aspects needed to cope with the inherent viscoplastic difficulties for such modeling?
The answers could be developed from the following two items:

(a) The treatment of nonlinearity

The traditional way to handle with the nonlinearity in nonlinear CFD's problem is either by an explicit coupling or straightforward linearization by first order fixed point iteration (see [183]), damping Newton iteration (see [61]) or decomposition/coordination method (see [220, 64]). In the presented case we choose a special treatment of the nonlinearity by calculating the Frechet derivative of the nonlinear term in continuous level which referred to the so-called continuous Newton method. The idea is explained in [166, 108] for shear and pressure dependent viscosity. Since the constitutive function is only dependent shear rate, so let assume that $\boldsymbol{X} = \mathbf{D}(\boldsymbol{u}^n), \boldsymbol{x} = \mathbf{D}(\boldsymbol{u}), F(\boldsymbol{x}) = \nu(\frac{1}{2}|\boldsymbol{x}|^2)\boldsymbol{x}$ and $f(t) = F(\boldsymbol{X} + t\boldsymbol{x})$ so that

$$\partial_{x_j} F_i(\boldsymbol{x}) = \partial_{x_j}\nu(\tfrac{1}{2}|\boldsymbol{x}|^2)x_j x_i + \nu(\tfrac{1}{2}|\boldsymbol{x}|^2)\delta_{ij}, \tag{5.6}$$

where δ_{ij} stands for the standard Kronecker symbol. Having

$$\begin{aligned} f_i^{'}(t) &= \textstyle\sum_j \partial_{x_j} F_i(\boldsymbol{X} + t\boldsymbol{x})x_j \\ &= \nu(\tfrac{1}{2}|\boldsymbol{X} + t\boldsymbol{x}|^2)\boldsymbol{x}_i \\ &+ \partial_{\|\mathbf{D}\|^2}\nu(\tfrac{1}{2}|\boldsymbol{X} + t\boldsymbol{x}|^2)\langle \boldsymbol{X} + t\boldsymbol{x}, \boldsymbol{x}\rangle(\boldsymbol{X}_i + t\boldsymbol{x}_i) \end{aligned} \tag{5.7}$$

then the Frechet derivative can be obtained when $t \to 0$ as follows:

$$\begin{aligned} &\nu(\|\mathbf{D}(\boldsymbol{u}^n)\|)\mathbf{D}(\boldsymbol{u}) \\ &+\partial_{\|\mathbf{D}\|^2}\nu(\|\mathbf{D}(\boldsymbol{u}^n)\|)(\mathbf{D}(\boldsymbol{u}^n) : \mathbf{D}(\boldsymbol{u}))\mathbf{D}(\boldsymbol{u}^n), \end{aligned} \tag{5.8}$$

where $\partial_{\|\mathbf{D}\|^2}\nu = \frac{\partial \nu}{\partial \|\mathbf{D}\|^2}$. This treatment can be used only for the explicit nonlinearity and for complicated non-linear flow models which is not recommended. It is noticed from [166] that the basic iterative solver behaves like the damped Newton method by using a damping and exhibits the quadratic convergence provided that the initial guess is sufficiently close the solution point.

(b) The treatment of non-differentiability

The treatment of the non-differentiability has the most interesting part in Bingham viscoplastic problem due to the noticed effect on the solution. The source of this difficulty comes from the unbounded effective viscosity where is the zero value of deformation tensor existed. Therefore, we use the regularized models instead. Such regularization is used to approximate the viscosity to be a smooth and differential. In [2] it is introduced simple regularized parameter added in the dominator having the dimension of the deformation tensor as follows:

$$\nu_\epsilon(\|\mathbf{D}\|) = 2\mu + \frac{\tau_s}{\epsilon + \|\mathbf{D}\|}, \tag{5.9}$$

In the same manner Bercovier and Engelman [18] proposed another regularized function as follows

$$\nu_\epsilon(\|\mathbf{D}\|) = 2\mu \ + \frac{\tau_s}{\sqrt{\epsilon^2 + \|\mathbf{D}\|^2}}, \tag{5.10}$$

They used the model to solve the flow in a closed square cavity subjected to a body force predicting the growth of a central unyielded zone and the dead zone at the corners. This model is also used by Taylor and Wilson [205] to simulate conduit flow of an incompressible Bingham fluid.
Tanner at el.[164] proposed a different model called bi-viscous model. This model is modified in our work to have the following form

$$\nu_\epsilon(\|\mathbf{D}\|) = \begin{cases} 2\mu \ + \frac{\tau_s}{\|\mathbf{D}\|} \text{ if} & \|\mathbf{D}\| > TOL, \\ 2\mu + \frac{\tau_s}{\epsilon} \quad \text{if} & \|\mathbf{D}\| \leq TOL. \end{cases} \tag{5.11}$$

This model is used to approximate only the solid regime by highly viscous regime(unyielded viscosity) representing it by the term $\frac{1}{\epsilon}$. In [20] it is used to study the die swell in viscoelastic materials with yield stress, using an adopted value of $\frac{1}{\epsilon}$ equivalent to 2000μ for an optimum configuration of the flow field, in addition to, in [171] for the motion and deformation of drops in Bingham fluid without mentioning of the chosen value of ϵ for the unyielded regime.
Papanastasiou [168] proposed a regularizing model with an exponential expression to hold for any shear rate by adding a small parameter leading to the smoothness and regularity of the non-differentiable function taking the following form.

$$\nu_\epsilon(\|\mathbf{D}\|) = 2\mu \ + \tau_s \frac{1 - exp(-\|\mathbf{D}\|/\epsilon)}{\|\mathbf{D}\|}. \tag{5.12}$$

Papanastasiou used this model to study several simple flows: one dimensional channel flow, two dimensional boundary layer flow and extrusion flow.

5.3 Formulation of Stationary Bingham Viscoplastic Problem

There are several tools to model Bingham viscoplastic fluid. The candidate is to apply generalized Navier-stokes equation in the shear region and the equation of motion of a rigid part. Let $\boldsymbol{\Omega}$ be a bounded domain of $\mathbb{R}^2$; we denote by $\partial\boldsymbol{\Omega}$, the boundary of $\boldsymbol{\Omega}$. The stationary incompressible viscoplastic fluid modeled by involving the regularized nonlinear viscosity using Bercovier-Engelman approach in momentum equation as the following:

$$\boldsymbol{u}\cdot\boldsymbol{\nabla}\boldsymbol{u}-\boldsymbol{\nabla}\cdot(\nu(\|\mathbf{D}\|)\mathbf{D}(\boldsymbol{u}))+\boldsymbol{\nabla}p=\boldsymbol{f}\qquad in\quad \boldsymbol{\Omega}, \tag{5.13a}$$

$$\nu(\|\mathbf{D}\|)=2\mu+\frac{\tau_s}{\sqrt{\epsilon^2+\|\mathbf{D}\|^2}}, \tag{5.13b}$$

$$\boldsymbol{\nabla}\cdot\boldsymbol{u}=0\qquad in\quad \boldsymbol{\Omega}, \tag{5.13c}$$

$$\boldsymbol{u}=\boldsymbol{u}^o\qquad on\quad \partial\boldsymbol{\Omega}, \tag{5.13d}$$

where $\boldsymbol{u}^o$ is the velocity prescribed on the boundary of $\boldsymbol{\Omega}$ such that $\int_{\partial\boldsymbol{\Omega}}\boldsymbol{u}^o.\boldsymbol{n}=0$ and $\boldsymbol{f}$ is the density of external forces. Let the set $\mathbf{V}\in[\mathbf{H}_0^1(\boldsymbol{\Omega})]^2$ of the test function be divergence free including the constitutive law in to the set of equations, $\boldsymbol{u}$ is the state of velocity and $\boldsymbol{v}$ is the a test function, the weak form reads *Find* $\{\boldsymbol{u},p\}\in\mathbf{H}_0^1(\boldsymbol{\Omega})\times\mathbf{L}^2(\boldsymbol{\Omega})\}$ *such that*

$$\int_{\boldsymbol{\Omega}}(\boldsymbol{u}\cdot\boldsymbol{\nabla}\boldsymbol{u})\boldsymbol{v}d\boldsymbol{x}+\int_{\boldsymbol{\Omega}}\nu(\|\mathbf{D}\|)\mathbf{D}(\boldsymbol{u}))):\mathbf{D}(\boldsymbol{v})d\boldsymbol{x}-\int_{\boldsymbol{\Omega}}p\,\mathrm{div}\,\boldsymbol{v}d\boldsymbol{x}=\int_{\boldsymbol{\Omega}}\boldsymbol{f}\boldsymbol{v}d\boldsymbol{x},\quad\forall\boldsymbol{v}\in\mathbf{H}_0^1(\boldsymbol{\Omega}), \tag{5.14a}$$

$$\int_{\boldsymbol{\Omega}}q\,\mathrm{div}\,\boldsymbol{u}d\boldsymbol{x}=0\forall q\in\mathbf{L}^2(\boldsymbol{\Omega}), \tag{5.14b}$$

$$\boldsymbol{u}=\boldsymbol{u}^o\quad on\quad\partial\boldsymbol{\Omega}. \tag{5.14c}$$

Incorporating the obtained parts from the Frechet derivative due to the nonlinearities either the effective viscosity or the convective part to get the regularized linearized problem in the following the compact weak form:
Find $(\boldsymbol{u},p)\in\mathbf{H}_0^1(\boldsymbol{\Omega})\times\mathbf{L}^2(\boldsymbol{\Omega})$ *such that*

$$[\mathbf{L}(\boldsymbol{u})\boldsymbol{u}^n,\boldsymbol{v}]+[\mathbf{L}^*(\boldsymbol{u}^n)\boldsymbol{u},\boldsymbol{v}]+[\mathbf{N}(\boldsymbol{u})\boldsymbol{u}^n,\boldsymbol{v}]+[\mathbf{N}^*(\boldsymbol{u}^n)\boldsymbol{u},\boldsymbol{v}]-[\mathbf{B}p,\boldsymbol{v}]=\int_{\boldsymbol{\Omega}}\boldsymbol{f}\boldsymbol{v}d\boldsymbol{x},\ \forall\boldsymbol{v}\in\mathbf{H}_0^1(\boldsymbol{\Omega}), \tag{5.15a}$$

$$[\mathbf{B}^Tq,\boldsymbol{u}]=0,\ \forall q\in\mathbf{L}^2(\boldsymbol{\Omega}), \tag{5.15b}$$

$$\boldsymbol{u}=\boldsymbol{u}^o\quad on\quad\partial\boldsymbol{\Omega}, \tag{5.15c}$$

where

$$[\mathbf{L}(\boldsymbol{u}^n)\boldsymbol{u},\boldsymbol{v}]=\int_{\boldsymbol{\Omega}}\nu(\|\mathbf{D}(\boldsymbol{u}^n)\|)\mathbf{D}(\boldsymbol{u}):\mathbf{D}(\boldsymbol{v})d\boldsymbol{x}, \tag{5.16a}$$

$$[\mathbf{N}(\boldsymbol{u}^n)\boldsymbol{u},\boldsymbol{v}]=\int_{\boldsymbol{\Omega}}(\boldsymbol{u}^n\cdot\boldsymbol{\nabla}\boldsymbol{u})\boldsymbol{v}\,d\boldsymbol{x}, \tag{5.16b}$$

$$[\mathbf{B}q,\boldsymbol{v}]=\int_{\boldsymbol{\Omega}}q\,\mathrm{div}\,\boldsymbol{v}\,d\boldsymbol{x}, \tag{5.16c}$$

$$[\mathbf{L}^*(\boldsymbol{u}^n)\boldsymbol{u},\boldsymbol{v}]=\int_{\boldsymbol{\Omega}}\partial_{\|\mathbf{D}\|^2}\nu(\|\mathbf{D}(\boldsymbol{u}^n)\|)[\mathbf{D}(\boldsymbol{u}^n):\mathbf{D}(\boldsymbol{u})][\mathbf{D}(\boldsymbol{u}^n):\mathbf{D}(\boldsymbol{v})]d\boldsymbol{x}, \tag{5.16d}$$

$$[\mathbf{N}^*(\boldsymbol{u}^n)\boldsymbol{u},\boldsymbol{v}]=\int_{\boldsymbol{\Omega}}(\boldsymbol{u}\cdot\boldsymbol{\nabla}\boldsymbol{u}^n)\boldsymbol{v}\,d\boldsymbol{x}. \tag{5.16e}$$

5.4 Finite Element Approximation

Two choices are candidate for the work with the finite element approximation for the viscoplastic problem; $\tilde{Q}_1Q_0$ and $Q_2P_1^{np}$. For the later which is generally believed that the best for the flow problems; the finite dimensional spaces V_h and Q_h for the velocity and the pressure approximations read

$$\mathbf{V}_h = \{\boldsymbol{v}_h \in \mathbf{H}_0^1(\boldsymbol{\Omega}_h)^2, \quad \boldsymbol{v}_{h|\mathcal{T}} \in Q_2(\mathcal{T})^2 \forall \mathcal{T} \in \mathbf{T}_h, \quad \boldsymbol{v}_h = 0 \, on \, \partial\boldsymbol{\Omega}_h\}, \tag{5.17}$$

$$P_h = \{p_h \in \mathbf{L}^2(\boldsymbol{\Omega}_h), \quad p_{h|\mathcal{T}} \in P_1(\mathcal{T}) \forall \mathcal{T} \in \mathbf{T}_h\}, \tag{5.18}$$

and consider for each $\mathcal{T} \in \mathbf{T}_h$ the bilinear transformation $\psi_{\mathcal{T}} : \hat{\mathcal{T}} \to \mathcal{T}$ to the unit square $\mathcal{T}$. So, $Q_2(\mathcal{T})$ and $\tilde{Q}_1$ is defined by

$$Q_2(\mathcal{T}) = \left\{q \circ \psi_{\mathcal{T}}^{-1} : q \in \text{span} < 1, x, y, xy, x^2, y^2, x^2y, y^2x, x^2y^2 > \right\} \tag{5.19a}$$

$$\tilde{Q}_1(\mathcal{T}) = \left\{q \circ \psi_{\mathcal{T}}^{-1} : q \in \text{span} < 1, x, y, x^2 - y^2 > \right\}, \tag{5.19b}$$

with nine local degrees of freedom located at the vertices, midpoints of the edges and in the center of the quadrilateral for Q_2 and with four local degrees of freedom at the midpoints for $\tilde{Q}_1$.
The space $P_1^{np}(\mathcal{T})$ and Q_0 consist of linear and constant functions defined respectively by

$$P_1^{np}(\mathcal{T}) = \left\{q \circ \psi_{\mathcal{T}}^{-1} : q \in \text{span} < 1, x, y > \right\}, \tag{5.20a}$$

$$Q_0(\mathcal{T}) = \left\{q \circ \psi_{\mathcal{T}}^{-1} : q \in \text{span} < 1 > \right\}. \tag{5.20b}$$

For both cases, the inf-sup condition is normally satisfied and the second order approximation is recovered for the unmapped pressure P_1^{np} (see [8, 25, 91]) and first order for the unmapped constant pressure $Q_0(\mathcal{T})$ is as follow:

$$\|p - p_h\|_0^{P_1^{np}} = O(h^2) \quad and \quad \|p - p_h\|_0^{Q_0} = O(h). \tag{5.21}$$

For a smooth solution, the approximation error for the velocity in the $\mathbf{L}^2$-norm is of order $O(h^3)$ and $\mathbf{H}^1$-norm is of order $O(h^2)$ for $Q_2P_1^{np}$ and is of order $O(h^2)$ and $\mathbf{H}^1$-norm is of order $O(h)$ for $\tilde{Q}_1Q_0$ which can easily be demonstrated for prescribed polynomials or for smooth data on appropriate domains (see chapter2 or [25, 166, 177, 214]).
Then, the finite element approximation reads :
Given $\boldsymbol{f}$ find $\boldsymbol{u}_h \in \mathbf{V}_h$, $p_h \in P_h$ such that $\forall \boldsymbol{v}_h \in \mathbf{V}_h$, $\forall q_h \in P_h$ the following expression is satisfied:

$$\int_{\boldsymbol{\Omega}} (\boldsymbol{u}_h \cdot \boldsymbol{\nabla}\boldsymbol{u}_h)\boldsymbol{v}_h + \int_{\boldsymbol{\Omega}} \boldsymbol{\nabla} p_h \boldsymbol{v}_h = -\int_{\boldsymbol{\Omega}} \mathbf{D}(\boldsymbol{v}_h) : \boldsymbol{\tau}(\boldsymbol{u}_h) + \int_{\boldsymbol{\Omega}} \boldsymbol{f}\boldsymbol{v}_h \quad in \quad \boldsymbol{\Omega}, \tag{5.22a}$$

$$\int_{\boldsymbol{\Omega}} \nabla \cdot \boldsymbol{u}_h q_h d\boldsymbol{\Omega} = 0 \quad in \quad \boldsymbol{\Omega}. \tag{5.22b}$$

By using the constitutive law to plug in instead the stress tensor $\boldsymbol{\tau}$ to get:

$$\int_{\boldsymbol{\Omega}} (\boldsymbol{u}_h \cdot \boldsymbol{\nabla}\boldsymbol{u}_h)\boldsymbol{v}_h - \int_{\boldsymbol{\Omega}} p_h \boldsymbol{\nabla} \cdot \boldsymbol{v}_h + \int_{\boldsymbol{\Omega}} \nu(\|\mathbf{D}\|)\mathbf{D}(\boldsymbol{u}_h) : \mathbf{D}(\boldsymbol{v}_h) = \int_{\boldsymbol{\Omega}} \boldsymbol{f}\boldsymbol{v}_h \quad in \quad \boldsymbol{\Omega}, \tag{5.23a}$$

$$\int_{\boldsymbol{\Omega}} \boldsymbol{\nabla} \cdot \boldsymbol{u}_h q_h d\boldsymbol{\Omega} = 0 \quad in \quad \boldsymbol{\Omega}. \tag{5.23b}$$

The presented equation has to be defined for the different flow regimes (shear and plug regions), so one can obtain

$$\int_{\boldsymbol{\Omega}|_{shear}} (\boldsymbol{u}_h \cdot \boldsymbol{\nabla}\boldsymbol{u}_h)\boldsymbol{v}_h - \int_{\boldsymbol{\Omega}|_{shear}} p_h \boldsymbol{\nabla}\cdot\boldsymbol{v}_h +$$
$$\int_{\boldsymbol{\Omega}|_{shear}} (2\mu + \frac{\tau_s}{\|\mathbf{D}\|})\mathbf{D}(\boldsymbol{u}_h) : \mathbf{D}(\boldsymbol{v}_h) = \int_{\boldsymbol{\Omega}|_{shear}} \boldsymbol{f}\boldsymbol{v}_h \quad in \quad \boldsymbol{\Omega}|_{shear}, \tag{5.24a}$$
$$\int_{\boldsymbol{\Omega}} \boldsymbol{\nabla}\cdot\boldsymbol{u}_h q_h d\boldsymbol{\Omega} = 0 \quad in \quad \boldsymbol{\Omega}, \tag{5.24b}$$
$$-\int_{\boldsymbol{\Omega}|_{plug}} p_h \boldsymbol{\nabla}\cdot\boldsymbol{v}_h = -\int_{\boldsymbol{\Omega}|_{plug}} \boldsymbol{\tau}_s : \mathbf{D}(\boldsymbol{v}_h) + \int_{\boldsymbol{\Omega}|_{plug}} \boldsymbol{f}\cdot\boldsymbol{v}_h \quad in \quad \boldsymbol{\Omega}|_{plug}. \tag{5.24c}$$

Instead of using the above equation, the following regularized form after dropping down the notations due the regularization is used to be an alternative for the whole domain then:

$$\int_{\boldsymbol{\Omega}} (\boldsymbol{u}_h \cdot \boldsymbol{\nabla}\boldsymbol{u}_h)\boldsymbol{v}_h - \int_{\boldsymbol{\Omega}} p_h \boldsymbol{\nabla}\cdot\boldsymbol{v}_h +$$
$$\int_{\boldsymbol{\Omega}} (2\mu + \frac{\tau_s}{\sqrt{\epsilon^2 + \|\mathbf{D}\|^2}})\mathbf{D}(\boldsymbol{u}_h) : \mathbf{D}(\boldsymbol{v}_h) = \int_{\boldsymbol{\Omega}} \boldsymbol{f}\boldsymbol{v}_h \quad in \quad \boldsymbol{\Omega}, \tag{5.25a}$$
$$\int_{\boldsymbol{\Omega}} \boldsymbol{\nabla}\cdot\boldsymbol{u}_h q_h d\boldsymbol{\Omega} = 0 \quad in \quad \boldsymbol{\Omega}. \tag{5.25b}$$

Introducing the discrete solution for the velocity and pressure

$$\boldsymbol{u}_h = \sum_{j=1}^{N_{\boldsymbol{u}}} \boldsymbol{u}_j \phi_j, \qquad p_h = \sum_{j=1}^{N_p} p_j \psi_j, \tag{5.26}$$

where $N_{\boldsymbol{u}}$ and N_p are the total number of unknowns and $\boldsymbol{u}_j$ and p_j the nodal values for velocity and pressure respectively. ϕ_j and ψ_j are the interpolation functions for velocity and pressure respectively. However, the choice of spaces for velocity and pressure is not arbitrary but in a case which both should be compatible and satisfying the LBB condition. So, the discrete approximated problem associated to the finite element spaces is defined in the following way:
Find $(\boldsymbol{u}_h, p_h) \in \mathbf{H}_0^1 h(\boldsymbol{\Omega}) \times \mathbf{L}_h^2(\boldsymbol{\Omega})$ *such that*

$$[\mathbf{L}(\boldsymbol{u}_h)\boldsymbol{u}_h^n, \boldsymbol{v}_h] + [\mathbf{L}^*(\boldsymbol{u}_h^n)\boldsymbol{u}_h, \boldsymbol{v}_h] + [\mathbf{N}(\boldsymbol{u}_h)\boldsymbol{u}_h^n, \boldsymbol{v}_h] + [\mathbf{N}^*(\boldsymbol{u}_h^n)\boldsymbol{u}_h, \boldsymbol{v}_h]$$
$$- [\mathbf{B}p_h, \boldsymbol{v}_h] = (\boldsymbol{f}, \boldsymbol{v}_h),\ \forall \boldsymbol{v}_h \in H_0^1(\boldsymbol{\Omega}), \tag{5.27a}$$
$$[\mathbf{B}^T q_h, \boldsymbol{u}_h] = 0,\ \forall q_h \in L^2(\boldsymbol{\Omega}), \tag{5.27b}$$
$$\boldsymbol{u}_h = \boldsymbol{u}_h^o. \quad on \quad \partial\boldsymbol{\Omega}. \tag{5.27c}$$

where $\boldsymbol{u}_h^o$ is the approximation of $\boldsymbol{u}^o$.
However, the choice of such element is not purely optimal for our problem in some cases due to the use of the regularization or the symmetric part of deformation form. There are three severely numerical situations, the first one is the convection dominated problem at high Reynolds number (Re=10000) and the second is the lower value of regularization parameter which is close to the Bingham constitutive law. The third is the lack of coercivity for low order approximation for symmetric deformation formulation.
The first it might be happened for all standard discretization schemes in the case of the convection dominated problems and coped by the Upwinding or the streamline diffusion methods. The second and the third can be dealt with the mentioned idea in [101, 215] by the jump term in the discrete problem.
In our case with $Q_2P_1^{np}$ to cure the numerical instability altogether, we are using the proposed stabilization term in [38, 101, 215], which acts only on the velocity $\boldsymbol{u}$ in the momentum equation and obtains the following form

$$[\mathbf{J}_h, \boldsymbol{v}_h] = \sum_{\text{edge E}} \max(\gamma\nu h_E, \gamma^* h_E^2) \int_E [\boldsymbol{\nabla}\boldsymbol{u}_h] : [\boldsymbol{\nabla}\boldsymbol{v}_h]\, ds, \tag{5.28}$$

where h_E is the length of the element edge, ν whether it can be equal to the viscosity(μ) or the regularized effective viscosity(ν_ϵ), and γ and γ^* are constants.
The optimal choice for the parameters γ and γ^* is not accurately recognized yet. Clearly, the increasing of these constants makes the problem somehow stiff particularly at lower level. However, in the present study, we optimize the choice of these constants as follows:
a) if $\epsilon < 10^{-3}$ then γ and $\gamma^* \leq 1$
b) if $\epsilon \geq 10^{-3}$ then $\gamma \propto \frac{1}{(\epsilon)^{1/4}}$ and $\gamma^* \propto \frac{1}{(\epsilon)^{1/2}}$.
Incorporate the jump term in Eq.(5.22a) to get the complete form of the approximated problem with damping parameters δ_d and δ_c as follows:
Find $(\boldsymbol{u}_h, p_h) \in \mathbf{H}_0^1 h(\boldsymbol{\Omega}) \times \mathbf{L}_h^2(\boldsymbol{\Omega})$ *such that*

$$[\mathbf{L}(\boldsymbol{u}_h)\boldsymbol{u}_h^n, \boldsymbol{v}] + \delta_d[\mathbf{L}^*(\boldsymbol{u}_h^n)\boldsymbol{u}_h, \boldsymbol{v}_h] + [\mathbf{N}(\boldsymbol{u}_h)\boldsymbol{u}_h^n, \boldsymbol{v}_h] + \delta_c[\mathbf{N}^*(\boldsymbol{u}_h^n)\boldsymbol{u}_h, \boldsymbol{v}_h]$$
$$+ [\mathbf{J}_h, \boldsymbol{v}_h] - [\mathbf{B}p_h, \boldsymbol{v}_h] = (\boldsymbol{f}, \boldsymbol{v}_h),\ \forall \boldsymbol{v} \in \mathbf{H}_0^1(\boldsymbol{\Omega}), \tag{5.29a}$$
$$[\mathbf{B}^T q_h, \boldsymbol{u}_h] = 0 \forall q \in \mathbf{L}^2(\boldsymbol{\Omega}), \tag{5.29b}$$
$$\boldsymbol{u}_h = \boldsymbol{u}_h^o \quad on \quad \partial\boldsymbol{\Omega}. \tag{5.29c}$$

.

5.5 The Solvers

The suggested monolithic technique is used to solve the nonlinear algebraic viscoplastic equations in the frame of continuous Newton-multigrid solver. This approach solves the complete system which arises from the discretization as one system with resulted solution vector from the velocity and pressure.
However, the segregated method which might be used is based on the decoupling of the pressure and the velocity. Then by using the Schur complement matrix $\mathbf{B}^T(\mathbf{A}+\mathbf{J})^{-1}\mathbf{B}$ which leads us to the pressure Schur complement approach. This approach solves the pressure Poisson equation firstly and consequently obtains the velocity solution. Thus, the first step is to obtain the velocity in the pressure from the momentum equation

$$\boldsymbol{u} = (\mathbf{A}+\mathbf{J})^{-1}(\boldsymbol{f} - \mathbf{B}p), \tag{5.30}$$

and the second step is to plug it in the continuity equation to obtain the pressure Schur complement approach (see [166, 214]),

$$\mathbf{B}^T(\mathbf{A}+\mathbf{J})^{-1}\mathbf{B}p = \mathbf{B}^T(\mathbf{A}+\mathbf{J})^{-1}\boldsymbol{f}. \tag{5.31}$$

By solving the pressure-poisson equation and with the direct substitution in momentum equation, one can get the velocity solution and then the solution vector $[\boldsymbol{u}, p]$. The draw back of this method is numerically unstable and the accuracy is not comparable with the monolithic approach.
Therefore, the approximate linearized problem may have the following algebraic system form in a monolithic way

$$\begin{pmatrix} \mathbf{A}+\mathbf{J} & \mathbf{B} \\ \mathbf{B}^T & 0 \end{pmatrix} \begin{bmatrix} \boldsymbol{u} \\ p \end{bmatrix} = \begin{bmatrix} \boldsymbol{f} \\ \boldsymbol{g} \end{bmatrix}. \tag{5.32}$$

where $\boldsymbol{f}$ and $\boldsymbol{g}$ are the corresponding rhs's for the momentum and continuity equations and $\mathbf{B}^T$ is the discrete divergence operator. So that, the residual vector $\mathbf{Res}_{\boldsymbol{u}}$ and $\mathbf{Res}_p$ for the (complete) discrete momentum and continuity equations involved by the complete stabilization term due to $\mathbf{J}$ can be casted in the following way

$$\begin{bmatrix} \mathbf{Res}_{\boldsymbol{u}}(\boldsymbol{u}^n, p^n) \\ \mathbf{Res}_p(\boldsymbol{u}^n, p^n) \end{bmatrix} = \left(\begin{bmatrix} \mathbf{L}+\mathbf{N}+\mathbf{J} & \mathbf{B} \\ \mathbf{B}^T & 0 \end{bmatrix} \begin{bmatrix} \boldsymbol{u}^n \\ p^n \end{bmatrix} - \begin{bmatrix} \boldsymbol{f} \\ 0 \end{bmatrix} \right). \tag{5.33}$$

The compact form of the whole system for continuous Newton step can be written as the following

$$\begin{pmatrix} \mathbf{A}+\mathbf{J} & \mathbf{B} \\ \mathbf{B}^T & 0 \end{pmatrix} \begin{bmatrix} \boldsymbol{u} \\ p \end{bmatrix} = \begin{bmatrix} \mathbf{Res}_{\boldsymbol{u}} \\ \mathbf{Res}_p \end{bmatrix}, \tag{5.34}$$

where the matrix $\mathbf{A}$ has the following form $\mathbf{A} = \mathbf{L} + \delta_d \mathbf{L}^* + \mathbf{N} + \delta_c \mathbf{N}^*$, where δ_d and δ_c are control parameters to switch simply to the standard fixed point if $\delta_d = \delta_c = 0$.

The solution algorithm can be outlined as follows:

Given: iterates $\boldsymbol{u}^n, p^n$
solve the auxiliary problem to obtain $\boldsymbol{v}$,q

$$\begin{bmatrix} \mathbf{Res}_{\boldsymbol{u}}(\boldsymbol{u}^n, p^n) \\ \mathbf{Res}_p(\boldsymbol{u}^n, p^n) \end{bmatrix} = \left(\begin{bmatrix} \mathbf{L}+\mathbf{N}+\mathbf{J} & \mathbf{B} \\ \mathbf{B}^T & 0 \end{bmatrix} \begin{bmatrix} \boldsymbol{u}^n \\ p^n \end{bmatrix} - \begin{bmatrix} \boldsymbol{f} \\ 0 \end{bmatrix} \right). \tag{5.35}$$

$$[\mathbf{C}] \begin{bmatrix} \boldsymbol{v}_i^{n+1} \\ q_i^{n+1} \end{bmatrix} = \begin{bmatrix} \mathbf{Res}_{\boldsymbol{u}}(\boldsymbol{u}^n, p^n) \\ \mathbf{Res}_p(\boldsymbol{u}^n, p^n) \end{bmatrix} \tag{5.36}$$

Choose an appropriate $\omega^n \in (0, 1]$ *and obtain the new iterates* $\boldsymbol{u}^{n+1}$ *and* p^{n+1}

$$\begin{bmatrix} \boldsymbol{u}^{n+1} \\ p^{n+1} \end{bmatrix} = \begin{bmatrix} \boldsymbol{u}^n \\ p^n \end{bmatrix} - \omega^n \sum_{\mathcal{T} \in \mathbf{T}_h} \begin{bmatrix} \boldsymbol{v}_i^{n+1} \\ q_i^{n+1} \end{bmatrix}. \tag{5.37}$$

This system can be solved by patch which may consist of only one element or the whole domain. The $\mathbf{C}$ represents the patch stiffness matrix or the global stiffness matrix (see [166])

$$[\mathbf{C}] = \begin{bmatrix} \mathbf{A}+\mathbf{J} & \mathbf{B} \\ \mathbf{B}^T & 0 \end{bmatrix}_{|\boldsymbol{\Omega}} \tag{5.38}$$

$$[\mathbf{C}]_{ij} = [\mathbf{A}]_{ij} + [\mathbf{J}]_{ij} \quad \text{for} \quad 1 \leq i, j \leq 4. \tag{5.39}$$

Typically, it is used to start with a few iterations having a standard fixed point method till the solution reaches a predefined tolerance and it is automatically switched to apply fully continuous Newton method with $\delta_d = 1$ and $\delta_c = 1$. In the frame of continuous Newton process we are using the geometric multigrid as linear solvers which is considered as the main nerve of the solution process due to the notable effect on the accuracy and the time consumption. Typically, a variety of linear solvers have been a candidate to solve a sparse system generated from the finite element discretization. Accordingly, they differ in their memory storage and CPU time. For instance, UMFPACK is a good candidate as a direct solver for small system less than 20.000 unknown, and Krylov subspace methods are working nicely for large system with a suitable preconditioner.
The strategy to use this method in our work is summarized by the following two-folds:
(a) The restriction step is applied to the residual after a fixed number of smoothing steps on all mesh levels and a direct linear solver is utilized to obtain the coarsest grid solution.
(b) The prolongation step is applied which is followed by a fixed number of post smoothing steps.
Normally we use here $\mathbf{F}_{cycle}$ algorithm which has the same convergence properties comparing with $\mathbf{W}_{cycle}$ when the number of smoothing steps is a bit high.

The $\mathbf{F}_{cycle}$ algorithm is explained in the following:

Given: $\boldsymbol{g} \in \mathbf{V}_k$, $\boldsymbol{z}_0 \in \mathbf{V}_k$ and the output of the algorithm is $MG_{\mathbf{F}}(k, \boldsymbol{g}, \boldsymbol{z}_k, m)$ where k=1,..,n the numbers of hierarchy levels, m is the number of presmoothing or postsmoothing steps and $\boldsymbol{z}_k$ is the approximated solution vector of the following linear equation

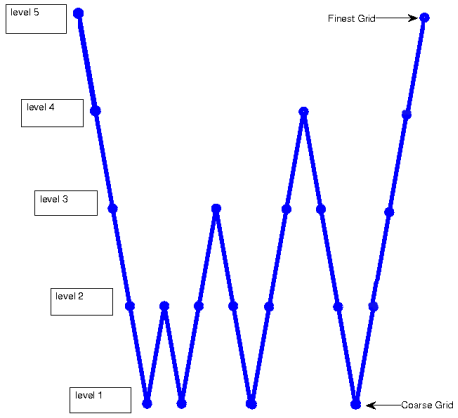

Fig. 5.1. Structure of multigrid F_{cycle} for five levels.

$$\boldsymbol{A}_k \boldsymbol{z} = \boldsymbol{g} \tag{5.40}$$

- **The coarse grid solution** $k = 1$
  $MG(1, \boldsymbol{g}, \boldsymbol{z}_0, m) = \boldsymbol{A}_1^{-1} \boldsymbol{g}$

- **Presmoothing step** $k \geq 2$**:**
  DO j=1,m
  $\boldsymbol{z}_j = \boldsymbol{z}_{j-1} + {\Lambda_k}^{-1} (\boldsymbol{g} - \boldsymbol{A}_k \boldsymbol{z}_{j-1})$
  END DO
  where $\rho(\Lambda_k) \leq C h_k^{-2}$.

- **Correction step:**
  $\boldsymbol{z}_{m+\frac{1}{2}} = \mathbf{I}_k^{k-1} MG(k-1, \mathbf{I}_k^{k-1}(\boldsymbol{g} - \boldsymbol{A}_k \boldsymbol{z}_m), 0, m)$
  $\boldsymbol{z}_{m+1} = \boldsymbol{z}_m + \mathbf{I}_k^{k-1} MG(k-1, \mathbf{I}_k^{k-1}(\boldsymbol{g} - \boldsymbol{A}_k \boldsymbol{z}_m), \boldsymbol{z}_{m+\frac{1}{2}}, m)$

- **Postsmoothing step** $k \geq 2$**:**
  DO j=m,2m+1
  $\boldsymbol{z}_j = \boldsymbol{z}_{j-1} + {\Lambda_k}^{-1} (\boldsymbol{g} - \boldsymbol{A}_k \boldsymbol{z}_{j-1})$
  END DO

- **Final Output:**
  $MG(k, \boldsymbol{g}, \boldsymbol{z}_0, m) = z_{2m+1}$.

The efficiency of the multigrid method is mainly associated with the efficiency of the smoother and the grid transfer operators(prolongation and restriction). In our case we use a fixed number of smoothing steps of full Vanka smoother which acts locally in each element on all levels. Comparing with the segregated techniques, it is already observed that the computational cost is higher than the segregated technique and the development of the efficient preconditioner for the whole problem is a bit difficult but the gain is the higher accuracy which is considered our first need in the viscoplastic problem.

5.6 Numerical Results

5.6.1 Channel Benchmark

The channel domain is considered as a domain between two parallel plates with a unit length apart and unit length long. The problem is solved under an assumption of constant pressure gradient(=-1) with homogenous boundary condition $u(x=0)=0, \quad u(x=1)=0, \quad \tau_{yx}(y=0.5)=0, \quad and \quad \tau_{yx}(y_s)=\tau_s$, where y_s the width of the plug region and the analytical solution reads:

$$u=\begin{cases}\frac{1}{8}[(1-2\tau_s)^2-(1-2\tau_s-2y)^2] & \text{if } 0\le y<\frac{1}{2}-\tau_s,\\ \frac{1}{8}(1-2\tau_s)^2 & \text{if } \frac{1}{2}-\tau_s\le y\le\frac{1}{2}+\tau_s,\\ \frac{1}{8}[(1-2\tau_s)^2-(2y-2\tau_s-1)^2] & \text{if } \frac{1}{2}+\tau_s<y<1.\end{cases} \tag{5.41}$$

5.6.1.a The Unyielded Zones

The creation of plug zone comes from the null deformation space ($\|\mathbf{D}\|=0$) over the domain which produces a constant velocity field ($\boldsymbol{u}=\boldsymbol{c}$) over the domain. From the solution and the depicted figure (Fig.5.2 to Fig.5.6), one can observe that the plug zone consists of a constantly moving kernel for $\frac{1}{2}-\tau_s\le y\le\frac{1}{2}+\tau_s$ and when $\tau_s\ge 0.5$ the velocity equals zero, and the domain will be completely blocked. In contrast, when $\tau_s<0.5$ the velocity equals constant in a certain region (plug region) and varies gradually (parabolic) in others (shear regions).
However, to explore the validation of the numerical algorithm look at Fig.5.2 and table(5.1) to measure the accuracy which is noticed tally well with the reference results. In these figures we have plotted the contours of the deformation tensor and of the rigid zones obtained for various values of regularization parameter and mesh size. One observes if $\|\mathbf{D}\|\le 10^{-3}$ is a fairly good prediction for the unyielded zones, the effect of regularization parameter is roughly dropped after 10^{-4} definitely at smaller values of mesh size (1/128).
The unyielded zone is predicted by moving kernel from 0.4 to 0.6 when $\tau_s=0.1$, and numerically it can be noticed after 10^{-3} accurately at the higher level. It might be true that the convergence of the yield surface predicted by $\tau_{s\epsilon}=\tau_s$ will not be close to the exact yield surface unless $\epsilon\to 0$. But we can claim that from these computational results, the convergence to the yield surface of the exact model could be roughly accepted.
However, the two main issues which affect the viscoplastic configuration, are raised by the regularization parameter and the mesh size. One can see the appearance of the unyielded zones associated mostly with the values of ϵ. Since we claim that the regularization parameter reduces apparently the unyielded zones from the flow domain but comparing with the mesh size it has minimal effect.
The creation of the dead zone comes from the null deformation space ($\|\mathbf{D}\|=0$) over the domain corresponding to null velocity field ($\boldsymbol{u}=\mathbf{0}$). This zone for channel flow is not formed since it always exists at the vicinity of the sharp edges for the Dirichlet boundary conditions.
The creation of the blocking property is a counterpart for the creation of the dead zones. Since if the yield limit is increased or high enough; the fluid is going to be blocked. For the channel flow it could not be observed since the null space of the velocity field is not existed anywhere in the domain.

5.6.1.b The Pressure Jump

The creation of this non-uniformity comes from the dependence of pressure on the yield stress value on the unyielded zones. Therefore, we introduce two numerical tests for viscoplastic flow in channel to

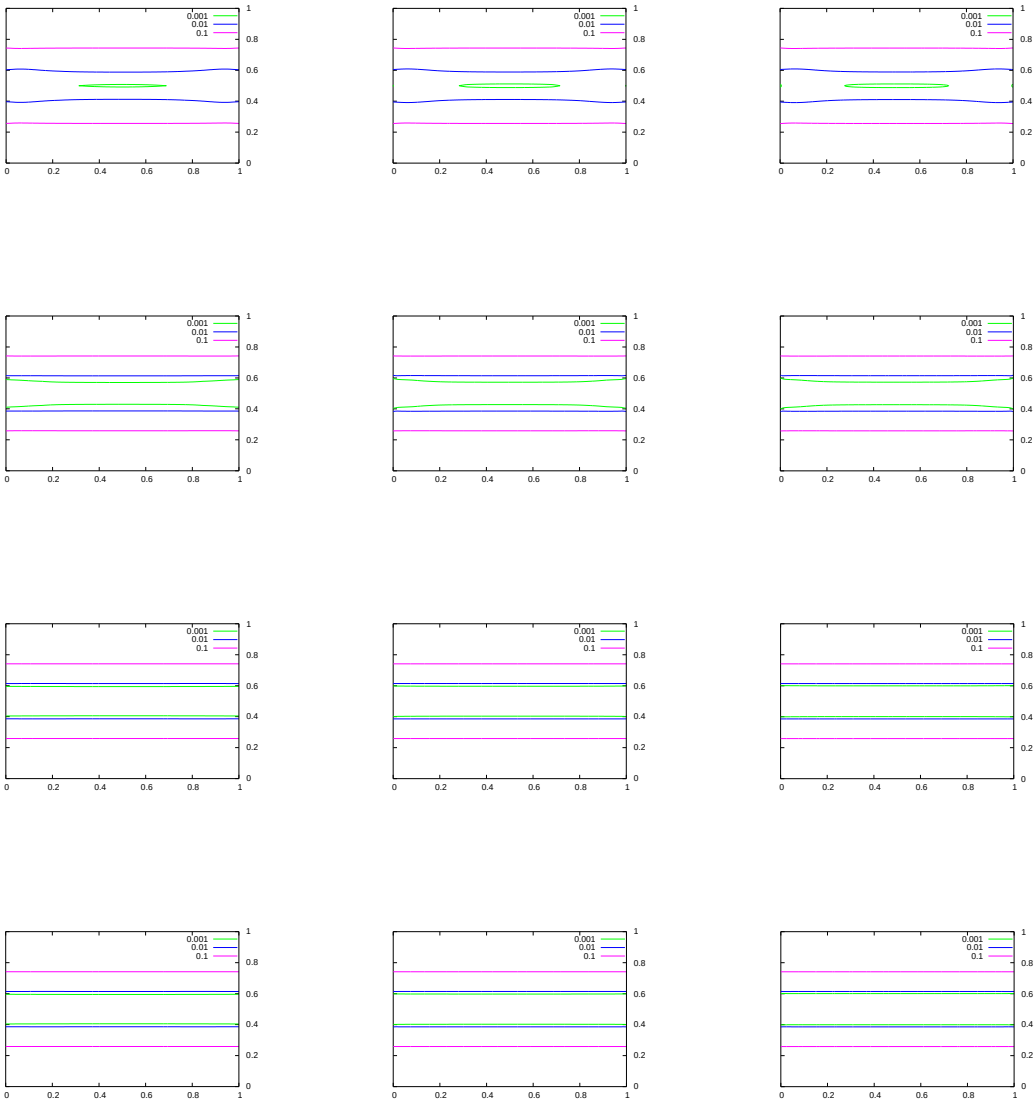

Fig. 5.2. *Bingham flow in channel:* The contour levels (0.1, 0.01, 0.001 and 0.0001) for $\mathbf{L}^2$-norm of the shear rate for the regularized Bingham flow with the yield stress $\tau_0 = 0.1$ and $\epsilon = 10^{-2}$, $\epsilon = 10^{-3}$, $\epsilon = 10^{-4}$ and $\epsilon = 10^{-5}$ (top to bottom) for different refinement mesh $h = 1/64$, $h = 1/128$ and $h = 1/265$ (left to right).

validate and to measure the difference between the proposed analytic solution and the numerical one for the pressure. This work allows us to predict numerically the distribution of pressure whether linear or nonlinear, by using $Q_2P_1^{np}$ finite element and bi-viscous model Eq(5.11). It is worth to follow many researchers for instance Glowinski in [95] and Veneziani in [7] to propose the assumed analytical solution by considering the global linearity of pressure over the whole domain by the following:

$$\boldsymbol{u} = (u, 0),\ p = -x + c, \quad c \quad constant \tag{5.42}$$

The values used for the parameters $cand\tau_s$ are 0.5 and 0.4 respectively.
The first test uses the gradient of velocity tensor to evaluate $\|\mathbf{D}\|$, with Dirichlet boundary conditions at the inlet and DO NOTHING at the outlet. The second test uses the symmetric part of deformation tensor with Dirichlet boundary condition at the inlet and outlet. As it was expected, the following tables (5.1) and (5.2) have shown us the velocity converges with correct rate by using the aligned mesh while the pressure has discrepancy to give the optimal convergence. This comes from the idea that introduced the global linearity for the proposed solution.
This would be more obvious from the following 2D and 3D pressure diagrams (see Fig.5.3 and Fig.5.5). These diagrams exhibit below y= 0.1 and above y=0.9 the shear regions where the pressure is linearly uniform and in between the plug zones where the pressure should be zero for source model and nonlinear for the regularized model. At the interfacial boundaries where y=0.1 or 0.9 which make a separating barrier between the shear zone and plug zone, the diagrams detect very steep gradient which would be singular values for pressure.

mesh	$\|\boldsymbol{u}-\boldsymbol{u}_h\|_{L^2}$	$\|p-p_h\|_{L^2}$	$\|\boldsymbol{u}-\boldsymbol{u}_h\|_{H^1}$	$\|p-p_h\|_{H^1}$
$\epsilon = 10^{-9}$				
5x5	5.294450E-4	3.012638E-1	1.016811E-2	1.880406E00
10x10	5.629174E-10	6.894007E-2	1.788744E-8	8.842954E-1
20x20	6.597077E-10	6.808133E-2	2.311303E-8	1.046791E00
40x40	6.477620E-10	6.774412E-2	2.217441E-8	1.227218E00
80x80	6.381442E-10	6.749366E-2	2.141124E-8	1.479351E00
160x160	6.172732E-10	6.670024E-2	2.010378E-8	1.810439E00
$\epsilon = 10^{-10}$				
5x5	5.294450E-4	3.012640E-1	1.016811E-2	1.880405E00
10x10	5.629224E-11	6.893996E-2	1.788773E-9	8.842947E-1
20x20	6.648554E-11	6.808111E-2	2.350160E-9	1.046791E00
40x40	6.526156E-11	6.774377E-2	2.259120E-9	1.227217E00
80x80	6.508722E-11	6.764985E-2	2.247150E-9	1.429287E00
160x160	6.506793E-11	6.762838E-2	2.245825E-9	1.646709E00
$\epsilon = 10^{-11}$				
5x5	5.294450E-4	3.012640E-1	1.016811E-2	1.880405E00
10x10	5.629175E-12	6.894016E-2	1.788743E-10	8.842956E-1
20x20	5.625442E-12	6.808161E-2	1.804768E-10	1.046792E00
40x40	5.798713E-12	6.774573E-2	1.838029E-10	1.227218E00
80x80	5.803527E-12	6.765371E-2	1.857906E-10	1.429290E00
160x160	6.241584E-12	6.764780E-2	2.047230E-10	1.646692E00

Table 5.1. *Bingham flow in channel:* Velocity/ pressure error estimates for Bingham flow in channel at $TOL = 10^{-8}$ by using the bi-viscous model and the gradient form at $\tau_s = 0.4$.

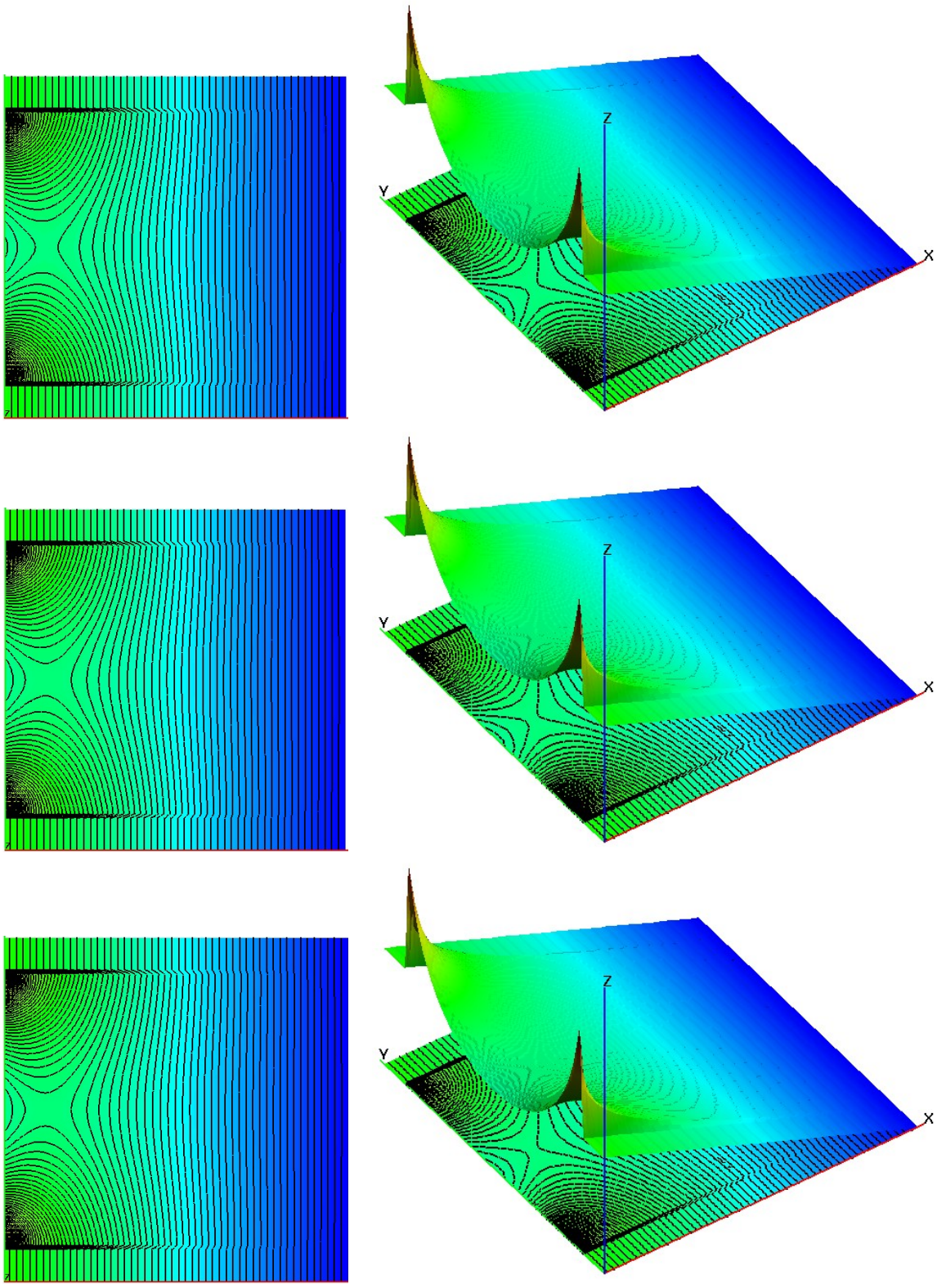

Fig. 5.3. *Bingham flow in channel:* The pressure 2D/3D diagrams at $h = 1/160$, $TOL = 10^{-8}$ and $\epsilon = 10^{-9}$ to 10^{-11} (top to bottom) by using the bi-viscous model and the gradient form at $\tau_s = 0.4$.

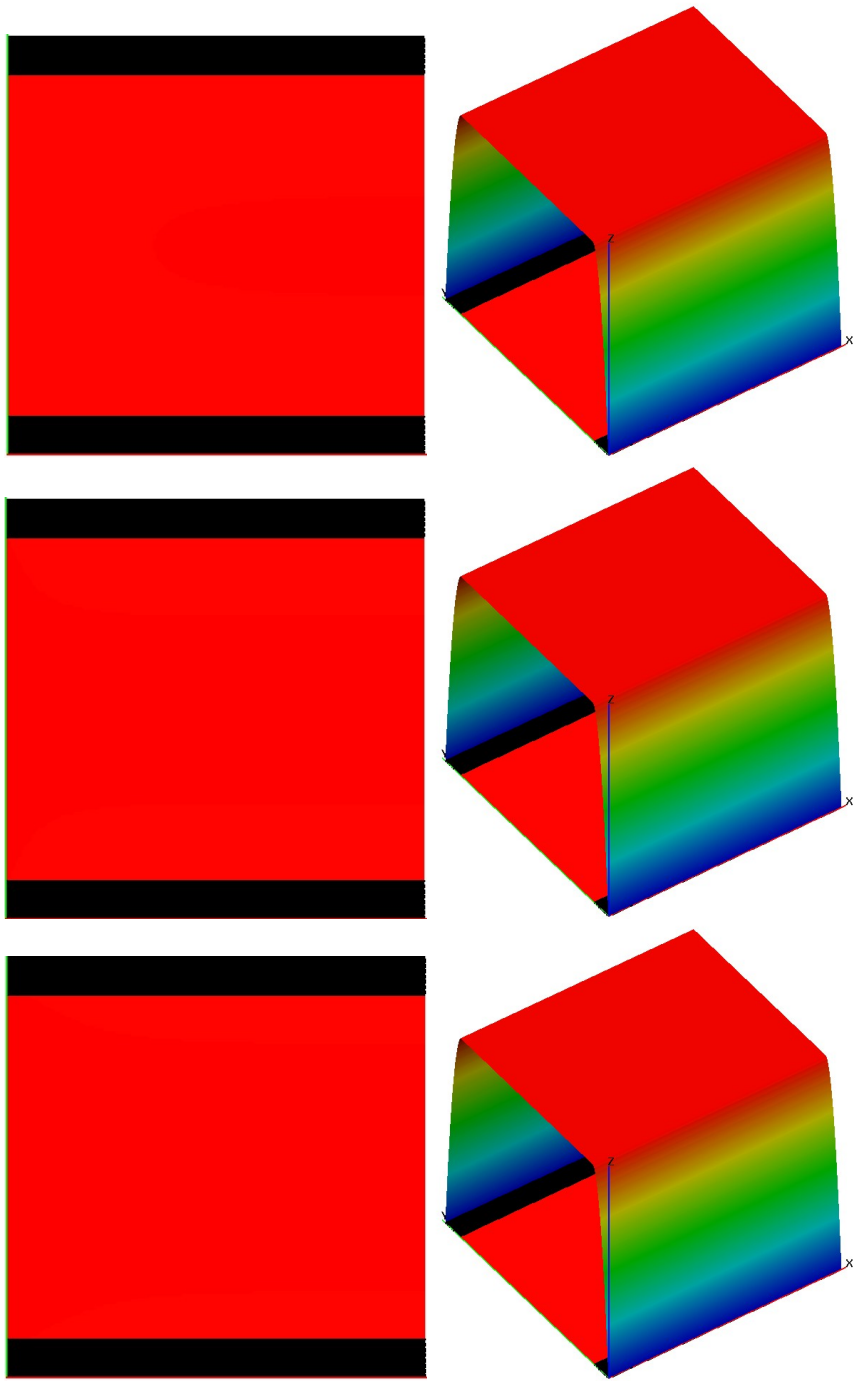

Fig. 5.4. *Bingham flow in channel:* The velocity 2D/3D diagrams at $h = 1/160$, $TOL = 10^{-8}$ and $\epsilon = 10^{-9}$ to 10^{-11} (top to bottom) by using the bi-viscous model and the gradient form at $\tau_s = 0.4$.

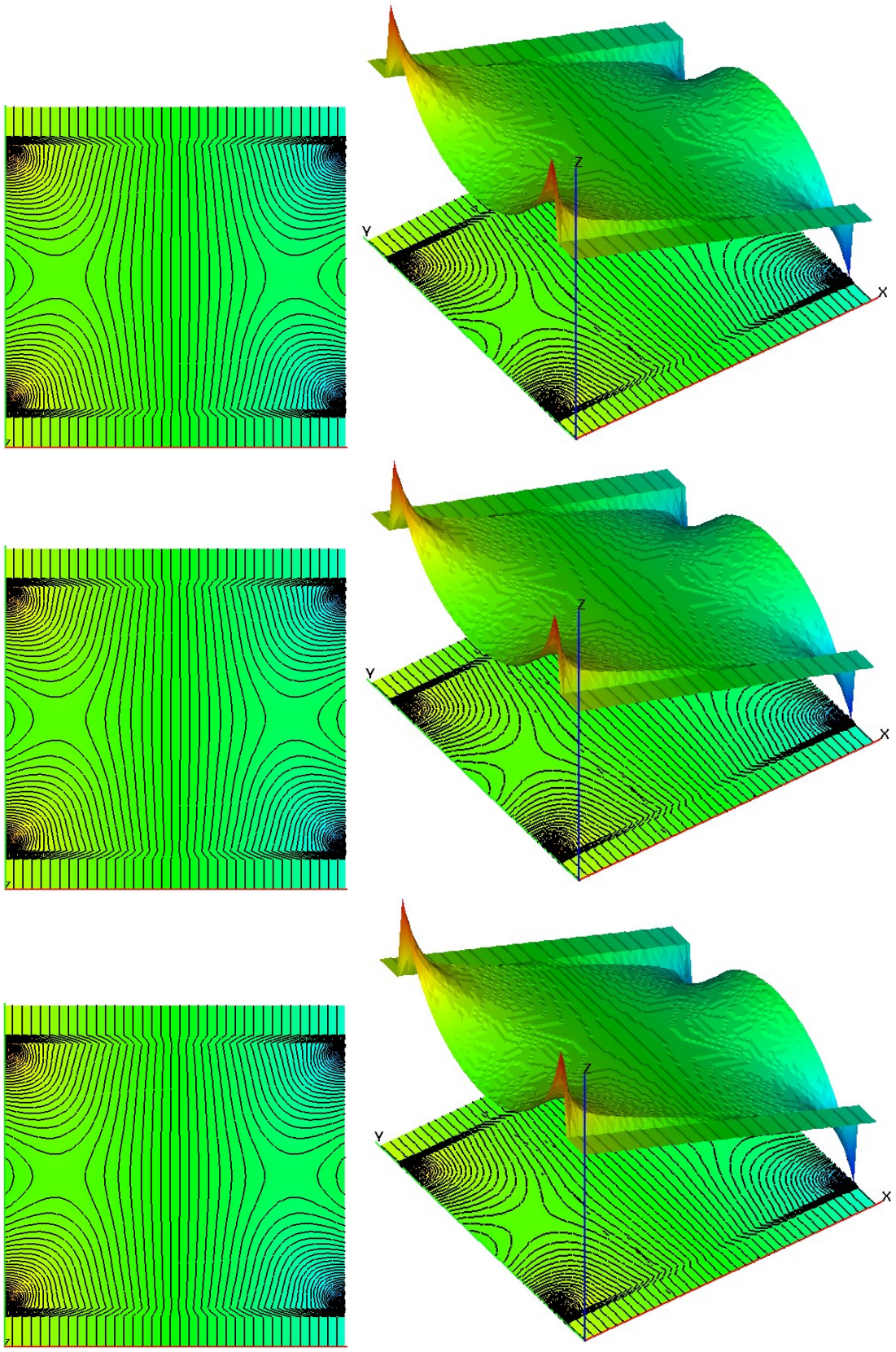

Fig. 5.5. *Bingham flow in channel:* The pressure 2D/3D diagrams at $h = 1/80$, $TOL = 10^{-8}$ and $\epsilon = 10^{-9}$ to 10^{-11} (top to bottom) by using the bi-viscous model and the deformation form at $\tau_s = 0.4$.

mesh	$\|\boldsymbol{u}-\boldsymbol{u}_h\|_{L^2}$	$\|p-p_h\|_{L^2}$	$\|\boldsymbol{u}-\boldsymbol{u}_h\|_{H^1}$	$\|p-p_h\|_{H^1}$
$\epsilon = 10^{-9}$				
5x5	4.851632E-4	2.854365E-1	9.584137E-3	1.930207E00
10x10	5.567813E-10	5.018035E-2	1.535836E-8	6.498267E-1
20x20	5.559640E-10	4.977226E-2	1.558598E-8	8.348825E-1
40x40	5.534524E-10	4.954947E-2	1.573563E-8	1.077819E00
80x80	5.481072E-10	4.945133E-2	1.601892E-8	1.392137E00
$\epsilon = 10^{-10}$				
5x5	4.853018E-4	2.859264E-1	9.584588E-3	1.946540E00
10x10	5.567830E-11	5.018033E-2	1.535839E-9	6.498268E-1
20x20	6.382992E-11	4.977222E-2	1.988231E-9	8.348830E-1
40x40	6.298163E-11	4.954932E-2	1.923075E-9	1.077822E00
80x80	5.769394E-11	4.945078E-2	1.632278E-9	1.392149E00
$\epsilon = 10^{-11}$				
5x5	4.853018E-4	2.859264E-1	9.584587E-3	1.946540E00
10x10	5.567833E-12	5.018034E-2	1.535836E-10	6.498271E-1
20x20	5.711306E-12	4.977231E-2	1.581818E-10	8.348831E-1
40x40	6.116750E-12	4.954945E-2	1.790372E-10	1.077824E-1
80x80	6.003924E-12	4.944805E-2	1.724496E-10	1.392179E00

Table 5.2. *Bingham flow in channel:* Velocity/ pressure error estimates for Bingham flow in channel by using the bi-viscous model and the deformation form at $TOL = 10^{-8}$ and $\tau_s = 0.4$.

5.6.2 Lid Driven Cavity Benchmark

A lid driven cavity benchmark is proposed here to be a unit square cavity. The viscoplastic fluid is motivated by a constant horizontal velocity profile on the upper lid while is zero on the other three edges. Our simulation here is going on for two different values of Reynolds number for the shear regime(Re=1 and Re=8000). In addition to the variation of unyielded zones due to the regularization parameter and mesh size are considered.

5.6.2.a The Unyielded Zone

In Fig.5.7 the simulation is performed when Re=1 to exhibit an important feature. As soon as the yield limit increases, the dead region increases occupying more of the cavity. The shear region is moved to be close to the driven lid. The square is blocked along three of its edges and driven along the last one. Surprisingly, the dead zones can be deduced inside the flow as expected in some articles which are already close to the three lower edges in the cavity.
The blocking property might be observed from the depicted figures (Fig.5.7, Fig.5.8 and Fig.5.9). It is shown that the increasing of yield stress increases the area of the dead zones which lead to no flow. Since the Bingham flow does not flow which means, it is blocked in the square. In this case the critical stress for the blocking occurs when $\|\mathbf{D}\| = 0$ and $\boldsymbol{u} = \mathbf{0}$ and can be computed from the following equation:

$$\tau_s \int_{\boldsymbol{\Omega}} \|\mathbf{D}(\boldsymbol{v})\| = \int_{\boldsymbol{\Omega}} \boldsymbol{f}\boldsymbol{v}. \tag{5.43}$$

5.6.2.b Main Vortex

The main vortex and its intensity (the minimum value of stream function in the eye of the vortex) is only one and its center lies in the axisymmetric vertical line position(x-coordinate has always the middle value and y changes) which approaches to the upper lid with increasing the yield limit. Consequently, In Fig.5.8 the figure highlights the same that the main vortex shrinks and goes up towards the moving side by increasing the yield value. The figure highlights the shifting of eye vortex to the lid by increasing its

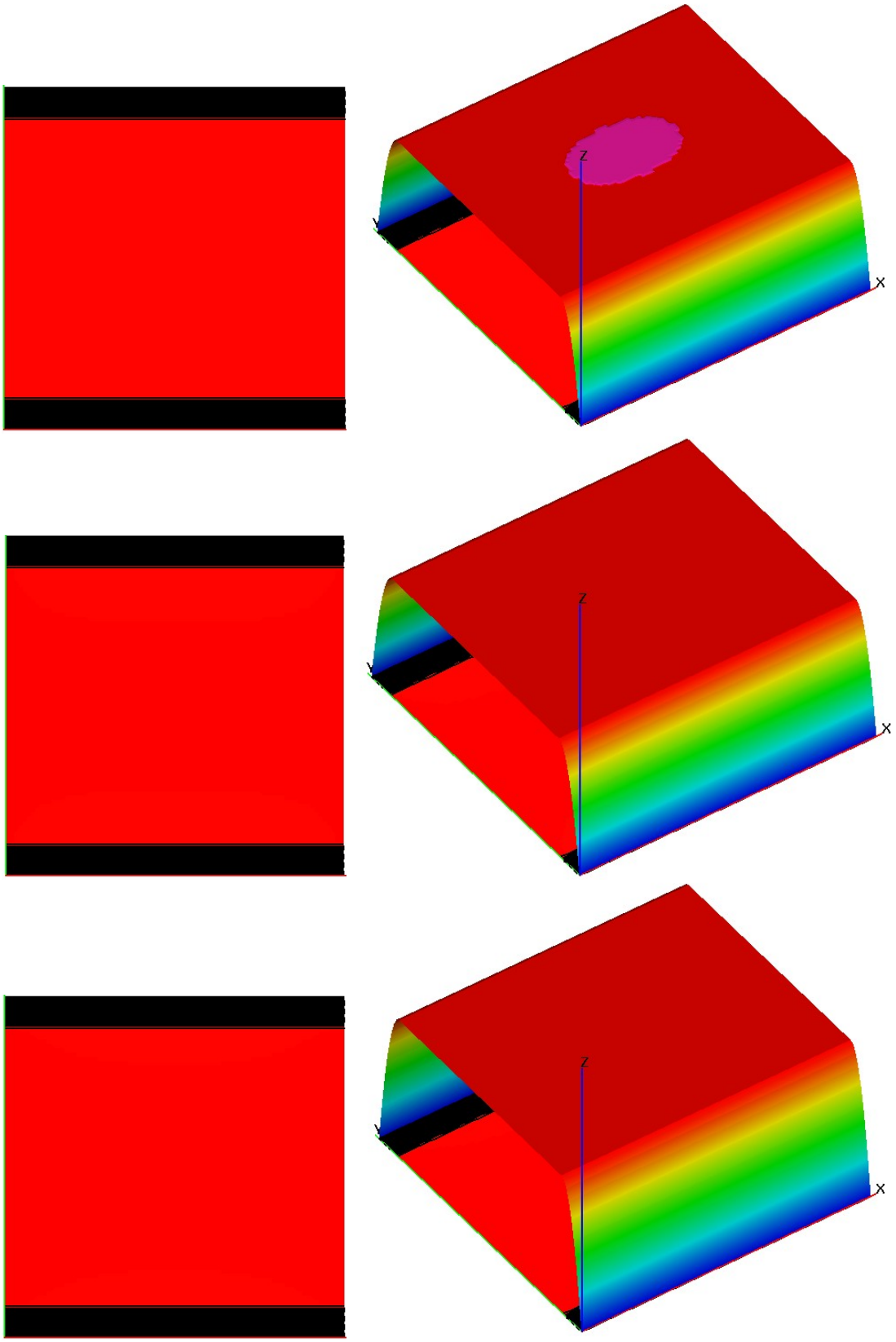

Fig. 5.6. *Bingham flow in channel:* The velocity 2D/3D diagrams at $h = 1/80$, $TOL = 10^{-8}$ and $\epsilon = 10^{-9}$ to 10^{-11} (top to bottom) by using the bi-viscous model and the deformation form at $\tau_s = 0.4$.

value definitely at the higher values of yield stress.
In Fig.5.9 at the high value of Reynolds number(=8000), like the Newtonian fluids, at small values of yield limit(τ_s) an additional secondary vortices appear and fade gradually away by the growth of rigid zone until they disappear. But, the location of the main vortex is shifted to the right and comes back to the a axisymmetric vertical line position in the cavity and moves to the driven lid if the yield stress increases.

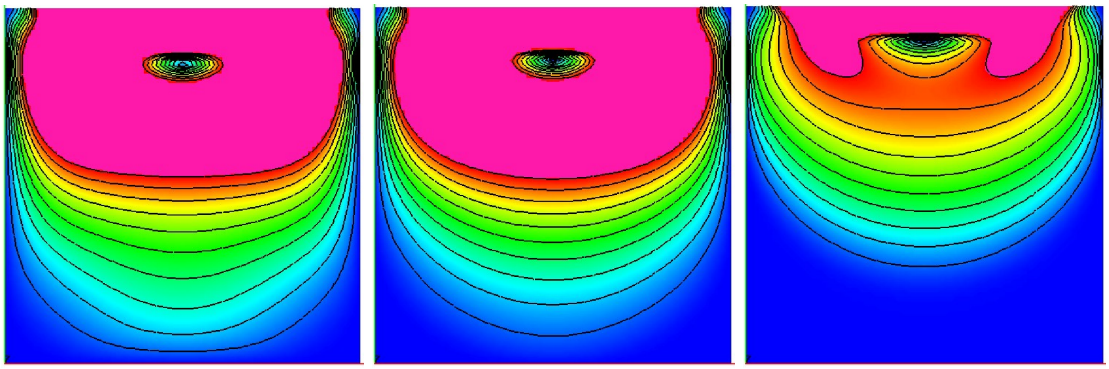

Fig. 5.7. *Bingham flow in driven cavity:* The yielded and unyielded regimes in a lid driven cavity at the yield stress $\tau_s = 0.1, 1, 10$ (left to right) for Bingham viscoplastic fluid.

5.6.3 Cylinder Benchmark

Finally, we consider the planar flow around the cylinder, where the inlet flow boundary condition is a parabolic profile and the outflow is set a natural boundary condition(DO NOTHING). In viscoplastic flow around a cylinder, the flow domain is categorized in the vicinity of the cylinder to the surrounding dead zone, the deformed zone around the cylinder, two dead pike-shaped zones(stick in front of and behind the cylinder) and two oval plug zones located between the fixed planes(lower and upper) of the cylinder, and the last two are already located inside the deformed zone (see [1, 15, 24, 62, 157, 158, 174, 180, 182, 210, 236]).

5.6.3.a The Unyielded Zones

From the analysis of the flow regimes around the cylinder, the shear stress has a singularity at the plug region between the lower or upper fixed planes and the cylinder. these is due to the vanishing of the deformation tensor. Therefore, the most numerical instabilities occurring at these regions have already unbounded viscosity values by nature. Here, the interested issue is to analyze the behavior of the flow along the vertical axis passing through the cylinder center to recognize the notable change due to the regularization.
The depicted figures(Fig.5.10, Fig.5.11 and Fig.5.12) exhibit the variation of pressure, velocity, norm of shear rate, norm of shear stress and viscosity along the axis of the gap passing through the center.
One can see from the velocity profile that, it has a maximum value and the profile looks like Poiseuille profile. This implies that there is a region is moved with a constant value with the flow located roughly in the middle. Correspondingly the pressure at these values, which represent the plug regions has the null, value due to the absence of the external force and constant yield stress value.
For the viscosity or the shear rate at the smaller value of ϵ each curve grows to higher value until ∞

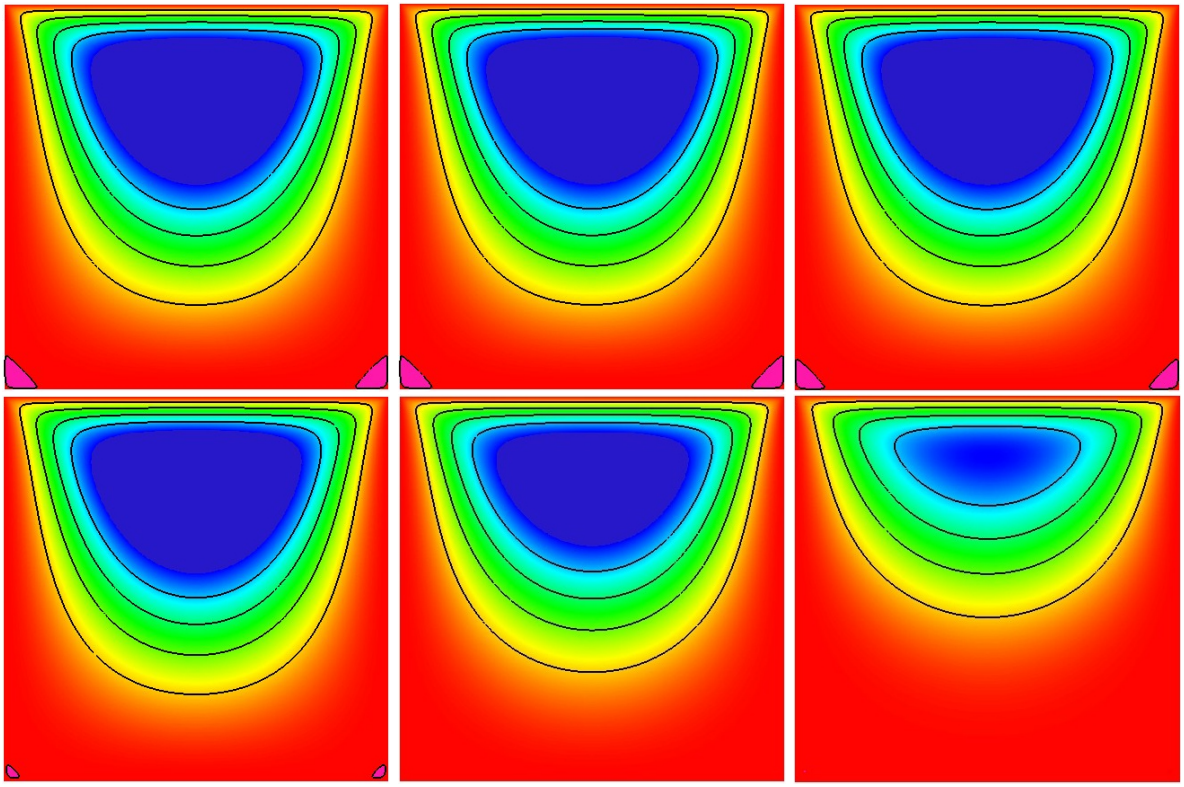

Fig. 5.8. *Bingham flow in driven cavity:* The contours of the stream function at h=1/256, $\epsilon = 10^{-2}$, $\tau_s = 10^{-4}, 10^{-3}, 10^{-2}$ (up), $\tau_s = 10^{-1}, 1, 5$ (down) and Re =1 for Bingham viscoplastic fluid.

or unbounded value when ϵ goes to zero. Therefore one can deduce the following: a plug zone is located roughly in the middle of the gap.
Furthermore from the shear rate profile; there is a point which has a zero value corresponding to the maximum velocity which leads to the viscosity to be singular. But, in contrast the corresponding value of the shear stress profile is not singular. This is because out of the definition, this part is already multiplied by zero but has a value due to regularization. This is a dangerous drawback due to regularization which can not detect the real value of the shear stress even if it has very small value of regularization parameter. Anyhow, from Fig.5.14 the different zones approximately detected at the higher value of the yield stress and smaller value of regularization parameter.
From the figures Fig.5.13 and Fig.5.14 two dead zones are being observed and their increasing follows the increase of the yield stress. The first one is surrounding dead zone which contains the deformed zone. The second is two rigid pike-shaped zones which are on the axis of the flow at the front and rear stagnation points. The unyielded zones have noted by previous researchers for the flow around cylinder. These zones become noticeable and increase apparently if the yield stress increases.

5.6.3.b The Distribution of Pressure

Due to the dependence of the pressure in the plug zone on the yield stress value, one can notice that the pressure at the plug zone roughly goes to zero (see Fig.5.10). This is due to the constant value of the yield stress and the absence of the external forces. This explanation can be recognized easily from the following

$$\boldsymbol{\nabla} p = \boldsymbol{\nabla} \cdot \boldsymbol{\tau}_s + \boldsymbol{f}, \quad in \quad \boldsymbol{\Omega}. \tag{5.44}$$

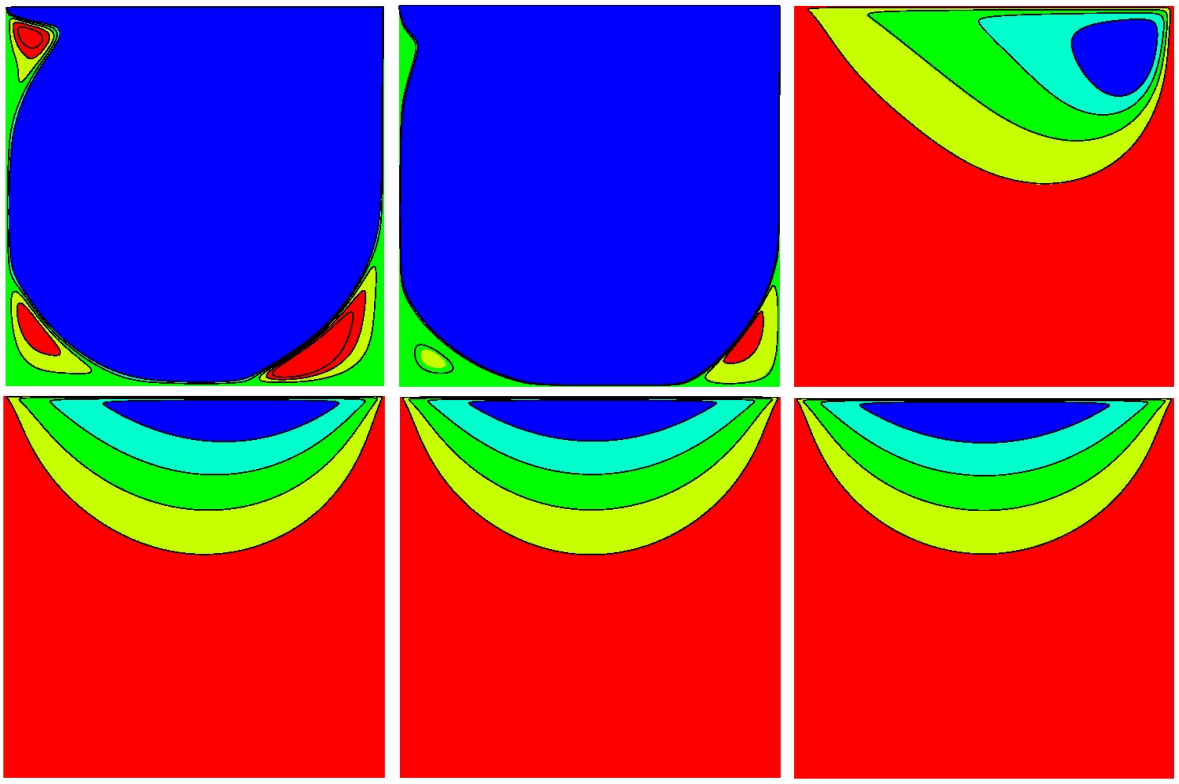

Fig. 5.9. *Bingham flow in driven cavity:* The contours of the stream function at h=1/256, $\epsilon = 10^{-2}$, $\tau_s = 10^{-4}, 10^{-3}, 10^{-2}$ (up), $\tau_s = 10^{-1}, 1, 5$ (down) and Re=8000 for Bingham viscoplastic fluid.

In dead and plug regimes, there are $\|\mathbf{D}\| = 0$, $\tau_s = const.$ and $\boldsymbol{f} = 0$ so that we have $\boldsymbol{\nabla} p = 0$ which leads to p=0. This is obvious from Fig(5.10) which exposes a vertical cut line passing through the center of the cylinder.

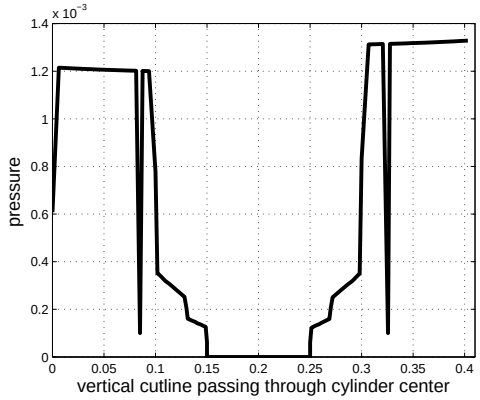

Fig. 5.10. *Bingham flow around cylinder:* The pressure distribution along the vertical axis passing through the center of cylinder for level 5, $\tau_s = 1$, $\epsilon = 10^{-3}$ and Re=1 for Bingham viscoplastic fluid.

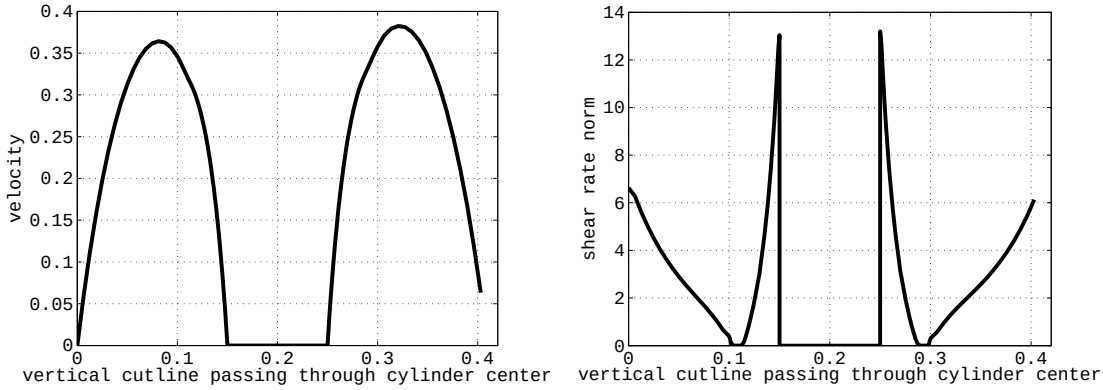

Fig. 5.11. *Bingham flow around cylinder:* The velocity (left) and the shear rate (right) distributions along the vertical axis passing through the center of cylinder for level 5, $\tau_s = 1$, $\epsilon = 10^{-3}$ and Re=1 for Bingham viscoplastic fluid.

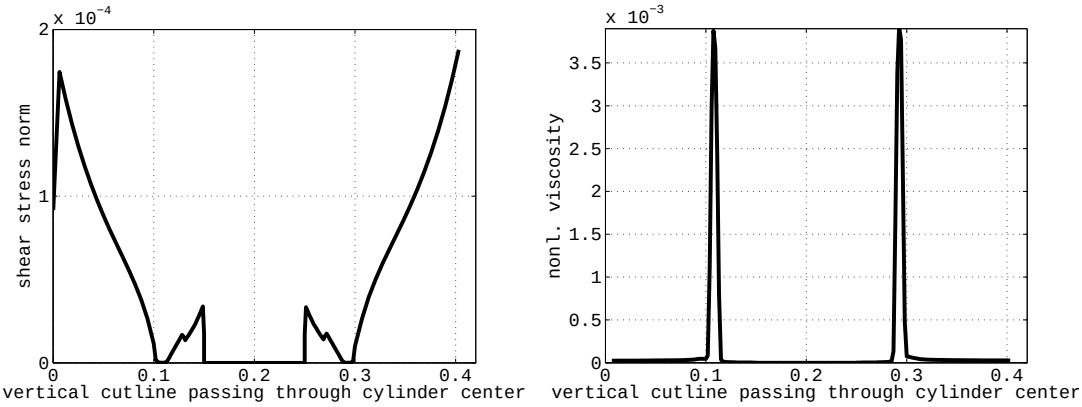

Fig. 5.12. *Bingham flow around cylinder:* The shear stress (left) and the viscosity distributions (right) along the vertical axis passing through the center of cylinder for level 5, $\tau_s = 1$, $\epsilon = 10^{-3}$ and Re=1 for Bingham viscoplastic fluid.

5.7 Summary

In this chapter, a numerical monolithic scheme is provided to cope with the viscoplastic problem with Bingham type due to its stability and accuracy. The complete nonlinear algebraic viscoplastic equations are solved as a whole to reach the required accuracy in the solution process via the monolithic approach. The scheme has several advantages. One of them is to use the continuous Newton method to treat the nonlinearity, and the second is to use the geometric multigrid as linear solver with full Vanka smoother for the arisen nonlinear algebraic equations. The exposition of stabilization techniques employing edge oriented stabilization is efficient to cope with nonlinear fluid problems with the use of low order finite elements generally and the high order finite element in the case of viscoplastic problems. The included results imply the use of regularized models instead of exact model. It is available to expose the main features of the fluid with the robust numerical method. The present results confirm early asymptotic studies on the Bingham viscoplastic fluid regarding the yielded/unyielded zones in benchmark problems. Computationally, it is noted that the appearance of flow properties by using the the regularized models is strongly associated to the regularization parameter. Therefore, the effect of regularization comparing

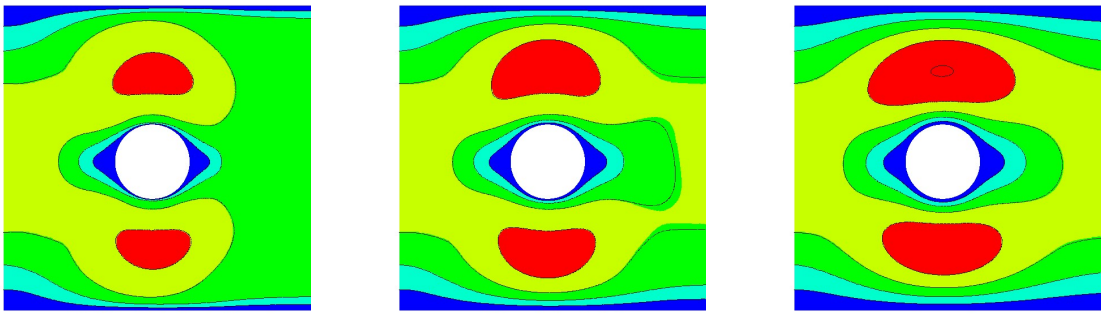

Fig. 5.13. *Bingham flow around cylinder:* The unyielded regimes for the velocity at yield stress 1,10,100 and Re=1 for Bingham viscoplastic fluid.

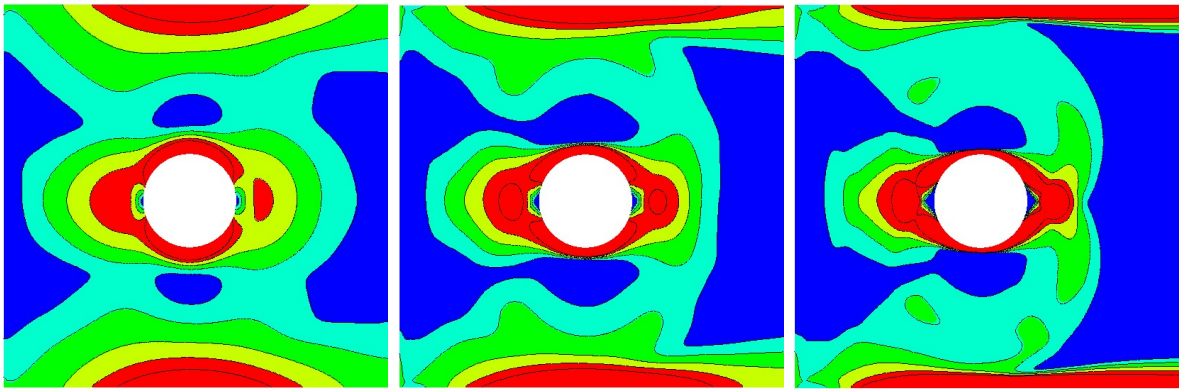

Fig. 5.14. *Bingham flow around cylinder:* The unyielded regimes for the rate of deformation tensor at yield stress 1,10,100 and Re = 1 for Bingham viscoplastic fluid.

with the effect of the size is approximately the same on the flow regimes. This can be noticed clearly from the contours of the norm of shear rate which reflects the effect on the shape of flow regimes which gives the possibility to predict the curvature of the flow boundaries of the dead/plug regions accurately. The predicted pressure contour is strongly related to the yield stress value. This confirms the nonuniform distribution of pressure over the flow domain and its dependence on the constitutive model in the worked benchmarks.

6

Monolithic Time Approach for Non-Stationary Viscoplastic Fluids

The presented algorithm is developed to solve the non-stationary Bingham viscoplastic equations via a monolithic time integration approach. In this approach, the nonlinear algebraic viscoplastic system is solved as a whole in each time step. The corresponding constitutive model is modified via the regularized Bercovier-Engelman regularization model. The algorithm uses one /fractional step theta schemes for the time discretization involving a parameter to allow fully implicit, semi-implicit or fully explicit handling. The domain of interest is discretized by using the finite element method which has unmapped pressure approaches either the higher conforming finite element or the lower finite element with edge oriented stabilization at the need. This stabilization is provided to guarantee the satisfactory of Korn's inequality in case of lower order finite elements.
In the frame of the monolithic time approach for each time step, we solve the discretized problem utilizing the continuous Newton solver to cope with the nonlinearity and applying the geometrical multigrid solver for linear problems involves the full Vanka smoother for the smoothing step. This methodology is tested by confirming the steady state parameters such as the energy norm, the drag and lift coefficients to obtain the stationary values for the Newtonian and viscoplastic fluids at low Reynolds numbers. Moreover, it is confirmed the periodic oscillatory behaviors for the drag and lift coefficients in Newtonian fluid and viscoplastic fluid at high Reynolds number.
The applied well-known benchmarks are used to confirm the early viscoplastic behavior and to predict the properties of non-stationary viscoplastic fluid for instance cessation, the existence of vortex shedding at the lower values of yield stress and periodic oscillating flow, both for medium values of Reynolds number.

6.1 Introduction

The most common fluids can be categorized according to the Newtonian and non-Newtonian fluids. This category is mainly based on the apparent viscosity of the fluids which is naturally associated with the shear stress. The general governing equations for the generalized Newtonian fluid read

$$\frac{\partial \boldsymbol{u}}{\partial t} + \boldsymbol{u} \cdot \boldsymbol{\nabla} \boldsymbol{u} + \boldsymbol{\nabla} p = \boldsymbol{\nabla} \cdot \boldsymbol{\tau} + \boldsymbol{f}, \quad in \quad \boldsymbol{\Omega} \times (0, T), \tag{6.1a}$$

$$\boldsymbol{\nabla} \cdot \boldsymbol{u} = 0 \quad in \quad \boldsymbol{\Omega} \times ([0, T), \tag{6.1b}$$

$$\boldsymbol{u}(\boldsymbol{x}, t) = \boldsymbol{u}^o \quad on \quad \partial \boldsymbol{\Omega} \times (0, T), \tag{6.1c}$$

$$\boldsymbol{u}(\boldsymbol{x}, 0) = \boldsymbol{u}_o \quad in \quad \boldsymbol{\Omega}. \tag{6.1d}$$

For the nonstationary case of generalized Newtonian fluids several discussions concerned the existence and uniqueness can be found in many standard monographs (see [12, 66, 82, 83, 86, 87, 173, 225] and the

references therein) and the solvability (weak and measure-valued) has been studied in details in [146] for certain models. Regarding the power law model, it is defined by the following forms

$$\boldsymbol{\tau} = 2\mu \left\|\mathbf{D}\right\|^{\frac{p-2}{2}} \mathbf{D}, \quad 1 < p < \infty \quad \mu = const, \tag{6.2a}$$

$$\boldsymbol{\tau} = 2\mu (1 + \left\|\mathbf{D}\right\|)^{\frac{p-2}{2}} \mathbf{D}, \quad 1 < p < \infty \quad \mu = const. \tag{6.2b}$$

In [225] the existence of weak solutions has been studied for the value of $p > \frac{2}{d+2} + \frac{2d}{d+2}$ and for the same model in [67] when $p > \frac{2d}{d+2}$ and in [138] when $p \geq 1 + \frac{2d}{d+2}$, where d is the number of dimensions.
A huge work of mathematical investigations analyzes the behavior of the solution for the following model

$$\boldsymbol{\tau} = 2\mu (1 + \left\|\mathbf{D}\right\|^2)^{\frac{p-2}{2}} \mathbf{D}, \quad 1 < p < \infty \quad \mu = const. \tag{6.3}$$

has been carried out in several monograph (see [98, 124, 145, 147, 148, 173, 181] and for results concerning the existence of weak and strong solutions for the unsteady case in particular in long time behavior. However, among these non-Newtonian fluids the class concerning our studying for the unsteady case is non-stationary Bingham viscoplastic fluids (see [21, 192]). These fluids from its natural definition have a property that the fluid behaves like a solid below a threshold value(yield stress ($\boldsymbol{\tau}_s$)) and viscous fluids otherwise. In the shear region, the shear stress($\boldsymbol{\tau}$) (beyond the threshold value) is linearly proportional to the shear rate($\mathbf{D}$). For the non-stationary viscoplastic problem, the shear stress is typically the domain and time space. The governing equations for the unsteady case read:

$$\frac{\partial \boldsymbol{u}}{\partial t} + \boldsymbol{u} \cdot \boldsymbol{\nabla} \boldsymbol{u} + \boldsymbol{\nabla} p = \boldsymbol{\nabla} \cdot \boldsymbol{\tau} + \boldsymbol{f} \quad in \quad \boldsymbol{\Omega} \times (0, T), \tag{6.4a}$$

$$\boldsymbol{\nabla} \cdot \boldsymbol{u} = 0 \quad in \quad \boldsymbol{\Omega} \times (0, T), \tag{6.4b}$$

$$\boldsymbol{u}(\boldsymbol{x}, t) = \boldsymbol{u}^o \quad on \quad \partial\boldsymbol{\Omega} \times (0, T), \tag{6.4c}$$

$$\boldsymbol{u}(\boldsymbol{x}, 0) = \boldsymbol{u}_o \quad in \quad \boldsymbol{\Omega}, \tag{6.4d}$$

$$\boldsymbol{\tau} = \begin{cases} (2\mu + \frac{\tau_s}{\|\mathbf{D}\|})\mathbf{D}(\boldsymbol{u}) \text{ if} & \|\mathbf{D}\| \neq 0, \\ \leq \boldsymbol{\tau}_s \text{ if} & \|\mathbf{D}\| = 0. \end{cases} \tag{6.4e}$$

The contained numerical difficulties for this problem can be outlined by the following threefold:

(1) Strong non-linearities (which are already presented in most interesting phenomenon in flow simulation resulted from strong nonlinear effect).

(2) Non-differentiability (which is the most crucial feature for the viscoplastic fluids)

(3) Incompressibility(which is the most crucial and CPU time consuming part of incompressible flow solver)

(4) Stability versus accuracy (which may be the most main part for any proposed scheme to capture any interesting phenomenon)
From this aspect, to cope with non-stationary viscoplastic problem, the proposed scheme should have good stabilities as well as the following threefold:

(1)- accurate spatial discretization,

(2)- stable, efficient and robust time discretization,

(3)- efficient monolithic solution of fully discrete problem.

(4)- minimum CPU time consumption.

So far, the segregated time integration techniques based on uncoupled calculations of the velocity and pressure have been the preferred candidate to circumvent the numerical difficulties in viscoplastic fluids. One of these methods which is based on the operator splitting techniques to decouple the containment inherent difficulties (nonlinearity and non-differentiability) which were mentioned by Sanchez in [183] and Glowinski in [64].
Sanchez[183] used the operator splitting methods to decouple the nonlinearities with the idea of multiplier function or tensor valued function which determines the rigid region. In his algorithm, he started to solve the nonlinear elliptic problem(convective and diffusive parts) by the fixed point method. In the intermediate step, the computation of multiplier function using Uzawa algorithm involves the multiplier function and finally the solution of Stokes problem by conjugate gradient method.
In the same manner but in different organized way Glowinski et al were introduced firstly to solve Stokes problem by using the preconditioned conjugate gradient method but in the intermediate step they solved the transport equation as a discrete wave like equation and in the last step the solution of the elliptic equation involved the tensor valued function using Uzawa algorithm.
However, mostly the segregated approaches differentiate between the monolithic ones according to their computational cost and computational efficiency (accuracy) as well as the stability. The underlined drawback in the regraded techniques which is generally believed in most monographs is numerically unstable (see [156]). However, our task here is not to compare between the two approaches while to give an insight why the monolithic time integration approach is chosen. The reason to candidate this approach is unconditionally stable as well as more accurate. But from the other hand the CPU time consumption is typically increased due to the complete solution of every step and the difficulty to construct such preconditioner for the whole system.

6.2 Discretization Techniques

The methodology of discretization for the non-stationary viscoplastic problem is based on separating between time and space. The first typical step is to discretize in time by one of the usual methods such as one step schemes or fractional θ step schemes. The second step is discretize in space by using the finite element method which will be by $\tilde{Q}_1Q_0$ or $Q_2P_1^{np}$ and both of them having the unmapped pressure approach.
Let $\boldsymbol{\Omega}$ be a bounded domain of $\mathbb{R}^2$; we denote by $\partial\boldsymbol{\Omega}$, the boundary of $\boldsymbol{\Omega}$. Let us recall the non-stationary isothermal incompressible viscoplastic fluid equations which are involved by the nonlinear viscosity by the following:

$$\frac{\partial \boldsymbol{u}}{\partial t} + \boldsymbol{u}\cdot\boldsymbol{\nabla}\boldsymbol{u} - \boldsymbol{\nabla}\cdot(\nu(\|\mathbf{D}\|)\mathbf{D}(\boldsymbol{u})) + \boldsymbol{\nabla}p = \boldsymbol{f} \quad in \quad \boldsymbol{\Omega}\times(0,T), \tag{6.5a}$$

$$\boldsymbol{\nabla}\cdot\boldsymbol{u} = 0, \quad in \quad \boldsymbol{\Omega}\times(0,T), \tag{6.5b}$$

$$\boldsymbol{u}(\boldsymbol{x},t) = \boldsymbol{u}^o \quad on \quad \partial\boldsymbol{\Omega}\times(0,T), \tag{6.5c}$$

$$\boldsymbol{u}(\boldsymbol{x},0) = \boldsymbol{u}_o \quad in \quad \boldsymbol{\Omega}, \tag{6.5d}$$

$$\boldsymbol{\tau} = \begin{cases} (\nu(\|\mathbf{D}\|)\mathbf{D}(\boldsymbol{u}) \text{ if} & \|\mathbf{D}\| \neq 0, \\ \leq \boldsymbol{\tau}_s \text{ if} & \|\mathbf{D}\| = 0, \end{cases} \tag{6.5e}$$

where $\boldsymbol{u}^o$ is the velocity prescribed on the boundary of $\boldsymbol{\Omega}$ such that $\int_{\partial\boldsymbol{\Omega}}\boldsymbol{u}^o.\boldsymbol{n} = 0$, $\boldsymbol{f}$ is the density of external forces and the nonlinear viscosity $\nu(\|\mathbf{D}\|) = 2\mu + \frac{\tau_s}{\|\mathbf{D}\|}$. It is noted that if $\tau_s = 0$ then, the system of equations of Bingham viscoplastic fluid is reduced to the modeling of Newtonian fluid.

6.2.1 Time Discretization

Consider an initial value problem of the following form, with $X(t) \in \mathbb{R}^d, d \geq 1$:

$$\begin{cases} \dfrac{dX}{dt} &= f(X,t) \quad \forall t > 0, \\ X(0) &= X_0. \end{cases} \tag{6.6}$$

Then, θ-scheme (see [212]) with macro time step Δt can be written again as three consecutive sub steps, where $\theta = 1 - 1/\sqrt{2}$, $X^0 = X_0$, $n \geq 0$ and X^n is known:

$$\frac{X^{n+\theta} - X^n}{\theta \Delta t} = f\left(X^{n+\theta}, t^{n+\theta}\right), \tag{6.7a}$$

$$X^{n+1-\theta} = \frac{1-\theta}{\theta} X^{n+\theta} + \frac{2\theta - 1}{\theta} X^n, \tag{6.7b}$$

$$\frac{X^{n+1} - X^{n+1-\theta}}{\theta \Delta t} = f\left(X^{n+1}, t^{n+1}\right). \tag{6.7c}$$

As shown in [93, 94], the most important properties of this θ-scheme are:

- it is fully implicit;
- it is strongly A-stable;
- it is second order accurate (in fact it is "nearly" third order accurate (see [94])).

These properties promise some advantageous behavior, particularly in implicit CFD simulations for non-stationary incompressible flow problems. The fractional $\theta - step$ scheme was introduced firstly in [94] and its temporal approximation accuracy was studied for a symmetric positive definite spatial operator. The method is widely used due to its accuracy to approximate the time discretization for the non-stationary Newtonian fluid in [119, 213, 214]. As it is shown, the idea of this algorithm is based on separating the updates into several substeps. Variables are alternatively lagged in the updates to reduce the size of the algebraic systems which have to be solved at each substep. The sequential nature of the splitting provides us an additional benefit to approximate the nonlinear terms to be linear in each time step via segregated way (see [64, 183]). Applying the basic fractional-θ step of this scheme following non-stationary viscoplastic equations obtains the following variants of the scheme.

$$\boldsymbol{u}_t + \boldsymbol{u} \cdot \boldsymbol{\nabla} \boldsymbol{u} - \boldsymbol{\nabla} \cdot (\nu(\|\mathbf{D}\|)\mathbf{D}(\boldsymbol{u})) + \boldsymbol{\nabla} p = \boldsymbol{f} \quad \text{in} \quad \boldsymbol{\Omega} \times (0,T), \tag{6.8a}$$

$$\operatorname{div} \boldsymbol{u} = 0 \quad \text{in} \quad \boldsymbol{\Omega} \times (0,T). \tag{6.8b}$$

for given force $\boldsymbol{f}$ and nonlinear viscosity ν, with prescribed boundary values on the boundary $\partial\boldsymbol{\Omega}$ and an initial condition at $t = 0$.

6.2.1.a Basic θ-Scheme

Given $\boldsymbol{u}^n$ and $\Delta t = t_{n+1} - t_n$, then solve for $\boldsymbol{u} = \boldsymbol{u}^{n+1}$ and $p = p^{n+1}$

$$\frac{\boldsymbol{u} - \boldsymbol{u}^n}{\Delta t} + \theta[\boldsymbol{u} \cdot \boldsymbol{\nabla} \boldsymbol{u} - \boldsymbol{\nabla} \cdot (\nu(\|\mathbf{D}\|)\mathbf{D}(\boldsymbol{u}))] + \boldsymbol{\nabla} p = \mathbf{g}^{n+1} \quad \text{in} \quad \boldsymbol{\Omega} \times (0,T). \tag{6.9a}$$

$$\operatorname{div} \boldsymbol{u} = 0 \qquad \text{in} \quad \boldsymbol{\Omega} \times (0,T). \tag{6.9b}$$

with right hand side
$\mathbf{g}^{n+1} = \theta \boldsymbol{f}^{n+1} + (1-\theta)\boldsymbol{f}^n - (1-\theta)[\boldsymbol{u}^n \cdot \boldsymbol{\nabla} \boldsymbol{u}^n - \boldsymbol{\nabla}.(\nu(\|\mathbf{D}^n\|)\mathbf{D}(\boldsymbol{u}^n))]$.

The parameter θ has to be chosen depending on the time-stepping scheme which refers one step-θ scheme, e.g., $\theta = 1$ for the Backward Euler scheme, or $\theta = 1/2$ for the Crank-Nicholson-scheme and $\theta = 0$ for the forward Euler scheme.
The pressure term $\nabla p = \boldsymbol{\nabla} p^{n+1}$, which is treated as fully implicit, may be replaced by $\theta \boldsymbol{\nabla} p^{n+1} + (1 - \theta)\boldsymbol{\nabla} p^n$, but with appropriate postprocessing, both strategies lead to solutions of the same accuracy. In all cases, we end up with the task of solving, at each time step, a nonlinear saddle point problem of given type which has to be discretized in space.

In the following, we use the more compact form for the nonlinear terms (diffusive and advective parts) to be easier to use in the equations:

$$\tilde{N}(\boldsymbol{u})\boldsymbol{u} = -\boldsymbol{\nabla} \cdot (\nu(\|\mathbf{D}\|)\mathbf{D}(\boldsymbol{u})) + \boldsymbol{u} \cdot \boldsymbol{\nabla}\boldsymbol{u}. \tag{6.10}$$

6.2.1.b Backward Euler-Scheme

$$\begin{aligned} [I + \Delta t \tilde{N}(\boldsymbol{u}^{n+1})]\boldsymbol{u}^{n+1} + \boldsymbol{\nabla} p^{n+1} &= \boldsymbol{u}^n + \Delta t \boldsymbol{f}^{n+1}, \\ \operatorname{div} \boldsymbol{u}^{n+1} &= 0. \end{aligned}$$

6.2.1.c Crank-Nicholson-Scheme

$$\begin{aligned} [I + \tfrac{\Delta t}{2} \tilde{N}(\boldsymbol{u}^{n+1})]\boldsymbol{u}^{n+1} + \boldsymbol{\nabla} p^{n+1} &= [I - \tfrac{\Delta t}{2} \tilde{N}(\boldsymbol{u}^n)]\boldsymbol{u}^n + \tfrac{\Delta t}{2} \boldsymbol{f}^{n+1} + \tfrac{\Delta t}{2} \boldsymbol{f}^n, \\ \operatorname{div} \boldsymbol{u}^{n+1} &= 0. \end{aligned}$$

6.2.1.d Fractional-Step-θ-Scheme

For the Fractional-Step-θ-scheme we proceed as follows. Choosing $\theta = 1 - \frac{\sqrt{2}}{2}$, $\theta' = 1 - 2\theta$, and $\alpha = \frac{1-2\theta}{1-\theta}$, $\beta = 1 - \alpha$, the macro time step $t_n \to t_{n+1} = t_n + \Delta t$ is split into the three following consecutive sub steps (with $\tilde{\theta} := \alpha\theta\Delta t = \beta\theta'\Delta t$):

$$\begin{aligned} [I + \tilde{\theta}\tilde{N}(\boldsymbol{u}^{n+\theta})]\boldsymbol{u}^{n+\theta} + \boldsymbol{\nabla} p^{n+\theta} &= [I - \beta\theta\Delta t \tilde{N}(\boldsymbol{u}^n)]\boldsymbol{u}^n + \theta\Delta t \boldsymbol{f}^n \\ \operatorname{div} \boldsymbol{u}^{n+\theta} &= 0 \end{aligned}$$

$$\begin{aligned} [I + \tilde{\theta}\tilde{N}(\boldsymbol{u}^{n+1-\theta})]\boldsymbol{u}^{n+1-\theta} + \boldsymbol{\nabla} p^{n+1-\theta} &= [I - \alpha\theta'\Delta t \tilde{N}(\boldsymbol{u}^{n+\theta})]\boldsymbol{u}^{n+\theta} \\ &\quad + \theta'\Delta t \boldsymbol{f}^{n+1-\theta} \\ \operatorname{div} \boldsymbol{u}^{n+1-\theta} &= 0 \end{aligned}$$

$$\begin{aligned} [I + \tilde{\theta}\tilde{N}(\boldsymbol{u}^{n+1})]\boldsymbol{u}^{n+1} + \nabla p^{n+1} &= [I - \beta\theta\Delta t \tilde{N}(\boldsymbol{u}^{n+1-\theta})]\boldsymbol{u}^{n+1-\theta} \\ &\quad + \theta\Delta t \boldsymbol{f}^{n+1-\theta} \\ \operatorname{div} \boldsymbol{u}^{n+1} &= 0 \end{aligned}$$

6.2.2 Space Discretization

Our treatment of the viscoplastic problem, since the fluid is incompressible is to choose a pair of finite element spaces known to be stable for problems with incompressibility constraint. In our work, two stable finite elements have been proposed to handle the viscoplastic problems which are preferable to have the

unmapped pressure approach. These two elements are $\tilde{Q}_1Q_0$ and $Q_2P_1^{np}$. Previously, these two particular quadrilateral nonconforming and conforming finite elements have been described as they have satisfactory approximation properties and can be applicable in two dimension problems as well as three dimensional problems. The first element is the nonconforming element (see [177]). It is used piecewise 'rotated' bilinear (reference) shape functions for the velocities spanned by $\{1, x, y, x^2-y^2\}$ and piecewise constant pressure. As for the nodal values, one may take the mean values of the velocity vector over the element edges and the mean values of the pressure over the elements. The second element is the conforming element, the velocity is spanned by $\{1, x, y, xy, x^2, y^2, xy^2, yx^2, x^2y^2\}$ and the pressure is spanned by a linear function either with the global coordinates.
The finite element approximation reads :
Given $\boldsymbol{f}$ find $\boldsymbol{u}_h \in \mathbf{V}_h$, $p_h \in P_h$ such that $\forall \boldsymbol{v}_h \in \mathbf{V}_h$, $\forall q_h \in P_h$, the following expression is satisfied:

$$\int_{\boldsymbol{\Omega}} \frac{\partial \boldsymbol{u}_h}{\partial t}\boldsymbol{v}_h + \int_{\boldsymbol{\Omega}} (\boldsymbol{u}_h \cdot \boldsymbol{\nabla}\boldsymbol{u}_h)\boldsymbol{v}_h + \int_{\boldsymbol{\Omega}} \boldsymbol{\nabla} p_h \boldsymbol{v}_h + \int_{\boldsymbol{\Omega}} \mathbf{D}(\boldsymbol{v}_h) : \boldsymbol{\tau}(\boldsymbol{u}_h) = \int_{\boldsymbol{\Omega}} \boldsymbol{f}\boldsymbol{v}_h \quad in \quad \boldsymbol{\Omega} \times (0,T), \tag{6.11a}$$

$$\int_{\boldsymbol{\Omega}} \boldsymbol{\nabla} \cdot \boldsymbol{u}_h q_h d\boldsymbol{\Omega} = 0 \quad in \quad \boldsymbol{\Omega} \times (0,T), \tag{6.11b}$$

Plug in the constitutive law in the place of stress tensor $\boldsymbol{\tau}$ to obtain the following:

$$\int_{\boldsymbol{\Omega}} \frac{\partial \boldsymbol{u}_h}{\partial t}\boldsymbol{v}_h + \int_{\boldsymbol{\Omega}} (\boldsymbol{u}_h \cdot \boldsymbol{\nabla}\boldsymbol{u}_h)\boldsymbol{v}_h - \int_{\boldsymbol{\Omega}} p_h \boldsymbol{\nabla} \cdot \boldsymbol{v}_h + \int_{\boldsymbol{\Omega}} \nu(\|\mathbf{D}\|)\mathbf{D}(\boldsymbol{u}_h) : \mathbf{D}(\boldsymbol{v}_h) = \int_{\boldsymbol{\Omega}} \boldsymbol{f}\boldsymbol{v}_h \quad in \quad \boldsymbol{\Omega} \times (0,T), \tag{6.12a}$$

$$\int_{\boldsymbol{\Omega}} \boldsymbol{\nabla} \cdot \boldsymbol{u}_h q_h d\boldsymbol{\Omega} = 0 \quad in \quad \boldsymbol{\Omega} \times (0,T), \tag{6.12b}$$

From the definition of the stress tensor $\boldsymbol{\tau}$ with the shear rate which is represented for the shear and plug regions, one can obtain

$$\int_{\boldsymbol{\Omega}|_{shear}} \frac{\partial \boldsymbol{u}_h}{\partial t}\boldsymbol{v}_h + \int_{\boldsymbol{\Omega}|_{shear}} (\boldsymbol{u}_h \cdot \boldsymbol{\nabla}\boldsymbol{u}_h)\boldsymbol{v}_h - \int_{\boldsymbol{\Omega}|_{shear}} p_h \boldsymbol{\nabla} \cdot \boldsymbol{v}_h + \tag{6.13a}$$

$$\int_{\boldsymbol{\Omega}|_{shear}} (2\mu + \frac{\tau_s}{\|\mathbf{D}\|})\mathbf{D}(\boldsymbol{u}_h) : \mathbf{D}(\boldsymbol{v}_h) = \int_{\boldsymbol{\Omega}|_{shear}} \boldsymbol{f}\boldsymbol{v}_h \quad in \quad \boldsymbol{\Omega}|_{shear} \times (0,T),$$

$$\int_{\boldsymbol{\Omega}} \boldsymbol{\nabla} \cdot \boldsymbol{u}_h q_h d\boldsymbol{\Omega} = 0 \quad in \quad \boldsymbol{\Omega} \times (0,T), \tag{6.13b}$$

$$-\int_{\boldsymbol{\Omega}|_{plug}} p_h \boldsymbol{\nabla} \cdot \boldsymbol{v}_h = -\int_{\boldsymbol{\Omega}|_{plug}} \boldsymbol{\tau}_s : \mathbf{D}(\boldsymbol{v}_h) + \int_{\boldsymbol{\Omega}|_{plug}} \boldsymbol{f} \cdot \boldsymbol{v}_h \quad in \quad \boldsymbol{\Omega}|_{plug} \times (0,T). \tag{6.13c}$$

The difficulty to use the above form leads us to use the following regularized form after dropping down the notations due to the regularization:

$$\int_{\boldsymbol{\Omega}} \frac{\partial \boldsymbol{u}_h}{\partial t}\boldsymbol{v}_h + \int_{\boldsymbol{\Omega}} (\boldsymbol{u}_h \cdot \boldsymbol{\nabla}\boldsymbol{u}_h)\boldsymbol{v}_h - \int_{\boldsymbol{\Omega}} p_h \boldsymbol{\nabla} \cdot \boldsymbol{v}_h + \tag{6.14a}$$

$$\int_{\boldsymbol{\Omega}} (2\mu + \frac{\tau_s}{\sqrt{\epsilon^2 + \|\mathbf{D}\|^2}})\mathbf{D}(\boldsymbol{u}_h) : \mathbf{D}(\boldsymbol{v}_h) = \int_{\boldsymbol{\Omega}} \boldsymbol{f}\boldsymbol{v}_h \quad in \quad \boldsymbol{\Omega} \times (0,T),$$

$$\int_{\boldsymbol{\Omega}} \boldsymbol{\nabla} \cdot \boldsymbol{u}_h q_h d\boldsymbol{\Omega} = 0 \quad in \quad \boldsymbol{\Omega} \times (0,T). \tag{6.14b}$$

Introducing the discrete solution for the velocity and pressure

$$\boldsymbol{u}_h = \sum_{j=1}^{N_{\boldsymbol{u}}} \boldsymbol{u}_j \phi_j, \qquad p_h = \sum_{j=1}^{N_p} p_j \psi_j. \tag{6.15}$$

where $N_{\boldsymbol{u}}$ and N_p are the total number of unknowns and $\boldsymbol{u}_j$ and p_j the nodal values for velocity and pressure respectively. ϕ_j and ψ_j are the interpolation functions for velocity and pressure respectively. However, the choice of spaces for velocity and pressure is not arbitrary but it should be compatible and satisfactory the LBB condition. These equations can be reduced to the form of matrix operator as the following:

$$\alpha \mathbf{M}\boldsymbol{u} + \theta \Delta t[\mathbf{L} + \mathbf{N}]\boldsymbol{u} + \Delta t \mathbf{B} p = \boldsymbol{f}, \quad \text{in} \quad \boldsymbol{\Omega} \times (0, T). \tag{6.16a}$$

$$\mathbf{B}^T \boldsymbol{u} = 0, \qquad \text{in} \quad \boldsymbol{\Omega} \times (0, T). \tag{6.16b}$$

with right hand side $\boldsymbol{f} = \theta \boldsymbol{f} + (1-\theta)\boldsymbol{f}^n - (1-\theta)[\mathbf{M}(\boldsymbol{u}^n) + \mathbf{L}(\boldsymbol{u}^n) + \mathbf{N}(\boldsymbol{u}^n)]\boldsymbol{u}^n$ and $\alpha = 1$.
where $\mathbf{M}$, $\mathbf{L}$, $\mathbf{N}$, $\mathbf{B}$ and $\mathbf{B}^T$ are the mass matrix, the nonlinear matrix, the gradient matrix, and the divergence matrix and α is constant coefficient, which are corresponding to the following variants

$$\mathbf{M} = \int_{\boldsymbol{\Omega}} \boldsymbol{u}\boldsymbol{v} d\boldsymbol{x}, \tag{6.17a}$$

$$\mathbf{L} = \int_{\boldsymbol{\Omega}} \nu(\|\mathbf{D}(\boldsymbol{u})\|)\mathbf{D}(\boldsymbol{u}) : \mathbf{D}(\boldsymbol{v}) d\boldsymbol{x}, \tag{6.17b}$$

$$\mathbf{N} = \int_{\boldsymbol{\Omega}} (\boldsymbol{u} \cdot \boldsymbol{\nabla}\boldsymbol{u})\boldsymbol{v} d\boldsymbol{x}, \tag{6.17c}$$

$$\mathbf{B} = \int_{\boldsymbol{\Omega}} q \,\mathrm{div}\, \boldsymbol{v} d\boldsymbol{x}, \tag{6.17d}$$

$$\mathbf{J} = \sum_{\text{edge E}} \max(\gamma \nu h_E, \gamma^* h_E^2) \int_E [\boldsymbol{\nabla}\boldsymbol{u}] : [\boldsymbol{\nabla}\boldsymbol{v}] ds, \tag{6.17e}$$

these equations can be reformulated to obtain the cast of saddle point problem

$$\begin{pmatrix} \mathbf{M} + \Delta t(\mathbf{L} + \mathbf{N} + \mathbf{J}) & \Delta t \mathbf{B} \\ \mathbf{B}^T & 0 \end{pmatrix} \begin{bmatrix} \boldsymbol{u} \\ p \end{bmatrix} = \begin{bmatrix} \boldsymbol{f} \\ 0. \end{bmatrix}. \tag{6.18}$$

The monolithic time integration approach is used (to be preferred) to solve the algebraic equations, and it is explained in the following section.

6.3 Method of Solution

The system of nonlinear algebraic equations arising from the viscoplastic equations can be expressed as 3×3 saddle point problem to read

$$\begin{pmatrix} \mathbf{S}_{11} & \mathbf{S}_{12} & \tilde{\mathbf{B}}_1 \\ \mathbf{S}_{21} & \mathbf{S}_{22} & \tilde{\mathbf{B}}_2 \\ \mathbf{B}_1^T & \mathbf{B}_2^T & 0 \end{pmatrix} \begin{bmatrix} u_1 \\ u_2 \\ p \end{bmatrix} = \begin{bmatrix} f_1 \\ f_2 \\ 0 \end{bmatrix}. \tag{6.19}$$

where $\boldsymbol{f} = \{f_1, f_2\}$ are the corresponding residual terms for the components of momentum and continuity equations, $\tilde{\mathbf{B}} = [\mathbf{B}_1 \quad \tilde{\mathbf{B}}_2] = \Delta t \mathbf{B}$ is the scaled discrete gradient operator with the time step (Δt), $\mathbf{J}$ is the stabilizer for the low order finite element, and the matrix $\mathbf{S}_{ij} = \mathbf{M}_{ij} + \Delta t(\mathbf{L}_{ij} + \mathbf{N}_{ij})$, i,j=1,2 taking into the account the off-diagonals mass matrix are zeros. This system is solved with the monolithic time integration approach which has several advantages for the stability and accuracy. Typically, this method is acknowledged to be more robust but it is expensive for the large scale problem and on the other hand it requires an efficient preconditioner to deal with the whole system.

6.3.1 Non-Linear Solver

The system of discretized equations is a highly nonlinear algebraic system due to the nonlinear convective and diffusive terms. The remedy is to use fixed point correction method as starting solution and afterwards the continuous Newton method in the frame of the monolithic approach. In our case, we use the continuous Newton method which is based on the Frechet derivative for the nonlinear terms applied to the nonlinear viscosity and the convective terms. This can be written as:

$$\begin{pmatrix} \mathbf{S}_{11} & \mathbf{S}_{12} + \Delta t(\delta_d \mathbf{L}^*_{12} + \delta_c \mathbf{N}^*_{12}) & \tilde{\mathbf{B}}_1 \\ \mathbf{S}_{21} + \Delta t(\delta_d \mathbf{L}^*_{21} + \delta_c \mathbf{N}^*_{21}) & \mathbf{S}_{22} & \tilde{\mathbf{B}}_2 \\ \mathbf{B}_1^T & \mathbf{B}_2^T & 0 \end{pmatrix} \begin{bmatrix} u_1 \\ u_2 \\ p \end{bmatrix} = \begin{bmatrix} f_1 \\ f_2 \\ 0 \end{bmatrix}, \tag{6.20}$$

where δ_d and δ_c are control parameters to switch simply to the standard fixed point method when $\delta_d = 0$ and $\delta_c = 0$. Then the corresponding variants read

$$[\mathbf{L}(\boldsymbol{u}^n)\boldsymbol{u}, \boldsymbol{v}] = \int_{\boldsymbol{\Omega}} \nu(\|\mathbf{D}(\boldsymbol{u}^n)\|)\mathbf{D}(\boldsymbol{u}) : \mathbf{D}(\boldsymbol{v}) d\boldsymbol{x}, \tag{6.21a}$$

$$[\mathbf{N}(\boldsymbol{u}^n)\boldsymbol{u}, \boldsymbol{v}] = \int_{\boldsymbol{\Omega}} (\boldsymbol{u}^n \cdot \nabla \boldsymbol{u})\boldsymbol{v} d\boldsymbol{x}, \tag{6.21b}$$

$$[\mathbf{B}q, \boldsymbol{v}] = \int_{\boldsymbol{\Omega}} q \operatorname{div} \boldsymbol{v} d\boldsymbol{x}, \tag{6.21c}$$

$$[\mathbf{L}^*(\boldsymbol{u}^n)\boldsymbol{u}, \boldsymbol{v}] = \int_{\boldsymbol{\Omega}} \partial_{\|\mathbf{D}\|^2} \nu(\|\mathbf{D}(\boldsymbol{u}^n)\|)[\mathbf{D}(\boldsymbol{u}^n) : \mathbf{D}(\boldsymbol{u})][\mathbf{D}(\boldsymbol{u}^n) : \mathbf{D}(\boldsymbol{v})] d\boldsymbol{x}, \tag{6.21d}$$

$$[\mathbf{N}^*(\boldsymbol{u}^n)\boldsymbol{u}, \boldsymbol{v}] = \int_{\boldsymbol{\Omega}} (\boldsymbol{u} \cdot \boldsymbol{\nabla} \boldsymbol{u}^n)\boldsymbol{v} d\boldsymbol{x}. \tag{6.21e}$$

The strongly coupled system is linearized through the continuous Newton approach which results in each solution step the form

$$\begin{bmatrix} \boldsymbol{u}^{n+1} \\ p^{n+1} \end{bmatrix} = \begin{bmatrix} \boldsymbol{u}^n \\ p^n \end{bmatrix} - \omega^n J^{-1} \begin{bmatrix} \mathbf{Res}_{\boldsymbol{u}}(\boldsymbol{u}^n, p^n) \\ \mathbf{Res}_p(\boldsymbol{u}^n, p^n) \end{bmatrix} \tag{6.22}$$

where $\omega^n \in (0, 1]$ represents the damping parameter and J represents the jacobian matrix which is

$$J = \begin{pmatrix} \mathbf{S} + \delta_d \mathbf{L}^* + \delta_c \mathbf{N}^* + \mathbf{J} & \mathbf{B} \\ \mathbf{B}^T & 0 \end{pmatrix}. \tag{6.23}$$

6.3.2 Multigrid Solver

Normally, the multigrid process can be used as a direct solver or an iterative solver from the associated solver with the coarse grid which is related to the size of the problem. In this work we have chosen the $\mathbf{F}_{cycle}$ multigrid algorithm to solve the linear problem iteratively. The performance of $\mathbf{F}_{cycle}$ is better than $\mathbf{V}_{cycle}$ and almost identical to $\mathbf{W}_{cycle}$ for high number of the steps of presmoothing and postsmoothing (see [33]).

The $\mathbf{F}_{cycle}$ algorithm used is explained as the following:

Given: $\boldsymbol{g} \in \mathbf{V}_k$, $\boldsymbol{z}_0 \in \mathbf{V}_k$ and the output of the algorithm is $MG_{\mathbf{F}}(k, \boldsymbol{g}, \boldsymbol{z}_k, m)$ where k=1,..,n the numbers of hierarchy levels, m is the number of presmoothing or postsmoothing steps and $\boldsymbol{z}_k$ is the approximated solution vector of the following linear equation

$$\boldsymbol{A}_k \boldsymbol{z} = \boldsymbol{g} \tag{6.24}$$

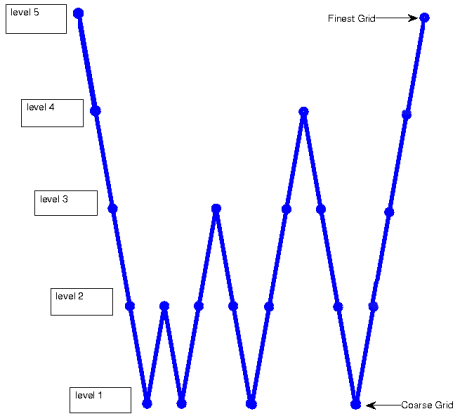

Fig. 6.1. Structure of multigrid F_{cycle} for five levels.

- **The coarse grid solution** $k = 1$
  $MG(1, \boldsymbol{g}, \boldsymbol{z}_0, m) = \boldsymbol{A}_1^{-1}\boldsymbol{g}$

- **Presmoothing step** $k \geq 2$**:**
  DO j=1,m
  $\boldsymbol{z}_j = \boldsymbol{z}_{j-1} + \Lambda_k{}^{-1}\,(\boldsymbol{g} - \boldsymbol{A}_k\boldsymbol{z}_{j-1})$
  END DO
  where $\rho(\Lambda_k) \leq Ch_k^{-2}$.

- **Correction step:**
  $\boldsymbol{z}_{m+\frac{1}{2}} = \mathsf{I}_k^{k-1} MG(k-1, \mathsf{I}_k^{k-1}(\boldsymbol{g} - \boldsymbol{A}_k\boldsymbol{z}_m), 0, m)$
  $\boldsymbol{z}_{m+1} = \boldsymbol{z}_m + \mathsf{I}_k^{k-1} MG(k-1, \mathsf{I}_k^{k-1}(\boldsymbol{g} - \boldsymbol{A}_k\boldsymbol{z}_m), \boldsymbol{z}_{m+\frac{1}{2}}, m)$

- **Postsmoothing step** $k \geq 2$**:**
  DO j=m,2m+1
  $\boldsymbol{z}_j = \boldsymbol{z}_{j-1} + \Lambda_k{}^{-1}\,(\boldsymbol{g} - \boldsymbol{A}_k\boldsymbol{z}_{j-1})$
  END DO

- **Final Output:**
  $MG(k, \boldsymbol{g}, \boldsymbol{z}_0, m) = z_{2m+1}$.

6.4 Continuation Techniques

The idea to use the continuation technique with the regularization parameter is to start with a high value of the regularization parameter ($\epsilon_0 = 10^{-1}$) to solve the problem and to compute the solution vector $[\boldsymbol{u}, p]$. By using this solution as start solution, one can compute for the smaller value of the regularization

parameter with rate $\frac{\epsilon_i}{\epsilon_{i-1}} = 0.1$. So that, after a number of continuation steps it is possible to get a solution vector at a very small value of regularization parameter. Here we reached to calculate the solution to 10^{-6} (see Fig.6.2 and Fig.6.3) with the following addressed algorithm.

Given: $p_0 \in \mathbf{V}_k$, $\boldsymbol{u}_0 \in \mathbf{V}_k$ and $\epsilon = \epsilon_0$ the output of the algorithm is $[\boldsymbol{u}, p]_{\epsilon_{target}}$ where ϵ_{target} corresponds to n_{target}.
$DO \quad i = 1, \quad n_{target}$
$[\boldsymbol{u}_i, p_i, \epsilon_i, success] = [\boldsymbol{u}_{i-1}, p_{i-1}, \epsilon_{i-1}]$
$if \quad (success = true) \quad then$
$\frac{\epsilon_i}{\epsilon_{i-1}} = 0.1$
$\boldsymbol{u} = \boldsymbol{u}_i \quad p = p_i$
$else$
$\frac{\epsilon_i}{\epsilon_{i-1}} = 0.5$
$end \quad if$
$ENDDO$
The output
$[\boldsymbol{u}, p] = [\boldsymbol{u}_i, p_i, \epsilon_{target}]$

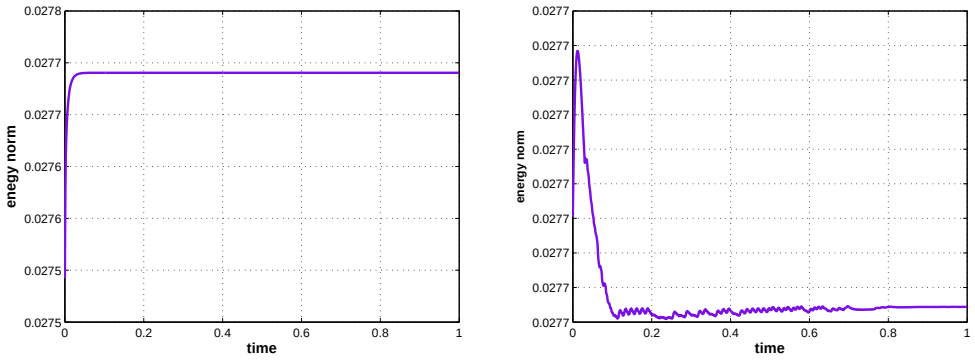

Fig. 6.2. *Continuation technique*: The energy norm ($E_{norm} = 2.7740351817E-2$) at $\epsilon = 10^{-3}$ (left) and the energy norm at $\epsilon = 10^{-4}(E_{norm} = 2.7740221999E-2)$ (right) from $\epsilon = 10^{-3}$ at h=1/128, $\Delta t = 10^{-3}$ and $\tau_s = 1$ for Bingham viscoplastic fluid in driven cavity.

6.5 Cessation Property of Bingham Viscoplastic Fluids

The cessation of time is a natural phenomenon in real viscoplastic fluids. The fluid is going to cease after a certain time. In contrast with the corresponding steady velocity in Newtonian fluid which decays to zero in an infinite amount of time (see [167]). Glowinski [92, 95] has provided the theoretical upper bounds of the time of Bingham fluid to come to rest in various flows. The theoretical upper bound is applied for the specific flows regimes (for instance axisymmetric flow Poiseuille flows and plane/circular Coutte flows

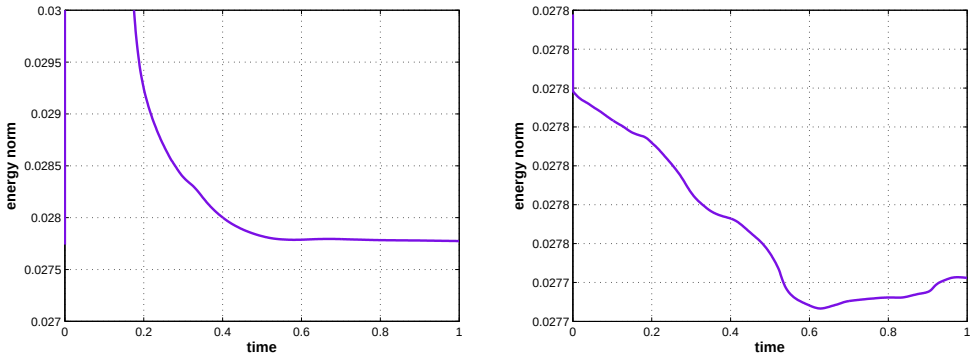

Fig. 6.3. *Continuation technique*: The energy norm at $\epsilon = 10^{-5}(E_{norm} = 2.7774634623)$ from $\epsilon = 10^{-4}$ (left) and energy norm at $\epsilon = 10^{-6}(E_{norm} = 2.7750593786E-2)$ from $\epsilon = 10^{-5}$ (right) at h=1/128, $\Delta t = 10^{-3}$ and $\tau_s = 1$ for Bingham viscoplastic fluid in driven cavity.

and Bingham flow in cylinder) in [45, 46, 65, 113, 235]. The mathematical result for the upper bound of the stopping time can be stated in the following theorem (see [64]).

Theorem 6.5.1 *Assume that* $\boldsymbol{u}_o \in \mathbf{L}^2(\boldsymbol{\Omega})$, $\boldsymbol{f} \in \mathbf{L}^2(\Omega)$ *with* $\|\boldsymbol{f}\| < \beta\tau_s$ *and* C *is a constant we have the following asymptotic behavior:* $\boldsymbol{u}(t) = 0, \quad \forall t > T_c$, *or in the discrete analog* $\boldsymbol{u}^n = 0, \quad \forall n > n_c$ *(*n_c *an integer number) then*

$$T_c = \frac{1}{\mu\lambda_o} Log(1 + \frac{\mu\lambda_o \|\boldsymbol{u}_o\|_{\mathbf{L}^2(\boldsymbol{\Omega})}}{\beta\tau_s - C|\boldsymbol{\Omega}|^{1/2}}) \quad if \quad C < \tau_s\beta|\boldsymbol{\Omega}|^{-1/2}, \tag{6.25a}$$

$$\|\boldsymbol{u}(t) - \boldsymbol{u}_\infty\|_{\mathbf{L}^2(\boldsymbol{\Omega})} \leq \|\boldsymbol{u}_o - \boldsymbol{u}_\infty\|_{\mathbf{L}^2(\boldsymbol{\Omega})} exp(-\mu\lambda_o t) \quad if \quad C \geq \tau_s\beta|\boldsymbol{\Omega}|^{-1/2}, \tag{6.25b}$$

$$\beta = \inf_{\boldsymbol{v} in \mathbf{V}} \frac{\int_{\boldsymbol{\Omega}} \|\mathbf{D}(\boldsymbol{v})\|}{\|\boldsymbol{v}\|_{\mathbf{L}^2}}, \boldsymbol{v} \in \mathbf{H}_0^1(\boldsymbol{\Omega}) - \{0\}. \tag{6.25c}$$

where $\boldsymbol{u}_\infty$ *the corresponding steady state solution and* λ_o *is the smallest eigenvalue of* $-\boldsymbol{\Delta} \in \mathbf{H}_0^1(\lambda_o > 0)$.

Proof:

By using the following classical variational inequality:

Find $\{\boldsymbol{u}(t), p(t)\} \in (\mathbf{H}_0^1)^d \times \mathbf{L}^2$ such that a.e on $(0, T)$ we obtain

$$(\frac{\partial \boldsymbol{u}}{\partial t}, \boldsymbol{v} - \boldsymbol{u}) + ((\boldsymbol{u} \cdot \boldsymbol{\nabla})\boldsymbol{u}, \boldsymbol{v} - \boldsymbol{u}) + \mu a(\boldsymbol{u}, \boldsymbol{v} - \boldsymbol{u}) +$$
$$\tau_s(j(\boldsymbol{v}) - j(\boldsymbol{u})) - (p, \boldsymbol{\nabla} \cdot (\boldsymbol{v} - \boldsymbol{u})) \geq (\boldsymbol{f}, \boldsymbol{v} - \boldsymbol{u}), \tag{6.26a}$$

$$\boldsymbol{\nabla} \cdot \boldsymbol{u} = 0, \tag{6.26b}$$

$$\boldsymbol{u}(\boldsymbol{x}, t) = \boldsymbol{u}^o \quad on \quad \partial\boldsymbol{\Omega} \times (0, T), \tag{6.26c}$$

$$\boldsymbol{u}(\boldsymbol{x}, 0) = \boldsymbol{u}_o \quad in \quad \boldsymbol{\Omega}. \tag{6.26d}$$

take $\boldsymbol{v} = 2\boldsymbol{u}$ then we have,

$$\frac{1}{2}\frac{d}{dt}\|\boldsymbol{u}(t)\|_0^2 + \mu\|\boldsymbol{\nabla}\boldsymbol{u}\|_0^2 + \tau_s j(\boldsymbol{u}) = (\boldsymbol{f}, \boldsymbol{u}), \quad and \quad \boldsymbol{u} = \boldsymbol{u}_0. \tag{6.27}$$

One can obtain using the definition of β,

$$\frac{d}{dt}\left\|\boldsymbol{u}\right\|_0 + \mu\lambda_o\left\|\boldsymbol{u}\right\|_0 + \tau_s\beta - C|\boldsymbol{\Omega}|^{1/2} \leq 0, \quad and \quad \left\|\boldsymbol{u}(0)\right\|_0 = \left\|\boldsymbol{u}_o\right\|_0. \tag{6.28}$$

Integrate this equation from 0 to t to obtain the following theoretical upper bound ,

$$T_c = \frac{1}{\mu\lambda_o} Log(1 + \frac{\mu\lambda_o}{\tau_s\beta - C|\boldsymbol{\Omega}|^{1/2}}\left\|\boldsymbol{u}_o\right\|_0), \quad if \quad C < \tau_s\beta|\boldsymbol{\Omega}|^{-1/2}. \tag{6.29}$$

Then $\boldsymbol{u}(t) = 0$ if $t \geq T_c$. The discrete analog for the theoretical upper bound (see [65])

$$n_c = \frac{Log(1 + \frac{\mu\lambda_o}{\tau_s\beta - C|\boldsymbol{\Omega}|^{1/2}}\left\|\boldsymbol{u}_o\right\|_0)}{Log(1 + \Delta t\mu\lambda_o)}, \quad if \quad C < \tau_s\beta|\boldsymbol{\Omega}|^{-1/2}. \quad \square \tag{6.30}$$

.

6.5.1 Non-stationary Bingham Viscoplastic Fluids in Lid Driven Cavity

The simulation is achieved in a square domain which is two dimensional $\boldsymbol{\Omega} = [0,1] \times [0,1]$, with the absence of the external forces $\boldsymbol{f} = 0$. To validate the monolithic time integration scheme to reach the steady values in Bingham fluid, we have chosen two yield stress values $\tau_s = 0.25$ and $\tau_s = 0.5$ to compute the energy norm in the case of unsteady state to reach the stationary value at low Reynolds number which are already previously computed in chapter 3. From Fig.6.4 the energy norm has rapidly reached the steady state value which is quite identical for the six digits for the two cases. When $\tau_s = 0.25$ the energy norm is $E_{norm} = 3.164850E-2$ and when $\tau_s = 0.5$ the energy norm is $E_{norm} = 3.015621E-2$. This confirms that the monolithic time integration approach is perfectly robust and accurate to handle the nonlinear viscoplastic problem. In the following second test, the boundary and initial conditions can

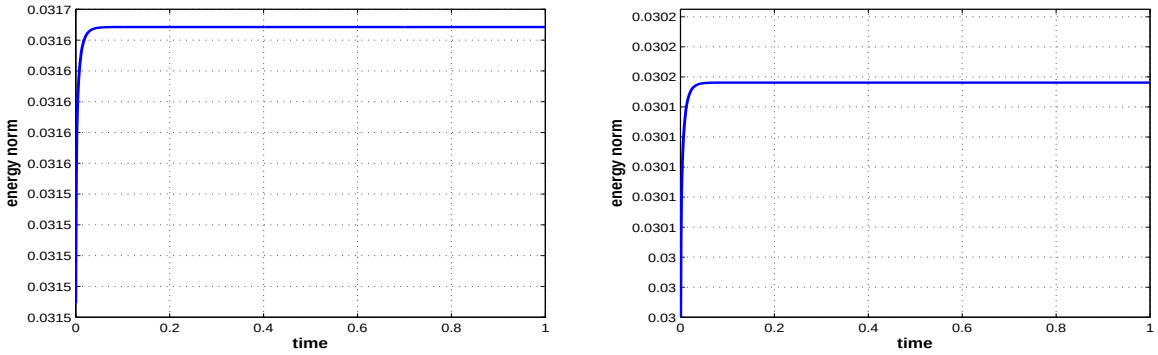

Fig. 6.4. *Bingham flow in driven cavity:* The steady state energy norms for $\tau_s = 0.25$ ($E_{norm} = 3.1648502887E-2$) (left) and for $\tau_s = 0.5$ ($E_{norm} = 3.0156212371E-2$) (right) at h=1/128, $\epsilon = 10^{-3}$ and $\Delta t = 10^{-3}$ for Bingham viscoplastic fluid in driven cavity.

be written as:

$$\boldsymbol{u} = \begin{cases} (1,0) \text{ at} & (t,y) = (0 \leq t \leq 0.5, 1), \\ (0,0) & otherwise. \end{cases} \tag{6.31}$$

the variation of the velocity over the viscoplastic domain is going to zero when the upper lid has been stopped at $t = 0.5^+$ for the viscoplastic fluid (see Fig.6.5). This is quite obvious from the magnitude of the velocity at different instants to show the decaying of the velocity over the domain.
To measure the cessation property in viscoplastic fluids comparing with the Newtonian fluid by drawing

the variation of the kinetic energy with time, we have chosen the stopping instant of the upper lid at $t = 0.0^+$ with the following boundary condition:

$$\boldsymbol{u} = \begin{cases} (1,0) \text{ at } & (t,y) = (0^+,1), \\ (0,0) & otherwise. \end{cases} \tag{6.32}$$

So that, due to the absence of the external forces and the immobility of the boundary, the fluid medium has to return to rest in finite time. From the depicted figures (Fig.6.6, Fig.6.7, Fig.6.8 and Fig.6.9) the decaying of the kinetic energy is going to zero very quickly since the upper wall has been stopped. The difference between the Newtonian and viscoplastic fluid is obvious definitely when the mesh size and regularization parameter approach zero, moreover the value of the stopping time decreases with the increase of the yield stress which confirms the cessation property as a yield stress result.

6.5.2 Standing Vortex

This test is introduced to measure the ability of the monolithic algorithm to detect the cessation property in viscoplastic fluids for the standing vortex problem. The standing vortex is a unit square configuration but it has a core of a solid body rotation. At r=R we switch to a decreasing linear function of r until r=2R, where the tangential velocity(u_t) returns to zero. The velocity field is decomposed to the radial velocity(u_r)and the tangential velocity(u_t) which are zero and linear functions as previously prescribed respectively (see [96, 97]). The initial condition is axisymmetric vortex which represents the exact steady state solution.

$$\boldsymbol{u}_t = \begin{cases} \frac{r}{R}\boldsymbol{u}_o & \text{for} \quad 0 < r < R, \\ (2 - \frac{r}{R})\boldsymbol{u}_o & \text{for} \quad R \leq r \leq 2R, \\ 0 & \text{for} \quad r > 2R, \end{cases} \tag{6.33}$$

where R=0.2, $\boldsymbol{u}_o = 1$, and $r = \sqrt{(x-0.5)^2 + (y-0.5)^2}$ denotes the distance from the center. The aim is to solve the inviscid flow of the Bingham flow and to predict the cessation w.r.t. the yield strength value. The well-known 'Standing Vortex' problem for Bingham model μ is set to null or $Re = \infty$ to drop down the standard diffusive terms.

$$\frac{\partial \boldsymbol{u}}{\partial t} + \boldsymbol{u} \cdot \boldsymbol{\nabla} \boldsymbol{u} + \boldsymbol{\nabla} \cdot (\frac{\tau_s}{\|\mathbf{D}\|}\mathbf{D}) + \boldsymbol{\nabla} p = 0 \quad \text{in} \quad \boldsymbol{\Omega} = [0,1] \times [0,1], \tag{6.34a}$$

$$\boldsymbol{\nabla} \cdot \boldsymbol{u} = 0 \quad \text{in} \quad \boldsymbol{\Omega} = [0,1] \times [0,1]. \tag{6.34b}$$

The numerical results from the depicted figure(Fig.6.10) are predicted with increasing of the yield stress. The figure shows us that the earlier cessation of the viscoplastic fluid is associated with high values of the yield stress.

6.6 Non-Stationary Bingham Viscoplastic Fluids Around A Cylinder

The standard benchmark problem of 2D flow around circular cylinder in a channel is considered. Generally, Two choices are introduced to express the inner boundary of the circle. The first to adapt the mesh with the geometry by prescribing two boundary components, one for the outer channel and the other for the inner circle. The second is a pure channel mesh geometry which does not capture the inner circle by grid points. The first choice is our interest in the calculations. Flow around cylinder is quite sensitive to the dimensionless Reynolds number (Re) which has a significant property to identify the flow regimes from laminar to turbulent(see [232]). However, flow past around circular cylinder is the subject of the mathematical modeling for viscoplastic fluids which investigate the influence of the yield stress on the drag and lift forces and the vortex shedding.

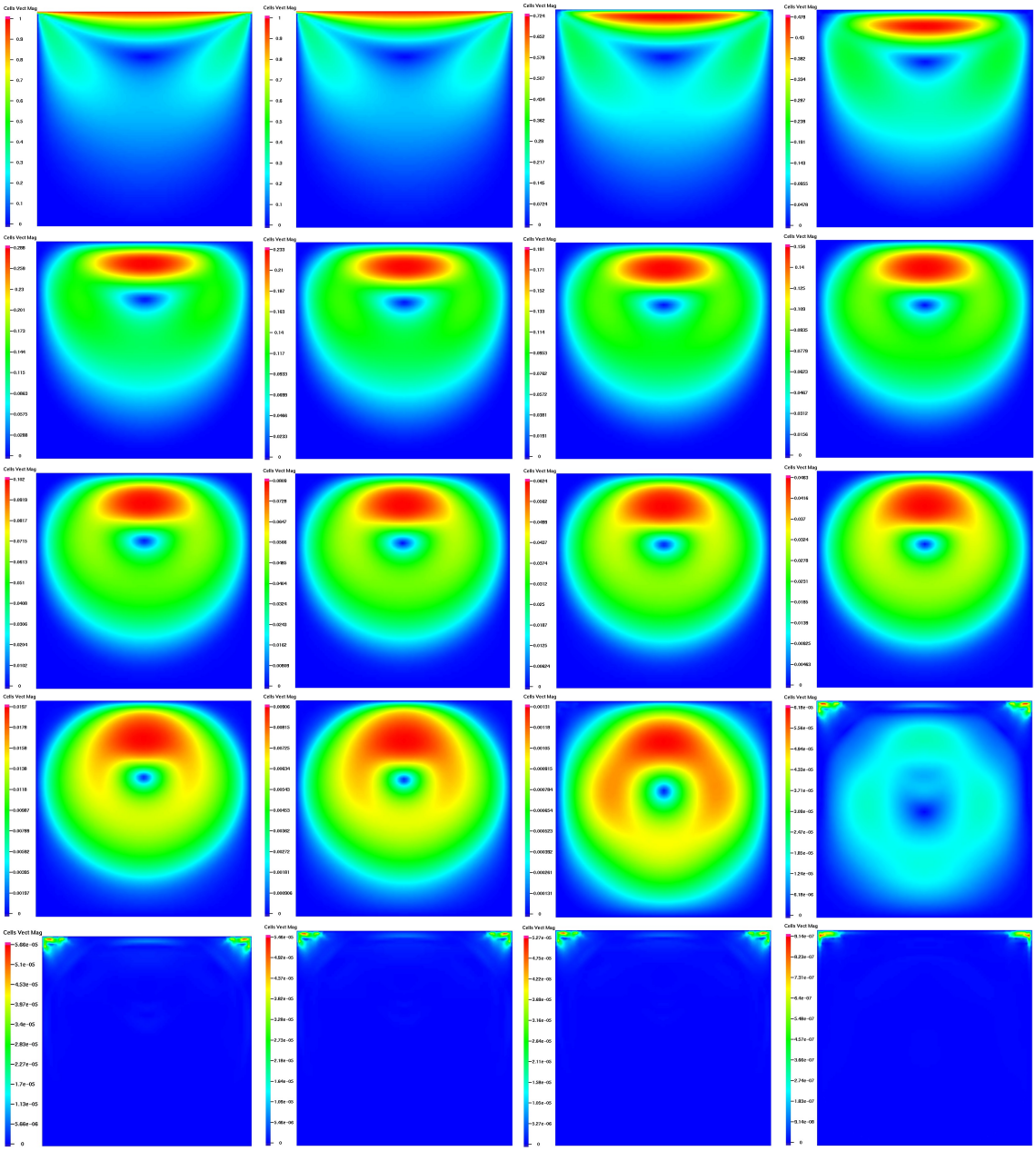

Fig. 6.5. *Bingham flow in driven cavity:* Cessation of time for Bingham viscoplastic fluid in driven cavity when the upper lid stopped at t=0.5 for the instants in the first row (t=0.25 and t=0.499 to 0.501), the second row (t=0.503 to 0.506), the third row (t=0.508 to 0.511), the fourth row (t=0.513 to 0.516) and the fifth row (t=0.518 to 0.520) at $\tau_s = 100$, $\Delta t = 10^{-3}$ and $\epsilon = 10^{-3}$.

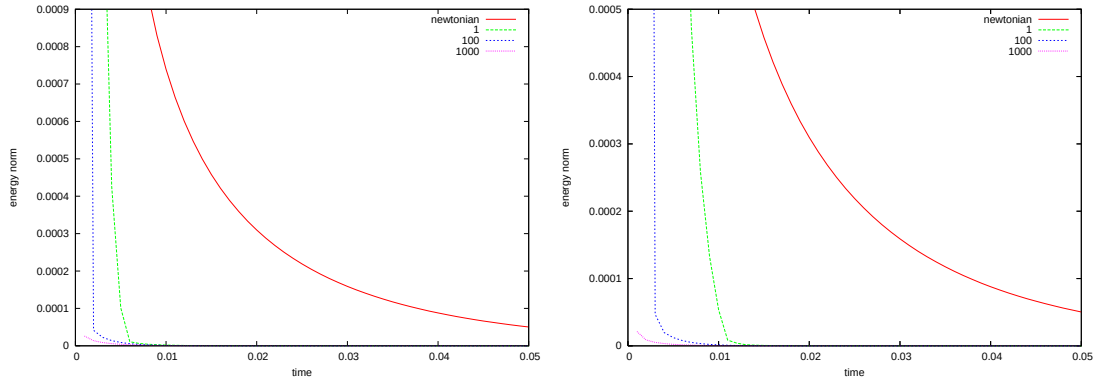

Fig. 6.6. *Flow in driven cavity:*Decaying of the kinetic energy for Newtonian fluid and Bingham viscoplastic fluid at different values of yield stress (1, 100, 1000) after the upper wall of the cavity has been stopped at t=0.0, for the macro time step ($\Delta t = 10^{-3}$), $\epsilon = 10^{-2}$ and the mesh sizes h=1/64(left) and h=1/128(right).

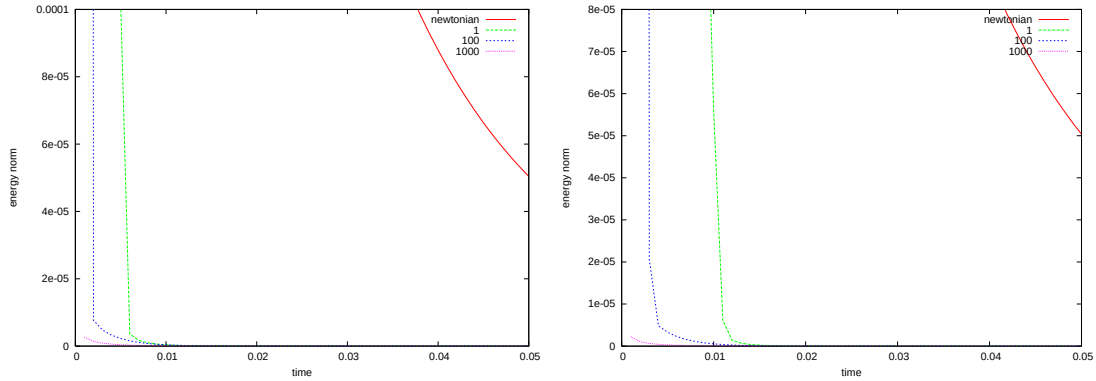

Fig. 6.7. *Flow in driven cavity:* Decaying of the kinetic energy for Newtonian fluid and Bingham viscoplastic fluid at different values of yield stress (1, 100, 1000) after the upper wall of the cavity has been stopped at t=0.0, for the macro time step ($\Delta t = 10^{-3}$), $\epsilon = 10^{-3}$ and the mesh sizes h=1/64(left) and h=1/128(right).

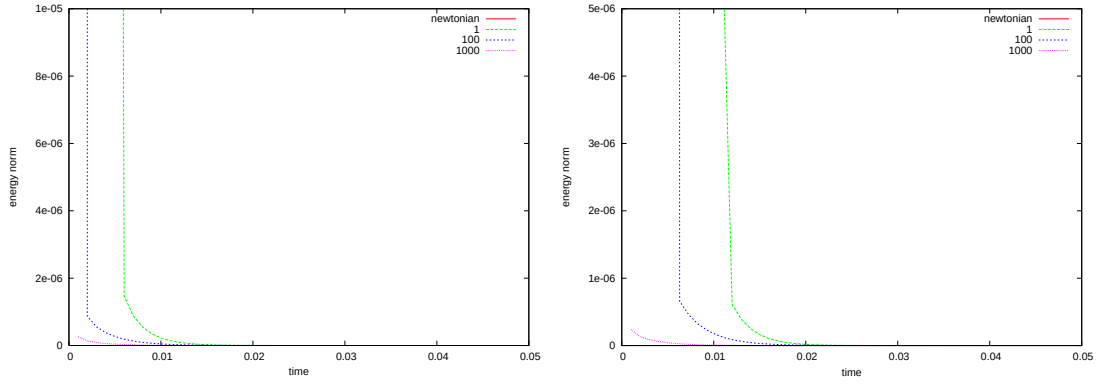

Fig. 6.8. *Flow in driven cavity:* Decaying of the kinetic energy for Newtonian fluid and Bingham viscoplastic fluid at different values of yield stress (1, 100, 1000) after the upper wall of the cavity has been stopped at t=0.0, for the macro time step ($\Delta t = 10^{-3}$), $\epsilon = 10^{-4}$ and the mesh sizes h=1/64 (left) and h=1/128(right).

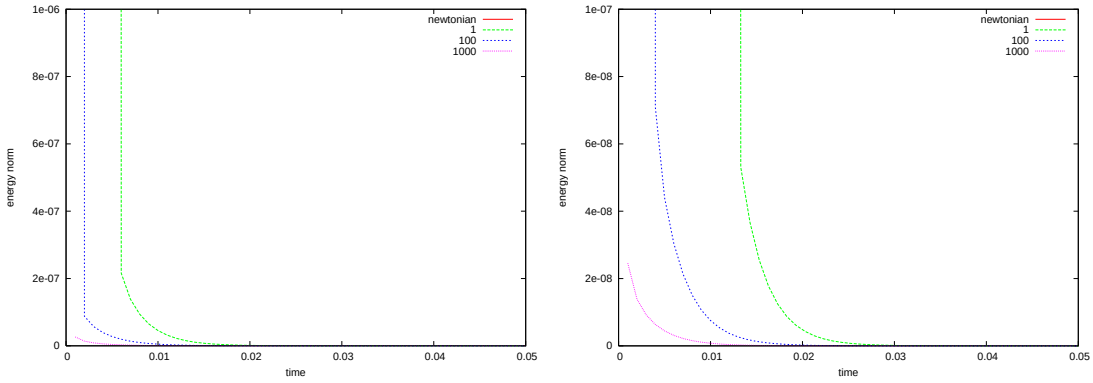

Fig. 6.9. *Flow in driven cavity:* Decaying of the kinetic energy for Newtonian fluid and Bingham viscoplastic fluid at different values of yield stress (1, 100, 1000) after the upper wall of the cavity has been stopped at t=0.0, for the macro time step ($\Delta t = 10^{-3}$), $\epsilon = 10^{-5}$ and the mesh sizes h=1/64(left) and h=1/128(right).

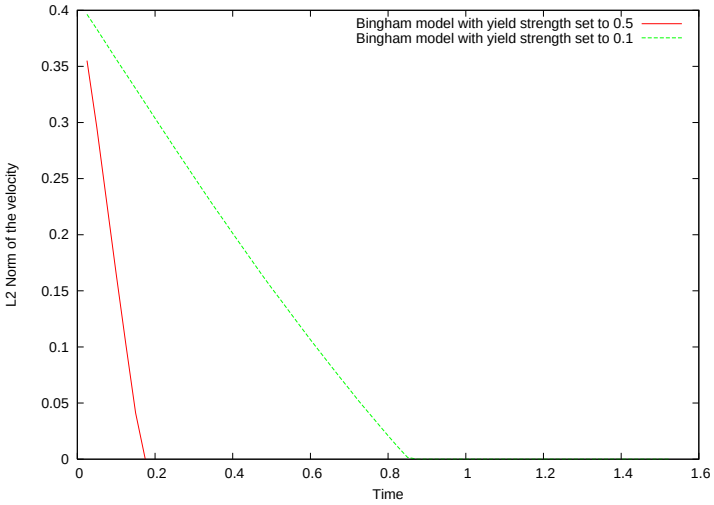

Fig. 6.10. *Standing vortex:* Cessation of Bingham viscoplastic fluid at yield stresses $\tau_s = 0.1, 0.5$ for the standing vortex.

6.6.1 Drag and Lift Forces in Non-Stationary Bingham Viscoplastic Fluids

We perform nonstationary tests to calculate the drag coefficient, lift coefficient and the pressure which mainly aim to examine the steady state case for low Reynolds numbers ≤ 50 and the periodically oscillating flow case for a medium Reynolds number($50 \geq Re \leq 160$) in case of viscoplastic fluids. Firstly, the following test is performed to validate the monolithic approach for Navier-Stokes equation ($\tau_s = 0$) with viscosity $\mu = 10^{-3}$ with maximum velocity 0.3 resulting in Re=20 for the inlet parabolic flow. The results should give the stationary value when the solution reached its steady state. Secondly, with the same viscosity and when the maximum velocity and the Reynolds number are 1.5 and 100 respectively, the results of the periodic oscillatory behavior for drag and lift coefficients as well as the pressure behavior are obtained.

In the depicted figures (Fig.6.11 to Fig.6.15) the lift side from these figures show that the drag coefficient and lift coefficient and the pressure value when Re=20 have been reached the steady state values which are close to the reference value $C_d = 5.579480$ and $C_l = 0.01061796$ for the first four digits in the previous stationary calculations. In addition to the pressure difference which is $\Delta p = 0.1153$ between the

two points (0.15.0.2) and (0.25,0.2), is achieved. The right side from these figures shows us the periodic oscillatory behavior when Re=100 for the same computational parameters. The results from this test

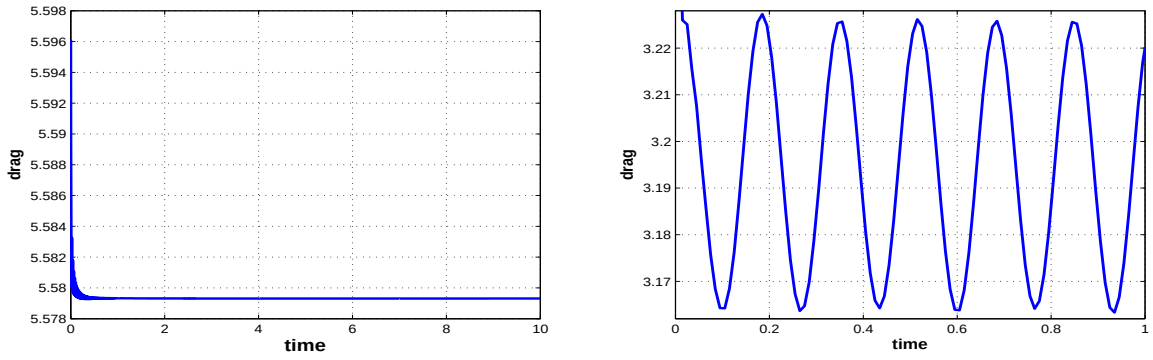

Fig. 6.11. *Newtonian flow around a cylinder:* The steady state reference result for the drag (5.5793133543) at Re=20(left) and periodic oscillatory behavior for drag at Re=100(right) for the Newtonian fluid.

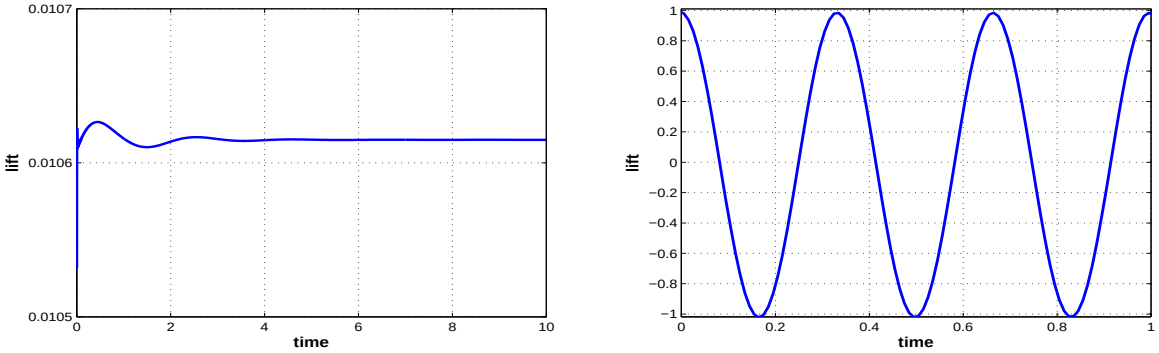

Fig. 6.12. *Newtonian flow around a cylinder:* The steady state reference result for the lift (1.0614958491E-2) at Re=20(left) and periodic oscillatory behavior at Re=100(right) for the Newtonian fluid.

are achieved to confirm the validity of monolithic time integration approach which is proved to be highly robust and accurate as well and quite comparable with the previous results in [216] with the maximum amplitude and the Strouhal number of the drag and lift in case of periodic behavior.
Similarly, we perform a second test to confirm these results to obtain the periodic behavior and to reach the steady state value at $Re = 100$ for the same parameters in case of the viscoplastic fluids for two values of yield stress $\tau_s = 0.01$ and 0.25 respectively. From these Figures (Fig.6.16 to Fig.6.20), the need to recognize the influence of the yield stress value on the parameters to suppress the periodic oscillatory behavior for its higher values is merely required.

6.6.2 Vortex Shedding in Bingham Viscoplastic Fluids

In the Newtonian fluids, the vortex has been observed in the wake region of the flow past cylinder at low Reynolds number between 40 to 250 . For Reynolds numbers that is greater than 250, the laminar periodic wake becomes unstable and the eddies start to become turbulent. Further increase of the Reynolds number

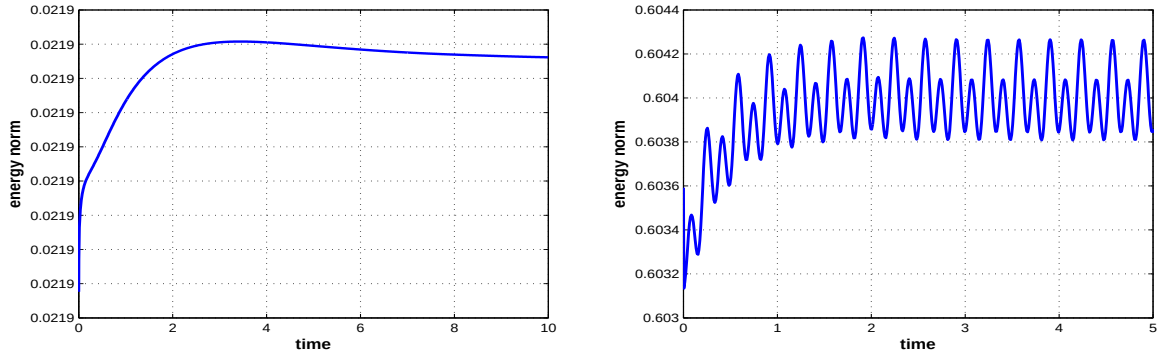

Fig. 6.13. *Newtonian flow around a cylinder:* The steady state reference result for the energy norm at Re=20(left) and periodic oscillatory behavior at Re=100(right) for Newtonian fluid.

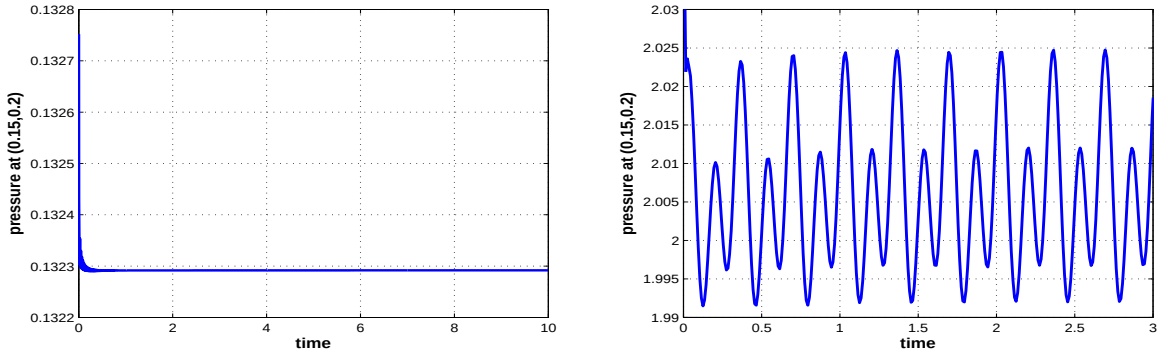

Fig. 6.14. *Newtonian flow around a cylinder:* The steady state reference result for the pressure (1.3229182909E-1) at Re=20(left) and periodic oscillatory behavior at Re=100(right) for the Newtonian fluid at the point (0.15,0.2).

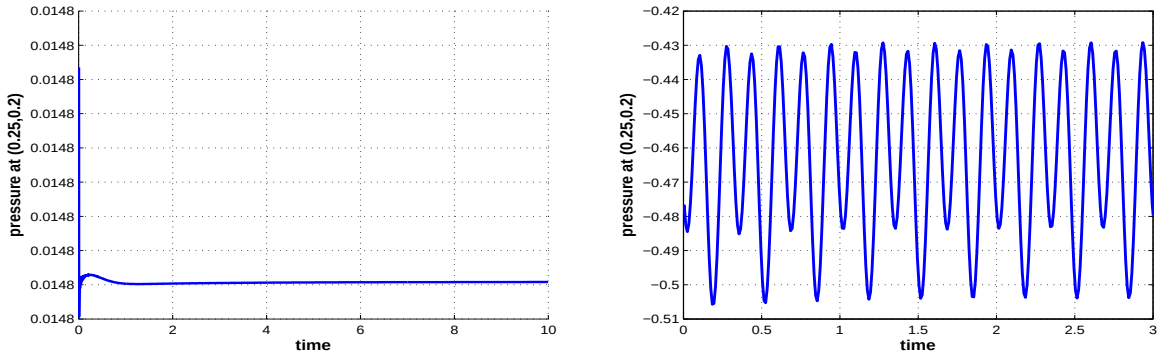

Fig. 6.15. *Newtonian flow around a cylinder:* The steady state reference result for the pressure (1.4760404223E-2) at Re=20(left) and periodic oscillatory behavior at Re=100(right) for the Newtonian fluid at the point (0.25,0.2).

turns the wake region into turbulent flow. Within certain range of Reynolds number ($250 < Re < 10,000$), the frequency at which vortices are shed in the flow around a circular cylinder tends to remain almost constant (see [221]).

In Bingham viscoplastic fluids, there are a few number of FEM based methods reported in the literature (for instance see [183, 64]) especially designed for the simulation of time dependent viscoplastic flows by

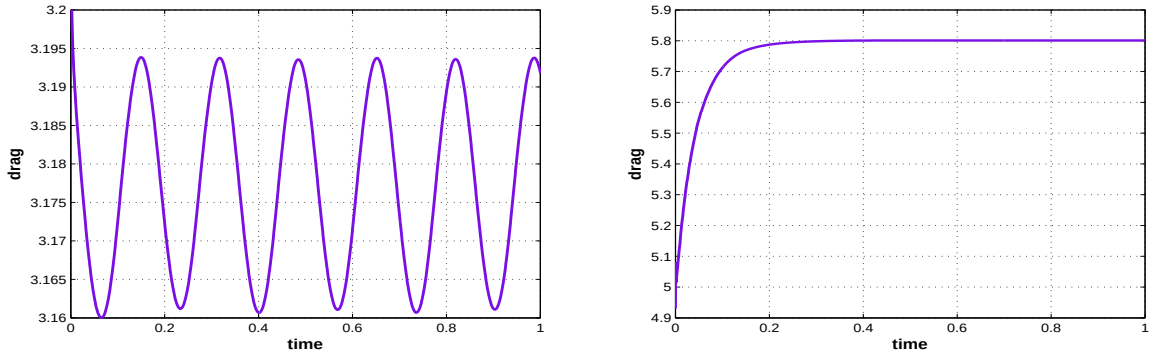

Fig. 6.16. *Bingham flow around a cylinder:* The drag for Bingham viscoplastic flow around cylinder at $\tau_s =$ 0.01(left) and $\tau_s = 0.25$ (5.8007866960)(right) at Re=100 and $\Delta t = 10^{-3}$.

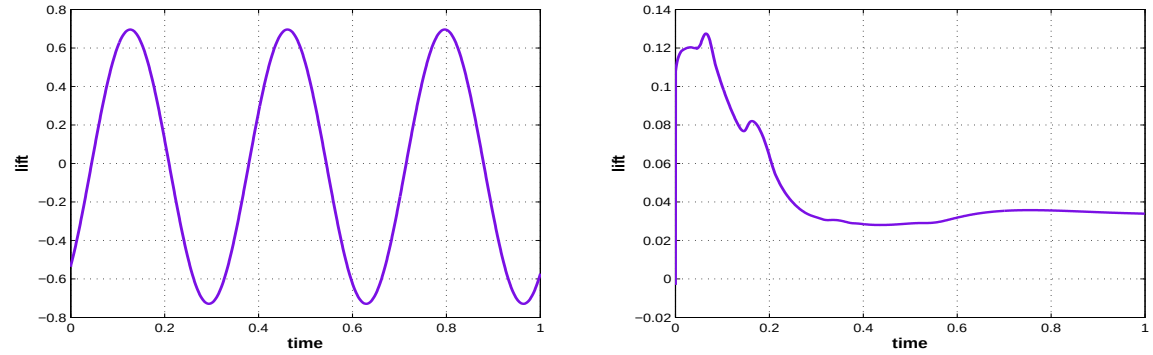

Fig. 6.17. *Bingham flow around a cylinder:* The lift for Bingham viscoplastic flow around cylinder at $\tau_s =$ 0.01(left) and $\tau_s = 0.25$ (3.3916802103E-2)(right) at Re=100 and $\Delta t = 10^{-3}$.

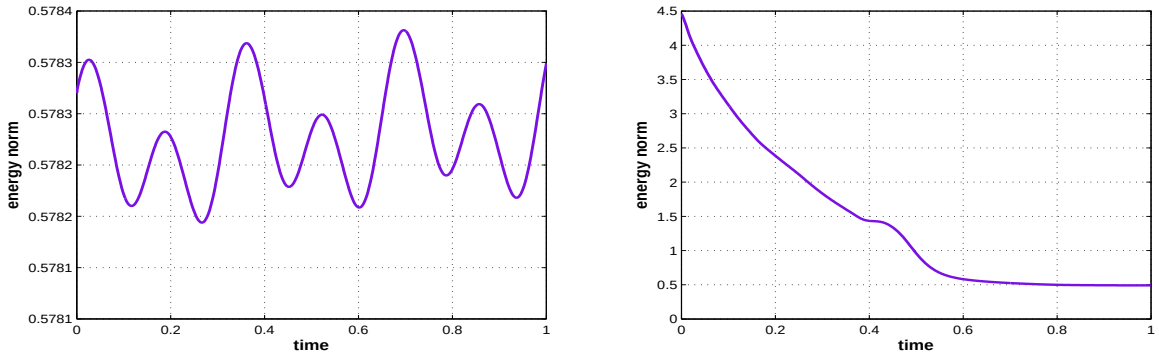

Fig. 6.18. *Bingham flow around a cylinder:* The energy norm for Bingham viscoplastic flow around cylinder at $\tau_s = 0.01$(left) and $\tau_s = 0.25$ (4.9103473922E-1)(right) at Re=100 and $\Delta t = 10^{-3}$.

using the splitting time techniques. In these monographs, they only have applied to obtain the steady state solution in addition to confirm the cessation property.
In this aspect to test the presence of the vortex shedding has not been reported up to our knowledge or at least the based one on experimental observations for viscoplastic problem. Our choice here for this problem is to be as a suitable test case for time dependent monolithic schemes and with the numerical

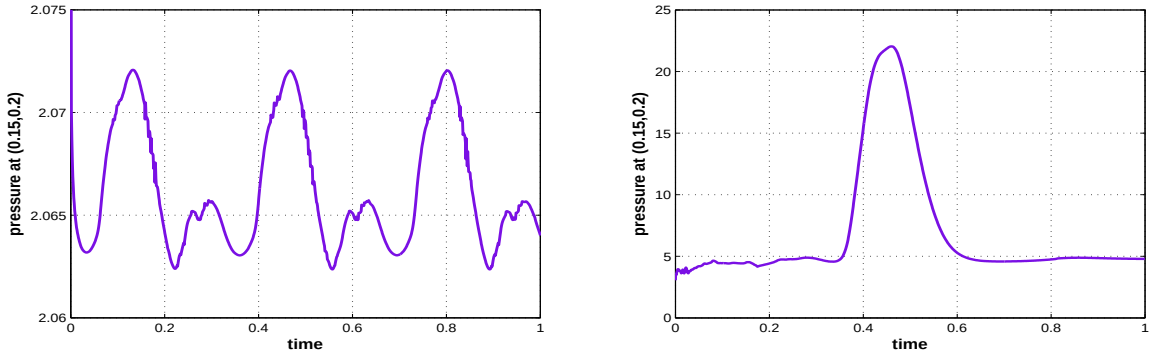

Fig. 6.19. *Bingham flow around a cylinder:* The pressure at (0.15,0.2) for Bingham viscoplastic flow around cylinder at $\tau_s = 0.01$(left) and $\tau_s = 0.25$ (4.7893334547)(right) at Re=100 and $\Delta t = 10^{-3}$.

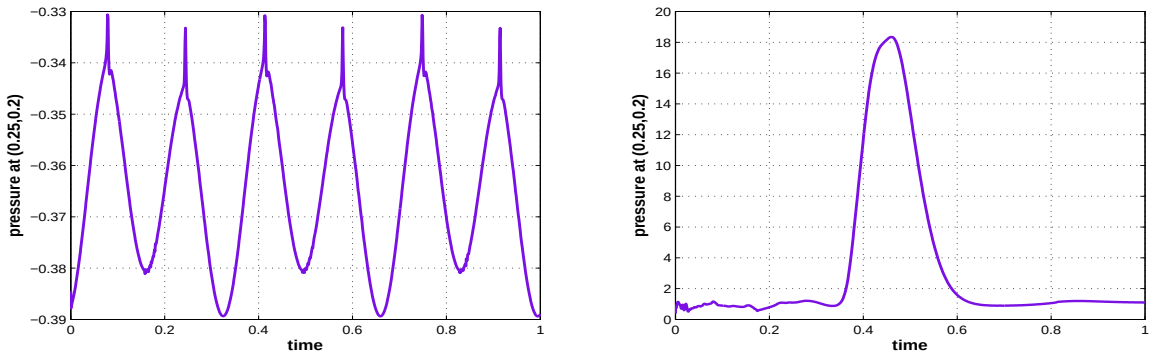

Fig. 6.20. *Bingham flow around a cylinder:* The pressure at (0.25,0.2) for Bingham viscoplastic flow around cylinder at $\tau_s = 0.01$(left) and $\tau_s = 0.25$ (1.1023358301)(right) at Re=100 and $\Delta t = 10^{-3}$.

predictions of this phenomenon with viscoplastic fluids as well as to recognize the influence of the yield stress parameter. As shown from the depicted figures (Fig.6.21 to Fig.6.26), the vortex is pushing up to be vanished with the increase of the yield stress which started to have the values 10^{-3}, 10^{-2}, 0.025, 0.0375, 0.05, 0.1 at Re = 160. This confirm that, the appearance or the absence of the vortex shedding is strongly related to the decreasing or the increasing of the yield stress correspondingly as soon as the Reynolds number is fixed.

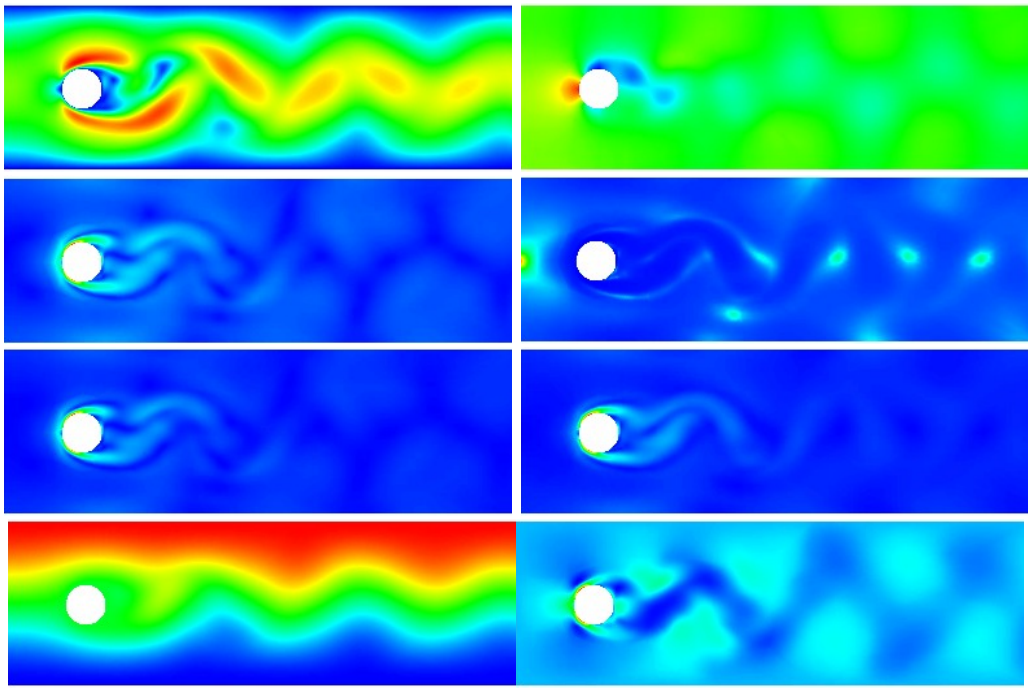

Fig. 6.21. *Shedding vortices*: (up to down) Contours of velocity-pressure, Stress norm-Viscosity, deformation norm-gradient norm and stream function-2^{nd} component of stress at Re=160 and $\tau_s = 10^{-3}$.

6.7 Summary

In this chapter the monolithic time integration approach is used to solve the viscoplastic fluid problem due its numerical stability and the accuracy for both large and small time steps. The resulting discrete nonlinear systems arise from the finite element discretization by using the low or high order FEM with the unmapped approach for the pressure which is solved via continuous Newton-Multigrid process is proved to be robust and efficient within the frame of monolithic approach. From the exposed results for the viscoplastic fluids, the advantages to use this approach are unconditionally stable and more accurate comparing with the splitting techniques. On the other hand, the disadvantages are the difficulty to construct an efficient preconditioner and its cost for the large problems.
This approach is validated in the Newtonian case and the viscoplastic case by calculating the reference value for the cylinder benchmark as well as comparing the stationary values for viscoplastic flow in a lid driven cavity. After validation, the numerical results obtained by using the finite element with the monolithic approach in cavity benchmark and the cylinder benchmark, confirm the cessation phenomenon in viscoplastic fluids and in the standing vortex problem which is theoretically proved. These results give us an insight for the solvers to be efficient and accurate. Moreover, the presented behavior of the flow around a cylinder for high Reynolds number is realistic to expose the shedding vortex for the real simulation. The calculation of drag and lift forces is already confirmed in our computation. The main findings of this chapter are listed below:

(a) The presented algorithm in the frame of monolithic approach using the continuous Newton solver and geometric multigrid method is quite robust and efficient for the viscoplastic problem due to the numerical stability and the accuracy.

(b) The idea to use higher order finite element with the unmapped pressure approach is quite preferable to obtain an accurate results.

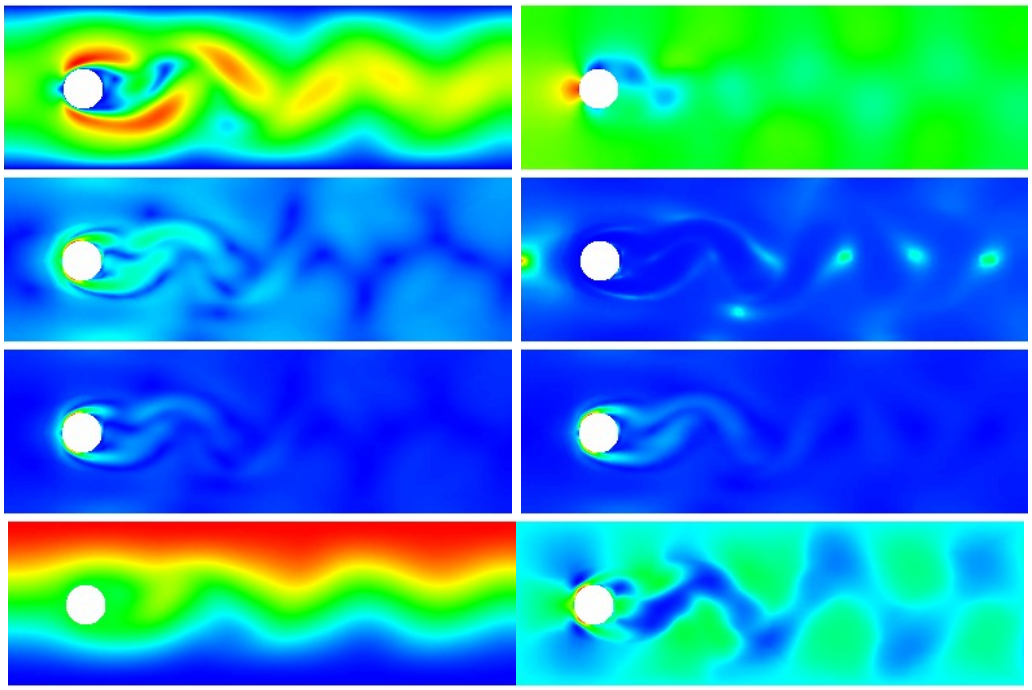

Fig. 6.22. *Shedding vortices*: (up to down) Contours of velocity-pressure, Stress norm-Viscosity, deformation norm-gradient norm and stream function-2^{nd} component of stress at Re=160 and $\tau_s = 10^{-2}$.

(c) Generally, the critical Reynolds numbers are marking the onset and the end of the various flow regimes, such that for viscoplastic flow around cylinder. It is clear that, the viscoplastic fluid obtains the same regimes to reach the steady state and periodic oscillatory motion.

(d) An increase in the yield stress value reduced the time used to cease the viscoplastic fluid.

(e) An increase in the yield stress value which reduced the critical Reynolds number leads to weaken the appearance of the shedding vortices.

(f) In the nonstationary flow, the time step might be used to relax the effect of the regularization parameter or the yield stress in the case of smaller or higher values respectively. So that, the nonstationary might be used to compute the solution in such cases to be close to the real constitutive equation at the low values of Reynolds number to reach the steady state case.

However, finally one can conclude that in the frame of the monolithic approach, the coupling of the finite element method together with the time stepping schemes for inertial viscoplastic fluids is a quite promising tool for the numerical simulation of the nonstationary viscoplastic problems.

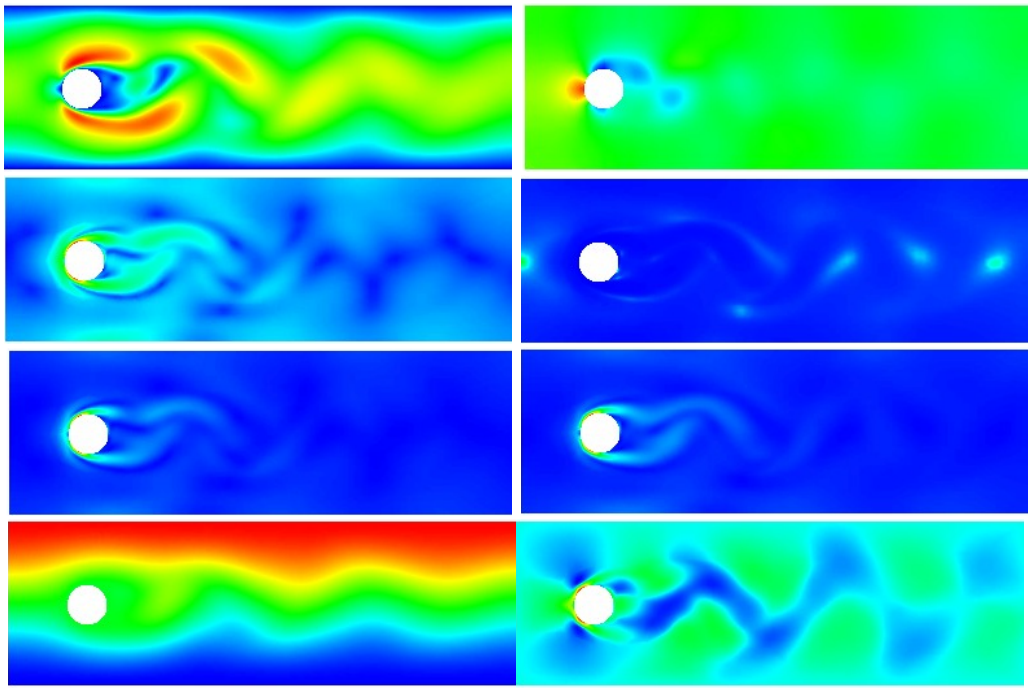

Fig. 6.23. *Shedding vortices*: (up to down) Contours of velocity-pressure, Stress-Viscosity, deformation-gradient and stream function-2^{nd} component of stress at Re=160 and $\tau_s = 0.025$.

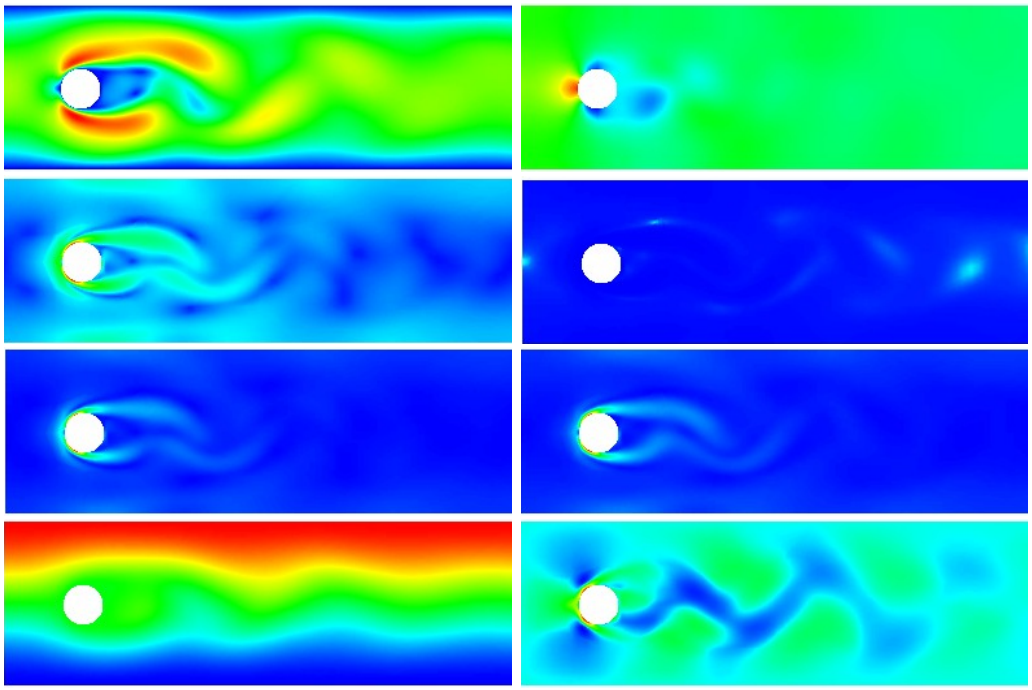

Fig. 6.24. *Shedding vortices*: (up to down) Contours of velocity-pressure, Stress-Viscosity, deformation-gradient and stream function-2^{nd} component of stress at Re=160 and $\tau_s = 0.0375$.

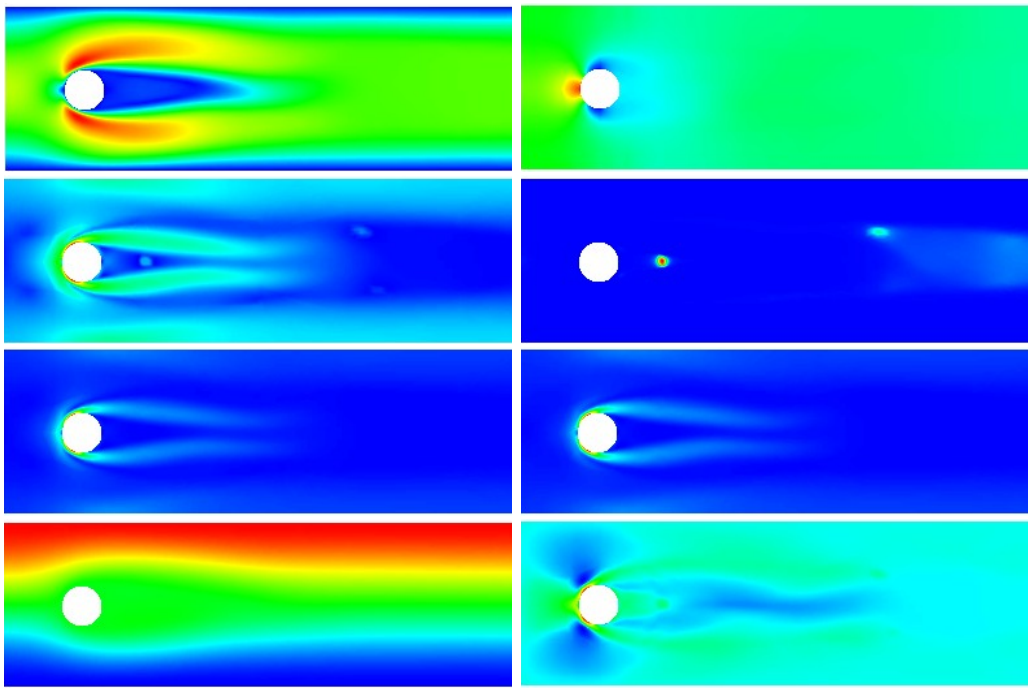

Fig. 6.25. *Shedding vortices*: (up to down) Contours of velocity-pressure, Stress-Viscosity, deformation-gradient and stream function-2^{nd} component of stress at Re=160 and $\tau_s = 0.05$.

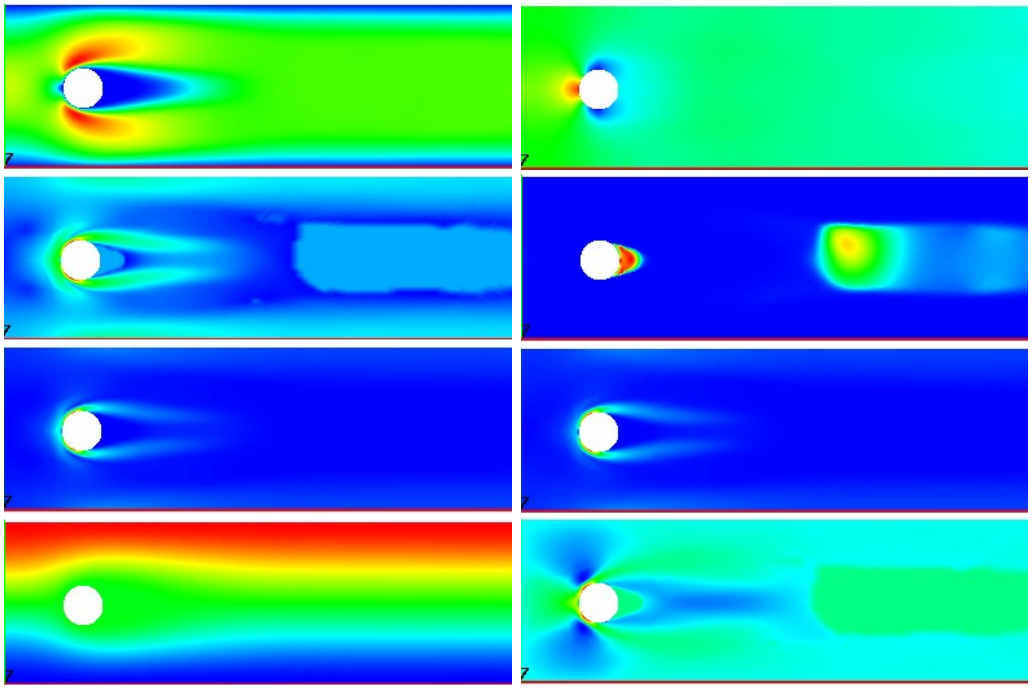

Fig. 6.26. *Shedding vortices*: (up to down) Contours of velocity-pressure, Stress-Viscosity, deformation-gradient and stream function-2^{nd} component of stress at Re=160 and $\tau_s = 0.1$.

7

Conclusion and Future Outlook

This thesis has developed new numerical methods and simulation tools for nonlinear fluids particulary viscoplastic fluids with Bingham type via finite element methods in the frame of a monolithic approach. The main aim is to develop flexible, robust and efficient simulation tools to analyzing the behavior of the solver as well as the predicted behavior of viscoplastic fluids. This methodology is used as an extension to improve the performance of the solver via a monolithic approach for the nonlinear fluid problems having special mathematical difficulties within the viscoplastic fluids. These difficulties reflect a lack in the case of accuracy and cost due to the unbounded functions for the solvers. However, this work presents an insight in the behavior of numerical simulation in the case of its ability to mimic the real behavior of the viscoplastic fluid. In brief, these issues can be summarized in the following items.

7.1 The Aspect of Modeling of Viscoplastic Fluids

Typically, the way of modeling is considered as an important issue for all aspects of the solvers and the simulation. This work begins by introducing the modeling of viscoplastic fluids from the physical law balances (momentum balance and mass balance) in addition to the constitutive equation to have the complete form. This form describes the viscoplastic fluid of Bingham type. This surely produces the strong form to capture the behavior of viscoplastic fluid with Bingham type. However, this form is adapted to have the cast of the variational form to facilitate the mathematical analysis of the problem. In the complementary part, alternative viscosity models are suggested to circumvent the non-differentiability of the apparent viscosity like modified biviscous model and Bercovier-Engelman regularization model. In fact, these regularized models have a severe influence on the accuracy and the prediction for properties of the viscoplastic fluid but from the implementation point of view they are easier to use.
On the other hand, another way is introduced to model the viscoplastic fluid by using the tensor valued function to define the unbounded mathematical part. This formulation leads us to use the double folded saddle point problem and to convert the problem as linear problem with no involved nonlinearity. Similarly, the modeling with the mixed dual weak form is as identical as with the tensor valued function.
The fluids with yield are the global class of viscoplastic fluids which enjoy natural properties. For the researchers, these properties are mandatory to be predicted in the field of numerical simulation. The most phenomenological viscoplastic properties are raised from the constitutive equation like the appearance of the plug and dead regimes in the flow domain, the pressure jump property, and the cessation property. However, these properties can be briefly explained from the following theorems:

Theorem 1. *(viscoplastic fluid regimes): For the fluids with yield, the presence of the flow regimes is mainly associated with the value of the deformation tensor and they can be categorized as follows:*
Shear flow regimes where $\|\mathbf{D}\| \neq 0$.

Plug flow regimes where $\|\mathbf{D}\| = 0$ *and* $\boldsymbol{u} = \boldsymbol{c}$.
Dead flow regimes where $\|\mathbf{D}\| = 0$ *and* $\boldsymbol{u} = \mathbf{0}$.

Theorem 2. *(the pressure jump property): For the fluids with yield, the distribution of the pressure is strongly related to the constitutive equation providing a nonuniform distribution over the flow domain with singularities at the interfacial boundary among the flow regimes. The predicted pressure distribution can be drawn over the whole domain whether there exist a solution for the following extra equation represented by the Pressure-Yield-Force equation over the unyielded regime* $\boldsymbol{\Delta} p = \boldsymbol{\nabla} \cdot (\boldsymbol{\nabla} \cdot \boldsymbol{\tau}_s) + \boldsymbol{\nabla} \cdot \boldsymbol{f}$ ***if*** $\|\mathbf{D}\| = 0$.

Theorem 3. *(the cessation property): For the fluids with yield, the flow ceases after some amount of time which can be theoretically calculated by the following upper bound* $\|\boldsymbol{u}\|_{\mathbf{L}^2} = 0$ *if* $t \geq \frac{1}{\lambda_0 \mu} Log(1 + \frac{\lambda_o \mu}{\beta \tau_s - \|\boldsymbol{f}\|_{\mathbf{L}^2}} \|\boldsymbol{u}_o\|_{\mathbf{L}^2})$ *where* λ_o *is the smallest eigenvalue of* $\boldsymbol{\Delta} \in \mathbf{H}_0^1(\lambda_o > 0)$ *and* $\beta = inf_{\boldsymbol{v} \in \mathbf{V}} \frac{j(\boldsymbol{v})}{\|\boldsymbol{v}\|_{\mathbf{L}^2}}$.

7.2 The Aspect of Discretization

The development of discretization techniques based on different finite elements and associated with different pressure approaches looking for a better accuracy, were handled for the viscoplastic fluid with Bingham type. The mixed finite elements are introduced in the case of low order and high order with rigorous definition on the pressure space being local or global to maintain the optimal order of convergence and highly accurate solution in the aspect of the uniform and perturbed meshes. The lack of Korn's inequality forced us to stabilize the low order finite element with Edge Oriented Stabilization(EOS) in the case of the symmetric part of the deformation tensor to simulate the real behavior of Bingham fluid. Mostly, the need to use the stabilization is optional in case of high order finite element, while for viscoplastic problems it might be used at the small value of regularization parameter. Unfortunately the choice of the value of the free parameter for EOS is not a delicated task which has a big influence on the accuracy of the solution particulary if the value is a bit higher. However, the accuracy aspect has led us to choose the unmapped pressure approach or the global approach in the case of the perturbed mesh. The global approach is preferable for its accuracy as it obtains the optimal convergence. In the case of $\tilde{Q}_1 Q_0$ which is an example for the compressible elements, it does not give the exact solution for the velocity whenever the velocity space does contain the exact solution. This is due to the pressure space which is far from the real space and the weakness of the incompressibility condition. This leads to very poor results for velocity and pressure solutions.

7.3 The Aspect of Newton-Multigrid Process

The coupling of multigrid process in the frame of the Newton process is conceived of the main issue for the core of the work. This work used the discretization technique instead of the Galerkin Discretization technique where the coarse grid matrix is obtained by direct transformation of the fine grid stiffness matrix. This leads us to use UMFPACK as coarse grid solver since the number of unknowns are not high enough (less than 20.000). Comparing with the other techniques either iterative or direct from the exposed numerical results, this coupling has an advantage to be promised in the case of the accuracy and the cost. With increasing the number of unknowns the CPU time for continuous Newton-multigrid process increases linearly which is not the case for direct strategies. However, in viscoplastic fluid problems the behavior of the coupling Newton-Multigrid process is quite sensitive to the viscoplastic parameters i.e. both regularization and yield stress parameters. At the lower value of the former with the higher values of the later, the behavior of Newton-multigrid and fixed point-multigrid is quite identical which might

be a reason to increase the cost, since in this case the Newton process does not converge quadratically. For the time dependent problem, the time step might be used somehow as a relaxation parameter to reduce the influence of to these parameters in the solver. The advantage to use the continuous Newton solver is to switch easily to the fixed point which is used as starting solution reaching a given tolerance to obtain the full Newton process and moreover, to avoid choosing the step-length of the difference method appropriately.

7.4 The Monolithic Approach

Generally, two main approaches are used to solve the viscoplastic problem, the segregated approach and the monolithic approach within Newton-multigrid process for the stationary and the nonstationary equations. The former decouples the velocity and the pressure to solve the flow equations in a segregated way. The later couples the calculation of the velocity and the pressure to solve the flow equations simultaneously. This work has developed the later within continuous Newton-multigrid methods. By using this approach, the complete nonlinear algebraic equations arising from the coupled discretization of the balance equations with the involved constitutive equations are solved as a whole. The difference between the two approaches might be involved in the cost, accuracy and the stability. It is widely believed that the monolithic solvers are too computationally expensive and it is difficult to design an efficient global preconditioner to maintain the state of the art of the scheme as well as the software modularity is not as the same extent of the segregated approach.
From the other points of view the monolithic approach is generally regarded to be more accurate and robust. The results produced in both stationary and nonstationary cases are quite reliable to describe the behavior of the viscoplastic fluids totally. In the stationary case, it is confirmed that the pressure is not uniform over the flow domain and has a strong dependence on the constitutive equation which is involved in the yield stress parameter. On the other hand the stability of the scheme to calculate at very small value for the regularization parameter is close to the real behavior of the viscoplastic fluid. Consequently, the flow regimes are confirmed in the standard benchmarks within the viscoplastic flow in a lid driven cavity and flow around cylinder. In the nonstationary cases the monolithic time approach allows us to calculate the theoretical upper bound numerically and to confirm the difference between the Newtonian fluids and the viscoplastic fluids in the time cessation as well. The behavior of the flow around a cylinder which is confirmed by the standard drag and lift in the Newtonian case has allowed us to calculate the same in the viscoplastic case. The influence of the yield stress which is quite significant to vanish the oscillatory periodic motion for drag and lift and the decaying of the vortex shedding is proved for the bigger values.

7.5 Future Outlook

The design of numerical algorithms to cope with the three dimensional realistic environmental problems is the most promising work in the field of fast iterative solvers. This work presents an insight to the numerical future to be an elegant alternative rather than experimental work. In the three dimensional cases, the computational complexity increases with the complicated constitutive models in the field of industrial fluids. The enhancement of these algorithms which are associated with viscoelastic and viscoplastic models in industrial fluid problems will be the first interest coupled with parallel scientific computing. These models typically require robust, efficient and flexible numerical schemes to cope with the finite element approach and the fast solvers within Newton and multigrid processes.

References

[1] Adachi, K. and Yoshioka, N. On creeping flow of a viscoplastic fluid past a circular cylinder. *Chem.Eng.Sci*, 28:215–226, 1973.

[2] Allouche, M., Frigaard, I.A and Sona, G. Static wall layers in the displacement of two viscous plastic fluids in a plane channel. *J.Fluid Mech.*, 424:243–277, 2000.

[3] Amadei, B. and Savage, W.Z. An analytical solution for transient flow of Bingham viscoplastic materials in rock fractures. *Int. J. of Rock Mech. & Mining Sci.*, 38:285–296, 2001.

[4] Amat, S., Buquier, S. and Candela, V. Third-order iterative methods without using any Frechet derivative. *J. Comp. and Appl. Math.*, 158:11–18, 2003.

[5] Andres, U.T. Equilibrium and motion of spheres in a viscoplastic liquid. *Sov. Phys.Dokl.(U.S.A.)*, 5:723, 1961.

[6] Ansely, R.W. and Smith, T.N. Motion of spherical particles in a Bingham plastics. *AIChE J.*, 13:1193, 1967.

[7] Aposporidis, A., Haber, E., Olshanskii, M. and Veneziani, A. A mixed formulation of the Bingham fluid flow problem: Analysis and numerical solution. *Comput. Methods Appl. Mech. Engrg*, 200:2434–2446, 2011.

[8] Arnold, D.N., Boffi, D. and Falk, R.S. Approximation by quadrilateral finite elements. *Math.Comp.*, 71(239):909–922, 2002.

[9] Atapattu, D.D. and Uhlherr, P.H.T. Creeping motion of spheres in viscoplastic fluids. *Proc.Xth Int. Cong Rheol.Sydeny*, 1:350, 1988.

[10] Atapattu, D.D., Chhabra, R.P. and Uhlherr, P.H.T. Wall effect for spheres falling at small Reynolds number in a viscoplastic medium. *J. Non-Newt. Fluid Mech.*, 38:31, 1990.

[11] Azouz, I., Shirazi, S.A., Pilehvari, A. and Azar, J.J. Numerical simulation of laminar flows of yield power law fluids in conduits of aribraray cross-section. *J.Fluids Eng.*, 115:710–716, 1993.

[12] Bao, W. and Barret, J.W. A priori and a posteriori error bounds for a nonconforming linear finite element approximation of a Non-Newtonian flow. *RAIRO Modelisation Math. Anal. Numer.*, 32:843–858, 1998.

[13] Baranger, J., Najib, K. and Sandri, D. Numerical analysis of a three-field model for a quasi Non-Newtonian flow. *Comput. Methods Appl. Mech. Engrg*, 109:281 – 292, 1993.

[14] Barnes, H.A., Hutton, J.F. and Walters, K. *An introduction to Rheology.* Elsevier, New York, 1989.

[15] Beaulne, M. and Mitsoulis, E. Creeping flow of a sphere in tubes filled with Herschel-Bulkely fluids. *J. Non-Newtonian Fluid Mech.*, 72:55–71, 1997.

[16] Bellout, H., Bloom, F. and Necas, J. Young measure-valued solutions for Non-Newtonian incompressible fluids. *Commun. P.D.E.*, 19:1763–1803, 1994.

[17] Bercovier, M. and Engelman, M. A finite element method for the numerical solution of viscous incompressible flows. *J. Comp. Phys.*, 30:181–201, 1979.

[18] Bercovier, M. and Engelman, M. A finite element method for incompressible Non-Newtonian flows. *J. Comp. Phys.*, 36:313–326, 1980.

[19] Beris, A.N., Tsamopoulos, J., Armstrong, R.C. and Brown, R.A. Creeping motion of a sphere through a Bingham plastic. *J. Fluid Mech.*, 158:219, 1985.

[20] Beverly C.R. and Tanner R.I. Numerical analysis of extrudate swell in viscoelastic material with yield stress. *J.Reol.*, 33:989–1009, 1989.

[21] Bingham, F.C. Fluidity and Plasticity. *New York*, 1922.

[22] Bird, R.B., Armstrong, R.C. and Hassager, O. *Dynamics of polymeric liquids*. Wiley, New York, 1977.

[23] Bird, R.B., Stewart, W.E. and Lightfoot, E.N. *Transport phenonmena*. Wily, New York, 1960.

[24] Blackery, J. and Mitsoulis, E. Creeping motion of a sphere in tubes filled with a Bingham plastic material. *J. Non-Newt. Fluid. Mech.*, 70:59, 1997.

[25] Boffi, D. and Gastaldi, L. On the quadrilateral Q2-P1 element for the Stokes problem. *Int.J.Numer.Meth.Fluids*, 39:1001–1011, 2002.

[26] Boffi, D., Brezzi, F. and Fortin, M. Finite elements for the Stokes problem. *Notes*.

[27] Bostan, M. and Hild, P. Starting flow analysis for Bingham fluids. *Nonlinear analysis*, 64:1119–1139, 2005.

[28] Braack, M. and Richter, T. Solutions of 3D Navier-Stokes benchmark problems with adaptive finite elements. *Computers & Fluids*, 35:372–392, 2006.

[29] Braess, D. Finite element: Theory, fast solvers, and applications in solid mechanics. *Cambridge University Press, Cambridge*, 1997.

[30] Braess, D. and Sarazin, R. An efficient smoother for the Stokes problem. *Appl. Numer. Math.*, 23(1):3–19, 1997.

[31] Brenner, S.C. Korn's inequalities for piecewise H^1 vector fields. *Mathematics of Computations*, 73:1067–1087, 2003.

[32] Brenner, S.C. and Scott, L.R. The mathematical theory of the finite element methods. *second edition, Springer*, 2002.

[33] Brenner, S.C. and Sung, L. Multigrid algorithms for C^0 interior penalty methods. *Industrial Mathematics Institute, Dep. of Math., Uni. of S.Carolina*, IMI Preprint series:1–31, 2004.

[34] Brezzi, F. and Fortin, M. Mixed and hybrid finite element methods. *Springer-Verlag New York*, 1991.

[35] Brooks, AN. and Hughes, TJR. Streamline upwind/Pertov-Galerkin formulations for convection dominated flows with particular emphasis on the incompressible Navier-Stokes equations. *Comp. Meth. Appl. Mech. Eng.*, 32:199–259, 1982.

[36] Burgos, G.R. and Alexandrou, A.N. On the deterimination of yield surfaces in Herschel-Bulkley fluids. *J.Rheol*, 43(3):463–483, 1999.

[37] Burman, E. A unified analysis for conforming and nonconforming stabilized finite element methods using interior penalty. *SIAM J. Num.*, 2004.

[38] Burman, E. and Hansbo, P. A stabilized non-conforming finite element method for incompressible flow. *Comput. Methods. Appl. Mech. Engrg.*, 195:2881–2899, 2003.

[39] Burman, E. and Hansbo, P. Edge stabilization for Galerkin approximation of convection-diffusion-reaction problems. *Comp. Meth. Mech. Eng.*, 193:1437–1453, 2004.

[40] Burman, E., Fernandez, M. and Hansbo, P. . Edge stabilization: An interior penalty method for the incompressible Navier-Stokes equations. *ECCOMAS4*, volume(I), 2004.

[41] Byron-Bird, R., Dai, G.C. and Yarusso, B.J. The Rheology and flow of viscoplastic materials. *Rev. Chem. Eng.*, 1(1):2–70, 1983.

[42] Carey, G.F. and Krishnan, R. Convergence of the iterative methods in penalty finite element approaximation of the Navier-Stokes equations. *Comp. Meth. Appl. Mech. Eng.*, 60:1–29, 1987.

[43] Carter, R.E. and Warren, R.C. Extrusion stress, die swell and viscous heating effects in double-base propellants. *J.Rheol.*, 31:151–173, 1987.

[44] Chatzimina, C., Georiou, G.C., Mitsoulis, E. and Huilgol, R.R. Finite stopping times in Couette and Poiseuille flows of viscoplastic fluids. *Proceedings of the XIVth Int. Cong. Rheol.,Seoul, Korea*, pp.NFF22-1-NF22-4, 2004.

[45] Chatzimina, M., Georgiou, G.C., Argyropaidas, I., Mitsoulis, E. and Huilgol, R.R. Cessation of Coutte and Poiseuille flows of a Bingham plastic and finite stopping times. *J. Non-Newtonian Fluid Mech.*, 129:117–127, 2005.

[46] Chatzimina, M., Xenophontos, C., Georgiou, G.C., Argyropaidas, I. and Mitsoulis, E. Cessation of annular Poiseuille flows of Bingham plastics. *J. Non-Newtonian Fluid Mech*, 142:135–142, 2007.

[47] Chhabara, R.P. *Bubbles, drops and particles in Non-Newtioan fluids.* CRC press, Boca Raton, FL, 1993.

[48] Chhabra, R.P. and Richardson, J.F. *Non-Newtonian flow in the process industries: fundemental and engineering applications.* Butterworth Heinemann Oxford, 1999.

[49] Ciarlet, P.G. The finite element method for elliptic problems. *North-Holland, Amsterdam*, MR 58:25001, 1978.

[50] Ciarlet, P.G., and Raviart, P.A. Interpolation theory over curved elements with applications to finite element methods. *Comput. Methods Appl. Mech. Eng.*, 1:217–249 MR 51:11191, 1972.

[51] Cliffe, K.A. and Lever, D.A. . A comparison of finite element methods for solving flow past a sphere. *J. comp. physics*, 62:321–330, 1986.

[52] Clift, R., Grace, J. and Weber, M.E. *Bubbles, drops and particles.* Academic Press, New York, 1987.

[53] Comparini, E. A one dimensinal Bingham flow. *J.Math.analy. and Applications*, 169:127–139, 1992.

[54] Covey, G.H. and Stanmore, B.R. Use of parallel plate plastometer for the characterization of viscous fluids with a yield stress. *J.Non-Newtonian Fluid Mech.*, 8:249–260, 1981.

[55] Cristescu, N. Plastic flow through conical converging dies using a viscoplastic constitutive equations. *Int. J. Mech. Sciences*, 17:425–458, 1975.

[56] Cristescu, N. Drawing through canonical dies-An analysis compared with experiments. *Int. J. Mech. Sciences*, 18(1):45–54, 1976.

[57] Cristescu, N. Speed influence in wire drawing. *Revue Roumaine de Sciences techniques- Mecanique Appliquee*, 22(3):391–400, 1977.

[58] Cristescu, N. On the optimum die angle in fast wire drawing. *Journal of Mechanics and Drawings Technology*, 3(3-4):275–287, 1980.

[59] Crouzeix, M. and Raviart, P.A. Conforming and Non-conforming finite element methods for solving the stationary Stokes equations. *RAIRO, Math.Model.Numer.Anal.*, 3:33–75, 1974.

[60] H. Damanik, J. Hron, A. Ouazzi, and S. Turek. Monolithic Newton–multigrid solution techniques for incompressible nonlinear flow models. *Fakultät für Mathematik, TU Dortmund*, 2011. Ergebnisberichte des Instituts für Angewandte Mathematik, Nummer 426.

[61] Damanik, H., Hron, J., Ouassi, A. and Turek, S. A monolithic FEM Approach for non-isothermal incompressible viscous flows. *J. Comp. Physics*, 228:3869–3881, 2009.

[62] De Besses, B.D., Magnin, A. and Jay, P. Viscoplastic flow around a cylinder in an infinite medium. *J. Non-Newtonian Fluid Mech.*, 115:27–49, 2003.

[63] De Los Reyes, J.C. and Gonzalez, S. Path following methods for steady laminar Bingham flow in cylinderical pipes. *Math. Modelling and Num. Analysis*, 43:81–117, 2009.

[64] Dean, E.J. and Glowinski, R. Operator splitting methods for the simulation of Bingham viscoplastic flow. *Chin. Ann. of Math.*, 2:187–204, 2002.

[65] Dean, E.J., Glowinski, R. and Guidoboni, G. On the numerical simulation of Bingham viscoplastic flow: Old and new results. *J. Non-New. Fluid Mech.*, 142:36–62, 2007.

[66] Diening, L. Theoritical and numerical results for electrorheological fluids. *PhD thesis*, 2002.

[67] Diening, L., Ruzicka, M. and Wolf, J. Existence of weak solutions for unsteady motions of generalized Newtonian fluids. *Uni. Freiburg, Math. Inst. Preprint 08-02*, 2008.

[68] Douglas, J. and Dupont, J.T. Interior penalty procedures for elliptic and parabolic Galerkin methods in: Computing methods in applied sciences. *Second Int. Sym. Versailles 1975*, 58, Springer, Berlin, 1976 Lec. Note in Phys.

[69] Duvaut, G. and Lions, J.L. *Inequalities in Mechanics and Physics.* springer-Verlag Berlin, 1976.

[70] EA de Souza Neto, D Peric and DRJ Owen. *Computational methods for plasticity: theory and application*. Wiley.

[71] Elborhamy, M. and Turek, S. Distribution of pressure for fluid with yield. *Technical Report, Faculty of Mathematics(LSIII), TU Dortmund*, pages 1–13, 2010.

[72] Engelman, M.S., Sani, R.L., Gresh, P.M. and Bercovier, M. Consistent vs. reduced integeration penalty methods for incompressible media using several old and new elements. *Int. J. Numer. Methods in Fluids*, 2:25–42, 1982.

[73] Foias, C., Manley, O., Rosa, R. and Temam, R. *Navier-Stokes equations and turblence* . Cambridge Uni. Press, 2004.

[74] Fornberg, B. A numerical study of steady viscous flow past a circular cylinder. *J. Fluid Mech.*, 98(4):819–855, 1980.

[75] Fortin, A., Fortin, M. and Gervais, J.J. A numerical simulation of the transition to turblence in a two dimensinal flow. *J. comp. physics*, 70:295–310, 1987.

[76] Fortin, M. *Calcul Numerique des ecoulements des fluides Newtonian incompressibles par la methode des elements finis,These d'Etat*. Universite Pierre et Marie Curie, Paris, France, 1972.

[77] Fortin, M. An analysis of the convergence of mixed finite element methods. *R.A.I.R.O. Anal. Numer.*, 11:341–354, 1977.

[78] Fortin, M. Old and new finite elements for incompressible flows. *Int.J.Num.Meth. in Fluids*, 1:347–364, 1981.

[79] Fortin, M. and Fortin, A. Experements with several elements for viscous incompressible flows. *Int.J.Numer.Meth.Fluids*, 5:911–928, 1985.

[80] Fortin, M. and Glowinski, R. Methodes de lagrangien augmente. Application a la resolution numerique de problemes aux limites. *Dunod-Bordas. Paris*, 1982.

[81] Freguson, J. and Kemblowski, Z. *Applied Fluid Rheology*. Elsevier, New York, 1991.

[82] Frehse, J., Malek, J. and Steinhauer, M. An existence result for fluids with shear dependent viscosity-steady flow. *Nonl. Analy., Theory Meth. Appl.*, 30:3041–3049, 1997.

[83] Frehse, J., Malek, J. and Steinhauer, M. An existence result for fluids with shear dependent viscosity-unsteady flow. *Partial Differential Equations, Chapman and Hall*, pages 121–129, 2000.

[84] Frigaard, I.A. and Nouar, C. On the usage of viscosity regularization methods for viscoplastic fluid flow computation. *J.of Non-Newtonian. Fluid Mech.*, 127:1–26, 2005.

[85] Frigaard, I.A. and Nouar, C. On the usage of viscosity regularization methods for viscoplastic fluid flow computation. *J.of Non-Newtonian. Fluid Mech.*, 127:1–26, 2005.

[86] Fuchs, M. and Seregin, G. Some remarks on Non-Newtonian fluids inculding nonconvex perturbations of the Bingham and Powell-Eyring models for viscoplastic fluids. *Math. Models Meth. Appl. Sci.*, 7:405–433, 1997.

[87] Fuchs, M. and Seregin, G. *Variational methods for problems from plasticity theory and for generalized Newtonian fluids*. Springer-Verlag, Berlin, 2000.

[88] Gatica, G.N. An application of Babuska-Brezzi theory to a class of variational problems. *Appl.Anal.*, 75:297–303, 2000.

[89] Gatica, G.N. Solvability and Galerkin approximations of a class of nonlinear operator equations. *Z. Anal. Anwendungen*, 21(3):761–781, 2002.

[90] Gatica, G.N., Golzlez, M. and Meddahi, S. A low-order mixed finite element method for a class of quasi-Newtonian Stokes flow. I. A priori error analysis. *Comput. Methods Appl. Mech. Engrg*, 193:881–892, 2004.

[91] Girault, V. and Raviart, P.A. Finite elements methods for Navier-Stokes equations, theory and algorithms. *Springer-Veralg, Berlin*, 1986.

[92] Glowinski, R. *Numerical methods for nonlinear variational problems*. Springer, New York, 1984.

[93] Glowinski, R. *Finite element method for incompressible viscous flow. In P.G Ciarlet and J.L. Lions, editors, Handbook of Numerical Analysis*. Volume IX, North-Holland, Amesterdam, 2003.

[94] Glowinski, R. and Periaux, J. Numerical methods for nonlinear problems in fluids dynamics. *Proc.Inter. Seminar on Scientific Supercomputers, Paris, Feb. 2-6 North-Holland*, 1987.

[95] Glowinski, R., Lion, J.L. and Tremolieres, R. *Numerical analysis of variational inequalities*. North-Holland, Amesterdam, 1981.

[96] Gresho, P.M. On the theory of semi-implicit projection methods for viscous incompressible flow and its implementation via finite element method that also introduces a nearly consistent mass matrix. part1: Theory. *Int. J. for Numer. Meth. in Fluids*, 11:587–620, 1990.

[97] Gresho, P.M. On the theory of semi-implicit projection methods for viscous incompressible flow and its implementation via finite element method that also introduces a nearly consistent mass matrix. part2: Implementation. *Int. J. for Numer. Meth. in Fluids*, 11:621–659, 1990.

[98] Guo, B. and Zhu, P. Partial regularity of suitable weak solutions to the system of the incompressible Non-Newtonian fluids. *J. Diff. Eq.*, 178:281–292, 2002.

[99] Han, W. Quantitative error estimate in modeling the laminar stationary flow of a Bingham fluid. *App. Math. and Comp.*, 47:15–24, 1992.

[100] Han, W. and Reddy, B.D. *Plasticity: mathematical theory and numerical analysis*. Springer, 1999. Vol. 9.

[101] Hansbo, P. and Larson, M.G. A simple nonconforming bilinear element for the elasticity problem. *Chalmers Finite Element Center, Chalmers Uni. Tech.*, 2001.

[102] Heywood, J.G. The Navier-Stokes equations: On the existence, regularity and decay of the solutions. *J. India Uni. Math.*, 29:639–681, 1980.

[103] Heywood, J.P., Rannacher, R. and Turek, S. Artificial boundaries and flux and pressure conditions for incompressible Navier-Stokes equations. *Int. J. Numer. Math. Fluids*, 22:325–352, 1996.

[104] Hild, P., Ionescu, I.R., Lachand-Robert, T. and Rosca, I. The blocking of an inhomogenous Bingham fluid . Applications to landslides. *Math. Modell. and Numer. Analy.*, 36:1013–1026, 2002.

[105] Hoerner, S.F. *Fluid-Dynamic drag: theoretical, experimental and statisical information*. 1965.

[106] Homeier, H. On Newton type methods with cubic convergence. *J. Comp. Appl. Math.*, 176:425–432, 2003.

[107] Homeier, H. A modified Newton method with cubic convergence: The multivariate case. *J. Comp. Appl. Math.*, 169:161–169, 2004.

[108] Hron, J., Ouazzi, A. and Turek, S. A computational comparison of two FEM solvers for nonlinear incompressible flow. *In Challenges in Scientific Computing. Springer*, Cisc, 2004.

[109] Hsu, J.P., Hsieh, Y.H. and Tseng, S. . Drag forces on a rigid spherical particle in a cylinder filled with Carreau model. *J. Collide and Interface Science*, 284:729–741, 2005.

[110] Hsu, J.P., YeH, S.J. and Tseng, S. Drag on a sphere in a dispersion containing Carreau fluid. *Powder Technology*, 183:34–41, 2008.

[111] Hughes, TJR. and Brooks, AN. A multidimensional upwind scheme with no crosswind diffusion. *In Finite Element Methods for Convection Dominated Flows, AMD*, 34, Hughes TJR(ed.). ASME: New York, 1979.

[112] Hughes, T.J.R, Franca, L.P. and Balestra, M. A new finite element formulation for computational fluid mechanics: V. Circumventing the Babuska-Brezzi condition: A stable Petrov-Galerkin formulation of the Stokes problem accommodating equal order interpolation. *Comp.Meth.Appl.Mech.Eng.*, 59:85–99, 1986.

[113] Huilgo, R.R., Mena, B. and Piau, J.M. Finite stopping time problems and Rheometry of Bingham fluids. *J. Non-Newt. Fluid Mech.*, 10:97–107, 2002.

[114] Huilgol, R.R. and Panizza, M.P. On the determination of plug flow region in a Bingham fluids through the application of varitional inequalities. *J. Non-Newtonian Fluid Mech.*, 58:207–217, 1995.

[115] Huyakorn, P.S., Taylor, C., Lee, R.L. and Gresh, P.M. A comparison of various mixed interpolation finite elements in the veocity pressure formulation of the Navier-Stokes equations. *Comp. Fluids*, 6:25–35, 1978.

[116] Ionescu, I.R. and Sofonea, M. The blocking property in the study of the Bingham fluid. *Int. J. Engrg Sci.*, 3:289–297, 1986.

[117] Jie, P. and Ke-Qin, Z. Drag force of interacting coaxial spheres in viscoplastic fluids. *J. Non-Newt. Fluid Mech.*, 135:83, 2006.

[118] John, V. Higher order finite element methods and multigrid solvers in a benchmark problem for the 3D Navier-Stokes equations. *Int. J. Numer. Math. Fluids*, 40:775–798, 2002.

[119] John, V. Analytical and numerical results for a class of LES models in large eddy simulation of turblent incompressible flows. *Springer-Verlag*, 34, 2004.

[120] John, V. and Mathies, G. Higher order finite element discretizations in a benchmark problem for incompressible flows. *Int. J. Numer. Meth. Fluids*, 37:885–903, 2001.

[121] John, V., Knobloch, P., Mathies, G., and Tobiska, L. Non-nested multilevel solvers for finite element discretisations of mixed problems. *computing*, 68, 2002.

[122] John, V., Maubach, J.M. and Tobiska, L. Nonconforming streamline diffusion finite element method for convection-diffusion problems. *Numer. Math.*, 78:2002, 1997.

[123] Johnson, C. *Numerical solution of partial differential equations by finite element method*. Cambridge University Press, 1987.

[124] Kaplicky, P., Malek, J. and Stara, J. Full regularity of weak solutions to a class of nonlinear fluids in two-dimensions-stationary periodic problem. *Comment.Math.Uni.Carolinae*, 38:681–695, 1997.

[125] Kilian, S. Ein verallgemeinertes Gebietszerlegungs/Mehrgitterkonzept auf Parallelrechnern. *PhD thesis, TU Dortmund*, 2001.

[126] Kilian, S. ScarRC als verallgemeinerter Mehrgitter-und Gebietszerlegungsansats für parallele Rechnerplatt-formen. *Logos Verlag, Berlin*, ISBN 3-8325-0092-8, 2002.

[127] Kim, S.D., Lee, Y.H. and Shin, B.C. Newton's method for Navier-Stokes equations with finite element initial guess of Stokes equations. *Comp. and Math. with Appl.*, 51:805–816, 2006.

[128] Kim, S.W. and Decker, R.A. Velocity-pressure integrated versus penalty finite element methods for high Reynolds number flows. *Int. J. Numer. Methods Fluids*, 9(1):43–57, 1989.

[129] Knobloch, P. Discrete Friedrichs' and Korn's inequalites in two and three dimensions. *East-West J. Numer. Math.*, 4:35–51, 1996.

[130] Knobloch, P. and Tobiska, L. On Korn's first inequality for quadrilateral nonconforming finite elements of first order approximation properties. *Int. J. Numer. Analy. Modell.*, 2(4):439–358, 2005.

[131] Köster, M. Robuste Mehrgitter-Krylowraum-Techniken fur FEM-Verfahren. *TU Dortmund*, Diplomarbeit, 2004.

[132] Kuzmin, D. Positive finite element schemes based on the flux-corrected transport procedure. *Comp. Fluid Solid Mech.*, pages 887–888, 2001.

[133] Kuzmin, D. and Turek, S. High resolution FEM-TVD schemes based on a fully multidimensional flux limiter. *Tech. Report, TU Dortmund*, Ergebnisbericht Nr. 229, April 2003.

[134] Kuzmin, D., Loehner, R. and Turek, S. Fulx-corrected transport. *Principles Alogritms and Applications*, Springer, 2005.

[135] Ladyzhenskaya, O.A. *The mathematical theory of viscous incompressible flow*. Gordon and Breach, London, 1969.

[136] Ladyzhenskaya, O.A. New equations for the description of the viscous incompressible fluids and solvability in the large if the boundary value problems for them. *Boundary Value Problems of Mathematical Physics V, Am. Math. Soc., Providence RI*, 1970.

[137] Linke, A., Mathies, G. and Tobiska, L. Non-nested multigrid solvers for mixed divergence free Scott-Vogelius discretizatons. *Computing*, 83(2-3):87–107, 2008.

[138] Lions, J.L. *Quelques methodes de resolution des problemes aux limites non lineaires*. Dunod, Gauthier-Villars,Paris, 1969.

[139] Liu, B.T., Muller, S.J. and Denn, M.M. Convergence of a regularization method for creeping flow of a Bingham material about rigid sphere. *J. Non-Newt. Fluid Mech.*, 102:179, 2002.

[140] Liu, B.T., Muller, S.J. and Denn, M.M. Interaction of two rigid spheres translating collinearly in creeping flow in a Bingham material. *J. Non-New. Fluid Mech.*, 113:49, 2003.

[141] Liu, H., Bau, H.H. and Hu, H. On the translation of a cylinder in a long tube. *Physics of Fluids*, 16(4):998–1007, 2004.

[142] Loula, A.F.D. and Gurreiro, J.N.C. Finite element analysis of nonlinear creaping flow. *Comput. Methods Appl. Mech. Engrg*, 79:87 – 109, 1990.

[143] Lube, G. and Tobiska, L. A nonconforming finite element method of streamline diffusion type for the incompressible Navier-Stokes equation. *J. Comp. Math.*, 8:147–158, 1990.

[144] Mahnken, R. A Newton-multigrid algorithm for elasto-plastic/viscoplastic problems. *Computational Mechanics*, 15:408–425, 1995.

[145] Malek, J., Necas, J. and Ruzicka, M. On the Non-Newtonian incompressible fluids. *Math. Models Methods Appl. Sci.*, 3:35–63, 1993.

[146] Malek, J., Necas, J. and Ruzicka, M. *Weak and measure valued solutions to evolutionary PDEs*. Champman & Hall, London, 1996.

[147] Malek, J., Necas, J. and Ruzicka, M. On weak solutions to a class of Non-Newtonian incompressible fluids in bounded three-dimensional domains. The case $p \geq 2$. *Adv. Diff. Equ.*, 6:257–302, 2001.

[148] Malek,J., Rajagobal, K.R. and Ruzicka, M. Existence and regularity of solutions and stability of the rest state for fluids with shear dependent viscosity. *Math. Models Methods Appl. Sci.*, 5:789–812, 1995.

[149] Malkus, D.S. Eigenproblems associated with the discrete LBB-condition for incompressible finite elements. *Int.J.Eng.Sc.*, 19:1299–1310, 1981.

[150] Malvern, L.E. *Introduction to the Mechanics of a continuous medium*. Prentice Hall Englewood Cliffs, New Jersey, 1969.

[151] Manouzi, H. and Fahloul, M. Mixed finite element analysis of a non-linear three-fields Stokes model. *IMA J. Numer. Anal*, 21:143–164, 2001.

[152] Masud, A. and Kwoek, J. A stabilized mixed finite element method for the incompressible shear rate dependent Non-Newtonian fluids: variational multiscale framework and consistent linearization. *Comput. Meth. Appl. Mech. Engrg*, 200:577–596, 2011.

[153] Mckinley, G. *Transport process in bubbles, drops and particles*. second ed. Taylor&Francis, New York, 2002.

[154] Merkak, O., Jossic, L. and Magnin, A. Spheres and interaction between spheres moving at very low velocities in a yield stress fluid. *J. Non-Newt. Fluid Mech.*, 133:99, 2006.

[155] Minev, P.D. and Shopov, P.J. XV Nat. summer school, Numerical methods and applications,Varna,1989. *Publ.HES"V.Lenin,"Sofia*, 39:1001–1011, 1990.

[156] Mishler, C., Hulshof, S.J., Brummelen, V. and De Borst, R. A monolithic approach to fluid structure interaction. *Computer & Fluids*, 33:839–848, 2004.

[157] Mitsoulis, E. Numerical simulation of confined flow of Polyethylene melts around a cylinder in a planar channel. *J.Non-Newt. Fluid Mech.*, 76:327–350, 1998.

[158] Mitsoulis, E. On creeping drag flow of a viscoplastic fluid past a circular cylinder: Wall effects. *Chem. Eng. Sc.*, 59:789–800, 2004.

[159] Möller, M., Kuzmin, D. and Turek, S. Implicit finite element discretizations based on the flux-corrected transport algorithms. *Int. J. Numer. Meth. Fluids*, 47(10):1197–1203, 2005.

[160] Mosolov, P.P. and Miasnikov, V.P. Variational methods in the theory of the fluidity of a viscoplastic medium. *J.Mech.Appl.Math.*, 29(3):468–492, 1965.

[161] Mosolov P.P. and Miasnikov V.P. On stangnant flow regions of a viscous plastic medium in pipes. *J.Mech.Appl.Math.*, 30(4):705–717, 1966.

[162] Mosolov, P.P. and Miasnikov, V.P. On qualititive singularties of the flow of a viscoplastic medium in pipes. *J.Mech.Appl.Math.*, 31(3):581–585, 1967.

[163] Nitsche, J. On Korn's second inequality. *R.A.I.R.O*, 15:562–580, 1981.

[164] O'Donovan, E.J. and Tanner, R.I. Numerical study of Bingham squeeze film problem. *J. Non-Newtonian Fluid Mech.*, 15:75–83, 1984.

[165] Oldroyd, J.G. Two dimensional plastic flow of a Bingham solid. *Proc. Camp. Phil. Soc.*, 43:383–395, 1947.

[166] Ouazzi, A. *Finite Element Simulation of Nonlinear Fluids. Application to Granular Material and Powder*. Shaker Verlag, 2006. ISBN 3-8322-5201-0.

[167] Papanastasio, T., Georgiou, G. and Alexandrou, A. *Viscous Fluid Flow*. CRC Press,BocaRaton, 1999.

[168] Papanastasiuo, T.C. Flow of materials with yield. *J.Rheol.*, 31:385–404, 1987.

[169] Patankar, S.V. and Spalding, D.B. A calculation procedure for heat and mass transfer in three-dimensional parabolic flows. *Int.J. Heat Mass Transfer*, 15:1787–1806, 1972.

[170] Patnana, V.K., Bharti, R.P. and Chabra, R.P. Two-dimensional unsteady flow of power-law fluids over a cylinder. *Chem. Eng. Sci.*, 64:2978–2999, 2009.

[171] Potapov, A., Spivak, R., Lavrenteva, O. and Nir, A. Motion and deformation of drops in Bingham fluids. *Ind. Eng. chem. Res.*, 45:6895–6995, 2006.

[172] Prager, W. On slow viscoplastic flow, studies in Mathematics and Mechanics. *Academic Press*, volume presented to Richard von Mises, 1954.

[173] Prohl, A. and Ruzicka, M. On fully implicit space-time discretization for motions of incompressible fluids with shear-dependent viscosities: the case $p \leq 2$. *Siam J. Numer. Anal.*, 39:214–249, 2001.

[174] Putz, A. and Frigaard, I.A. Creeping flow around particles in a Bingham fluid . *J.Non-Newt. Fluid Mech.*, 165:263 – 280, 2010.

[175] Putz, A.M.V., Burghelea, T.I., Frigaard, I.A. and Martinez, D.M. Settling of an isolated spherical particle in a yield stress shear thinning fluid. *Physics of Fluids*, 20:1–11, 2008.

[176] Rannacher, R. Numerical analysis of the Navier-Stokes equations. *Appl. Math.*, 38:No.4–5(361–380), 1993.

[177] Ranncher, R. and Turek, S. Simple non-conforming quadrilateral Stokes element. *Num. Meth. P.D.E.*, 8:97–111, 1992.

[178] Rodrigue, D., Dee Kee, D. and Chan Man Fong, C.F. Bubble velocities: further developments on the jump discontinuity. *Chem. Eng. Commun.*, 67:325–334, 1996.

[179] Roquet, N. and Saramitto, P. An adaptive finite element method for viscoplastic fluid flows in pipes. *Comp.Meth.Appl.Mech.Eng.*, 190:5391–5412, 2000.

[180] Roquet, N. and Saramitto, P. An adaptive finite element method for Bingham fluid flows around a cylinder. *Comput. Meth. Appl. Mech. Eng.*, 192:3317–3341, 2003.

[181] Ruzicka, M. A note on steady flow of fluids with shear dependent viscosity. *Nonl. Anal. Theo. Meth. Appl.*, 30:3029–3039, 1997.

[182] Sahu, A.K., Chhabra, R.P. and Eswaran, V. Two-dimensional laminar flow of a power-law fluid across a confined square cylinder. *J. Non-Newt. Fluid Mech.*, 165:752–763, 2010.

[183] Sanchez, F.J. Application of a first order operator splitting method to Bingham fluid flow simulation. *Computers Math. Appl.*, 36:71–86, 1998.

[184] Sandri, D. Sur l'approximation numerique des ecoulements quasi-Newtoniens dont la viscosite suit la loi puissance ou la loi de Carreau. *Math. Model. Anal.*, 27:131–155, 1993.

[185] Sandri, D. A posteriori estimators for mixed finite element approximations of a fluid obeying the power law. *Comp. Methods Appl. Mech. Engrg*, 166:329–340, 1998.

[186] Schieweck, F. Parallele Lösung der stationaeren inkompressiblen Navier-Stokes Gleichungen . *Otto-von Guericke Uni. Magdeburg, Fakuetaet fuer Mathematik*, Habilitation, 1997.

[187] Schieweck, F. and Tobiska, L. A nonconforming finite element method of upstream type applied to the stationary Navier-Stokes equations. *R.A.I.R.O. Modelisation Math. Anal.*, 23(4):627–647, 1989.

[188] Schieweck, F. and Tobiska, L. An optimal order error estimate for an upwind discretization of the Navier-Stokes equations. *Numer. Meth. P.D.E.*, 12:407–421, 1996.

[189] Schmachtel, R. Robuste lineare und nichtlineare Lösungsverfahre fuer die inkompressiblen Navier-Stokes Gleichungen. *Universität Dortmund*, Ph.D. thesis, 2003.

[190] Scott, L.R. and Vogelius, M. Norm estimates for a maximal right inverse of the divergence operator in spaces of piecewise polynomials. *Modelisation Mathematique et Analyse Numerique*, 19:111–143, 1985.

[191] Shopov, P.J. and Iordanov, Y.I. Numerical solution of Stokes equations with pressure and filteration boundary conditions. *J. of Comp. Physics*, 112:12–23, 1994.
[192] Shwedov, F.N. La rigidite de liquides. *Rapport Congr.Intern. Phys., Paris*, 1:478–486, 1900.
[193] Simo, J.C. and Hughes, T.J.R. *Computational inelasticity*. New York:Springer-Verlag, 1998.
[194] Sivakumar, P., Bharti, R.P. and Chhabra, R.P. Effect of power-law index on critical parameters for power-law flow across an unconfined circular cylinder. *Chem. Eng. Sci.*, 61:6035–6046, 2006.
[195] Sofonea, M. Variational inequalities with blocking property. *Int.J.Engrg Sci.*, 20:1001–1007, 1982.
[196] Stenberg, R. Analysis of mixed finite elements methods for the Stokes problem: a unified approach. *Mathematics of Computation*, 42(165):9–23, 1984.
[197] Stenberg, R. On the construction of optimal mixed finite element methods for the linear elasticity problem. *Numer. Math.*, 48:447–462, 1986.
[198] Stenberg, R. On the some three-dimensional finite elements for icompressible media. *Comp. Meth. Appl. Mech. Eng.*, 63:261–269, 1987.
[199] Stenberg, R. Error analysis of some finite element methods for the Stokes problem. *Math. Comp.*, 54(190):495–508, 1988.
[200] Stokes, G.G. On the theories of internal friction of fluids in motion and of the equilibrium and motion of elastic solids. *Trans. Cambridge Phil. Soc.*, 8:287, 1845.
[201] Stynes, M. and Tobiska, L. The streamline diffsion method for nonconforming q_1^{rot} elements on rectangular tensor product meshes. *IMA J. Numer. Analy.*, 21:123–142, 2001.
[202] Suttmeier, F. An adaptive displacement/pressure finite element scheme for treating incompressibilty effects in elasto-plastic materials. *Numer. Meth. for PDE*, 17(4), 2001.
[203] Tabata, M. and Fujima, S. Finite element analysis of high Reynolds number flows past a circular cylinder. *J. Comp. Appl. Math.*, 38:411–424, 1991.
[204] Tabata, M. and Tagami, D. Error estimates for finite element approximations of drag and lift in Nonstationary Navier-Stokes flows. *Japan J. Appl. Math.*, 17:371–389, 2000.
[205] Taylor, A.J. and Wilson, S.D.R. Conduit flow of an incompressible yield stress fluid. *J. Rheol.*, 41:93–101, 1997.
[206] Taylor, C. and Hughes, T.G. Finite element programming of the Navier-Stokes equation. *Pineridge Press*, Swansea,1980.
[207] Temam, R. *Navier-Stokes equations*. North-Holland, Amesterdam, 1977.
[208] Tobiska, L. and Verfürth, R. Analysis of streamline diffusion finite element method for the Stokes and Navier-Stokes equations. *SIAM J. Numer. Analy.*, 33(1):107–127, 1996.
[209] Tokpavi, D.L., Jay, P. and Magnin, A. Interaction between two circular cylinder in slow flow of Bingham viscoplastic fluid. *J. Non.Newt. Fluid Mech.*, 157:175–187, 2009.
[210] Tokpavi, D.L., Magnin, A. and Jay, P. Very slow flow of Bingham viscoplastic fluid around a circular cylinder. *J. Non-Newt. Fluid Mech.*, 154:65–76, 2008.
[211] Turek, S. Ein robustes und effizientes Mehrgitterverfahren zur Lösung der instationären inkompressiblen 2D Navier-Stokes Gleichung mit diskret divergenzfreien finiten Elementen. *Universität Heildelberg*, Dissertation, 1991.
[212] Turek, S. Tools for simulating non-stationary incompressible flow via discretely divergence free finite element models. *Int. J. for Numer. Methods in Fluids*, 18:71–105, 1994.
[213] Turek, S. A comparative study of time stepping techniques for the incompressible Navier-Stokes equations: From fully implicit non-linear schemes to semi-implicit projection methods. *J. Numer. Meth. Fluids*, 22(10):987–1011, 1996.
[214] Turek, S. *Efficient solvers for incompressible flow problems: An algorithmic and computational approach*. Springer, 1999. LNCSE 6.
[215] Turek, S. and Ouazzi, A. Unified edge–oriented stabilization of nonconforming FEM for incompressible flow problems: Numerical investigations. *J. Numer. Math.*, 15:299–322, 2007.
[216] Turek, S. and Schäfer, M. Benchmark computations of laminar flow around cylinder. In E. H. Hirschel, editor, *Flow Simulation with High-Performance Computers II*, volume 52 of *Notes on Numerical Fluid Mechanics*, pages 547–566. Vieweg, 1996. co. F. Durst, E. Krause, R. Rannacher.

[217] Turek, S., Ouazzi, A., and Schmachtel, R. Multigrid methods for stabilized nonconforming finite elements fo incompressible flow involvig the deformation tensor formulation. *J. Numer. Math*, 10:235–248, 2002.

[218] Vanka, S. Block-implicit multigrid calculation of two dimensional recirculating flows. *Comp. Meth. Appl. Mech. Eng.*, 59(1), 1986.

[219] Verfürth, R. Erorr estimates for a mixed finite element approximation of the Stokes equation. *R.A.I.R.O Anal Numer.*, 18:175–182, 1984.

[220] Vola, D., Boscardin, L. and Latche, J.C. Laminar unsteady flows of Bingham fluids: a numerical strategy and some benchmark results. *J.Comp.Physics*, 187:441–456, 2003.

[221] Von Karman, T. Über den Mechanismus dem Widerstands, den ein bewegter Korper in einer Flussigkeit erfahrt. *Gottingen Nachr. Math. Phys. Kl. 12(512)*, 1912.

[222] Wang, Y. Finite element analysis of the duct flow of Bingham plastics fluids: an application of the variational inequality. *I.J.Numeric Methods Fluids*, 25:1025–1042, 1997.

[223] Wathen, A.J., Silvester, D.J. and Elman, H.C. *Finite element and fast iterative solvers*. Oxford University Press.

[224] Wesseling, P. Theoritical and practical aspects of a multigrid methods. *siam J.sci stat. comput*, 3(4):387–407, 1982.

[225] Wolf,J. Existence of weak solutions to the equations of non-stationary motion of Non-Newtonian fluids with shear dependent viscosity. *J.Math.Fluid.Mech.*, 9:104–138, 2007.

[226] Yoshioka, N., Adachi, K. and Ishimura, H. . On creeping flow of a viscolastic fluid past a sphere. *Kagaku Kogaku*, 10:1144, 1971.

[227] Yoshioka, N., Adachi, K., Nakamura, A. and Ishimura, H. An experimental investigation of viscoplastic flow past a circular cylinder at high Reynolds numbers. *Rheol. Acta*, 14:993, 1975.

[228] Yoshioka, N. and Adachi, K. On variational principles for a Non-Newtonian fluid. *J. Chem. Eng. Japan*, 4:217, 1971.

[229] Yoshioka, N. and Adachi, K. Some deductions from the extremum principles for Non-Newtonian fluids. *J. Chem. Eng. Japan*, 6:134, 1973.

[230] Yoshioka, N. and Adachi, K. Problems of Non-Newtonian fluid flow. *Kagaku Kagaku*, 38:727, 1974(in Japanise).

[231] Yoshioka, N. and Nakamura, R. On the creeping flow of generalized Newtonian fluid around a shpere. *Kagaku Kagaku*, 4:130, 1966.

[232] Zdravkovich, M.M. *Flow around circular cylinders Vol1 : Fundementals*. Oxford University Press, New York, 1997.

[233] Zhang, Y. Error estimates for the numerical approximation of time-depenedent flow of Bingham fluid in cylinderical pipes by the regularization method. *Numer. Math.*, 96:153–184, 2003.

[234] Zhanlav, T., Chuluubaatar, O. and Ankhbayar, G. On Newton-type methods with fourth and fifth-order convergence. *Bullrtin of BFUR series Mathematics. Information sciences. Physics*, 2(2):29–34, 2010.

[235] Zhu, H. and De Kee, D. A numerical study for the cessation of Coutte flow of Non-Newtonian fluids with a yield stress. *J. Non-Newt. Fluid Mech.*, 143:64–70, 2007.

[236] Zisis, T. and Mitsoulis, E. Viscoplastic flow around a cylinder kept between parallel plates. *J. Non-Newtonian Fluid Mech.*, 105:1–20, 2002.